Advances in Diffusion Magnetic Resonance Imaging with Application to Multiple Sclerosis

by

Diana Valdés Cabrera

A thesis submitted in partial fulfillment of the requirements for the degree of

Doctor of Philosophy

Department of Biomedical Engineering

University of Alberta

© Diana Valdés Cabrera, 2022

Abstract

Multiple Sclerosis (MS) is a chronic neurodegenerative disease which is mainly characterized by inflammation, demyelination, and axonal loss. Conventional Magnetic Resonance Imaging (MRI) has become the most established imaging tool in the diagnosis and follow-up of MS in clinical practice. However, the high sensitivity of these standard MRI techniques is mainly restricted to the detection of focal demyelinating MS lesions, mainly in white matter (WM), as they fail to depict further damage in normal appearing WM (NAWM) and grey matter (GM) involvement. More advanced quantitative MRI methods, including diffusion MRI, have been applied in MS research and they have improved the detection and interpretation of heterogeneous MS pathologic features in lesions and in normal-appearing brain tissue. Abnormal diffusion tensor imaging (DTI) metrics, although not fully pathologically specific, have helped characterize the disease burden with progression and they have shown correlations with several disability and cognitive measures in MS. So far, MS DTI studies with consistent results and interpretations are still uncommon in the clinical practice. Furthermore, research diffusion MRI studies properly targeting small brain structures such as the limbic system WM and deep GM, or even areas with crossing fibers in MS are also rare and show conflicting results. This is largely because these experiments require careful considerations regarding acquisition protocols (e.g., high spatial resolution, imaging artifacts) and post-processing strategies (e.g., eddy currents correction, tensor fitting, higher order models).

This thesis aims to address these MS literature gaps and limitations by using advanced diffusion MRI methods in two cross sectional datasets of individuals diagnosed with MS over four chapters, the first in cohort 1 at 4.7 T and the final three in cohort 2 at 3 T: (i) high resolution DTI tractography of limbic WM tracts, (ii) CSF-suppressed DTI tractography of the fornix, (iii) high

resolution DTI of the hippocampus, and (iv) novel b-tensor encoding diffusion MRI in lesions and NAWM. Data presented here reveal new information on how small WM and GM structures such as the fornix and the hippocampus, which are linked to cognitive and mood disorders in several neurodegenerative diseases, appear to be affected early and consistently in MS regardless of the patient's phenotypic classification and disability status. Cross sectional analyses in the two MS cohorts studied here reveal robust reductions of fornix volume and abnormal diffusion metrics such as low fractional anisotropy (FA) and higher mean (MD), axial (AD), and radial (RD) diffusivities when compared to controls. Other affected limbic areas in terms of atrophy or microstructure include the uncinate fasciculus, thalamus and hippocampus, with fornix RD and thalamus atrophy standing out as predictors of cognitive impairment in MS. Hippocampus atrophy, abnormal diffusion metrics and long T2 values are reported in MS patients with cognitive impairment (CI), while greater regional mean diffusivity (MD), potentially indicative of demyelination, is evident in MS subjects independent of their CI status when compared to controls. This regional hippocampus analysis shows elevated MD and T2 relaxometry values, which are variable and widespread in MS, greater in patients with CI and high lesion volume, and linked with disability in the case of T2 relaxometry. In addition, b-tensor diffusion metrics complement standard metrics, and they differ between lesions and NAWM and between different WM fiber configurations in MS and controls. In conclusion, this thesis outlines a repertoire of advanced diffusion MRI methods, which has shown important insight about the limbic system microstructural changes as well as lesion and NAWM alterations in MS and their relationships with memory and behaviour.

Preface

This thesis is an original work by Diana Valdés Cabrera. All research projects for which this thesis was a part received ethics approval from the University of Alberta Research Ethics Board. All subjects were scanned at the Peter S. Allen MRI Research Centre in the University of Alberta Hospital and written informed consent was obtained from all patients and controls included here. The four research chapters of this dissertation contain unique contributions to the international MRI research community.

Chapter 2 of this thesis has been published as Valdés Cabrera, D., Stobbe, R., Smyth, P., Giuliani, F., Emery, D., Beaulieu, C. "Diffusion tensor imaging tractography reveals altered fornix in all diagnostic subtypes of multiple sclerosis". Brain Behav. 2020, 10:e01514, https://doi.org/10.1002/brb3.1514. Data for this chapter was acquired on a Varian 4.7 T MRI system (N=39) initially by Dr. Robert Stobbe (24 MS and 3 control subjects) and then assisted and performed by me in the latest stages of the acquisition (4 MS and 8 control subjects). Patient recruitment was done at the Multiple Sclerosis Clinic (Kaye Edmonton Clinic) by Dr. Penelope Smyth and Dr. Fabrizio Giuliani, and the cognitive and clinical battery of MS tests were performed by the registered MS nurses Leah White and Roxane Billey. I conducted the literature review and all other aspects of the work, including image processing, statistical analysis, and figure creation. I wrote the full manuscript with the feedback and guidance of my co-authors. DTI data from supplementary analyzed white matter (WM) tracts, not reported in this chapter, were utilized in the published sodium MRI manuscript: Stobbe R, Boyd A, Smyth P, Emery D, Valdés Cabrera D, Beaulieu C. "Sodium Intensity Changes Differ Between Relaxation- and Density-Weighted MRI

in Multiple Sclerosis". Front Neurol. 2021, 12:693447, https://doi.org/10.3389/fneur.2021.693447.

Chapter 3 of this thesis has been published as Valdés Cabrera, D., Smyth, P., Blevins, G., Emery, D., Beaulieu, C. "Diffusion imaging of fornix and interconnected limbic deep grey matter is linked to cognitive impairment in multiple sclerosis". European Journal of Neuroscience, 55(1), 277–294, https://doi.org/10.1111/ejn.15539. Data for Chapters 3, 4, and 5 was acquired on a Siemens Prisma 3 T MRI system (N=86) largely by myself (43 MS patients, 11 healthy controls). The remaining healthy controls were selected from a larger normative study on healthy brain development by carefully choosing their age and sex to be comparable to the MS cohort. They were similarly scanned by other lab members (Dr. Sarah Treit, Dr. Pascal Tetreault, Dr. Graham Little, Kevin Solar and Emily Stolz) in a time period that partially overlapped with the MS patient data acquisition. Patient recruitment was done at the Multiple Sclerosis Clinic (Kaye Edmonton Clinic) by Dr. Penelope Smyth and Dr. Gregg Blevins and the cognitive and clinical battery of MS tests were performed by me after receiving training from the MS nurse Leah White together with the cognitive test manuals. I conducted all literature review, image and statistical analysis, created all figures and wrote the manuscript with the feedback and guidance of my co-authors.

Chapter 4 has not been previously published but is currently under review for publication as Valdés Cabrera, D., Smyth, P., Blevins, G., Solar, K.G., Emery, D., Beaulieu, C. "High Resolution Diffusion Tensor Imaging and T2 Mapping Detect Regional Changes within the Hippocampus with Links to Cognitive Impairment in Multiple Sclerosis". The original T2 mapping code was developed by former members of Dr. Alan Wilman's Lab (Dr. Mark Lebel and Dr. Kelly McPhee). I performed all literature search, code modifications, image processing and statistical analysis, and

created all figures. I wrote the full manuscript draft currently under review with guidance from my co-authors.

Chapter 5 is an original contribution to this thesis and has not been published elsewhere. The original image acquisition protocols and post-processing analysis framework applied here were developed by Dr. Markus Nilsson and Dr. Filip Szczepankiewicz from Lund University in Sweden. All other aspects of the work, including slight protocol modifications, image quality assessment, processing, statistical analysis, figure creation, and writing the full manuscript draft were performed by me with the feedback and assistance of my co-authors.

Dedication

To the women in my life, my mother and grandmother, thanks for everything.

To my husband…

“You can't suddenly know something just by assembling a committee of words. That's it! I'll assemble your committee!”

— Professor Farnsworth

“Sometimes, science is more art than science, Morty. A lot of people don’t get that.

— Rick Sanchez

Acknowledgements

This work was funded by the Canadian Institutes of Health Research (CIHR) and the United States National MS Society. Specifically, I would like to thank the Multiple Sclerosis Society of Canada for partially providing support for my salary and to the University of Alberta and the Alberta Multiple Sclerosis Network for national travel support. I would like to thank all the students and faculty in the Department of Biomedical Engineering at the University of Alberta. Thanks to Maisie Goh, Carol Hartle, and Dr. Alan Wilman for their administrative and student support over the years. Thanks to Peter Seres for all the help designing, setting up, and troubleshooting my protocols and all the great MRI scanning advice and support. Thanks to all members of the Beaulieu lab who provided help with my research, especially Dr. Robert Stobbe for his appreciated technical expertise. Thanks to Dr. Gregg Blevins for helping me recruiting MS participants from his clinical practice. Thanks to the registered MS nurses for helping on the cognitive testing, mainly Leah White for providing me with the knowledge and the manuals that allowed me to screen MS patients by myself. Thanks to my supervisory committee for providing insightful feedback, mainly Dr. Penelope Smyth for her always positive replies and great advice regarding multiple sclerosis, and for allowing me to shadow her in her clinical practice. Thanks to my supervisor Dr. Christian Beaulieu for sharing his research ideas, feedback and funding through my PhD program. Finally, thanks to my family and friends for all their immense support over the years. Especially to my mom and my husband Kevin for their blind confidence in me and for making all my days brighter. I could not have accomplished this without both of you by my side. Thanks to my little MC.

Table of Contents

List of Tables

List of Figures

List of Symbols and Abbreviations

γ: Gyromagnetic ratio (MHz/Tesla)

δ: Duration of the diffusion gradients

$\lambda_{1, 2, 3}$: Diffusion ellipsoid eigenvalues

τ: Gradient time

φ: Spin phase shift

ω: Larmor frequency

μFA: Microscopic fractional anisotropy

2D: Bidimensional

3D: Tridimensional

9-HPT: 9-Hole Peg Test

ACID: Artefact Correction in Diffusion MRI

AD: Axial diffusion

ADC: Apparent diffusion coefficient

ADNI: Alzheimer's Disease Neuroimaging Initiative

AUC: Area under the curve

BBB: Blood-brain barrier

BDI-II: Beck Depression Inventory-II

BET: Brain Extraction Tool

BICAMS: Brief International Cognitive Assessment for MS

BVMT-R: Brief Visual Memory Test Revised

BW: Bandwidth

CA: Cornu ammonis

CIS: Clinically isolated syndrome

CMSC: Consortium of Multiple Sclerosis Centres

CNS: Central nervous system

CSD: Constrained spherical deconvolution

CSF: Cerebrospinal fluid

D: Diffusion coefficient

D: Diffusion tensor

DDE: Double diffusion encoding

DG: Dentate gyrus

DIVIDE: Diffusional variance decomposition

DKI: Diffusion kurtosis imaging

DTD: Diffusion tensor distribution

DTI: Diffusion tensor imaging

DWI: Diffusion weighted image

EADC: European Alzheimer's Disease Consortium

$E_\lambda[\boldsymbol{D}]$: Isotropic diffusivities

EC: Entorhinal cortex

ECMOCO: Eddy current/motion correction

EDSS: Kurtzke Expanded Disability Status Scale

EPG: Extended Phase Graph

EPI: Echo-Planar Imaging

FA: Fractional anisotropy

FACT: Fiber assignment by continuous tracking

FDR-BH: Benjamini-Hochberg False Discovery Rate

FID: Free induction decay

FWE: Free water elimination

FLAIR: FLuid Attenuated Inversion Recovery

FOD: Fiber orientation distribution

FOV: Field of view

FSE: Fast Spin-Echo

FSL: FMRIB Software Library

FT: Fourier transform

G: Gradient strength

GM: Grey matter

Gd: Gadolinium

GRAPPA: GeneRalized Autocalibrating Partially Parallel Acquisitions

HARDI: High Angular Resolution Diffusion Imaging

Harp: Harmonized Hippocampal Protocol

ICC: Intracranial cavity

isoVF: Isotropic signal fraction

LST: Lesion Segmentation Tool

M: Magnetization vector

MAGNIMS: Magnetic Resonance Imaging in Multiple Sclerosis

MD: Mean diffusion

MFIS: Modified Fatigue Impact Scale

MK: Mean kurtosis

MK_a: Anisotropic diffusional variance

MK_i: Isotropic diffusional variance

MK_t: Total diffusional variance

MNI: Montreal Neurological Institute

MPRAGE: Magnetization Prepared RApid Gradient Echo

MRI: Magnetic resonance imaging

MS: Multiple sclerosis

NAIMS: North American Imaging in Multiple Sclerosis

NDI: Neurite density index

NMR: Nuclear magnetic resonance

NODDI: Neurite Orientation Dispersion and Density Imaging

NSA: Number of signal averages

ODI: Orientation dispersion index

qMAS: Magic angle spinning of the q-vector

QTI: q-space trajectory imaging/encoding

PASAT: Paced Auditory Serial Addition Test

PEC: Patch-based Ensemble Corrector

PGSE: Pulsed Gradient Spin Echo

PPMS: Primary progressive MS

PROPELLER: Periodically Rotated Overlapping ParallEL Lines with Enhanced Reconstruction

RARE: Rapid Acquisition with Relaxation Enhancement

RD: Radial diffusion

RESTORE: Robust estimation of tensors by outlier rejection

RF: Radiofrequency

RI-NLM: Rotation-invariant multi-contrast non-local means

RIS: Radiologically isolated syndrome

ROC: Receiver operator curve

ROI: Region of interest

RRMS: Relapsing remitting MS

SDE: Single diffusion encoding

SDMT: Symbol Digit Modalities Test

SLM: Stratum lacunosum moleculare

SLR: Shinnar-Le Roux

SNR: Signal to noise ratio

SPACE:

SPM: Statistical Parametric Mapping

SPMS: Secondary progressive MS

SRLM: Stratum radiatum lacunosum moleculare

SS-EPI: Single-shot EPI

T25-FW: Timed 25-Foot Walk

TBSS: Tract-based spatial statistics

TDE: Triple diffusion encoding

TE: Echo time

TI: Inversion time

TR: Repetition time

TLN: Total lesion number

TLV: Total lesion volume

TSE: Turbo Spin-Echo

$V[\boldsymbol{D}_i]$: Variance of the distribution of isotropic diffusivities

WM: White matter

1. Introduction

This chapter briefly describes the human brain from brain cell structure and function to the overall brain matter areas known to be greatly affected in multiple sclerosis (MS). Specific brain regions associated with cognitive functions, fatigue and depression, which are additionally impacted by MS and later assessed in the research contributions of this thesis, are likewise illustrated here. Furthermore, the chapter outlines essential theoretical concepts needed to understand Magnetic Resonance Imaging (MRI) techniques, mainly diffusion MRI methods used throughout this dissertation. Finally, an overview of MS is presented, as the disease that motivated this thesis, and a summary of MS diagnosing and monitoring MRI techniques mainly established in the clinical but also in the research practice are reviewed here, with a focus on diffusion MRI and its current literature gaps in MS.

1.1. The Human Brain

1.1.1. From Brain Cells to Brain Matter

Brain cells encompass two major types: the neurons and the non-neuron cells called glia. The human brain has around 100 billion neurons, outnumbered by nearly 10 times more glial cells [1]. The neurons transmit information between different brain areas, and between the brain and the rest of the nervous system, through electrical impulses and chemical signals [2], [3]. A neuron has three basic parts (Figure 1.1A): the cell body or soma; the dendrites that branch off the cell body and receive information from adjacent neurons through synapses; and the axon, frequently myelinated, which is a long extension of the cell body where the action potential from the cell

body travels through, synapses, and then it is received by neighboring cell's dendrites. There are several neuronal subtypes with different structure, polarity, axonal length, among other features. The glial cells consist mainly of oligodendrocytes, astrocytes, ependymal cells and microglia. They carry out numerous functions [4], [5], such as the formation of myelin sheaths around axons performed by the oligodendrocytes (Figure 1.1A), and homeostasis and biochemical support of the blood-brain barrier performed by the astrocytes (Figure 1.1A), although many of these functions are still unknown to a certain extent. As opposed to the neurons, which are mainly formed by the time we are born, glial cells are capable to multiply through the lifespan and they can repair neurons after injury, but they can also malfunction and have key roles in neurodegenerative diseases [6], such as MS.

At the macrostructural level, geometrically arranged packs of myelinated axons, together with oligodendrocytes, astrocytes and microglia comprise the white matter (WM) (Figure 1.1D). The WM connects other brain parenchyma areas (e.g., the outer surface of the brain called the cortex with deep 'nuclei' areas, such as the basal ganglia) called grey matter (GM) (Figure 1.1D), which is mainly made of cell bodies, dendrites, and glia. The cerebrospinal fluid (CSF) is a clear fluid that surrounds and cushions the brain (Figure 1.1D), but also circulates nutrients, chemicals and removes brain waste products. Immune cells, pathological antibodies, cytokines and other molecules that indicate inflammation in the central nervous system (CNS), are present in the CSF of MS patients and serve as biomarkers for MS diagnosis and therapy [7]. A meta-analysis paper that analyzed a large sample of 7539 adults over 21 previous studies, reported average volumes of 488 cm^3 for total WM, 692 cm^3 for GM and 159 cm^3 for CSF at the age of 20 [8]. WM volume

increases with age until ~45 years and then decreases, GM decreases with age in a linear fashion through adulthood [8], [9], while CSF linearly increases with age [8]. Abnormal total WM and GM volumes and more specific regional atrophy have been reported in the early stages of several neurological diseases like MS [10], [11]. The brain is structured into the cerebrum, the cerebellum and the brain stem. The cerebrum is further split into two cerebral hemispheres, each subdivided mainly into four lobes identifiable on the cerebral cortex and the limbic lobe on the medial surface (Figure 1.1C).

1.1.2. White Matter, Axons and Myelin

The WM is located underneath the cortical GM, and it is mainly composed of insulated axon bundles or tracts that link neurons from different brain regions into functional circuits. These axons are coated with a 'white' tightly compressed cell membrane called myelin (Figure 1.1B), which wraps up to 150-160 times around them (and up to 60 times in the corpus callosum and cortex) [12], [13] leaving small gaps (nodes of Ranvier), effectively providing them with insulation to achieve the high-speed transmission of information through saltatory electrical impulses [14]. The myelin is a substance rich in lipids and proteins produced by the oligodendrocytes within the central nervous system (CNS), and its cytoplasmic and extracellular water components can be measured at a macroscopic level with myelin water fraction imaging [15]. Its damage can impair or even halt conduction and therefore different brain functions, causing the neurologic signs and various symptoms often displayed in MS.

WM keeps developing and undergoing myelination until the third decade of life [16]. Even though not all axons in WM tracts are myelinated or fully myelinated, there is a great degree of microscopic variability in the number of myelinated axons, myelin thickness and internodal length between and within WM tracts [17], and both the radial and the longitudinal dimensions of CNS myelin sheaths are coupled to axon diameter [13]. The WM forms densely packed bundles of myelinated nerve fibers, also called tracts or fascicles (Figure 1.1E), which are further classified according to which areas they connect into projection (cortex with other areas in the CNS), commissural (the same cortical area in opposite hemispheres) and association (different areas in the same hemisphere) tracts.

1.1.3. Deep Grey Matter

The GM in the brain is classified into the cerebral cortex (Figure 1.1F), surrounding WM in each cerebral hemisphere (out of the scope of this thesis), and several deep GM structures (Figure 1.1F) that are located under the cortex and beneath the WM within each cerebral hemisphere. One major deep GM structure is the thalamus, which also has some areas of WM [18], and comprises different nuclei in charge of the relay of sensory and motor signals, regulation of awareness, sleep and wakefulness, and is also involved in learning and episodic memory [19] due to its connection to other limbic structures such as the hippocampus and the fornix via the mammillothalamic tract [20]. Another vital GM structure located within the medial temporal lobe is the hippocampus, also part of the limbic system, which plays a key role in regulating learning, memory encoding, memory consolidation, and spatial navigation [21]. The basal ganglia (e.g., caudate, putamen, globus

pallidus, substantia nigra) is a group of small GM structures involved primarily in motor control, but also motor learning, behavior, and emotions.

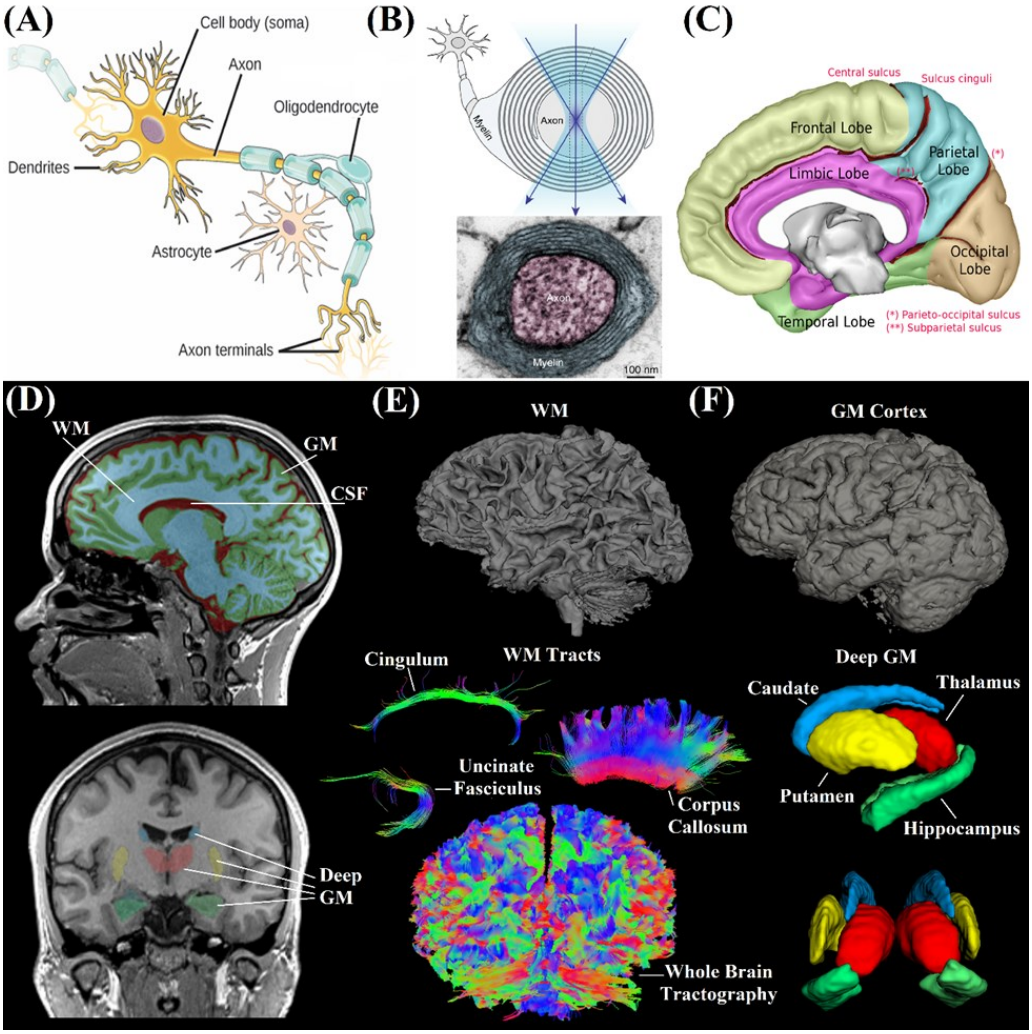

Figure 1.1: Overview of brain structure. Adapted from WikimediaCommons (A&C; public domain) and from [22] (B, under a Creative Commons Attribution 4.0 International License http://creativecommons.org/licenses/by/4.0/) showing (A) a typical neuron; (B) a schematic cross-sectional view of the myelinated axon with a corresponding cross-sectional image of a myelinated axon in the mouse brain obtained using transmission electron microscopy; (C) the frontal, temporal, parietal, occipital, and limbic brain lobes; (D) sagittal and coronal T1-weighted MRI from a 29-year-old healthy female subject with white (WM) and grey matter (GM), including several deep GM structures, and cerebrospinal fluid (CSF) segmentations performed in Volbrain; (E) 3D rendered WM and whole brain tractography with several WM tract examples; and (F) 3D rendered cortical and deep GM structures from the same subject.

1.1.4. The Limbic System: Fornix-Hippocampus-Thalamus Connections

The limbic system was first described by Paul Broca in 1878 as the curved rim of the cortex which includes the cingulate and the parahipoccampal gyri (Figure 1.1C), although it was James Papez in 1937 who first described its involvement in emotion [23]. The limbic system plays an important role in memory, emotions and behavior and there is no general agreement on all the cortical and subcortical GM and WM structures that comprise it [24]. Overall, this system comprises three nested arches (outer, middle and inner) (Figure 1.2A). The outer arch includes the different portions of the parahippocampal gyrus starting at the uncus, then curves inward at the isthmus of cingulate gyrus, and ends at the subcallosal area. The middle arch starts with the hippocampus and ends at the paraterminal gyrus, and the inner arch starts at the alveus, progresses to the fimbria, and continues through the rest of the fornix [25].

The fornix is the major efferent pathway of the hippocampus and connects it with the mammillary bodies in the hypothalamus and with the anterior nuclei of the thalamus (Figure 1.2B) [26]. It is a discrete, C-shaped WM tract located in the medial aspect of the cerebral hemispheres, which contains ~1.2-2.7 million fibers in each hemisphere [27]. The fornix is mainly divided into the fimbria, crus (crura for both hemispheres), body, and columns (Figure 1.2B). The fornix starts at the level of the alveus, a strip of WM fibers arising from the pyramidal cells of the hippocampus. The alveus runs along the superior lateral surface of the hippocampus and extends posteriorly under the ependymal surface of the lateral ventricle to become the fimbria (Figure 1.2B, C) [25]. The fimbria continues posteriorly and splits from the hippocampus, beneath the splenium of the corpus callosum, to become the crus of the ipsilateral fornix. The two crura keep ascending and

bend below the corpus callosum, mirroring its curvature but tighter. Then, they merge medially to form the fornix body (~0.7 cm wide at the apex and ~2.8 cm wide at the base on an axial plane) [28], which goes forward, and it is attached to the inner surface of the corpus callosum via the septum pellucidum [29]. As the left and right crura join at the midline, they form a thin sheet of crossing fibers called the fornix (or the hippocampus) commissure [30]. The fornix body separates once again at the level of the interventricular foramen of Monro, into the columns and they curve inferiorly toward the anterior commissure in a manner that reflects the areas of origin in the hippocampus [26], [31]. The columns divide into anterior (precommissural) and posterior (postcommissural) fibers. Most of the columns' fibers are postcommissural and they arise from the subiculum of the hippocampus and go mostly to the mamillary bodies, with some contributions to the anterior thalamic, midbrain tegmentum, and red nucleus of the stria terminalis [26]. The precommissural fibers develop into the hippocampal pyramidal cell layer (along with the entorhinal cortex and subiculum) and terminate in the basal forebrain, ventral striatum, and prefrontal cortex [26].

The hippocampus is a bilateral GM structure located in the temporal lobe, forming the medial and inferior borders of the lateral ventricles and surrounded by the entorhinal (EC), parahippocampal and perirhinal cortices. The majority of its neocortical inputs originate from the perirhinal/parahippocampal cortex, through EC, while its outputs are mainly through the subiculum (and then towards the alveus and the fimbria of the fornix), which also projects back to EC [21]. The hippocampus has an elongated seahorse shape in the anterior-posterior direction (Figure 1.2C) with a mean length of 4 to 4.5 cm and a width of 1 to 2 cm [32]. It can be divided

into head (anterior, largest part, with digitations), body (middle part) and tail (posterior, narrowest part) (Figure 1.2C, D). Anatomically, the hippocampus is composed of two laminae interlocking one inside the other: the cornu ammonis (CA) or 'hippocampus proper" and the dentate gyrus (DG), which are separated by the vestigial hippocampal sulcus [32] (Figure 1.2D). CA consist of three GM layers (stratum oriens, stratum pyramidal and the stratum moleculare) divided into four subfields (Figure 1.2D): CA1, which is the largest one, composed of pyramidal cells and triangular soma and located closest to the subiculum; CA2, composed of dense, large and ovoid soma; CA3, composed of less dense mossy fibers; and CA4, also composed of less dense soma cells within the hilus of the DG [32], [33]. DG (Figure 1.2D) is composed by a stratum of granular cells and granular neurons and it process information from EC to CA3 [34], [35]. The granular neurons are afferent and receive the information directly from EC via the perforant path which perforates the subiculum to reach the DG granular cells. The stratum radiatum, lacunosum and moleculare (SRLM) are also important gateways involving EC and CA1, and it contains numerous apical dendrites and axonal bundles parallel to the CA internal surface and blending with the stratum moleculare of DG [36].

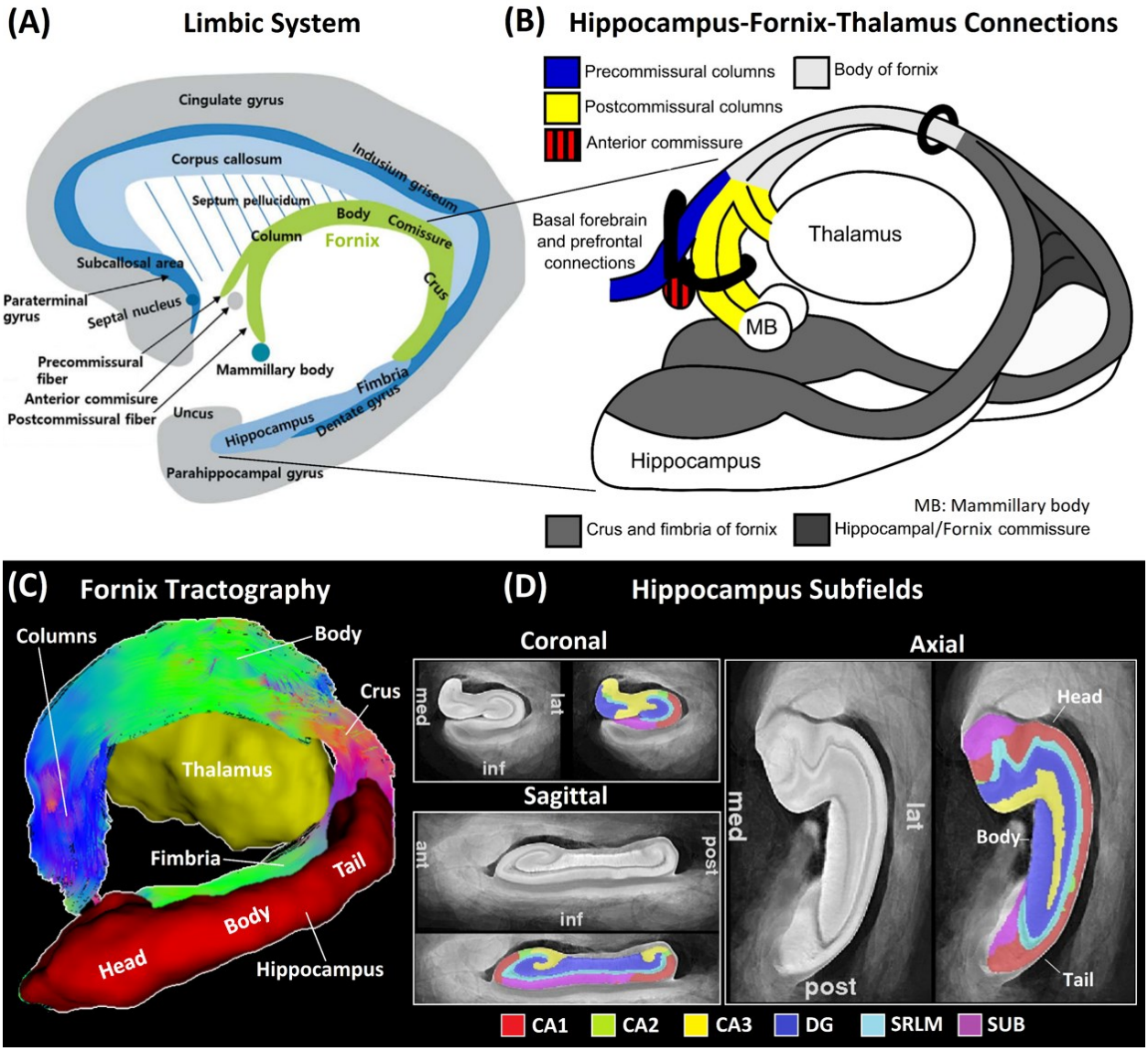

Figure 1.2: The limbic system: Hippocampus and Fornix. Adapted from [25], [37] (A, B under a Creative Commons Attribution 4.0 International License http://creativecommons.org/licenses/by/4.0/) and from [38] (D, under a Proceedings of the National Academy of Sciences of the United States of America (PNAS) License). Schematic diagrams of (A) the three nested arches comprising the limbic system, and (B) the hippocampus-fornix-thalamus connections of the inner limbic arch. (C) 3D rendered fornix tractography (CSF-suppressed) and automatic hippocampus and thalamus segmentations (sagittal view) in a 44-year-old healthy female subject. (D) Hippocampus atlas from multi-slice spin echo MRI (performed on a Varian 9.4T scanner at 200×200×200 μm^3) of 31 ex vivo specimens and its hippocampal subfield segmentation (CA: Cornu ammonis, DG: Dentate gyrus, SRLM: Stratum radiatum lacunosum moleculare, SUB: Subiculum) derived from serial histology in 9 specimens.

1.1.5. Memory and Cognition

Most available research suggests that memory functions are performed by the hippocampus, amygdala and other related limbic structures in the temporal lobe [39], as well as the prefrontal cortex and the cerebellum. The process of memory consolidation appears to be dependent on the hippocampus, fornix and other basal structures of the limbic system, such as the thalamus; and the integrity of the entire Papez circuit is more important than that of its individual structures [26], [37].

Declarative memory, where one can intentionally store and retrieve information, is mainly encoded by the hippocampus, EC, and the perihinal cortex. Semantic memory, which relates to general factual knowledge, is mainly encoded, stored, and retrieved by medial temporal lobe areas, such as the hippocampus and neighboring structures [40]. Research suggests that semantic memories are retrieved from areas of the frontal cortex and stored in areas of the temporal lobe [41], [42], although many other areas of the brain appear to be involved. Implicit memory refers to those acquired and recalled unconsciously and are stored and retrieved by the cerebellum, the basal ganglia (voluntary motor control, procedures, emotions, and other behaviors), the motor cortex, and various areas of the cerebral cortex [43].

1.2. Magnetic Resonance Imaging (MRI)

MRI is an imaging technique used to produce high quality images of the inside of the human body mainly for medical practice and research. It is built on nuclear magnetic resonance (NMR) theories and spectroscopic techniques used for chemical and physical molecular analysis.

1.2.1. MRI Physics and Tissue Relaxation Times

The human body is primarily composed of water (which has two hydrogen atoms or protons) [44]. Hydrogen is the primary nucleus measured with MRI due to its favourable magnetic properties (NMR signal) and abundance in our bodies. The Larmor frequency of a nucleus in a static magnetic field B_0 is calculated from the Larmor Equation:

$$\omega_0 = \gamma B_0, \qquad \text{(Equation 1.1)}$$

where ω_0 is the Larmor frequency (MHz), γ is the gyromagnetic ratio (MHz/Tesla) and B_0 is the strength of the static magnetic field (in Tesla, T). To produce the NMR signal, the external magnetic field B_0 must be static, strong, and uniform; it is used to align the protons that are normally randomly oriented within the water nuclei of the tissue being examined, creating a net magnetization parallel to the B_0 direction (equilibrium magnetization M_0) (longitudinal magnetization $M_z = M_0$ in this equilibrium state). The free induction decay (FID) signal is achieved by tipping the longitudinal magnetization M_z into the transverse plane using a time-varying, external radiofrequency (RF) pulse (B_1, Figure 1.3) at a frequency that matches the Larmor frequency. Then, the transverse component of the net magnetization (M_{xy}) precesses in the transverse plane at the Larmor frequency. The nuclei return to their equilibrium state through

different relaxation processes. Different types of MRI contrast can be achieved by adjusting the flip angles and timing of the RF pulses. The time between successive slice-selective excitation RF pulses applied to the same slice is called the repetition time (TR), and the time between the RF pulse application and the echo signal measurement is the echo time (TE).

Each voxel of an image of the human body contains one or more tissues and the time evolution of their corresponding NMR signals can be characterized by two different relaxation time constants – T1 and T2, introduced by Felix Bloch in 1946 [45] in his equations of the net magnetization vector (M), with longitudinal M_z, and transverse M_{xy} components (Figure 1.3). T1 is the longitudinal relaxation time (or spin-lattice), which establishes the rate at which the excited hydrogen nuclei return to equilibrium as they realign with the B_0 magnetic field. At T1, the M_z vector recovers from 0% to 63% of its original state M_0 (Figure 1.3). T2 is the transverse relaxation time (or spin-spin), which defines the rate at which the excited hydrogen nuclei reach equilibrium due to a loss of spin phase coherence induced by destructive interference from neighboring spins perpendicular to the main B_0 field. At T2, the M_{xy} vector decays to 37% of its original state M_0 (assuming a 90° RF excitation pulse) (Figure 1.3). The NMR signal can be heavily T1, T2 or proton density 'weighted', although it will generally be influenced by these factors all together [46].

The transverse magnetization M_{xy} has its maximum when all protons are initially precessing in phase, but it decreases when protons start going out of phase due to interactions at the atomic and molecular levels. Transverse relaxation (R2, reciprocal to T2) is mainly produced by the intrinsic field caused by adjacent protons, which is irreversible. However, it is also caused by local but

reversible field inhomogeneities (main magnetic field, magnetic susceptibilities, chemical shift, gradients) which are overall characterized by the T2* relaxation time. This reversible dephasing can be eliminated by applying a 180° pulse, which is known as the basis of the Spin-Echo sequence, where only the 'true' T2 relaxation is achieved [47].

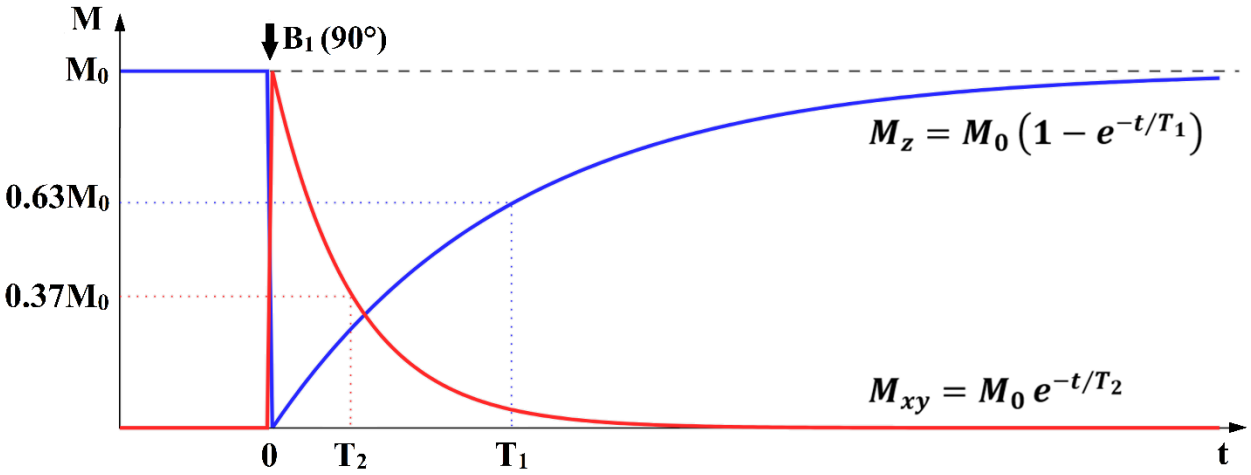

Figure 1.3: Longitudinal (M_z) and transverse (M_{xy}) components of the magnetization vector and their longitudinal (T1) and transverse (T2) relaxation times.

1.2.2. MRI Encoding

When nuclear spins are exposed to a magnetic gradient of strength G their resonance frequency ω changes as a function of their location r along the gradient direction:

(Equation 1.2) $$\omega(r) = \gamma(B_0 + G \cdot r),$$

Different combinations of magnetic field gradients along each orthogonal direction (G_x, G_y, G_z) are utilized to spatially select and encode the NMR signal, as shown in a typical Gradient-Echo pulse sequence (Figure 1.4A). A single slice can be selected by first applying a gradient (in any gradient direction or combination of directions) simultaneously during the application of the RF

pulse. This slice selecting gradient G_z causes the resonant frequency of the spins to deviate from the Larmor frequency by $\Delta\omega$ as a function of its position, z. The RF pulse only interacts with positions where the resonant frequency lies with the RF pulse bandwidth (BW), to create a slice with thickness Δz ($\Delta z = BW/\gamma G_z$). Gradients can be used to alter the phase of the NMR signal. After a gradient is turned off, the resulting spins will have acquired a phase shift (φ) proportional to both the gradient strength G and time τ:

$$\varphi(r) = \gamma(G \cdot r \cdot \tau), \quad \text{(Equation 1.3)}$$

After slice selection, the signal is encoded along the two remaining dimensions using phase and frequency encoding [48], [49]. Both phase-encoding and frequency-encoding gradients work in the same manner but are used for different purposes. A phase encoding gradient is first applied for a fixed length of time and then a frequency encoding gradient is applied at the same time the signal is read out. The frequency encoding gradient strength is typically constant while the signal is read out in increments of time to acquire a set of data points over the frequency range. The sequence of phase encoding followed by frequency encoding is repeated in steps with each step varying the phase encoding gradient strength to sample a 2D grid of frequency space (k-space), which is the Fourier transformation of an image slice (Figure 1.4B).

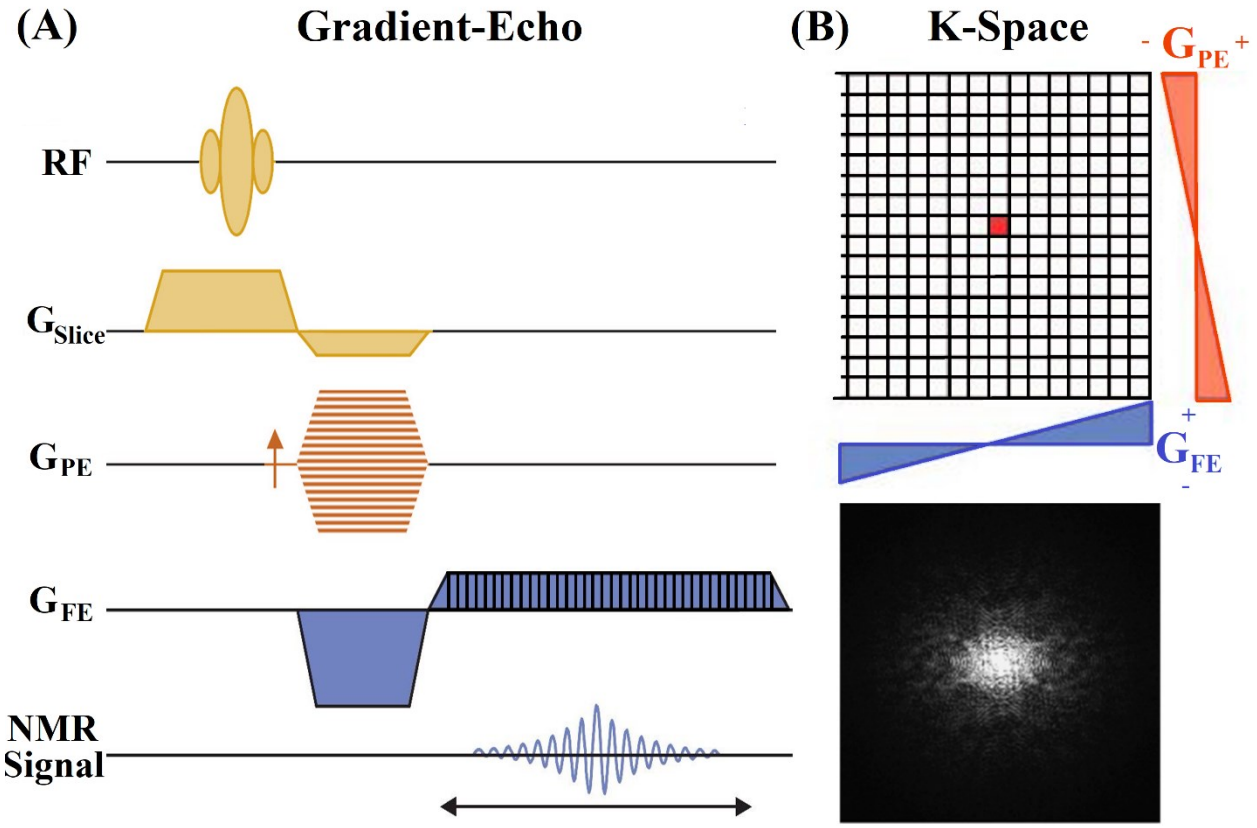

Figure 1.4: Gradient-Echo MRI sequence and k-space. (A) A basic Gradient-Echo pulse sequence where a radiofrequency (RF) pulse begins with slice selection (RF pulse and G_{Slice} in yellow), followed by phase encoding (G_{PE} in red) and frequency encoding (G_{FE} in blue). The phase-encoding gradient is incremented each time the pulse sequence is repeated, and each repetition measures one line in (B) k-space. (B) 2D Fourier transform of the image in a k-space (k_x,k_y). An inverse Fourier transform (FT^{-1}) is applied to k-space to obtain an MR image.

1.2.3. Structural MRI Acquisitions

T1- and T2-weighted sequences are widely used in the clinical practice and many pathological mechanisms are frequently described in terms of T1 and T2 signal behaviour, tissue contrast, anatomical location, and structural volumes. MRI technical advances have been developed to improve spatial resolution (high resolution, 3D imaging) and sensitivity of these already established structural acquisitions. Regional differences in T1- and T2-weighted signal intensity

between WM, GM, CSF, and even between different cortical and subcortical deep GM structures have led to the development of manual and automated segmentation methods, which necessitate high resolution imaging (~1 mm isotropic) to accurately segment and calculate volumes of individual brain structures (e.g., small deep GM structures) and total WM, GM and CSF tissues. Changes in total and regional brain volumes have been reported in many volumetric analyses in both healthy [50]–[52] and disease [53]–[56] cohorts. Likewise, conventional T1-weighted and T2-weighted sequences are also employed to identify and characterize MS pathology beyond total and regional atrophy (e.g., T2 lesion burden, postcontrast enhancement, T1 hypointensities) [57].

T1-weighted images are created by using short TE and TR, thus different tissue contrast and brightness are mostly determined by their T1 properties (Figure 1.5A). In contrast, T2-weighted acquisitions are produced by applying longer TE and TR so that the tissue contrast and brightness are mainly controlled by their T2 properties (Figure 1.5B). For example, fluid tissue like CSF is dark on T1-weighted MRI and bright on T2-weighted MRI. The FLuid Attenuated Inversion Recovery (FLAIR) sequence is also frequently applied in clinical environments (e.g., to depict MS lesions) and it employs an inversion pulse with an appropriate inversion time (TI) delay before the excitation pulse to null signal from CSF, while still keeping T2-weighted contrast (Figure 1.5C) [58]. These structural sequences are vital for the diagnosis of neurodegenerative diseases such as MS and they will be briefly described in the next subsections.

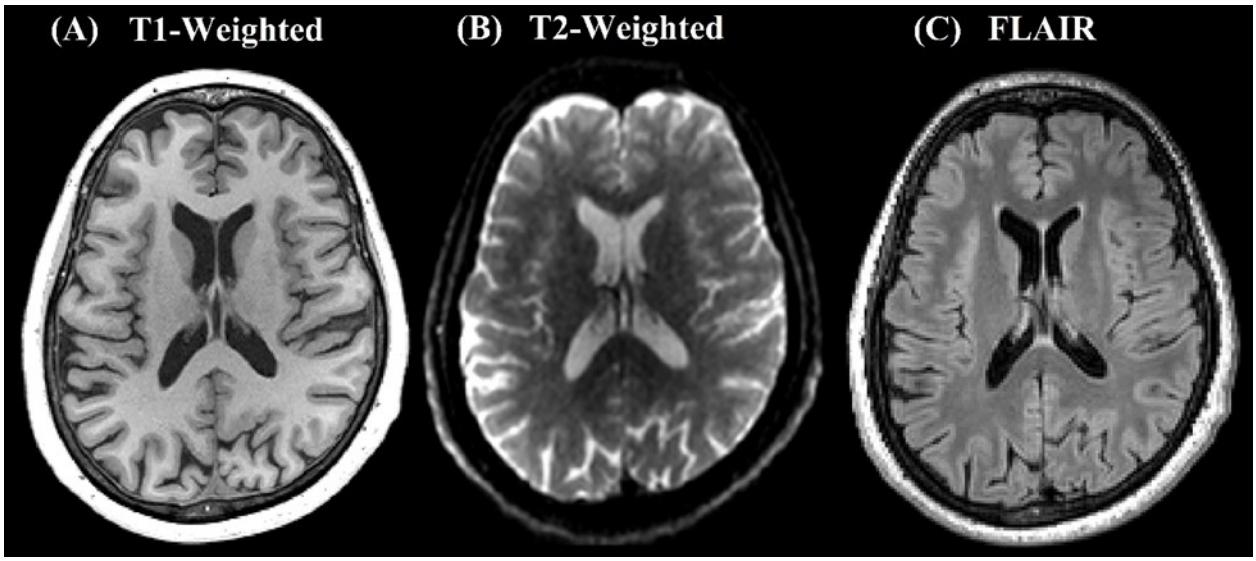

Figure 1.5: T1-weighted, T2-weighted and FLuid-attenuated inversion-recovery (FLAIR) images. Example of (A) T1-weighted MPRAGE, (B) T2-weighted and (C) FLAIR images of a 58-year-old female healthy control.

In addition, Gadolinium-based contrast enhancement MRI agents can be combined with several MRI contrasts such as T1-weighted. Gadolinium (Gd) is a strongly paramagnetic material that can become temporarily magnetized when placed in an external magnetic field. Gd facilitates the relaxation of hydrogen protons on water molecules and it shortens the T1 relaxation times of the tissues where it accumulates making them bright on T1-weighted images. Gd-enhanced T1-weighted images are very useful for MS diagnosis and important for monitoring MS lesion activity [59], as they allow to distinguish ‘acute’ from ‘chronic’ lesions and to detect the breakdown of the blood-brain barrier (BBB) [60] typical of MS (Figure 1.6). However, the selection of the most appropriate T1-weighted sequence after contrast injection is still a matter of debate at lower magnetic fields (e.g., 1.5T) [59], while 3D Gradient-Echo or 3D Fast Spin-Echo sequences at 3.0

T have yielded higher detection rates for Gadolinium-enhancing MS lesions than standard 2D Gradient-Echo sequences in more recent work [61].

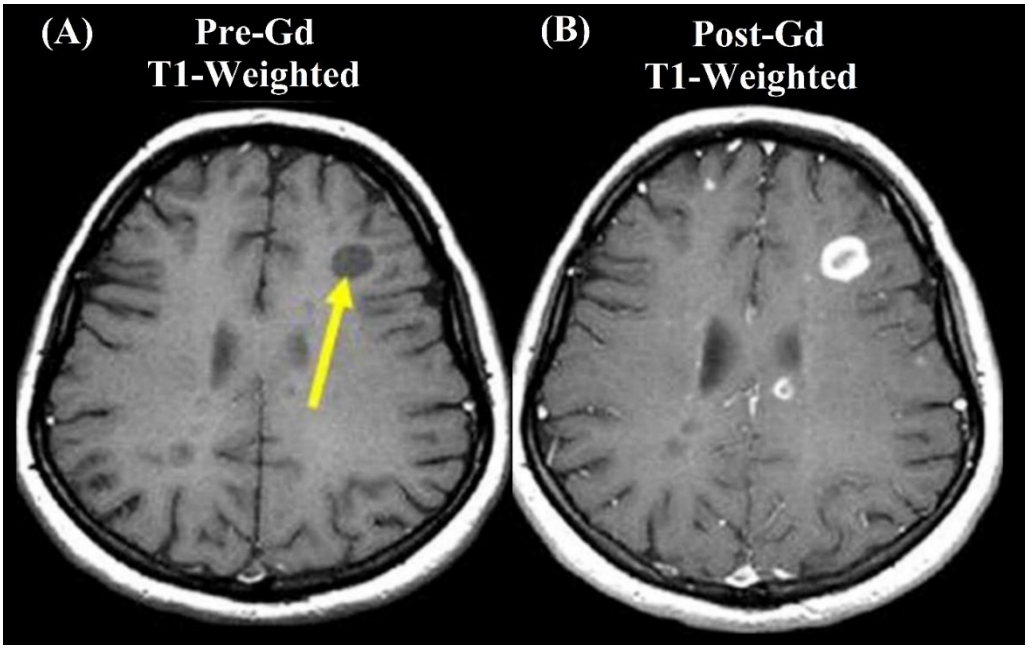

Figure 1.6: Unenhanced T1-weighted and Gadolinium contrast-enhanced T1-weighted MRI. Example of (A) unenhanced pre-Gadolinium injection T1-weighted and (B) contrast-enhanced post-Gadolinium injection T1-weighted images, both obtained at baseline in a relapsing-remitting multiple sclerosis patient (Adapted from [62] and reprinted by permission from SAGE Publications, Ltd., copyright 2013).

1.2.3.1. 3D Magnetization Prepared RApid Gradient Echo (MPRAGE)

MPRAGE stands as a useful sequence for T1-weighted imaging in both the clinical and research practice (Figure 1.5A) due to its high WM/GM signal difference-to-noise, high WM signal-to-noise ratios (SNR) as well as GM SNR suppression (due to longer T1s) [63]. Basic MPRAGE is a 3D technique consisting of the application of a non-selective 180º inversion pulse to invert the longitudinal component of the magnetization vector M_z, which grows back to $+M_z$ due to T1

relaxation mechanisms over the TI period. After this TI period, the signal is read by acquiring spoiled gradient echoes at short TE times of ~2-4 ms and low flip angles α of ~5- 12º. Typical TR and TI times for MPRAGE are ~2000 ms and ~600-900 ms respectively. These parameters are determined by the desired contrast properties of the image, the T1 relaxation properties of the tissues, and the state of the longitudinal magnetization M_z at the end of the Gradient-Echo acquisition [64].

1.2.3.2. T2-weighted MRI

Spin-Echo pulse sequences are largely used to achieve T2-weighted contrast (Figure 1.5B) [47]. In a simple Spin-Echo sequence the 90° RF pulse is followed by a 180° refocusing pulse at TE/2. Then, the signal is read at TE, with a single echo measured during each TR. The Fast Spin Echo technique (FSE, also known as Turbo Spin-Echo (TSE) or Rapid Acquisition with Relaxation Enhancement (RARE)) [65] is more efficient because multiple echoes are recorded per TR, which is achieved by a series of 180º refocusing pulses after the single 90º excitation pulse to generate a train of echoes. The echo train length (or turbo factor) is the total number of echoes acquired in each TR interval. Axial T2-weighted FSE sequences are a reference standard for detecting focal hyperintense T2 lesions in MS regardless of their brain location [59]. Moreover, these are part of the standardized brain MRI protocols for MS diagnosis (recommended 1 mm isotropic voxel resolution at 3 T according to the latest 2021 Magnetic Resonance Imaging in Multiple Sclerosis (MAGNIMS) and Consortium of Multiple Sclerosis Centres (CMSC) consensus recommendations [66]). However, these sequences are optional for the assessment of disease activity and monitoring effectiveness of the disease-modifying treatment if high-quality sagittal

3D T2-weighted FLAIR and multiplanar reconstruction in axial and sagittal planes are available (see table 2 in [66]).

1.2.3.3. FLuid-Attenuated Inversion Recovery (FLAIR)

FLAIR is an inversion recovery sequence (often acquired as T2-weighted) with a long TI needed to remove the CSF signal (Figure 1.5C) [58]. It begins with a 180° pulse, which reverses the longitudinal magnetization M_z for all tissues, which regrows via T1-relaxation. When M_z of CSF is close to zero at the end of the TI interval, it will produce a small or zero signal contribution to the reconstructed image. For FSE acquisitions, TI can be derived from the following equation:

$$TI = T1\left[ln\ 2 - ln\left(1 + e^{-(TR - TE_{last})/T1}\right)\right], \quad \text{(Equation 1.4)}$$

where TE_{last} is the time of the last echo, thus recovery could start after the last refocusing pulse. When TR>>T1, equation 1.4 reduces to TI ≈ 0.69 x T1. TI values are 3000 ms and 1800 ms for 2D and 3D FSE FLAIR at 4.7 T and 3 T, respectively (TI values reported in Research Chapters for FLAIR protocols performed in this thesis). Like T2-weighted images, FLAIR is largely employed for T2 lesion detection in demyelinating disorders such as MS. These lesions appear hyperintense on T2-weighted images and the high signal intensity of CSF often precludes their visibility in periventricular areas with conventional T2-weighted images but not with FLAIR [67]. Both 2D and 3D FSE FLAIR (3D FSE is called Sampling Perfection with Application optimized Contrasts using different flip angle Evolution (SPACE) in Siemens MRI scanners) have been applied in MS, with sagittal 2D or 3D FLAIR scans deemed as mandatory for baseline MS diagnosis in earlier consensus [59]. 3D FLAIR has been stated as “preferable” over 2D FLAIR in

the latest revisions of the McDonald MS diagnostic criteria due to its improvement of lesion detection and the possibility of realignment of anatomical orientation that is necessary to detect new lesions when comparing serial MRI scans [66]. Furthermore, several MS studies have reported improved lesion detection in supratentorial and infratentorial regions in MS with 3D FLAIR when compared to 2D FLAIR [68], [69].

1.2.4. Transverse Relaxation (T2) Mapping

The transverse magnetization M_{xy} is characterized by the exponential decay of the NMR signal in the transverse plane with a T2 relaxation time constant (discussed in Section 1.2.1). Quantification of T2 relaxation times provides an absolute measure of the transverse relaxation independent of other factors, which plays an important role for in vivo tissue characterization in healthy and diseased human brain [70], [71]. Multicomponent multi-echo T2 relaxation measurements in healthy brain tissue, such as myelin water imaging, can generally separate the NMR signal into three T2 components (long, intermediate and short). The long T2 (> 2 s) is attributed to CSF, the intermediate T2 (~80 ms) is associated with intra/extracellular water, and the short T2 component (~20 ms) is credited to water trapped between myelin bilayers called myelin water [70], [72]. In order to measure the shortest T2 component, as it is aimed with myelin water fraction (MWF), the echo spacing should ideally be as short as possible (10 ms or less), typically 32 echoes, and the echo train should exceed 1 s reporting only noise in the last echoes [71]. In MS, for example, several previous multicompartmental T2 relaxation studies have shown brain water content abnormalities with a focus on lower MWF in both normal appearing WM (NAWM) and lesions in MS when compared to healthy WM [73]–[77].

Additionally, single component analyses that measure the voxel mean T2 relaxometry values can identify increased water content occurring in WM pathology that arise from other water reservoirs such as edema or inflammation [72], [78], [79]. Longer T2 times have been considered an indicator of neuronal damage in MS, caused by pathology like demyelination and inflammation/edema, as seen in WM lesions and in NAWM beyond lesions [72], [78], [80], [81] but also in cortical normal appearing GM (NAGM) [82]. Furthermore, shorter T2 times (also reflected by longer transverse relaxation rates R2=1/T2) have become a reliable measure of brain iron accumulation mainly at high MRI fields and have been reported in deep GM and basal ganglia structures such as the caudate, globus pallidus, pulvinar nucleus of the thalamus, and substantia nigra of MS patients [83], [84].

T2 relaxometry mapping can be performed by using the Carr-Purcell-Meiboom-Gill sequence [85], [86], which is a multi-echo Spin-Echo protocol consisting of a 90° pulse and followed by a train of 180° refocusing pulses. These refocusing pulses are 90° out of phase to reduce the effects of imperfect 180° pulses [85], however perfect 180° refocusing pulses at 3 T or higher field strengths are impractical to achieve due to slice profile variations, B_1 calibration errors, and RF inhomogeneity [87], [88]. T2 can be determined by modeling the spin response from multi-echo spin echo experiments with existing fitting methods such as the Extended Phase Graph (EPG) with Fourier slice approximations [89][90], or Bloch simulations [91], which yield accurate T2 values despite imperfect refocusing pulses by employing computational modelling of the signal response for all echo pathways. The EPG model with Shinnar-Le Roux (SLR) slice profiles [92] have been evaluated and compared with other fitting methods providing excellent results in most cases when

SNR is adequate and sufficient data points are available (Figure 1.7) [93], and it was utilized in Chapter 4 of this thesis to evaluate T2 values in the hippocampus in MS.

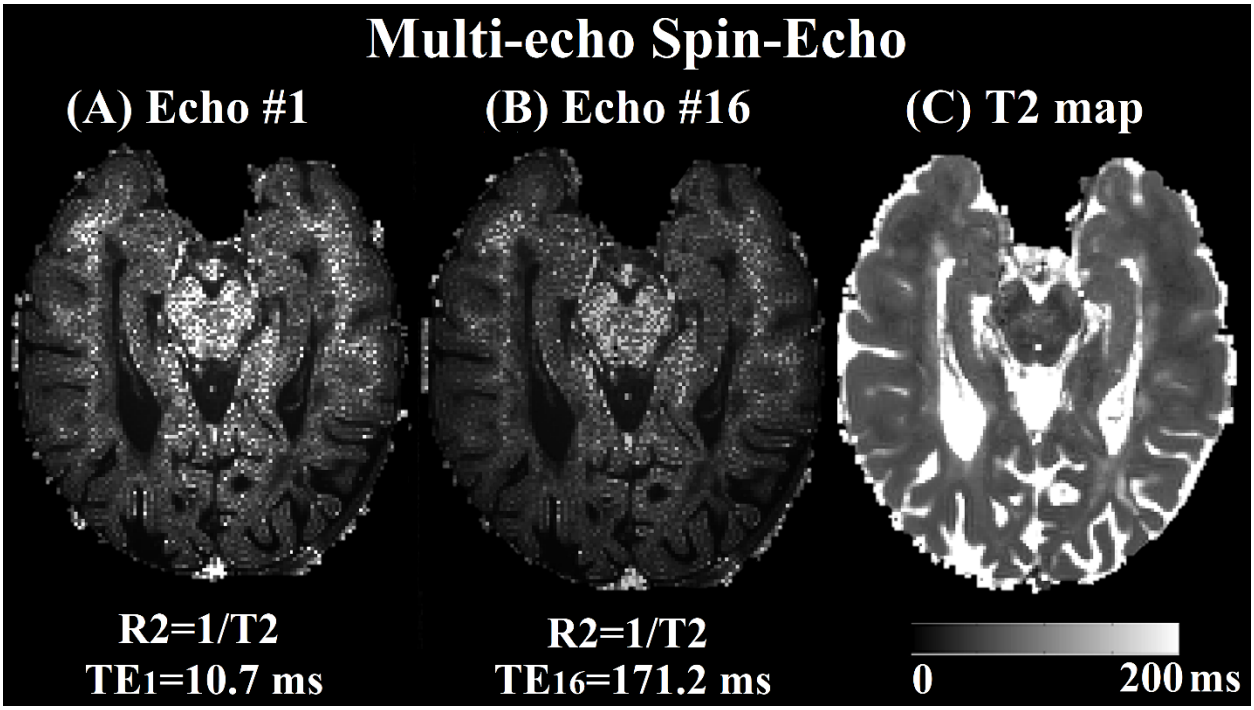

Figure 1.7: Multi-echo Spin-Echo Images acquired from transverse T2 relaxometry mapping of the hippocampus. Images were acquired with axial-oblique orientation along the long axis of the hippocampus in a 34-year-old relapsing-remitting MS male subject. Single slice Spin-Echo R2 images (1/T2) for the (A) first and (B) last echo of a train of 16 echoes, acquired with a TR of 3.56 s at 3 T. (C) T2 relaxometry map calculated with the Extended Phase Graph model with Shinnar-Le Roux slice profiles.

1.2.5. Diffusion MRI

Another type of contrast or 'weighting' of the NMR signal is by the diffusion of water molecules, called diffusion weighted imaging (DWI). This dissertation is strongly focused on different advanced diffusion MRI techniques and their application to MS. Their basics, imaging analyses and applications will be described in the next following subsections.

1.2.5.1. Background and Acquisition

Water molecules are in constant and random movement caused by thermal energy (Brownian motion). According to Einstein [94], when the medium is homogeneous and there are no boundaries, the diffusion of water molecules is free and will have a mean squared displacement $\langle r^2 \rangle$ which depends on the diffusion time t and the diffusion coefficient D of the substance.

$$\langle r^2 \rangle = 2Dt \quad \text{(Equation 1.5)}$$

However, in biological tissues, water molecules are restricted as they interact with cell membranes and macromolecules, and they are confined in the intracellular or extracellular space. The contributions of the water pools within these microscopic spaces vary as they are dependent on the tissue biological features and susceptible to several processes (e.g., cellular swelling, edema) and pathologies (e.g., ischemic and chronic strokes, necrotic tumors, gliomas). During these random diffusion walks, the water molecules probe the tissue microscopic structure at a resolution beyond MRI. Characteristic diffusion times of ~50 ms, assuming the average diffusion coefficient of biological tissues at body temperature (~1.0 x 10^{-3} mm^2/s), allow the water molecules to randomly move ~10 μm in the brain as they interact with several tissue and cellular components. Then the diffusion signal observed in a DWI voxel (~8 mm^3 resolution in standard acquisitions) represents the average displacement distribution of the water molecules within this voxel which are associated to the structural and geometric organization of the underlying microstructural compartments [95]. Diffusion can become more directional or anisotropic when there are oriented geometric barriers hindering the water in specific directions, such as in WM [95], [96]. In organized WM axonal

bundles, water molecules can travel along the length of the axon, and perpendicular movement is restricted mainly by membranes and myelin [97], [98]. Therefore, we can infer information about the tissue microenvironment by measuring its diffusion properties.

Recalling the basics of MRI and image encoding (discussed in Sections 1.2.1 and 1.2.2), when a linear gradient is applied it modifies the frequency of precession of the protons by spatially varying the magnetic field they perceive according to Equation 1.2. The NMR signal could be sensitized to diffusion by employing a pair of "dephasing/rephasing" gradients [99] (Figure 1.8). After applying an RF excitation pulse, protons at different locations precess at the same frequency. When a gradient is applied, protons at different locations perceive different magnetic fields and resonate at different frequencies, depending on their locations. After the application of this first "dephasing" gradient, protons will be out of phase (Equation 1.3) leading to an overall NMR signal loss. If a second "rephasing" gradient is applied with identical strength and length but opposite polarity to the first gradient, and there are no diffusing protons, then the 'refocusing' will be perfect as the rephasing gradient will cancel the phase difference induced by the dephasing gradient, and the corresponding NMR signal will be strong (see the "without motion" pixel example in Figure 1.8). In the case of diffusing protons (exemplified as the three pairs of protons switching locations during the diffusion time between the "dephasing/rephasing" gradients in Figure 1.8), the rephasing gradient does not eliminate the phase differences of the diffusing protons and the corresponding NMR signal will be weaker (see the "with motion" pixel example in Figure 1.8).

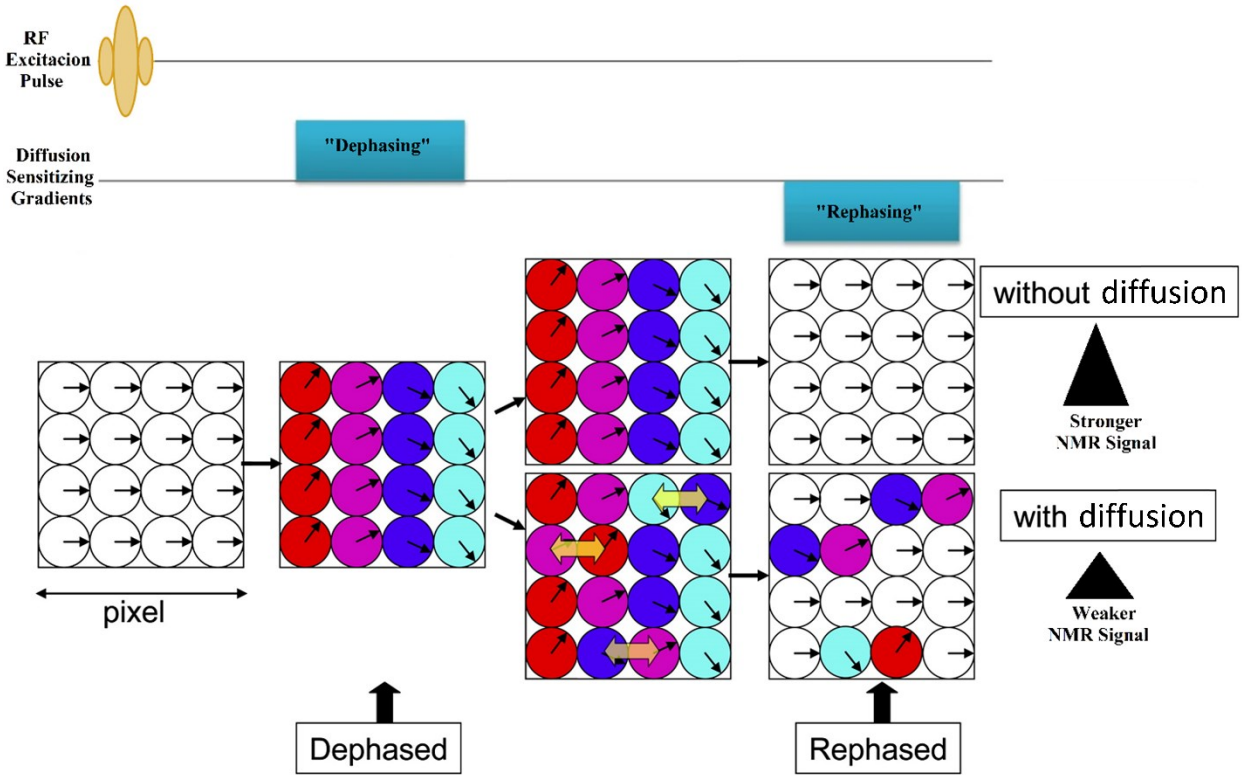

Figure 1.8: Schematic representation of the dephasing/rephasing diffusion sensitizing gradients and the behavior of stationary and moving spins. Each circle represents proton spins at different locations in a pixel while the arrows within the circles indicate the phase's location. If protons move within the direction of the gradient, between the two gradient applications (indicated by yellow arrows), the rephasing gradient cannot perfectly refocus the phases, which leads to signal loss. (Adapted from [99] and reprinted by permission from Elsevier, License Number 5301061095313).

1.2.5.2. Diffusion MRI Pulse Sequences: Echo Planar Imaging

In general, diffusion MRI measures the diffusion of spins by applying a Pulsed Gradient Spin Echo (PGSE) method [100], which consists of a pair of pulsed gradients on a spin-echo sequence (Figure 1.9) [47]. The diffusion gradients must be strong, and they are applied on either side of the 180° RF pulse with the same duration, amplitude, and direction (the 180° RF pulse is equivalent to the opposite polarity of the dephasing/rephasing diffusion gradients in Figure 1.8). The first diffusion

gradient is applied between the 90° RF pulse and the 180° refocusing pulse, causing the spins to dephase in its direction. The second gradient is applied between the 180° refocusing pulse and the signal readout, so that the stationary spins reverse any phase accumulated from the first gradient.

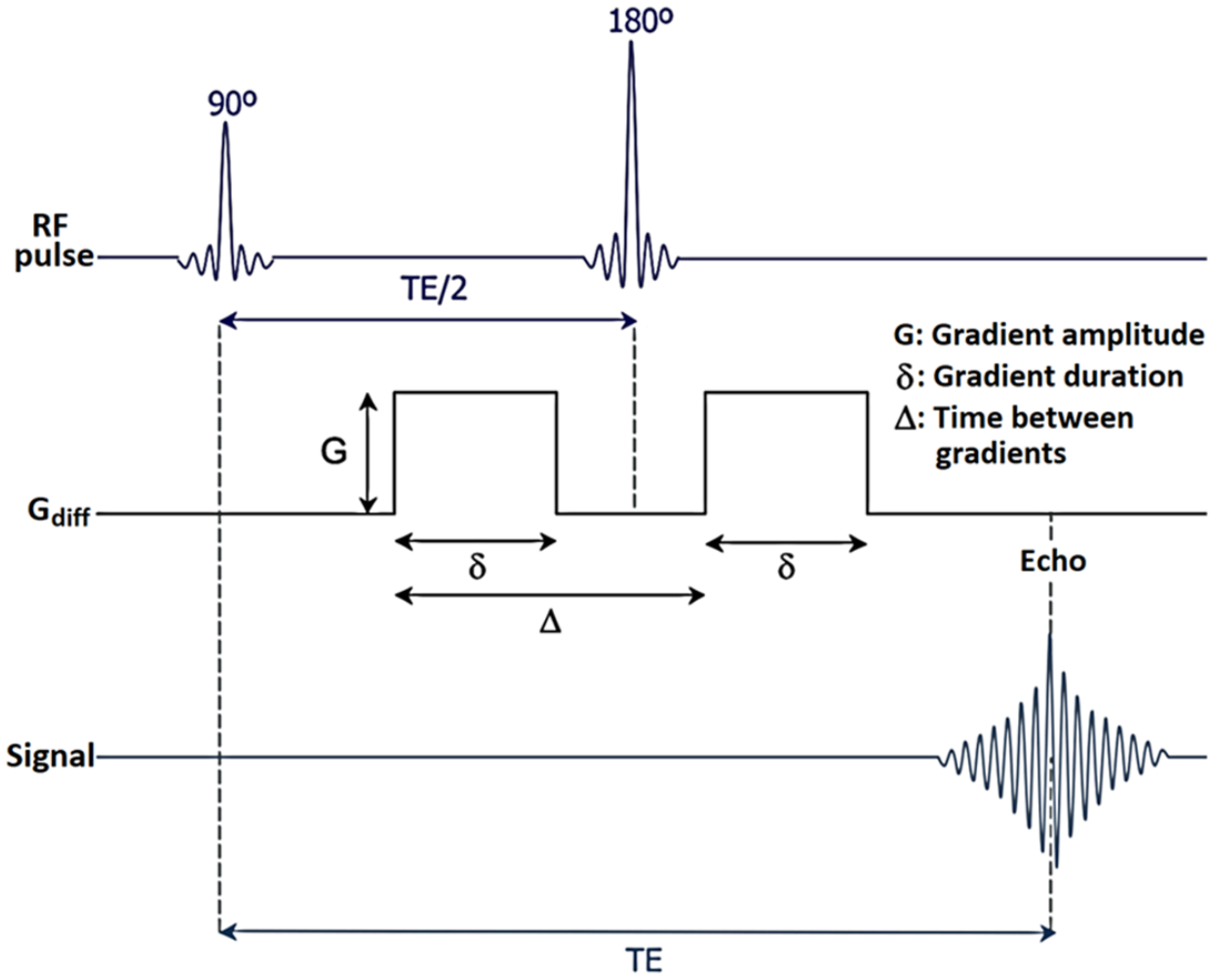

Figure 1.9: Stejskal and Tanner Pulsed Gradient Spin Echo (PGSE) sequence for diffusion encoding. Two gradients of the same amplitude (G) and duration (δ) are paired on either side of a 180° RF pulse to 'weight' the sequence on diffusion along the gradient direction.

Nevertheless, the diffusing spins that have moved along the gradient's axis between the first and second gradients, are still out of phase and have lost signal, which can be measured by the equation:

(Equation 1.6) $$\frac{S}{S_0} = e^{-\gamma^2 G^2 \delta^2 \left(\Delta - \frac{\delta}{3}\right) ADC} = e^{-bADC}$$

where the b-value measures the degree of diffusion weighting applied [101]. The diffusion coefficient is referred as the apparent diffusion coefficient (ADC) because it is not the intrinsic diffusion coefficient of water but instead is impacted by the geometry of the tissue microstructure. Higher b-values (e.g., by increasing the gradient strength or diffusion times) lead to more signal loss from diffusion as well as due to increased T2 relaxation. To calculate the ADC, two images must be acquired at different b-values to obtain the slope from Equation 1.6 (usually a non-diffusion weighted image (non-DWI) with b=0 s/mm^2 (b_0) as the S_0 input of Equation 1.6 and a DWI with a higher b-value as S).

Diffusion MRI protocols in this dissertation were mainly acquired with single-shot Spin-Echo Echo-Planar Imaging (SS-EPI) (Figure 1.10), which is one of the fastest MRI acquisition schemes and one of the main methods for collecting DWI data. As shown in Equation 1.6, the b-value is a diffusion sensitization factor that reflects the strength and timing of the gradients used to generate diffusion-weighted images. This leads to a monoexponential signal decrease in simple solutions and in some tissues. However, non-monoexponential behavior has been observed mostly within those single voxels where a multicomponent mixture of tissues with different microstructure and diffusion properties contribute to a fraction of the total signal [95]. Thus, as CSF long T2 values cause a relative enhancement of the observed signal, a biexponential behavior might occur in regions with CSF partial volume contamination , such as cortical GM and WM areas near the brain ventricles [102]. This motivated the application of a CSF-suppressed, inversion-recovery SS-EPI

diffusion sequence for the first time in 1991 to demonstrate the dominant contribution of CSF to the non-monoexponential diffusion decay behavior observed in cortical GM [102]. The addition of a FLAIR preparation pulse to EPI diffusion sequences have allowed a more accurate and precise determination of diffusion values in cortical GM and parenchymal tissues bordering the ventricles [103] but also a marked improvement of fiber tracking of small limbic WM connections such as the fornix, which lies adjacent to the lateral ventricles [104]. This has motivated the application of a high resolution FLAIR diffusion protocol to suppress CSF (note the CSF-suppression in the ventricles/cortical GM in Figure 1.10C) and to evaluate fornix damage in MS as part of this thesis.

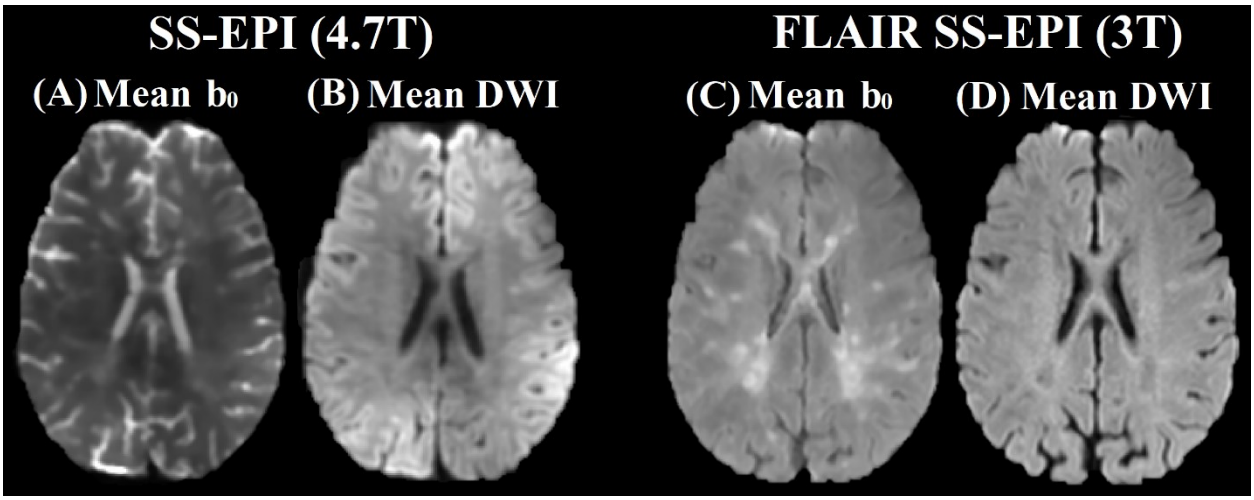

Figure 1.10: Mean b_0 and Mean Diffusion Weighted Images (DWI) acquired with single-shot Spin-Echo Echo Planar Imaging (SS-EPI) at 4.7 T and 3 T (with CSF suppression). Examples of (A, C) mean b_0 and (B, D) mean DWI acquired at (A, B) 4.7 T (5 b_0, 1.7 mm isotropic voxels, b=1000 s/mm^2, 30 directions, TR=9500 ms, TE=54 ms, GRAPPA=2, Partial Fourier (PF)=0.69, Anterior-Posterior (AP) phase encoding direction, BW=2604 Hz/Pixel) and (C, D) 3 T (5 b_0, 1.2 × 1.2 × 2 mm^3 voxels, b=1000 s/mm^2, 20 directions, TR=9000 ms, TE=69 ms, TI=2300 ms, GRAPPA=2, PF=0.75, AP phase encoding direction, BW=1900 Hz/Pixel) in a 34-year-old relapsing-remitting MS female subject (A, B and C, D were acquired 4 years apart).

In a SS-EPI pulse sequence imaging data is collected in a single shot which remove the shot-to-shot variation in phase from diffusion data collected with multi-shot acquisitions (Figure 1.11A). A SS-EPI pulse sequence is designed so that the trajectory oscillates back and forth in k_x while progressing along k_y [105]. In SS-EPI with partial k-space coverage a typical trajectory begins near the center of k-space, and cross over to the far side of it, with the spin echo occurring just as the sampling trajectory is positioned at the k-space origin (Figure 1.11B), consequently removing gross dephasing effects [106]. This previously described partial k-space coverage reduces the duration of the pulse sequence as well as the T2 signal decay for the k-space center. However, the acquired part of k-space must be large enough to cover phase variations due to motion-induced phase and to reduce the prevalence of other motion artifacts such as head rotation [106].

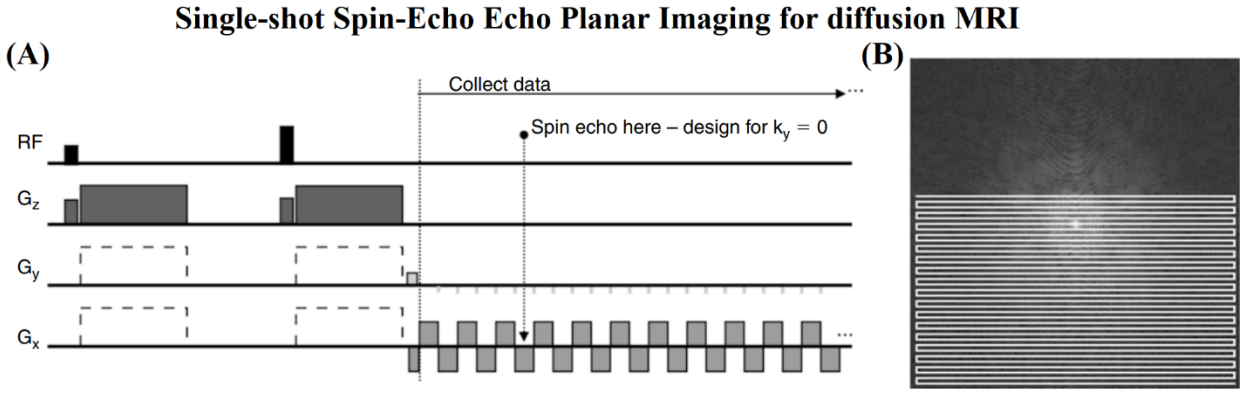

Figure 1.11: Single-shot Spin-Echo Echo Planar Imaging (SS-EPI) pulse sequence for diffusion MRI. (A) SS-EPI pulse sequence with asymmetric read out by making the sum of G_y equal to zero at the spin echo. (B) Sampling trajectory with partial k-space coverage from pulse sequence in (A). (Reprinted from [106] by permission from Elsevier, License Number 5301110404611).

Although the rapid slice acquisition of SS-EPI reduces the time interval of the echo train read thus decreasing the probability of inter volume subject motion, it leads to eddy current distortions. These distortions can be corrected or minimized with several approaches such as bipolar gradients [107], correcting/calibrating the distortions in k-space by using reference measurements of eddy current fields [108], post-acquisition image processing (e.g., scaling, shear, translation in the phase encoding direction) to register the DWIs to reference undistorted baseline images [109] or to images collected twice for each diffusion gradient, once traversing k-space bottom-up and once top-down, which provides information on the displacement fields and intensity maps [110].

Any subject motion in the diffusion encoding direction can still cause erroneous diffusion measurements, while local magnetic field inhomogeneities and signal loss due to T2* dephasing could arise in air tissue interfaces, such as in the sinus area, creating spatial distortions as well. One common alternative to further correct for these magnetic field inhomogeneities and warping, which worsen at higher magnetic fields, is to use parallel imaging reconstruction methods, which use the signals from individual receive coils in an array of multiple coils to perform some of the spatial encoding [111]. Parallel imaging takes advantage of the local sensitivity of each coil in the phased array and artificially reduces the field of view (FOV) of each coil in the phase encoding direction which effectively increases the allowable spacing between k-space samples [106]. The FOV is the distance over which MRI is acquired and it is related to the k-space according to the following rule:

(Equation 1.7) $$\frac{1}{\Delta k_x} < FOV,$$

which is the Nyquist condition to avoid the occurrence of aliasing. As decreasing the FOV results in aliasing or wraparound artifact, the spatial dependence of the phased-array coil elements is used to remove or prevent the aliasing in parallel imaging [112], while reducing the number of phase-encoding steps by a factor of R [111]. SS-EPI diffusion sequences in this dissertation utilizes a GeneRalized Autocalibrating Partially Parallel Acquisitions (GRAPPA) method with R=2, which uses multiple k-space lines from all coils to fit one single coil acquired autocalibration signal line resulting in high accuracy of the fitting procedure and good artifact suppression [111]. The increased temporal resolution of parallel imaging in SS-EPI acquisitions allows to improve spatial resolution and to reduce susceptibility distortions in the acquired images, while decreasing the SNR by √R. However, other alternatives could be used to increase SNR, such as increasing the number of signal averages (NSA), mainly of the b_0 images in diffusion MRI, which will increase the SNR by √NSA although increasing the total acquisition time as well.

Other diffusion pulse sequences include FSE and multi-shot methods, as well different methods to collect k-space data such as Periodically Rotated Overlapping ParallEL Lines with Enhanced Reconstruction (PROPELLER) [113] and spiral-based pulse sequences [114], where k-space data is respectively collected in strips/blades or in an spiral trajectory.

1.2.5.3. Mean DWI, ADC, and T2 Shine-Through

Earlier diffusion MRI studies used to first acquire an image without diffusion weighting (non-DWI with b_0=0 s/mm^2) and then 3 images with diffusion weighting along 3 orthogonal diffusion

gradient directions to compute the rotationally invariant geometric mean known as the isotropic, trace or mean DWI according to Equation 1.8:

(Equation 1.8) $$S_{DWI} = \sqrt[3]{S_x S_y S_z} = S_0 e^{-b(D_{xx}+D_{yy}+D_{zz}/3)} = S_0 e^{-b(D_{trace}/3)} = S_0 e^{-b \cdot ADC},$$

where S_0 is the signal intensity for the b_0 image, S_x, S_y and S_z are the signal intensities from the x-, y-, and z- diffusion gradient directions, while D_{xx}, D_{yy}, and D_{zz} are the diffusion coefficients from the corresponding orthogonal gradient directions. From Equation 1.8, the mean DWI is inversely related to the average value of the trace $(D_{xx} + D_{yy} + D_{zz})/3$, which is the previously defined ADC (Equation 1.8). As the mean DWI is only 'diffusion-weighted', it is substantially influenced by T2-weighting. As such, a tissue with a long T2 decay time will have a high T2 signal which 'shines through' the DWI image. This is known as "T2-shine-through", and in order to confirm true restricted diffusion the region of increased DWI signal will show low signal on ADC. Nowadays, DWI studies are still commonly performed in the clinical practice for evaluation of pathologies such as acute ischemic stroke (high mean DWI signal and low ADC), mostly due to the inherent acquisition speed of these methods but also to remove anisotropic effects which allows the differentiation of acute stroke from other acute neurologic events [115].

1.2.5.4. The Diffusion Tensor Imaging (DTI) Model

As many biological tissues, for example, WM in the brain, are highly anisotropic, DWI does not consider this complexity and reduces diffusion to a single average value, which is a very simplistic interpretation. The DTI model was developed to deal with this problem by emphasizing and quantifying areas that are dependent on anisotropic effects and to acquire diffusion measures not

dependent on the direction of the diffusion gradients [96]. Instead of scalar ADC, DTI employs a second order tensor **D** (Figure 1.12A) which is a matrix of the diffusion coefficients in each combination of directions and contains six free parameters to be fit. D_{xx}, D_{yy}, D_{zz}, D_{xy}, D_{yz}, and D_{zz} are the tensor's six independent elements, and the tensor **D** can be represented by an ellipsoid (Figure 1.12B). The main greater axis of the diffusion tensor ellipsoid can indicate the principal direction of well-aligned WM fibers (along the axons) where the other axes are more limited by barriers (myelin sheaths, cellular membranes) indicating a more restricted diffusion.

The diffusion tensor can be estimated by fitting an adapted Stejskal and Tanner equation to at least six DWI acquired for at least six noncollinear gradient directions and a b_0 image [116]. For each image voxel, the ellipsoid model is fitted from the directional diffusivities through matrix diagonalization, and it can be decomposed in three eigenvectors (e_1, e_2, e_3) and three eigenvalues (λ_1, λ_2, λ_3) ordered in descending order (Figure 1.12A). The eigenvalues are the ADC values of the tensor along the directions of the eigenvectors, and they describe the shape and size of a tensor, independently of its orientation (rotationally invariant) [117].

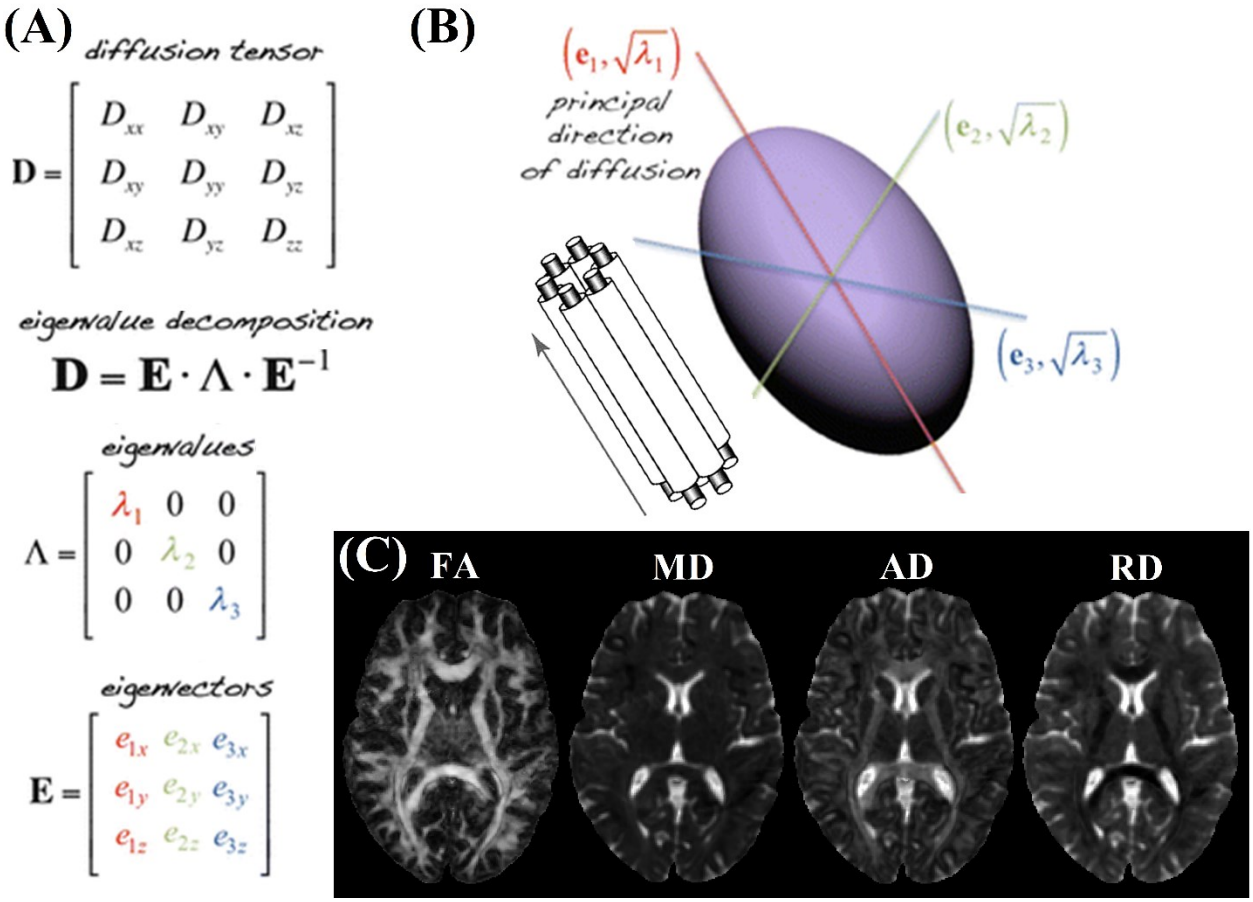

Figure 1.12: The diffusion tensor D and the DTI parameter maps. (A) The diffusion tensor **D** is acquired as a matrix of diffusivities with different diffusion directions (6 non-collinear directions), which can be decomposed into eigenvectors (e) and eigenvalues (λ). (B) The tensor is geometrically represented as an ellipsoid, which eccentricity characterizes the degree of diffusion anisotropy. The longest axis is the first eigenvector (e_1) that represents the direction of maximal diffusion. (C) Several metrics, such as fractional anisotropy (FA), mean diffusivity (MD), axial diffusivity (AD) and radial diffusivity (RD) can be derived from the diffusion tensor (from a 27-year-old female control). (A and B were adapted from [118] by permission from Springer Nature, License Number 5253920329702).

1.2.5.5. Scalar DTI Metrics and Biological Interpretations

Several scalar diffusion metrics can be calculated from the diffusion tensor (Figure 1.12C).

Important DTI metrics for this dissertation are:

Mean diffusivity (MD): It characterizes the overall mean squared displacement of molecules (average ellipsoid size). It is numerically different from ADC in that it is rotationally invariant whereas the ADC differs per gradient direction in an anisotropic sample [119]. MD is sensitive to the amount of water diffusion (edema, inflammation) but also to myelin loss [120]–[122].

(Equation 1.9) $$\mathrm{MD} = \frac{\lambda_1+\lambda_2+\lambda_3}{3} = \frac{D_{xx}+D_{yy}+D_{ZZ}}{3}$$

Fractional Anisotropy (FA): It quantifies the ratio between the magnitude of the anisotropic component of the diffusion tensor **D** and its entire magnitude. Hence, FA is the ratio of the tensor that can be assigned to anisotropic diffusion [123]. FA values range between zero and one. FA can be considered an overall measure of microstructural diffusion anisotropy [116], mainly in highly coherent WM structures, and it usually decreases in WM diseases. Even though FA is very sensitive to microstructural changes, it is less specific to the type of change, ranging from degree of myelination to axonal ordering, density and loss [124],

(Equation 1.10) $$\mathrm{FA} = \sqrt{\frac{1}{2}\frac{(\lambda_1-\lambda_2)^2+(\lambda_2-\lambda_3)^2+(\lambda_1-\lambda_3)^2}{{\lambda_1}^2+{\lambda_2}^2+{\lambda_3}^2}}$$

Axial diffusivity (AD): It describes the diffusion coefficient of water molecules diffusing parallel to the tract within the voxel of interest. It has been hypothesized to be sensitive mainly to axonal degradation [121], although it tends to be variable in WM changes and different pathologies. For example, AD measurements can be higher in MS subjects when compared to

healthy controls [125] as a result of the replacement of axonal structure with extra-cellular space in MS lesions [126].

(Equation 1.11) $$AD = \lambda_1$$

Radial diffusivity (RD): It is the magnitude of water diffusion perpendicular to the tract. It may reflect myelin changes, as myelin damage leads to increased RD in mouse models [121], [127].

(Equation 1.12) $$RD = \frac{\lambda_2 + \lambda_3}{2}$$

The brain tissue is highly complex, and the WM bundles are composed of diverse orientations, location, fiber population, degree of myelination and axonal sizes. The main determining factor of anisotropy in nervous tissue are the 'intact' cell membranes. Myelin itself, it is not necessary for diffusion to be anisotropic in the brain, however it serves to modulate anisotropy [97]. Furthermore, although DTI is sensitive to many of these features, the interpretation of the diffusion metrics is not always straightforward. For example, DTI is sensitive to microscopic diffusion anisotropy however the measurements of these microscopic information are averaged over macroscopic voxel volumes. When these averages come from more than one fiber population differently oriented, or when there is some sort of macroscopic heterogeneity, their contributions to the signal could be averaged, thus preventing us from seeing anisotropy at voxel level. Hence, if pathology intermingles with the complex brain cytoarchitecture it is difficult to directly infer those microstructural abnormalities by typical DTI metrics (mainly FA), which could be likewise

influenced by macroscopic reorganization as a confounder in healthy and diseased cohorts [128]–[130].

1.2.5.6. DTI Pre-Processing and Analysis Techniques. Fiber Tractography

Standard DTI processing includes several pre-processing steps of the data, followed by the diffusion tensor estimation (Figure 1.13). In addition to accounting for subject motion, the most comprehensively analyzed and corrected EPI distortions in DTI are those induced by eddy-currents (discussed in Section 1.2.5.1) (ECMOCO). These distortions must be corrected to guarantee a reliable analysis (see row 4 in Figure 1.13) and they have been performed with several postprocessing software tools in this manuscript, such as mutual information-based registration techniques and a spatial transformation models containing parameters that correct for eddy current-induced image distortion (affine, 12 degrees of freedom) ([131] for Chapter 2; [132], [133] for Chapter 3; [110] for Chapter 4; [134] for Chapter 5 and discussed in a later section) and rigid body motion in three dimensions when feasible (e.g., FLAIR DTI data in Chapter 3 was registered to MPRAGE) for all diffusion analyses in this thesis. Physically implausible signals that arise from negative eigenvalues were not considered during ECMOCO, in diffusion data in Chapter 2 and 3 as these images were acquired with high SNR, thus this default parameter wouldn't bias the DTI data processing [135].

Denoising is an important step at low SNR data (e.g., axial-oblique slab for hippocampus DTI with SNR ~3-5 [136]), which should be performed as the first step of the processing pipeline (see row 1 in Figure 1.13C), as further steps may alter the noise characteristics from which noise mapping

is based [137]. Other pre-processing steps before tensor calculation includes correcting for Gibbs artifacts (Figure 1.13), which typically appear as multiple fine parallel lines adjacent to high-contrast interfaces as a consequence of using truncated Fourier transforms to reconstruct MR signals and worsen with Partial Fourier [138] as acquired in all the diffusion data in this dissertation (Partial Fourier of 0.69 in Chapter 2 and 0.75 (6/8) in Chapter 3, 4, and 5). Gibbs artifacts can be corrected with approaches such as total-variation [135], [139]. While scanning, B_1 inhomogeneity was minimized by rotating/translating the birdcage transmit RF coil according to [140] at 4.7 T or by applying a prescan normalize filter at 3 T that can minimize B_1 inhomogeneity through the slice and improve ventricular visualization/registration between scans with no detrimental effects on DTI parameters. This can be further corrected with post-processing strategies such as B_1 field inhomogeneity correction [141], applied to the axial-oblique slab for hippocampus DTI.

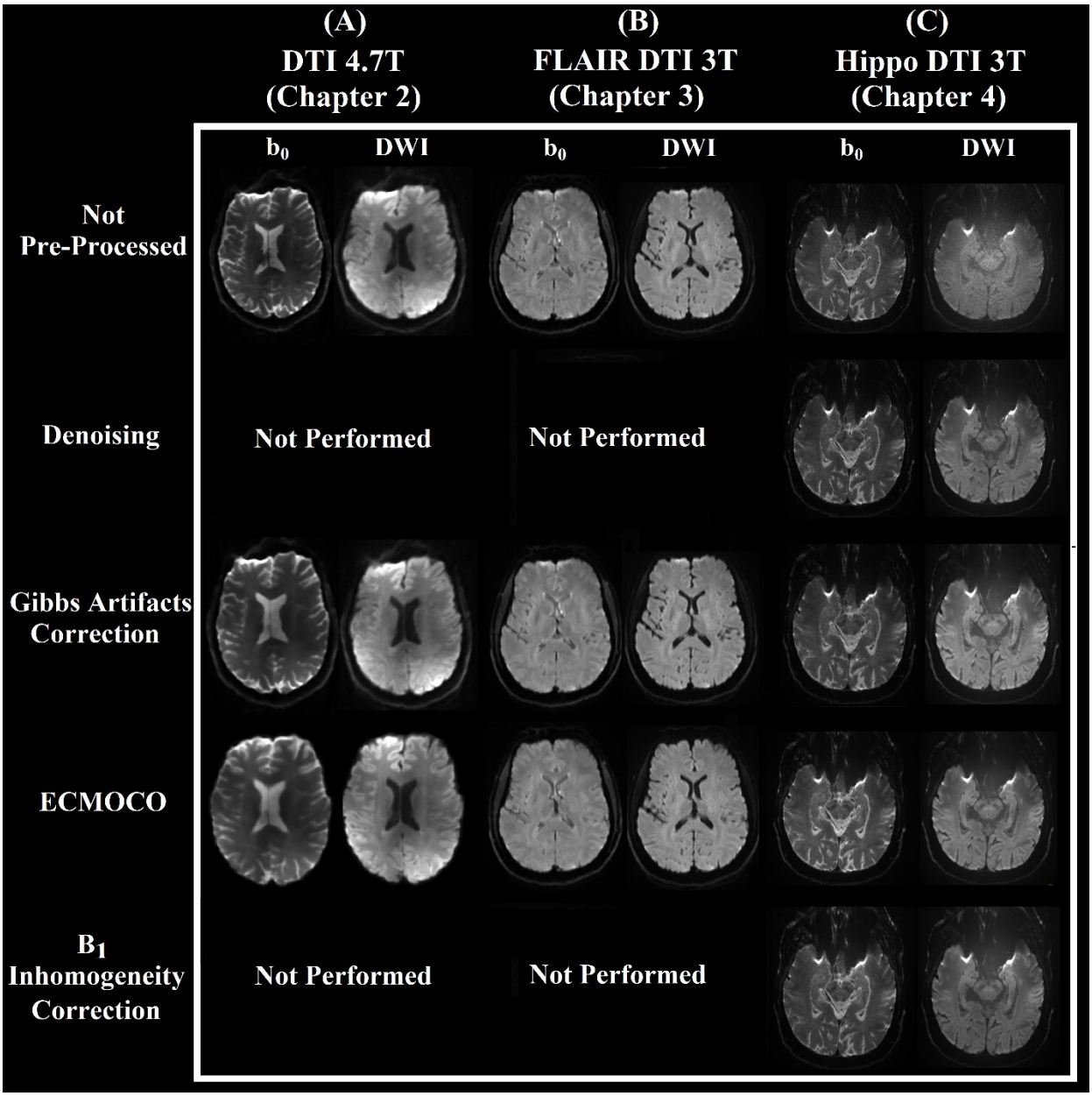

Figure 1.13: Standard pre-processing pipelines for DTI data in a **(**A) 57-year-old primary-progressive MS female), a (B) 37-year-old relapsing-remitting MS female and a (C) 70-year-old healthy male. Corrections for eddy current distortion and subject movement (ECMOCO) are essential in all diffusion datasets (A, B, C) while denoising is particularly beneficial in DTI acquisitions with low SNR (C).

Several analysis techniques can be applied to DTI after the diffusion tensor calculation, each one with its own strengths and limitations. The most optimal analysis method depends on many factors inherent to the study design, such as the data acquisition protocol and quality, the purpose of the analysis and the hypothesis about the brain location(s) of interest, among other aspects. Analyses can be voxel-based (whole-brain or not), specific to one or several regions of interest (ROI) or to one or several fiber bundles. For example, tract-based spatial statistics (TBSS) [142] is considered as the typical approach for voxel-based DTI analysis in large whole-brain multi-subject DTI studies. In TBSS the skeletonization step yields measures only from the nearest voxel with highest FA perpendicular to the skeleton presumably reflecting the core of many WM tracts without needing data smoothing, however this is particular difficult and inaccurate when studying smaller tracts like the fornix [143].

Fiber tractography has also become a preferred analysis method when investigating DTI parameters in specific WM bundles, in heathy individuals and a rising number of brain pathologies, MS included [122], [144], [145]. The goal of fiber tracking is to render 3D trajectories of anisotropic structures (e.g., WM tracts) by connecting voxel-based estimates of the underlying continuous fiber orientation field [146]. Tractography algorithms can be classified as deterministic and probabilistic. Deterministic tractography infers only one fiber orientation estimate per voxel, thus providing a single streamline trajectory per seed point. The generated fibers could be prone to errors due to image artifacts and algorithm integration errors [147]. In contrast, probabilistic tractography creates a distribution of possible trajectories from each seed point, and results are quantified from generated visitation count maps of the number of trajectories that traverse each

voxel. As a result, brain regions that contain higher density trajectories correspondingly have a higher probability of "connection" with the seed point. Probabilistic tractography algorithms are subject to similar errors and limitations of deterministic tractography [148] and they were not the main focus of this thesis so they will not be further discussed.

Fiber assignment by continuous tracking (FACT) deterministic tractography, relies on the assumption that in each voxel, the principal eigenvector e_1, which is associated with the largest eigenvalue λ_1 of the diffusion ellipsoid, is parallel to the dominant fiber orientation [123]. It forms a tangent to the space curve outlined by the WM tract (Figure 1.14A, B) [149]. This axonal projection curve can be tracked only if nearby 3D continuous vector fields are strongly aligned [146]. It propagates parallel to e_1, from a single voxel, several voxels belonging to an ROI or from a whole brain 'seed point'. By combining Boolean ROIs (AND, OR and NOT) in specific anatomical locations, WM tracts can be depicted and further refined (Figure 1.14C), although the process demands anatomical knowledge and it is conditional on inter-operator variability [148]. Different conditions can be set to define when to stop the tracking process, which are frequently the local FA and the angle of curvature between voxels. These conditions help eliminate spurious tracts caused by noise or tensor model artifacts. A streamline stops when the FA falls below a certain threshold value or surpasses a certain maximum angle of curvature within a voxel. Other conditions that are also useful to discard short spurious tracks is setting a minimal fiber length. FACT deterministic fiber tracking has been applied in Chapter 2 and Chapter 3 of this thesis. Comparisons of the tractography results when applying different threshold conditions for a specific WM bundle (the fornix) are shown in Appendix A.

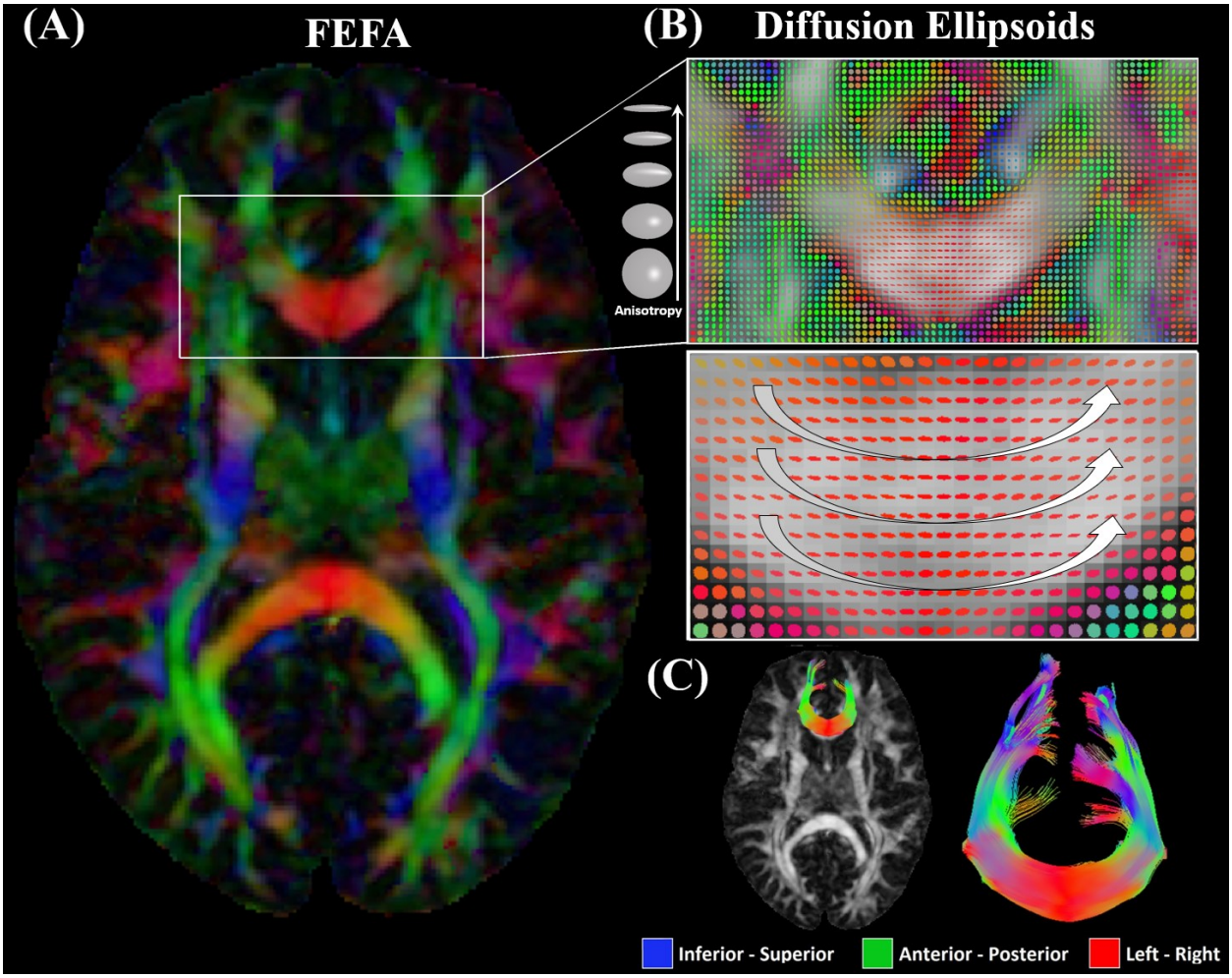

Figure 1.14: First eigenvector FA (FEFA) map, diffusion ellipsoids and 3D fiber pathway depiction with deterministic tractography. (A) An axial FA map in a 27-year female control displaying the genu of the corpus callosum enclosed in a white box. (B) The box area in (A) is zoomed to show the diffusion ellipsoids which follow a coherent directional pattern and a strong left-right orientation (red ellipsoids with white arrows following the main diffusion direction) in the genu of the corpus callosum. (C) FACT deterministic tractography with proper ROIs allows the reconstruction of the genu of the corpus callosum.

1.2.5.7. DTI Limitations

The main limitations of the DTI model is the assumption of its Gaussian diffusion, which preclude modeling more than one fiber population within a voxel [128], [129], as well as the information reduction due to the six-parameter tensor approach [99]. This is a major disadvantage when imaging voxels that have multiple fiber populations 'crossing', 'fanning' or even 'brushing' past each other, which constitute a significant fraction of the brain WM [130]. This drawback worsens with typical DTI resolution (~8 mm^3 voxels) in clinical studies and it can be partially improved by increasing image resolution [99] which reduces partial volume effects. An important part of this thesis focuses mainly on the fornix, which is an isolated WM tract devoid of crossing fibers, hence DTI and deterministic tractography are suitable for the fornix analyses performed here.

1.2.5.8. Higher Order Models

Currently, many alternatives to overcome the tensor model have been established, which are mainly called q-space approaches that use higher order models to capture more diffusion information. These methods provide an estimate of the angular dependence of the spin propagator from its Fourier relationship with the diffusion signal measured as a function of the q-vector (related to the direction and intensity of the diffusion gradient pulse). They are usually acquired with high angular resolution diffusion imaging (HARDI) [150]. HARDI is frequently sampled with a spherical scheme and a large number of diffusion directions with a constant b- or q-value (single-shell) or multiple b-values (multi-shell), although the optimal b-value and diffusion directions are still a topic of research. From all HARDI based approaches, the constrained spherical

deconvolution (CSD) technique [151] stands out as it can provide a reliable estimate of the fiber orientation distribution (FOD) by assuming the diffusion signal measured from any fiber bundle is adequately described by a single response function. Other approaches such as diffusion kurtosis imaging (DKI) has been utilized to characterize the non-Gaussian behavior in diffusion MRI [152], by extending the linear relationship between the logarithm of the diffusion-weighted signal and the b-value to a higher order with the introduction of a quadratic term. DKI requires higher b-values of at least 2000 s/mm^2 and a modified image postprocessing strategy and it provides an estimate for the excess kurtosis of the diffusion displacement probability distribution. One of the metrics that can be estimated with DKI is the mean kurtosis (MK), which is defined as the average of directional kurtosis coefficients across all spatial directions [153]. As DKI, HARDI based approaches such as CSD are recommended to be employed in diffusion datasets with relatively high b-values (2000-3000 s/mm^2) and a minimum of 45 different diffusion encoding directions [154]. In three of the Research Chapters in this thesis, the maximum b-values were limited to 1000 s/mm^2 (Chapter 2 with 30 diffusion directions and Chapter 3 with 20 diffusion directions) or 500 s/mm^2 (Chapter 4 with 10 diffusion directions), thus necessitating the DTI model previously discussed in Section 1.2.5.4.

A popular two-shell HARDI based model is the Neurite Orientation Dispersion and Density Imaging (NODDI) [155], which adapts the orientation-dispersed cylinder model in [156] to describe brain tissue as a simplified combination of three compartments: (1) a Watson distribution assumption of sticks models the first compartment, known as the intracellular compartment (axons and dendrites); (2) a Gaussian anisotropic diffusion, as seen in DTI for the extracellular

compartment; (3) a free water compartment which is isotropic Gaussian diffusion such as CSF. NODDI estimates the neurite density and orientation dispersion indexes (NDI, ODI), which are two main factors contributing to FA in DTI, as well as the isotropic signal fraction (isoVF) [157]. Nevertheless, even when assuming simplistic approximations such as modeling the axons as sticks rather than cylinders and standard 2 mm isotropic voxels, long scanning times (~25 minutes) are needed in order to achieve good accuracy in estimating the dominant fiber orientation [155]. This scan time can be shortened to about 10 minutes with negligible effects on neurite morphology parameter' estimates [155]. Although not extensively applied, NODDI has been proven helpful in MS by providing in vivo measurements of tissue microstructural changes, such as decreased NDI and increased ODI, which are often complementary to DTI measurements such as decreased FA and increased MD in lesions [158], [159] and in NAWM [157]–[159] when compared to controls. Although NODDI qualitatively provides better contrast between NAWM and lesions in MS patients and a more precise characterization of WM microstructures [155] than DTI, most of the group differences in the aforementioned NODDI MS studies were also significant with standard DTI metrics.

1.2.5.9. Multidimensional/b-tensor Diffusion MRI

Previously mentioned diffusion MRI methods are acquired with single diffusion encoding (SDE) acquisition. However, other family of higher order methods based on multidimensional b-tensor diffusion encoding approaches, such as double (DDE), triple (TDE), and isotropic time-varying diffusion encoding gradient waveforms have also been developed to discriminate tissue

microstructure from macrostructure by modifying the shape of the b-tensor with diffusion encoding gradients in more than one direction before the image readout [160]–[162].

A framework for the quantification of a set of microstructural diffusion metrics beyond DTI, such as microscopic diffusion anisotropy and orientation dispersion (similar to NODDI concepts discussed in Section 1.2.5.8) using b-tensor encoding was formulated in previous work [163]. The contrast between the NMR signals acquired with conventional diffusion encoding (e.g., Stejskal and Tanner PGSE discussed in Section 1.2.5.2) and isotropic encoding based on magic angle spinning of the q-vector (qMAS) [164], both acquired with several b-values as high as b=2000 s/mm^2 (e.g., b=100, 500, 1000, 1500 and 2000 s/mm^2 in Chapter 5), is utilized to fit diffusion tensor distribution (DTD) models and obtain a variety of microstructural diffusion metrics. Magic angle spinning is a known NMR spectroscopy method where a sample is rotated around its own axis at a specific angle relative to B_0 to minimize the influence of chemical shift anisotropy on the observed NMR signal spectrum. In qMAS, a time efficient harmonic gradient modulation is used to create a q-vector that performs a precession at the magic angle in order to exert equal diffusion encoding in all spatial directions while the sample remains stationary [165].

In Chapter 5 of this thesis b-tensor diffusion encoding MRI was successfully implemented in a high-performance gradient MRI system (3 T with 80 mT/m gradients) capable to facilitate sufficient data quality in tolerable acquisition times [166]. A schematic diagram of the pulse sequence utilized is showed in Figure 1.15A. The isotropic (qMAS) and the conventional (PGSE) encoding in Figure 1.15A will be respectfully denoted as ‘spherical’ and ‘linear’ tensor encoding

(STE and LTE) for the rest of this dissertation. The actual STE and LTE waveforms implemented in our MRI system and utilized in Chapter 5 are respectively shown in Figure 1.15B and Figure 1.15C.

Conventional SDE acquisitions, which conflate the effects of microscopic anisotropy and isotropic heterogeneity, cannot separate the anisotropic and isotropic sources of diffusional variance that originate from markedly different microstructural features [168]. DTD models mentioned above rely on the assumption that tissue heterogeneity can be captured by describing the diffusion in each coherent tissue segment on short length scales, each called microenvironment, with a microscopic diffusion tensor [160]. The microenvironments within a voxel can be described by a collection of diffusion tensors, which is referred to as the DTD. From the DTD, it is possible to estimate standard voxel scale diffusion metrics, metrics associated with the diffusional variance, as well as the diffusion anisotropy on the voxel and microscopic scales.

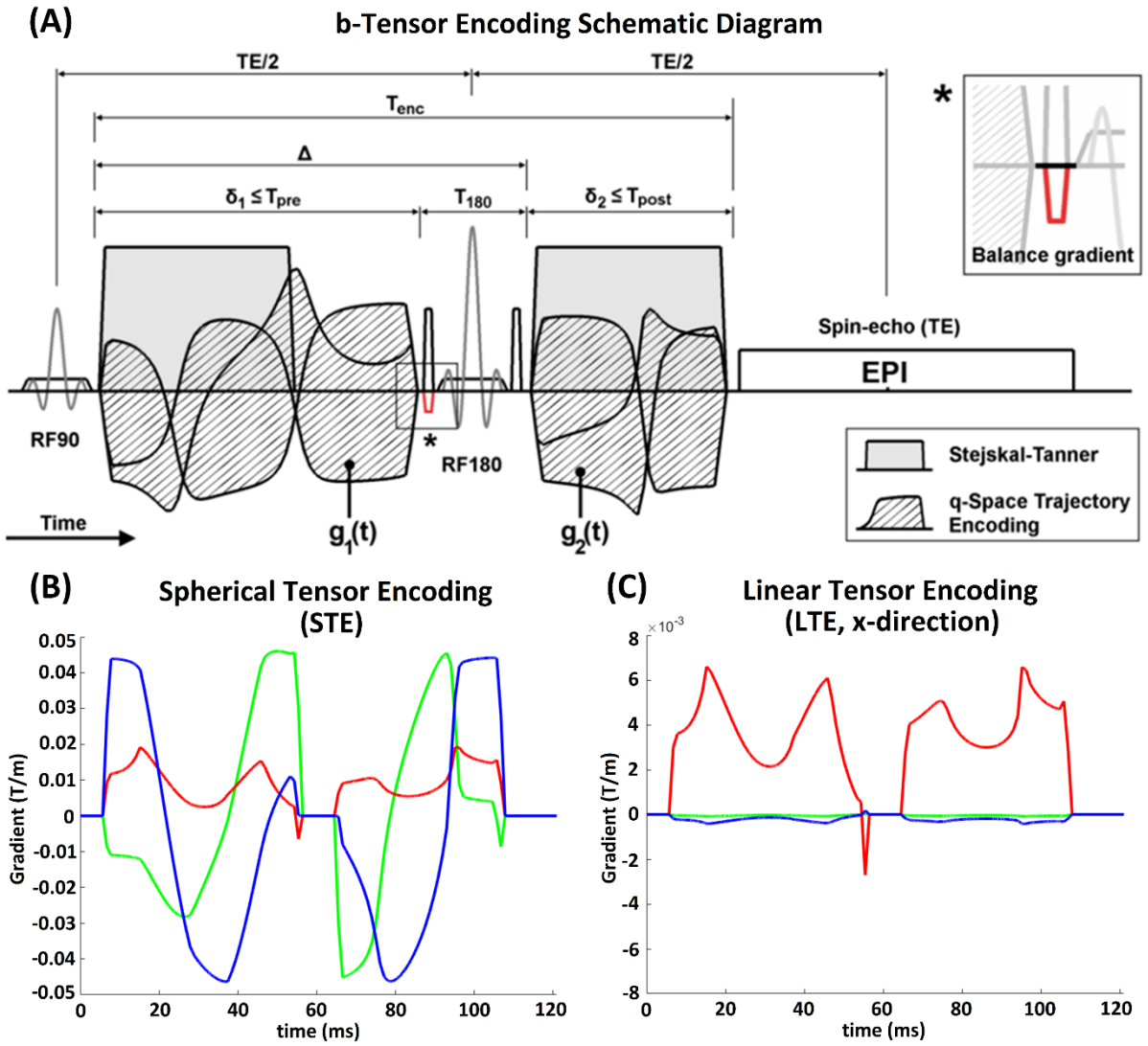

Figure 1.15: (A) Schematic diagram of the b-tensor encoding with its timing variables. Note that the Stejskal-Tanner and q-space trajectory encoding gradients are shown together for visual reference although they are not executed simultaneously in practice, but sequentially. The gradient waveforms are executed between the excitation pulse, the refocusing 180° RF pulse, and the EPI readout. The timing variables show the maximal time available for encoding (T_{pre} and T_{post}), the duration of each gradient waveform (δ1 and δ2), the gradient waveform separation (Δ), the duration of the refocusing block including the crushers (T_{180}), the total encoding time (T_{enc}), and TE. The balance gradient (red) is executed at the same time as the first crusher. Image and caption in (A) modified and reprinted from [167] under the BSD 3-Clause License, Filip Szczepankiewicz Copyright (c) 2019. (B) Spherical (STE) and (C) Linear (LTE) Tensor Encoding sequences implemented for Chapter 5. The goal was to match the diffusion times of the STE and LTE sequences; thus LTE use the gradient shape from one of the orthogonal STE directions (x-gradient direction in red here).

A DTD method that aims at separating the two sources of variance, referred to as 'diffusional variance decomposition' (DIVIDE) [161] was utilized in Chapter 5 to assess the presence of microscopic anisotropy and isotropic heterogeneity. DIVIDE estimates diffusion metrics such as the isotropic (MK_i) and anisotropic (MK_a) components of the total diffusional variance (MK_t), which is equivalent to the mean kurtosis (MK) from the DKI model [152], the microscopic fractional anisotropy (μFA) from the diffusion tensor microenvironments, as well as standard diffusion metrics derived form the DTI model. Equations for MK_i, MK_a, MK_t and μFA are provided below [161], [167]:

$$MK_i = V[D_i] = V\left[E_\lambda[\boldsymbol{D}]\right], \quad \text{(Equation 1.13)}$$

where $V[\boldsymbol{D}_i]$ is the variance of the distribution of isotropic diffusivities $D_i = E_\lambda[\boldsymbol{D}]$.

$$MK_a = \frac{2}{5}\langle V_\lambda[\boldsymbol{D}]\rangle, \quad \text{(Equation 1.14)}$$

where the factor 2/5 relates the eigenvalue population variance $V_\lambda[\cdot]$ to the variance of the distribution of diffusivities [**D**] in the powder sample.

$$MK_t = MK_i + MK_a, \quad \text{(Equation 1.15)}$$

$$\mu FA^2 = \frac{3}{2} \cdot \frac{\langle V_\lambda[\boldsymbol{D}]\rangle}{\langle E_\lambda[\boldsymbol{D}]^2\rangle + \langle V_\lambda[\boldsymbol{D}]\rangle} \quad \text{(Equation 1.16)}$$

The difference between μFA and FA is that FA is calculated from the diffusion anisotropy that is observed on the voxel-scale whereas the μFA is calculated from the anisotropic diffusional variance. Mathematically, the difference is determined by the stage at which the averaging

operation is applied, with averaging over tensors first probing FA while averaging over variance and expectancy first probes μFA [160], [161], [167]. μFA is indicative of the microscopic diffusion anisotropy, independent from the orientation coherence [163], while MK_i and MK_a parameters appear to be respectively related with cell density variance and cell eccentricity [161]. Schematic representations of how these metrics relate to different diffusion tensor distributions are shown in Figure 1.16.

Similar b-tensor protocols and DTD analyses have been applied to the study of healthy subjects and brain tumor discrimination (meningioma versus glioma) [161], [169], where μFA has been reported as relatively homogeneous in large portions of the WM in the healthy brain in agreement with other studies that have aimed to remove effects of orientation dispersion from the quantification of local anisotropy (note differences between the FA and μFA maps in Figure 1.17D, E) [170], [171]. Moreover, in these analyses μFA [169], MK_a and MK_t [161] metrics (Figure 1.17) allowed to reliably differentiate between two types of brain tumors by indicating that microscopic diffusion anisotropy was more pronounced and the main cause of diffusion variance in the meningioma, while isotropic heterogeneity was evident in the glioma in agreement with histology. In MS, although the isotropic MK_i and anisotropic MK_a contributions of the diffusional variance have not yet been studied, μFA maps calculated from DDE acquisitions [162] and b-tensor encoding [172] have shown improved delineation of lesions and higher correlations with T1 and T2 lesion intensities compared with conventional FA maps, and lesions have displayed lower values when compared to NAWM, complementary to FA values. Examples of LTE, STE, μFA,

MK_a, MK_i and MK_t maps are shown in Figure 1.17 in comparison with MPRAGE and FA maps from the same slice (for reference) in a healthy subject.

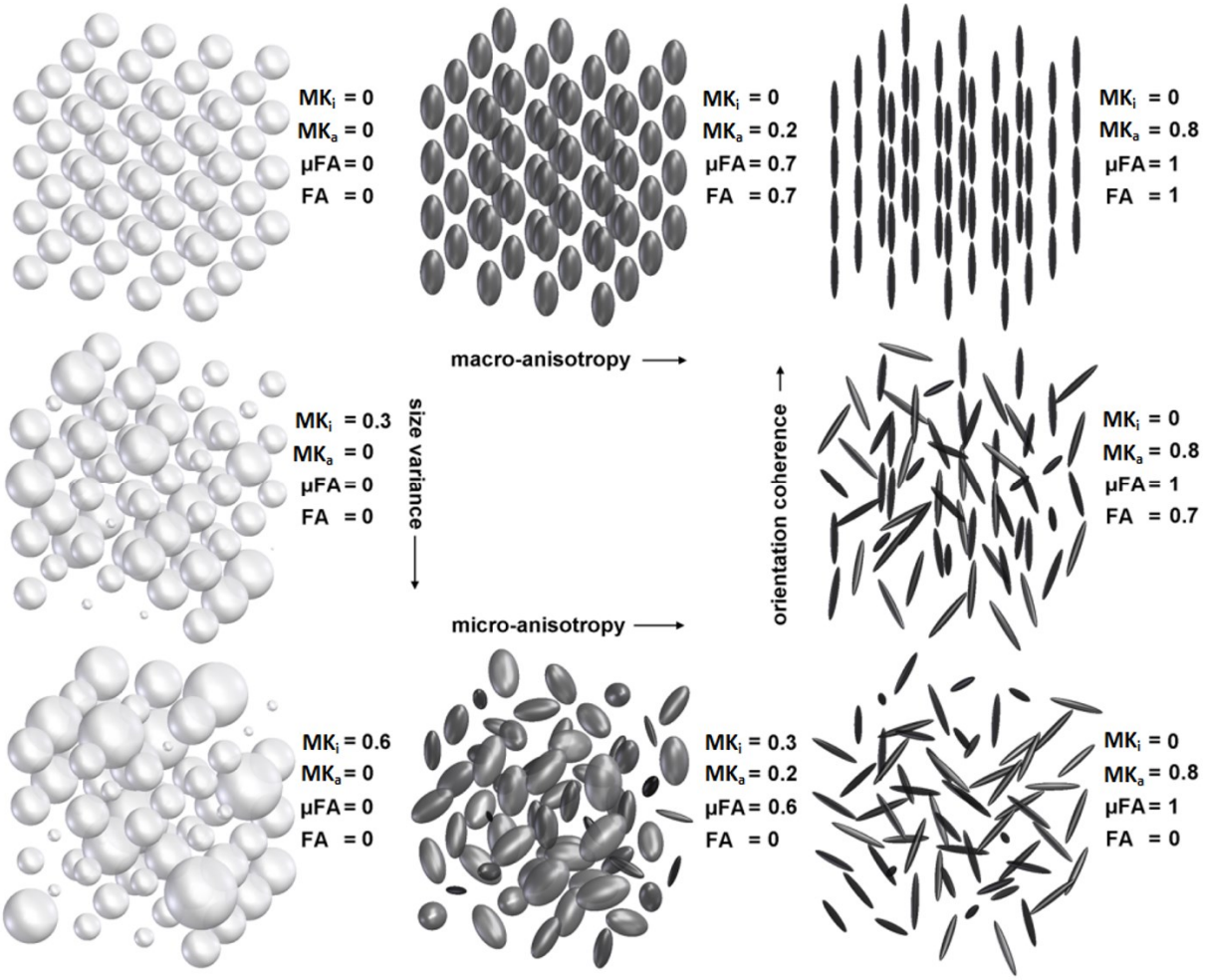

Figure 1.16: Schematic representation of DIVIDE parameters in eight different diffusion tensor distributions (DTD). The parameters show the isotropic and anisotropic diffusional variance (MK_i and MK_a), and the fractional anisotropy on the microscopic and voxel scale (μFA and FA). For example, in a perfectly homogeneous tissue, all four parameters are zero (top left), and for randomly oriented anisotropic structures the μFA is high whereas the FA is zero (bottom right). MK_a seems particularly sensitive to the anisotropic shape (eccentricity) of the microscopic diffusion tensors irrespective of their orientation (bottom right), while MK_i seems sensitive to the variable densities of the microscopic diffusion tensors (bottom left). Image and caption modified and reprinted from [167] under the BSD 3-Clause License, Filip Szczepankiewicz Copyright (c) 2019.

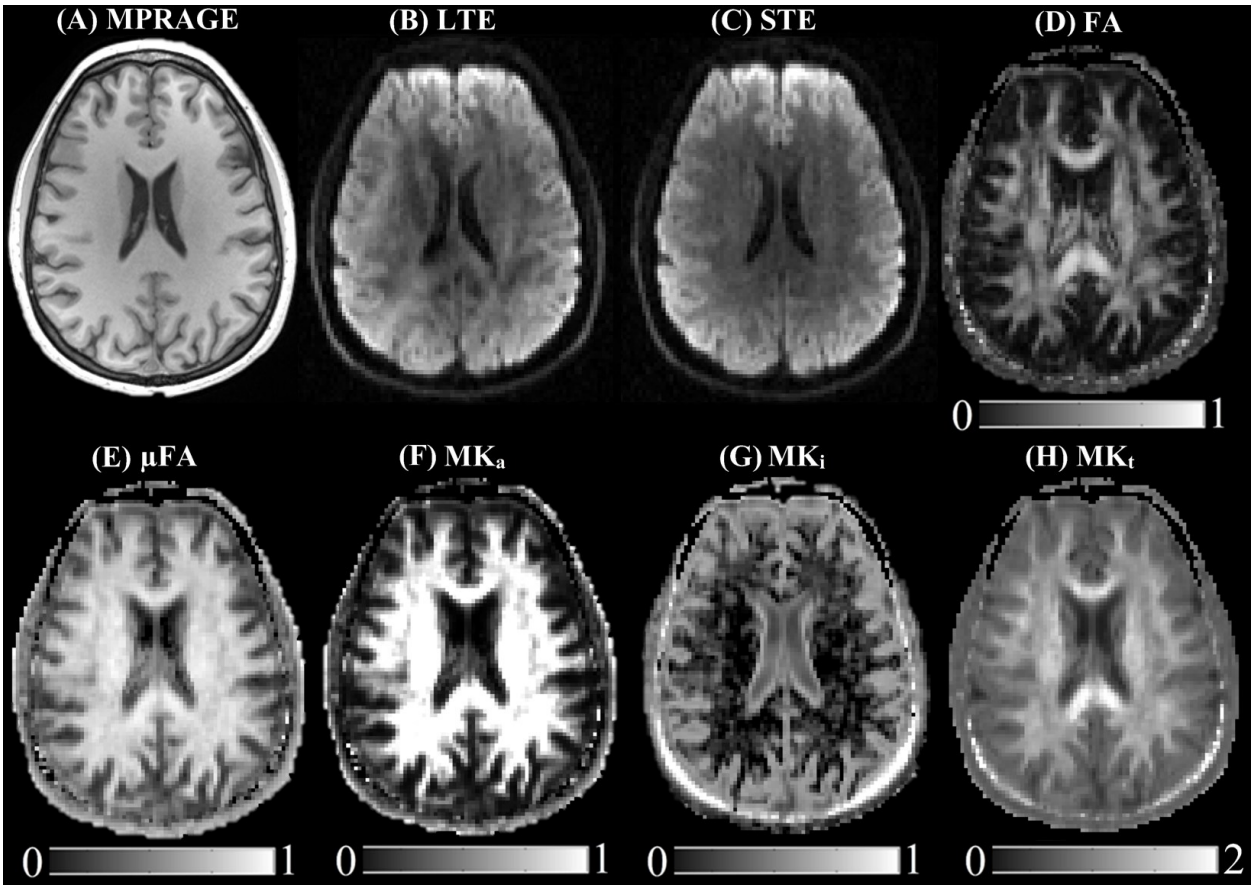

Figure 1.17: DIVIDE maps in a 29-year-old healthy female. (A) MPRAGE, DWIs from (B) Linear (LTE) and (C) Spherical (STE) tensor encoding at b=1000 s/mm^2, and (D) FA, (E) μFA, (F) MK_a, (G) MK_i and (H) MK_t maps. Similar to FA, μFA and MK_a maps highlight the brain WM. However, μFA (and to a lesser extent MK_a) does it regardless of the local orientation dispersion as it exhibits high values in areas where FA values are low due to crossing and fanning fibers. The μFA and MK_a maps exhibit strong similarity to the WM morphology in MPRAGE, with GM showing lower intensity, which indicates that the microscopic anisotropy and the anisotropic variance are lower in GM as compared to WM. In contrast, MK_i highlights areas where the isotropic variance dominates, and it is generally low in brain tissue and high in areas with CSF interfaces due to partial volume effects.

1.3. Multiple Sclerosis (MS)

MS is a demyelinating, inflammatory, and neurodegenerative disease of the brain and spinal cord. The following section succinctly outlines clinical and pathologic aspects of the disease, the MS diagnosis criteria, and the clinical value of MRI for MS diagnosis and follow-up. In addition, previous diffusion MRI MS studies will be briefly discussed.

1.3.1. Epidemiology and Causal Factors

According to the MS International Federation report in 2020 [173], there are 2.8 million people worldwide who have MS. In Canada only, there are 90,000 people living with MS, which translates to a prevalence of 250 in every 100,000 inhabitants, one of the highest in the world (Figure 1.18). Even though MS can occur at any age, the average age of diagnosis is 32 years worldwide, and 43 years in Canada. Females are at least twice as likely to be diagnosed with MS, however this ratio is at least three times in Canada where 75% of people with MS are women. Around the globe, 85% of people with MS are at first diagnosed with the relapsing-remitting form with 12% diagnosed with more progressive forms, whereas in Canada these are 90% and 10%, respectively.

Although the underlying cause of this disease is not known, both environmental factors (e.g., colder climates with low exposure to sunlight, vitamin D deficiency) and involvement of genetic factors (e.g., family history of MS, previous autoimmune diseases and virus infections) have been proposed to play a role in triggering MS. However, very recent research [174] suggested a strong connection between the Epstein-Barr virus and MS, wherein subjects previously infected with this virus were 32 times as likely to develop MS as uninfected people.

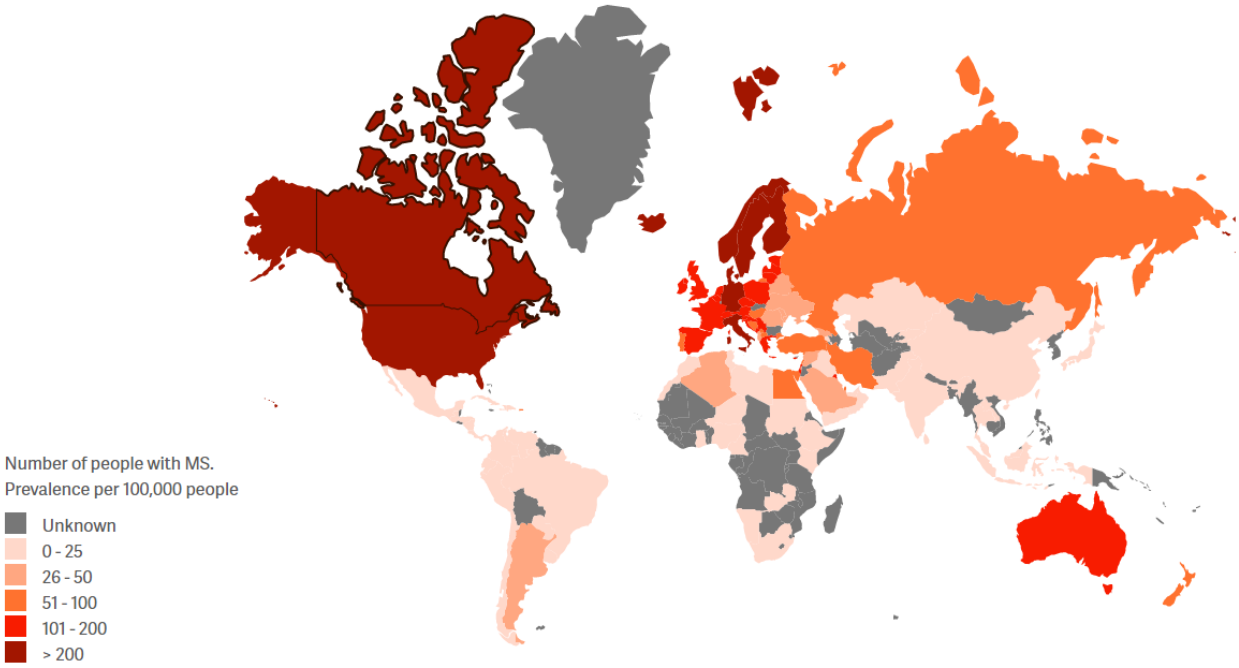

Figure 1.18: 3rd Edition of the MS International Federation Atlas of MS in 2020. The atlas shows the worldwide MS prevalence per country, expressed as the number of people with MS per 100,000 people. Among the countries classified with the highest prevalence (dark red), Germany has the highest world prevalence, which is 303, followed by the United States with 288 and Canada with 250. Cuba, for example, has a low prevalence of 15, however the most commonly used MS diagnostic criteria is "unknown" for the country, according to MS International Federation.

1.3.2. Clinical Phenotypes

The different MS clinical phenotypes, as described in the 2013 MS clinical course revisions [175], are:

- *Radiologically Isolated Syndrome (RIS):* It refers to subjects in which brain or spine MRI (or both) demonstrate incidental lesions that are characteristic of a demyelinating disease, fulfilling the revised 2017 McDonald Criteria for dissemination in space but without a

clinical history of demyelinating attacks, ongoing neurologic deterioration or other alternative causes [176].

- *Clinically Isolated Syndrome (CIS):* It is the first clinical presentation of MS showing characteristics of inflammatory demyelination but has not yet fulfilled the criteria of time and space dissemination [177].
- *Relapsing-remitting MS (RRMS):* It features clearly defined relapses or periods of clinical decline that are followed by full recovery or some partial or residual deficit after recovery. Remission periods between the relapses are characterized by a lack of disease progression. Around 80% of all RRMS will develop secondary progressive MS later in the disease course [178].
- *Secondary Progressive MS (SPMS):* It progresses after an initial RRMS disease course, with or without intermittent relapses, and only minor remissions sometimes. The inflammatory component of the disease becomes less important with more emphasis on neurodegeneration and potential axonal loss [179].
- *Primary progressive MS (PPMS):* It follows a progressive disease course from onset, with intermittent plateaus and occasionally temporary minor improvements. PPMS is present in approximately 10% of the MS patients, and no PPMS palliative treatment has been identified as opposed to RRMS, where inflammation can be targeted to modify the disease course [180].

1.3.3. Pathology

Pathological mechanisms behind MS are not fully elucidated yet [181]. The most important pathological hallmark of MS is focal inflammatory demyelination lesions or plaques in the WM with varying degrees of inflammation, gliosis, and axonal degeneration [182]. The BBB separates the circulating blood in the brain from the extracellular fluid in the central nervous system. It selectively allows passage of some substances but blocks the passage of neurotoxins and immune white blood cells that may disrupt the function of the brain. In MS, BBB disruption occurs at the time of a relapse or attack caused by autoreactive lymphocytes (CD4 and CD8 T-cells) entering the CNS where they cause local inflammation that results in demyelination, gliotic scarring, and axonal loss [183]. BBB breakdown can be detected using Gd-enhanced T1-weighted MRI (Figure 1.6) [60]. This initial autoimmune response leads to an inflammatory response from dendritic cells, microglia, astrocytes, and B-cells and to a release of cytokines that cause damage to glial cells, axons, and promotes BBB dysfunction [184]. Cellular damage is initially mainly towards myelin surrounding the axons in WM [185] around postcapillary venules and veins which fuse into confluent demyelinated lesions or plaques and expand into the surrounding NAWM [186]. GM lesions with less inflammation, edema, microglia activation, and macrophage recruitment than in WM lesions have also been documented in MS and they are more frequent in long-standing MS patients [187], [188]. These lesions can be seen in deep GM [189]–[191], cortex [191]–[193] and spinal cord [194]–[196][188], mainly in the inner layers closest to the ventricles and in the subpial layer [188], [197].

Diffuse changes such as moderate brain edema, microglia activation, axonal injury and gliosis secondary to focal lesions also occurs in MS and are more pronounced with disease progression [186]. These changes partially develop because of anterograde (Wallerian) and retrograde degeneration from focal lesions but also independent of lesions [198]. Pathological analyses on large cohorts of patients at several disease stages have show that chronic active and slowly expanding (smoldering) lesions are common in progressive MS patients [199]–[201] and compartmentalized within the CNS [202]. The compartmentalized inflammation within the leptomeninges and the parenchyma due to T-cells and B-cells inflammatory infiltrates appears to be a critical driver [203]. Although this compartmentalized mediated inflammation prospectively remains as the fundamental driver of clinical progression in MS, recent perspectives have also highlighted the role of the CNS tissue response to this lifetime inflammatory damage as an important actor for both pathological and clinical outcomes [202], [204].

1.3.4. Clinical Symptoms and Cognitive Impairment

Symptoms vary widely between different MS patients, depending on their disease course, the location of nerve fibers directly affected by lesions, and even retrograde or anterograde degeneration (‘Wallerian’ degeneration) [205]. A very common example of this location specificity and an early MS symptom is the unilateral loss of vision (optic neuritis) due to inflammatory demyelination of the optic nerve. Other frequent symptoms are motor impairment, imbalance, sensory and cognitive impairment, depression, fatigue, and bladder and bowel dysfunction [206], [207].

Cognitive impairment is frequently present in MS patients, affecting 40% to 65% of them at some point during their disease course [208]. Cognitive symptoms can vary from minor to severe impairments with memory, attention, and information processing speed as frequently affected cognitive domains in MS. These cognitive and clinical symptoms can be detected using a variety of neuropsychological/clinical tests and questionaries, some of them specific for MS pathology. Forms and questionnaires utilized as part of the battery of clinical and cognitive tests performed by the MS cohorts in this dissertation are listed in Appendix B. The pathological substrates behind cognitive impairment in MS are still largely unknown, but the atrophy and abnormal microstructure of specific WM matter structures such as the limbic tracts (e.g., the fornix) [26], [209], [210], and deep GM structures in the medial temporal lobe (e.g., the hippocampus) and the basal ganglia (e.g., the thalamus) [211]–[213] are related to cognitive decline in MS.

1.3.5. Type of Lesions

Lesions are frequently classified as either active, chronic active, or chronic without providing an exact definition, and several classification systems [214]–[218] have been established mainly to assess lesion activity (e.g., Bö/Trapp system, De Groot/van der Valk modification, Lucchinetti/Lassmann/Brück system, Vienna consensus system). Activity can be inflammatory, demyelinating, or neurodegenerative, and chronic is used to define an inactive or chronic active lesion. When combined, these earlier histological classification systems aid classifying lesions based on macrophages/microglia inflammatory activity and ongoing demyelinating activity, and they can differentiate between active, mixed active/inactive, and inactive lesions with or without ongoing demyelination [219]. Active lesions are characterized by macrophages/microglia

throughout the lesion area, and mixed active/inactive lesions have a hypocellular lesion center with macrophages/microglia limited to the lesion border. Active and mixed active/inactive lesions can be further subdivided into lesions with ongoing demyelination and post-demyelinating lesions, where demyelination has stopped but macrophages are still present. Inactive lesions almost completely lack macrophages/microglia.

1.3.6. Diagnosis: McDonald Criteria

The McDonald Criteria, first introduced in 2001 [220], and its most updated revisions contain the MS diagnosis guidelines created by the International Panel on Diagnosis of Multiple Sclerosis. These criteria have been designed and updated by combining available clinical, imaging, and laboratory evidence of CNS damage with the most recent revisions in 2017 [221]. Clinical evidence of MS damage can be demonstrated by two or more attacks with at least one lesion with objective clinical evidence and dissemination in space evident on MRI. An attack, also known as a relapse or an exacerbation, are defined as "patient-reported symptoms and objective findings reflecting a focal or multifocal inflammatory demyelinating event in the CNS, developing acutely or subacutely, with a duration of at least 24 h, with or without recovery, and in the absence of fever or infection". When there is only one clinical attack in a typical CIS patient and fulfilment of clinical or MRI criteria for dissemination in space together with the presence of CSF-specific oligoclonal bands, an MS diagnosis is also probable, and this recommendation was an addition to the 2010 McDonald criteria. The diagnosis flowchart describing the 2017 McDonald criteria for MS diagnosis in patients with an attack at onset is shown in Figure 1.19.

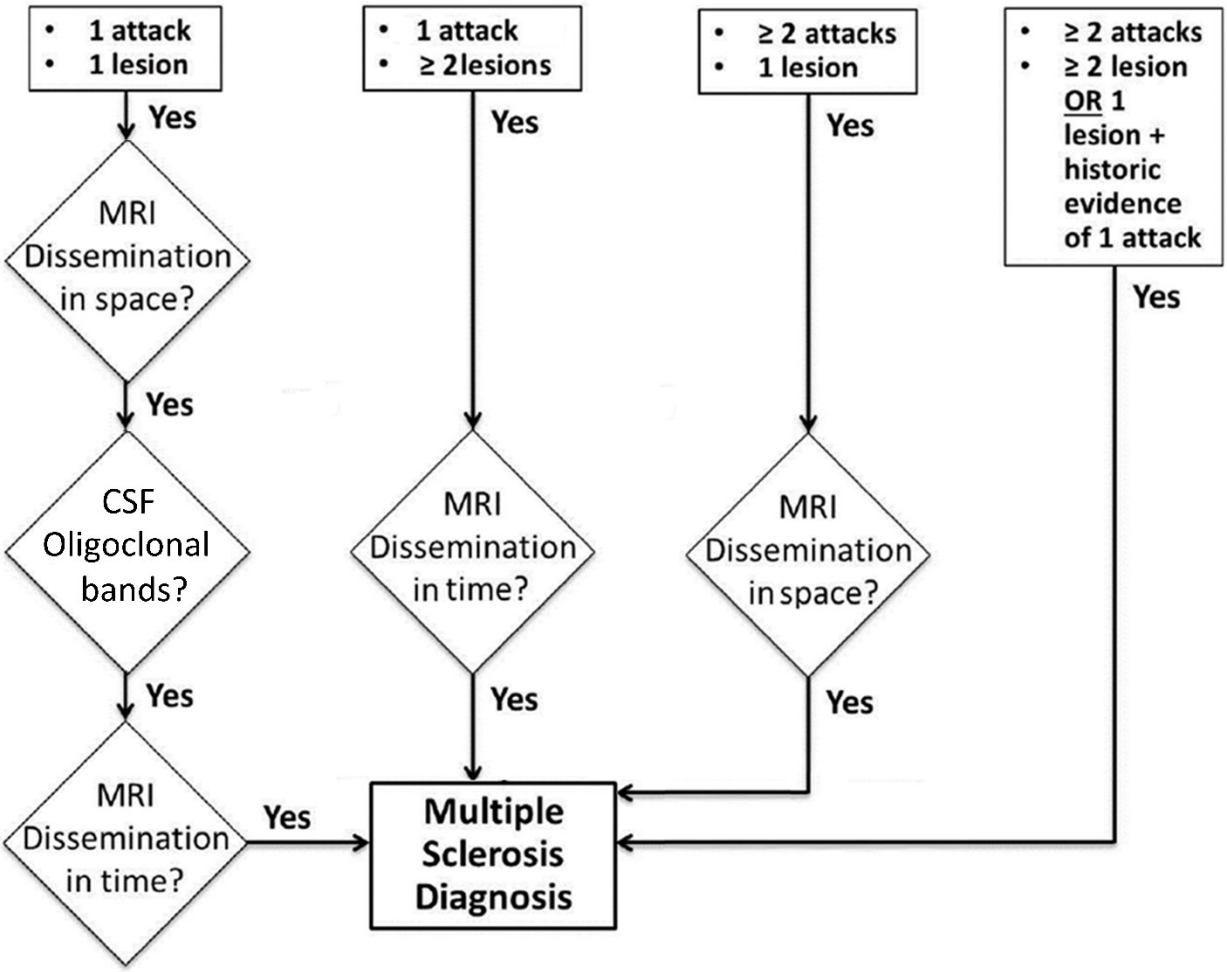

Figure 1.19: 2017 McDonald criteria diagnosis flowchart for MS diagnosis in patients with an attack at onset.

Dissemination in space and time can be demonstrated by MRI. Dissemination in space can be demonstrated by symptomatic and asymptomatic T2-hyperintense lesions (Figure 1.20B) [221] that are characteristic of MS in at least two of four areas of the CNS (periventricular, cortical or juxtacortical, infratentorial, spinal cord) (Figure 1.20). Dissemination in time can be shown by the concurrent presence of Gd-enhancing and non-enhancing lesions at any time, or by Gd-enhancing

and new T2-hyperintense lesions on follow-up MRI, when compared to a baseline MRI scan disregarding when it was taken.

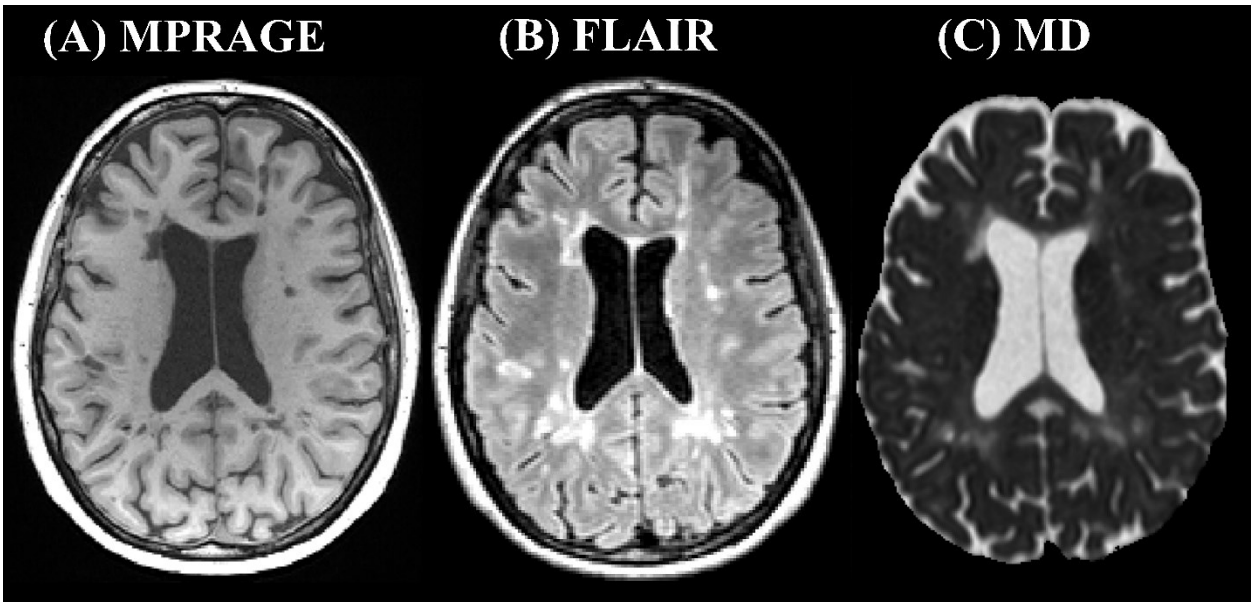

Figure 1.20: Typical periventricular lesions characteristic of MS. MS lesions in a 50-year-old female SPMS as (A) hypointense 'black holes' on 3D T1-weighted MPRAGE, and hyperintense on (B) T2-weighted 3D FLAIR and on (C) MD maps reflecting faster water diffusion in the lesions.

In addition to the previously discussed diagnosis flowchart in Figure 1.19, the McDonald criteria also define the diagnosis of PPMS. To detect PPMS in patients with a disease course characterised by progression from onset, one year of disability progression could be determined in a retrospective or a prospective fashion, and independent of clinical relapse. Additionally, two of the following criteria should be fulfilled: (i) one or more T2-hyperintense MS characteristic lesions in one or more brain regions (periventricular, cortical or juxtacortical, infratentorial), (ii) two or more T2-hyperintense lesions in the spinal cord, (iii) CSF-specific oligoclonal bands.

1.3.7. Treatment

Although there is no cure for MS yet, an increasing range of treatment options have become available during the last three decades. First line treatments for MS are injectable disease modifying therapies focused on RRMS, such as beta-interferons and glatiramer acetate, which target the inflammatory component of the disease, therefore effectively decreasing the inflammatory response and the relapses [222]. Regrettably, most treated RRMS patients keep progressing into SPMS suggesting that the MS pathological substrates are not substantially delayed by most of these treatments. More recent, alternative treatment options such as monoclonal antibodies (e.g., natalizumab, fingolimod, ocrelizumab) are usually employed when first line disease modifying therapies are not working, or when the disease course is progressing aggressively. These second line treatments [223]–[225] although also very effective in reducing inflammation and relapses, could have more severe side effects and the long-term effects in the disease outcome are either still undetermined or have shown no changes.

1.3.8. MRI as a Diagnosing and Monitoring Tool

Several consensus papers authored by the MAGNIMS and the CMSC have highlighted the importance and clinical value of MRI for MS diagnosis and follow-up [59], [226]. These guidelines on the use of MRI for MS have helped with the standardization of MRI acquisition protocols and have incorporated the perspectives of the North American Imaging in Multiple Sclerosis (NAIMS) Cooperative. The most updated international consensus guidelines were published in 2021 [66] and instructed the use of axial and sagittal T2-weighted and FLAIR sequences, and contrast enhanced axial T1-weighted sequences for initial brain protocols.

However, they endorsed 3D acquisition techniques over 2D acquisitions as the former improve MS lesion detection and the alignment of anatomic orientation/structures when comparing MRI scans (Figure 1.10A, B) [66]. They also advised MRI field strength of at least 1.5T (preferable 3 T), anatomical in-plane resolution of 1×1 mm^2, with slice thickness not greater than 1.5 mm for 3D imaging and equal or less than 3 mm for 2D imaging, except for DWI, which if performed, should be equal or less than 5 mm with a 10–30% gap. These MRI acquisitions should have identical slice positioning, pulse sequences, magnetic field strengths, and spatial resolution between baseline and follow-up scans [66].

On baseline scans, the use of Gd-based contrast agents is recommended to show dissemination in time and to predict future disease activity and progression, and only when needed for assessing disease activity or treatment during follow-up scans. Other additional advanced MRI protocols not needed in typical clinical routine but often incorporated for MS monitoring and research to gain a better understanding of the pathogenesis of the disease and to quantify damage beyond lesions are DWI (Figure 1.10C) [227], FLAIR* [228], susceptibility-weighted sequences [229], magnetization transfer imaging [230] and multi-exponential T2 relaxation [231], although insufficient evidence exists to support their use in standard clinical practice.

1.3.9. DTI Studies in Human MS

Numerous diffusion MRI research studies, particularly DTI, have shown brain diffusion abnormalities in MS patients when compared to healthy subjects. T2-hyperintense WM lesions have consistently displayed lower FA [120], [232] and higher MD [232]–[235]. In some previous

work, MD values were even higher in T1 hypointense lesions with a more advanced disruption, gliosis, and axonal loss [236], [237]. Nevertheless, these values are highly heterogeneous as they reflect several stages of tissue damage occurring within a diversity of lesions which could be permanent neurodegeneration or could be related to edema, demyelination and remyelination [122], [238].

In MS, tissue abnormalities in NAWM throughout the brain, which are unseen or 'occult' with several conventional MRI techniques, have been detected with DTI**.** Again, these DTI tissue anomalies in MS patients usually encompass lower FA [239]–[242] and higher MD [240], [242]–[245], while higher directional diffusivities AD and RD have also been reported [242], [246], [247] as potentially related to increased extra-cellular space and demyelination, respectively. Additionally, DTI studies have shown that NAWM damage correlated with longer disease duration and greater clinical disability [120], [240], [248], [249] suggesting that metrics like FA are sensitive to several pathological processes that could be happening in MS, although unspecific in many cases [250]. Numerous diffusion works have further focused on mainly large WM tracts with preferential MS lesion incidence or known to be involved in particular brain functions, such as the corpus callosum, and the optic radiation, among others, and their abnormal diffusion metrics have been related to greater lesion burden, longer disease times, disability, and memory functions [251]–[255].

A number of previous DTI studies have focused on other WM bundles, such as the limbic tracts [125], [256]–[260], which although small, connect many cortical and subcortical brain areas and appear to be located near the epicentre of periventricular regions with high lesion incidence.

Specifically, one of these tracts, the fornix, interconnects important structures (Figure 1.2) that together are deeply implicated in cognitive functions (memory, information processing speed) and mood shifts (fatigue, depression) [261], which are affected in MS [26]. However, accurately imaging and depicting the fornix with DTI comes with technical challenges due to its size and location [28], [30], such as high resolution, CSF suppression, anatomical knowledge of the structure and careful selection of the post-processing analysis.

NAGM diffusion abnormalities in MS have also been studied to a lesser degree, although results are not always consistent, probably due to several factors such as different image quality and resolution, analysis methods, the heterogeneity of the sample size, which could conceivably highly influence small GM structures with microarchitecture not as anisotropic as WM. Several studies have detected FA and MD abnormalities, such as lower MD, higher or lower FA, or no diffusion changes, in both cortical and deep NAGM [248], [262]–[268]. Some DTI studies applied to deep GM regions like the thalamus and the hippocampus have encountered abnormalities in these structures beyond atrophy and correlated them with cognitive deficits in MS [267], [269]–[271]. A full list of up-to-date DTI studies focusing on limbic WM or deep GM structures in MS is shown in Appendix C.

1.4. Thesis Objectives

Clinical MRI has provided many valuable insights and confirmatory information of pathological brain damage in MS, including lesion classification and lesion load calculation, and reductions in total and regional WM and GM volume. More unconventional quantitative techniques such as

diffusion MRI have shown widespread MS abnormalities in the so called NAWM, in specific WM tract bundles and even in NAGM. However, several important limitations of previous findings should be noted, and the need of continued research by either pushing into higher resolution DTI studies or through the application of more advanced diffusion MRI methods in MS should be emphasized. The following describes the rationale that motivated much of the content of this thesis.

At the onset of my graduate program, there were few MS DTI studies directly assessing the limbic WM tracts as opposed to neurodegenerative dementias like Alzheimer's disease. Most of them were region of interest/atlas based [256]–[259], [272], [273]. Only four diffusion studies [125], [260], [274], [275] employed tractography analysis, which is a more suitable method for depicting small, partially isolated and curved tracts like the fornix [28], [276], [277] versus other whole brain voxel-analyses such as TBSS [143]. Furthermore, they were largely acquired at typical low spatial resolutions (e.g.,>2 mm isotropic, voxel size>8 mm^3) and treated MS patients as a single cohort. This led to the results presented in research Chapter 2 where WM damage in the fornix, the cingulum and the uncinate fasciculus bundles was shown in an MS cohort comprised of all phenotypes.

Chapter 3 improved the technical DTI acquisition of Chapter 2 by applying a higher resolution DTI protocol at 3 T, coupled to a CSF suppression FLAIR pulse, which successfully minimized partial volume effects with CSF and rendered superior fornix tracts. This DTI research in Chapter 3 applied FLAIR-DTI in MS for the first time in a bigger cohort when compared to Chapter 2 (28 MS patients in Chapter 2 and 43 MS patients in Chapter 3). In Chapter 3, volumetric analyses were

also performed, and analyses were extended to the thalamus and the hippocampus, as deep GM structures interconnected by the fornix. These three structures have proven to be involved in MS cognitive impairment [255], [278] and are shown here to be more severely affected in terms of volume and DTI metrics in cognitively impaired MS patients versus not impaired MS patients and controls, with strong correlations to poorer memory, slower information processing speed and fatigue. Here, fornix volume and diffusion metrics were found as the most abnormal within these limbic structures in MS and mainly linked with cognitive impairment, while thalamus volume and hippocampus FA were also lower in cognitively impaired MS patients.

Chapter 4 focused on the application of a novel 1 mm isotropic DTI protocol with axial-oblique slab coverage of the hippocampus acquired in less than 6 min at 3 T [136] in a cohort of MS patients for the first time. Whole and regional hippocampal DTI analyses were performed through manual segmentation and areas with abnormally high MD were identified to calculate the relative area of abnormal MD relative to the total hippocampal volume. In addition, 1.1x1.1x1 mm^3 high resolution T2 relaxometry and T2-weighted signal were evaluated in the whole and regions of the hippocampus. DTI and T2 mapping showed whole hippocampus diffusion and T2 abnormalities with regional elevations of MD/T2 in MS, likely indicators of demyelination, which overall were more extensive in patients with larger total brain lesion volumes and cognitive impairment and was consistent with what has been reported with previous post-mortem hippocampus histology.

Chapter 5 reports the use of a novel b-tensor diffusion encoding protocol in the same MS cohort of Chapters 3 and 4 providing new diffusion metrics that can help disentangle contributions from microscopic environments within a voxel. Most of these new metrics, mainly μFA, MK_a, and MK_t

were complementary to standard diffusion metrics in lesions, NAWM and highly coherent WM in MS and controls. In crossing WM fiber areas where FA did not differ between groups, these three microstructural metrics (μFA, MK_t and MK_a) were lower and deemed as abnormal in MS patients compared to controls, providing more sensitive indicators of microstructure when compared to FA.

All research chapters here (except Chapter 2 where only FLAIR was acquired), also utilized different anatomical sequences, such as MPRAGE, FLAIR, T2-weighted, which were acquired with high in-plane resolution, in order to aid with the interpretation of the results, provide robust quantitative analyses and a more complete characterization of the MS cohorts under study here. These scans allowed the calculation of lesion volumes, total WM, GM, CSF volumes and deep GM volumes. In Chapter 4, hippocampus T2 relaxometry values calculated from high resolution T2 multi-echo spin echo sequences were analyzed in MS for the first time and supplemented by T2-weighted signal analyses. Advanced brain imaging, including the work presented in this thesis, will help to provide a more complete understanding of the pathological mechanisms behind MS with a focus on the limbic system microstructural changes and its associations with cognition including memory, clinical symptoms such as fatigue and depression, and disability.

Research Contributions

2. Diffusion Tensor Imaging Tractography Reveals Altered Fornix in All Diagnostic Subtypes of Multiple Sclerosis[1]

Abstract

Diffusion tensor imaging (DTI) has shown abnormalities of the fornix and other limbic white matter tracts in multiple sclerosis (MS), mainly focusing on relapsing-remitting MS. The goal here was to evaluate the fornix, cingulum, and uncinate fasciculus with DTI tractography at 1.7 mm isotropic resolution in three MS subgroups (11 relapsing-remitting (RRMS), 9 secondary progressive (SPMS), 8 primary progressive (PPMS)) versus 11 controls and assess correlations with cognitive and clinical scores. The MS group overall showed extensive diffusion abnormalities of the fornix with less volume, lower fractional anisotropy (FA), and higher mean and radial diffusivities, which were similarly affected in all three MS subgroups. The uncinate fasciculus had lower FA only in the secondary progressive subgroup and the cingulum had no DTI differences in any MS subgroup. The FA and/or volumes of these tracts correlated negatively with larger total lesion volume. The only DTI-cognitive correlation was lower right cingulum FA and greater depression over the entire MS cohort. Diffusion tractography identified abnormalities in the fornix that appears to be affected early and consistently across all three primary MS phenotypes of RRMS, SPMS, and PPMS regardless of Expanded Disability Status Scale, time since diagnosis, or cognitive scores.

---

[1] Published as: Valdés Cabrera, D, Stobbe, R, Smyth, P, Giuliani, F, Emery, D, Beaulieu, C. Diffusion tensor imaging tractography reveals altered fornix in all diagnostic subtypes of multiple sclerosis. Brain Behav. 2020; 10:e01514. https://doi.org/10.1002/brb3.1514.

2.1. Introduction

Inflammation, demyelination and axonal degeneration of white matter (WM) pathways are hallmarks of multiple sclerosis (MS) [279]. The progressive deterioration of specific WM tracts may cause disconnections between cortical/subcortical regions that are associated with particular cognitive impairments [258]. Diffusion tensor imaging (DTI) is well suited to the virtual identification of WM pathways and can yield quantitative metrics that are sensitive to microstructural damage of WM, not just limited to the clinical-MRI visible lesions in MS. A whole brain meta-analysis of the WM 'skeleton' using tract based spatial statistics (TBSS) has shown lower fractional anisotropy (FA) in the corpus callosum, which has been a major focus of prior work due to its preferential location for MS lesions and its large size, – but also in smaller tracts such as the fornix and cingulum where lower FA has been associated with greater physical disability and impaired cognition [280]. Separate whole brain analyses of mostly relapsing-remitting MS (RRMS) participants have reported lower FA throughout much of the WM with FA in some specific WM regions (e.g., again including cingulum and fornix) correlating to deficits such as processing speed and working memory [255], [281]–[283].

Tracts of the limbic system, like the fornix, play crucial roles in aspects of cognition, memory, behavior and reasoning [284], and they have been implicated in the above whole brain analyses of MS. Given this relevance, limbic system tracts have been the focus in MS diffusion MRI studies assessed with either region of interest/atlas [256]–[259], [285] or tractography [125], [209], [260], [274], [275], both targeted analyses that can have distinct advantages over whole brain voxel-based methods (e.g., far fewer multiple comparisons, do not need inter-subject registration for native

space tractography). The majority of these DTI studies have been in patients with RRMS, but FA abnormalities in the limbic WM tracts, including the fornix, have also been demonstrated in primary progressive (PPMS) [273] and secondary progressive MS (SPMS) [272]. One such voxel-wise whole brain DTI study showed that PPMS had widespread diffusion abnormalities in WM and that SPMS had more extensive WM diffusion changes than either RRMS or PPMS [286].

Three key limitations can be identified from these limbic white matter DTI studies of MS. First, with the exception of the latter three studies above [272], [273], [286], analyses were based on mainly RRMS participants or analyses that treated all MS patients as a single cohort. Second, the fornix is a very small tract (~3, 3.5, and 6.5 mm mean cross-sectional diameters in the posterior and anterior columns and body respectively, even in healthy participants) [28] that passes through cerebrospinal fluid (CSF) and hence is not ideal for analysis when DTI data is acquired at typical low spatial resolutions (e.g.>2 mm isotropic, voxel size>8 mm^3). Third, the typically used TBSS voxel-wise analysis of the WM has been shown to have particular difficulty with the FA skeleton of the fornix [143].

The purpose of this study was to (i) use DTI deterministic tractography at high field strength (4.7 T) and spatial resolution of 1.7 mm isotropic to investigate whether microstructural damage to specifically the small limbic tracts (fornix, cingulum and uncinate fasciculus) is similar in all three diagnostic subgroups of MS (RRMS, SPMS and PPMS), and (ii) correlate the DTI-derived tract diffusion metrics and volumes of the entire MS cohort with both lesion numbers/volumes and cognitive impairments (visuospatial memory speed, depression and fatigue), disability (EDSS) and time since diagnosis.

2.2. Materials and Methods

2.2.1. Participants

This study was approved by the University of Alberta Human Research Ethics Board. All 39 participants gave written informed consent including 28 diagnosed with MS (11 RRMS, 9 SPMS, and 8 PPMS) that were recruited from the University of Alberta MS Clinic, as well as 11 typical controls with no history of neurological/psychiatric disease or brain injury that covered the same age range and had similar sex distribution. MS participants were not targeted for their subtype, but a goal was to have similar proportions from RRMS, SPMS and PPMS with a target MS sample of 30 total (28 actual) given other constraints. There were no patients with relapses or taking steroids at the time of the MRI scan. However, there was no available information regarding whether they had recent prior relapses or not. Therefore, none of the MS participants were excluded from the study. The SPMS and PPMS participants were not receiving medications or treatments specific for MS at the time of the MRI study, except one SPMS participant on IV infused natalizumab. Three RRMS participants were not taking any medications, but the other 8 RRMS were on different disease modifying therapies (dimethyl fumarate, glatiramer acetate, fingolimod, natalizumab). Three participants (RRMS, SPMS, PPMS) were on antidepressant medications (escitalopram, duloxetine, bupropion). The demographic and clinical data are summarized in Table 2.1 in the Results.

2.2.2. Cognitive Assessment

Cognitive and clinical tests were performed by experienced MS research nurses from the University of Alberta MS Clinic in order to characterize the MS population and to correlate with quantitative MRI metrics. The tests consisted of: Kurtzke Expanded Disability Status Scale (EDSS) for overall disability in MS, Brief Visual Memory Test Revised (BVMT-R) for visuospatial learning and memory (Total Recall score only), Symbol Digit Modalities Test (SDMT) for visual scanning/tracking memory and decision making, Paced Auditory Serial Addition Test (PASAT) for auditory information processing speed, Fatigue Severity Scale (FSS) for degree of fatigue, Modified Fatigue Impact Scale (MFIS) for effects of fatigue in terms of physical, cognitive, and psychosocial functioning, Beck Depression Inventory-II (BDI-II) for depression, Timed 25-Foot Walk (T25-FW) for mobility and leg function, and 9-Hole Peg Test (9-HPT) for upper extremity function (dominant/non-dominant hand raw scores averaged).

2.2.3. MRI Protocol and Analysis

MRI was acquired on a Varian Inova 4.7 T MRI with a birdcage transmit and 4-channel receive array coil. Fast Spin-Echo Fluid-Attenuated Inversion Recovery (FSE FLAIR) was acquired with FOV 256×192 mm2, 1×1 mm^2 in-plane resolution, 38 4 mm slices (no gap), TR=34 s, TE=204 ms, TI=3000 ms and scan time 3:24 min. DTI was acquired with single-shot spin-echo Echo-Planar Imaging (EPI), GRAPPA R=2, 80 1.7 mm slices (no gap) and coverage of 136 mm, FOV 218×238 mm^2, matrix 128×140, 1.7×1.7×1.7=4.9 mm^3 voxel resolution, zero-filled to 0.85×0.85 mm^2 in-plane, TR=9500 ms, TE=54 ms, 30 directions, b=1000 s/mm^2, 5 b0 and scan time 6:13 min.

MS lesions were segmented on FLAIR by a probabilistic lesion prediction algorithm in the Lesion Segmentation Tool (LST) MatLab toolbox (v2.0.15) for SPM to yield total lesion number (TLN) and volume (TLV) and all the lesion maps results were visually checked. DTI was corrected for subject motion and eddy current distortions with the Artefact Correction in Diffusion MRI (ACID) toolbox (SPM12) and none of the datasets were discarded for excessive movement (all were less than 2˚ rotations and 2 mm translations). The ACID rotation and translation corrections for the axial, sagittal and coronal planes for each subgroup were not significantly different between the subgroups (data not shown).

The brain was extracted with BET (Brain Extraction Tool) in FSL. Gibbs ringing, EPI distortion corrections and tensor fitting using RESTORE were performed in ExploreDTI (v4.8.6) [287]. Deterministic tractography was performed with an FA threshold of 0.2, a turning angle of 30˚, step size of 1 mm and minimum fiber length of 10 mm. These tracking parameters, primarily FA and angle thresholds, range from 0.13-0.3 and 30-70˚ respectively in previous healthy and MS cohorts [104], [125], [209], [260], [282], [288]

Tractography analysis was performed by the first author (DVC), who was blinded to group classification, based on published protocols for the limbic system tracts [104], [288] which reported excellent inter-rater/intra-rater intraclass correlations (ICC≥0.8) and percent coefficients of variation (CV≤2.5%) for FA and MD. Fornix: “SEED” ROIs were placed on an axial slice around the fornix column above the anterior commissure and in two coronal slices, one between the crus and fimbria, and one in the fornix body. These ROIs were placed on three distinct portions for the left and right hemispheres separately at first, and then the two fornices were concatenated

into one. “NOT” ROIs were placed on axial and coronal slices above, anterior and posterior to the fornix to avoid spurious fibers when necessary. Cingulum: “SEED” ROIs were placed in three coronal slices at the axial location of the genu, mid-body and splenium of the corpus callosum in order to track the superior/dorsal portion of the cingulum, including short u-fibers, and a “NOT” ROI in a midbrain sagittal slice to avoid fibers of corpus callosum. The ventral portion projecting to the entorhinal cortex was not tracked. Uncinate fasciculus (UF): Two “AND” ROIs were placed in the coronal slice where the frontal and temporal lobes are still separated and one ROI in an axial slice in the anterior temporal lobe, just lateral to the amygdala. “NOT” ROIs were placed posterior to the UF. The left and right cingulum and UF were reconstructed separately. Volume, FA, mean (MD), axial (AD), and radial (RD) diffusivities were calculated in ExploreDTI over the entire tracts.

Along the tracts analysis also was performed in ExploreDTI bilaterally in the body of the fornix, which was the fornix tract area consistently identified across the whole MS cohort. The body was segmented by using two “AND” ROIs placed on the columns and the commissural area of the fornix just at the start of the left and right crus to guarantee streamlines connecting both ROIs. FA was calculated along 35 tract location points from anterior to posterior.

2.2.3. Statistical Analysis

Statistical analysis was performed using Minitab 19. Multivariate normality was confirmed for all diffusion and volume parameters for each of the three WM tracts under study with a matrix of bivariate scatter plots (data not shown) and outliers were visually inspected by plotting Q-Q plots

of the Mahalanobis distances with Chi-Square test distribution and 5 degrees of freedom (Volume, FA, MD, AD, RD). Demographics for controls and MS were compared via two-sample t-test for the whole MS cohort, while MS subgroups were compared with ANOVA for numerical data and Chi-Square t-test for categorical data ($p \leq 0.05$). FLAIR-derived total lesion number and volume, and DTI-derived diffusion parameters (average of right and left) and volumes (total right and left) of the three WM tracts were compared between the MS subgroups and healthy controls with a One-Way ANOVA and a post-hoc Tukey's HSD test to control the family-wise error rate and to check for differences amongst diagnostic subgroups. The significance levels were corrected for multiple comparisons by using the Benjamini-Hochberg False Discovery Rate (FDR-BH) method in MatLab R2017a ($p \leq 0.011$). The FA values along 35 tract points in the left and right fornix body were compared with a General Linear Model (Two-Way ANOVA) to assess along the tract FA differences per group (FDR-BH corrected $p \leq 0.032$ for the left fornix body, $p \leq 0.029$ for the right fornix body).

For the combined MS group (n=28), Partial Pearson correlation coefficients corrected for age and sex assessed the relationship between FA and volume for each tract (right and left kept separate), total lesion number and volume, cognitive/clinical scores related with the limbic system functions (EDSS, BVMT-R, SDMT, MFIS, BDI-II), and time since diagnosis. Correlation coefficients were controlled for multiple comparisons with the FDR-BH method ($p \leq 0.0086$).

2.3. Results

2.3.1. MS Subgroup Characteristics, Lesion Numbers and Volumetric Load

The control group and full MS cohort did not differ in sex (p=0.74) and age (p=0.38). There were differences between the three MS subgroups; namely, RRMS were younger, had lower EDSS and scored higher in PASAT, SPMS had longer time since diagnosis, and PPMS had more males than females and lower scores in PASAT. Lesion number and volumetric load were quite variable between MS participants and were not different between MS subgroups (Table 2.1), although SPMS and PPMS had some individuals with larger lesion volumes than the RRMS group.

Lesion location patterns were similar across all MS subgroups (Figure 2.1A, B, C) mainly around and perpendicular to the body of the lateral ventricles and/or callosal junction areas (Dawson's fingers), consistent with the common lesion locations and shapes associated with the pathology. Within these groups, lesion numbers and volume did not correlate with age and sex although the lesion number showed a correlation trend toward statistical significance with age for the entire MS cohort (r=0.36, p=0.058). No significant associations were found between number of lesions or total lesion volumes with EDSS, time since diagnosis or cognitive scores (Table 2.2).

Table 2.1: Demographics for controls and the MS subgroups with range and mean +/- SD where appropriate (* $p \leq 0.05$ for differences between MS subgroups).

	Controls (n=11)	MS Cohort (n=28)	RRMS (n=11)	SPMS (n=9)	PPMS (n=8)
Sex (M/F)	4/7	10/18	2/9	2/7	6/2*
Age (years)	21-75 44 ± 16	21-66 48 ± 12	21-58 40 ± 12*	45-66 55 ± 7	41-65 54 ± 7
Time Since Diagnosis (years)	-	1-34 13 ± 10	1-28 9 ± 8	2-34 22 ± 9 *	3-17 8 ± 6
Expanded Disability Status Scale, EDSS†	-	1.5-8.5 4.8 ± 1.7	1.5-6 3.5 ± 1.5 *	4-8.5 5.6 ± 1.5	4-7 5.8 ± 1
Brief Visuospatial Memory Test-Revised, BVMT-R‡	-	5-34 21 ± 9	10-34 23 ± 8	11-34 21 ± 9	5-28 17 ± 9
Symbol Digit Modalities Test, SDMT	-	23-89 52 ± 14	36-71 52 ± 9	34-89 57 ± 17	23-62 46 ± 13
Paced Auditory Serial Addition Test, PASAT	-	19-59 42 ± 9	37-54 44 ± 7*	19-59 43 ± 12	30-45 36 ± 6*
Fatigue Severity Scale, FSS	-	1.1-7 5.0 ± 1.5	2.9-7 5.0 ± 1.3	1.1-6.9 4.7 ± 1.7	3.5-7 5.4 ± 1.3
Modified Fatigue Impact Scale, MFIS	-	2-73 42 ± 19	2-73 38 ± 23	21-73 39 ± 19	34-64 50 ± 11
Beck Depression Inventory-II, BDI-II	-	0-31 13 ± 9	0-31 12 ± 10	0-29 14 ± 10	5-21 13 ± 7
Timed 25-Foot Walk, T25-FW (seconds)	-	3.6-20.6 8.5 ± 4.8	3.6-12.0 6.5 ± 2.4	5.3-19.5 10.8 ± 6.0	5.8-20.6 9.7 ± 6.3
9-Hole Peg Test, 9-HPT (seconds)	-	18.7-65.2 29.4 ± 10.8	18.7-39.8 24.9 ±5.6	19.2-54.1 28.9 ± 11.0	20.7-65.2 36.2 ± 14.0
Total Lesion Volume (cm^3)	-	0.19-37.2 7.1 ± 8.8	0.23-8.82 3.0 ± 3.1	0.19-27.9 9.3 ± 9.1	0.83-37.2 10.2 ± 12
Total Lesion Number (range, mean ± SD)	-	3-32 15.9 ± 7.4	4-24 13.1 ± 7.3	3-32 18.3 ± 8.4	7-24 16.9 ± 5

† EDSS was not obtained in two PPMS and BVMT-R, PASAT, T25-FW, and 9-HPT were not acquired all in a SPMS and a PPMS participant for PASAT, T25-FW, and FSS. In total, two SPMS and three PPMS participants were not able to complete the T25-FW.

‡ Only the Total Recall score of the BVMT-R was reported.

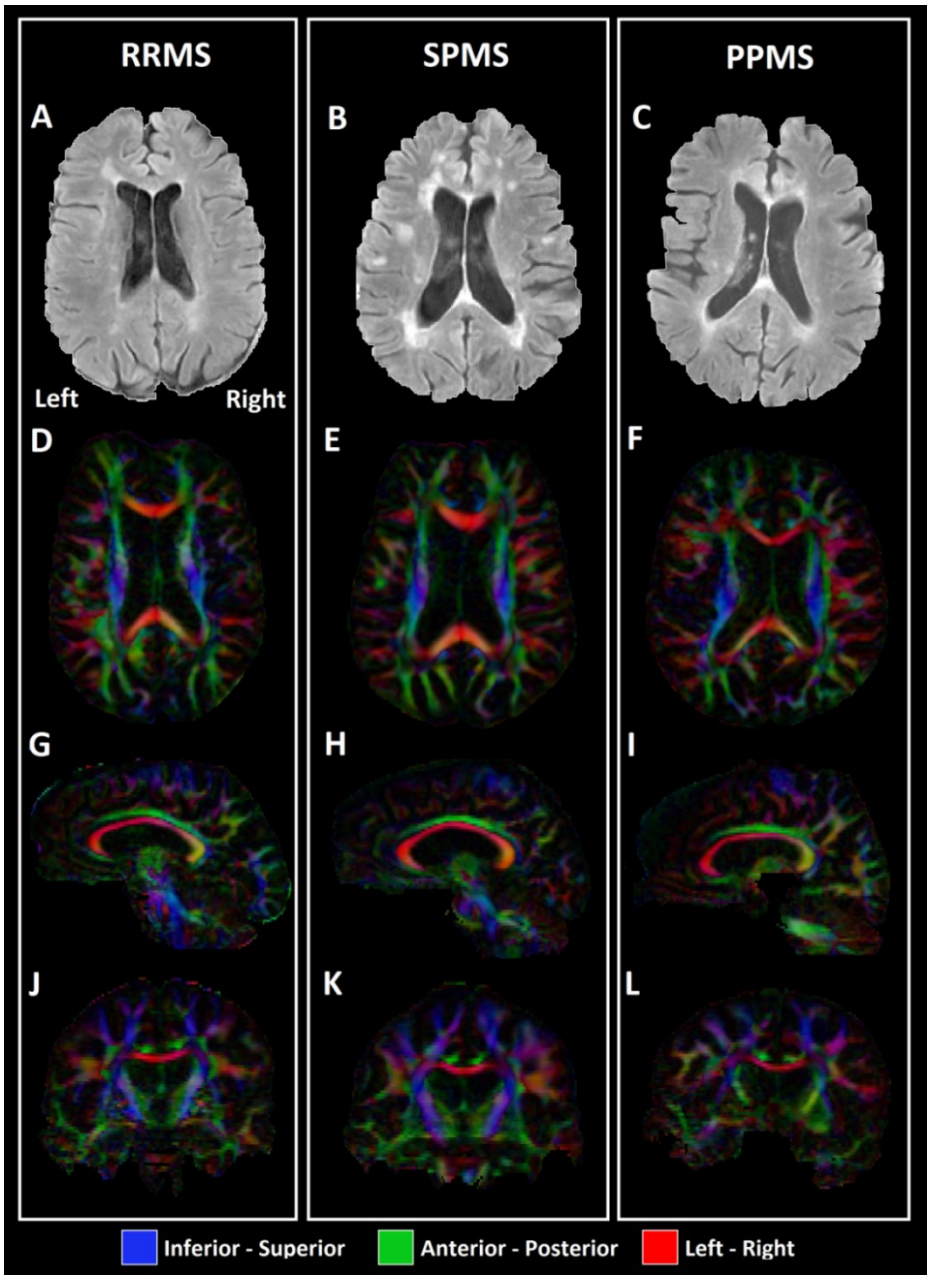

Figure 2.1: Axial FLAIR images showing periventricular lesions, and axial, sagittal and coronal views of the 1.7 mm isotropic first eigenvector fractional anisotropy (FEFA) maps in a RRMS (A, D, G, J, 51 years old, male, lesion number=24, total lesion volume=8.8 cm^3, time since diagnosis=14 years, EDSS=6.0), a SPMS (B, E, H, K, 52 years old, female, lesion number=17, total lesion volume=19.1 cm^3, time since diagnosis=24 years, EDSS=6.5), and a PPMS patient (C, F, I, L, 54 years old, male, lesion number=21, total lesion volume=15.5 cm^3, time since diagnosis=3 years, EDSS=6.5). Red – left/right, green – anterior/posterior, blue – inferior/superior.

2.3.2. Qualitative Assessment of the Tracts

When using the spatial resolution of 1.7 mm isotropic at high magnetic field of 4.7 T (Figure 2.1D-L), the full extent of the fornix, with high FA, was achievable by DTI tractography in 10/11 healthy controls over ages of 21 to 62 years. The only exception was a 75-year-old female control whose fornix tractography was "transected" at the bilateral crus, but she is 9 years older than the oldest MS volunteer. In the case of the MS cohort only 36% of the participants (3/11 in RRMS, 27%; 3/9 in SPMS, 33%; and 4/8 in PPMS, 50%) had the full extent of the fornix and in the remaining cases there were different degrees of tractography "transections" in all three MS subgroups (RRMS - 1 left side, 2 right side, 5 bilateral; SPMS - 2 right side, 4 bilateral; PPMS - 1 right side, 3 bilateral) with lower FA and fewer streamline projections (Figure 2.2 B-D) relative to controls (Figure 2.2A).

This current finding of incomplete fornix tracts is in spite of an ~40% voxel volume reduction compared to previous 8 mm^3 voxel size typical in MS DTI studies at lower fields. These "transections", even in one control, are caused by not reaching the FA threshold for tractography (0.2) due to partial volume with CSF leading to lower FA in the curvy and thin crus relative to the body (Figure 2.2B-D), when it passes through the lateral ventricles. These errors give partially reconstructed tracts and 'artificial disconnections' that could be worse for MS if the fornix is thinner and smaller, increasing partial volume with adjacent CSF and stopping tracking.

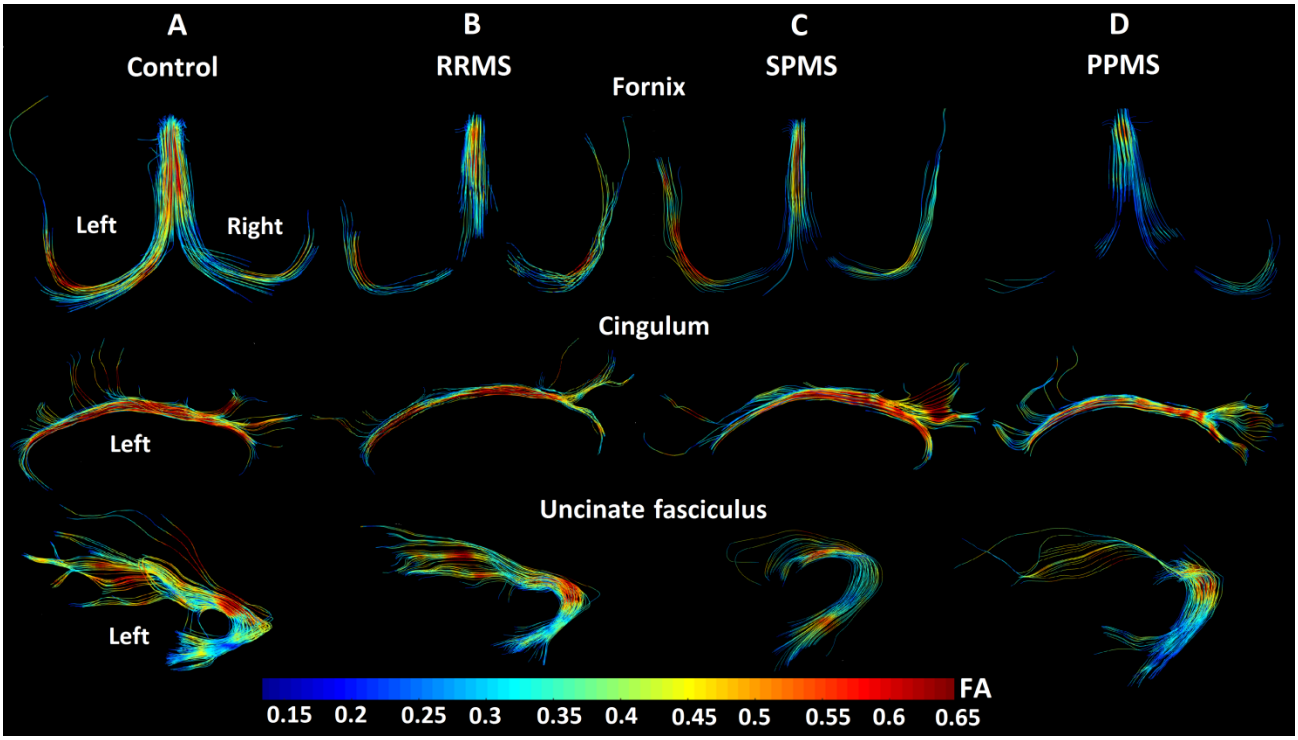

Figure 2.2: DTI tractography of the fornix (view from top), left cingulum and left uncinate fasciculus (views from left side) with an FA color encoding scale for one example per group: (A) control, 50 years old, female; (B) RRMS, 48 years old, female, EDSS=2.5; (C) SPMS, 59 years old, male, EDSS=6.0; (D) PPMS, 54 years old, male, EDSS=5.0. The fornix shows streamline disruptions and low FA in the three MS subtypes relative to controls. The cingulum tractography appears unaffected while the uncinate fasciculus is quite variable in the extent of streamline projections to the anterior portion.

In these same participants, the superior portion of the cingulum tracked well in all cases with no apparent qualitative differences in FA (Figure 2.2A-D). Tracking of the uncinate fasciculus was more variable (Figure 2.2A-D) and some MS participants showed shorter fibers than controls with fewer projections from the temporal lobe to the frontal lobe (4/28 MS patients – 1 RRMS, left side; 2 SPMS, left side; 1 PPMS, right side).

Two more examples per group are shown to highlight non-disrupted (Figure 2.3A, B, C, E, G) and varying degrees of disrupted fornix (Figure 2.3D, F, H) on DTI tractography for the three MS subgroups. Transected fornices with apparently lower FA and volume appeared to be related with greater total lesion volumes and enlarged ventricles regardless of subgroup classification (Figure 2.3D, F, H; Figure 2.4B, C, D). Overall, for the entire MS cohort (Figure 2.4B, C, D), 4/13 participants with less than 3 cm^3 total lesion volume (TLV) and 14/15 participants with more than 3 cm^3 total lesion volume showed transected fornices. There is a progressive deterioration of the tracts in the MS cohort for all the phenotypes, which is coupled with FA decrease and it could be associated with greater total lesion volume in the whole brain. In the case of the controls, tracts are not deteriorated at the same degree but slightly lower volumes and FA could be qualitatively appreciated as the controls get older showing bilateral discontinuities in the oldest control due to aging (Figure 2.4A).

If the FA threshold for tracking is modified from 0.2 to 0.13, qualitative tract differences could be appreciated in the MS cohort primarily, due to a greater number of streamlines arising from the lower FA threshold. In some participants, this lower FA threshold enables streamlines to connect across the previously "transected" crura and there are fewer disconnections compared to the tracts previously presented here (FA threshold 0.13 vs FA threshold 0.2): Controls - no transections vs 1 bilateral transection; RRMS – 4/11 transections (2 left side, 2 right side) vs 8/11 transections (1 left side, 2 right side, 5 bilateral); SPMS – 5/9 transections (2 left side, 1 right side, 2 bilateral) vs 6/9 transections (2 right side, 4 bilateral); PPMS – 2/8 transections (1 left side, 1 bilateral) vs 4/8 transections (1 right side, 3 bilateral) (Figure A.1 in Appendix A).

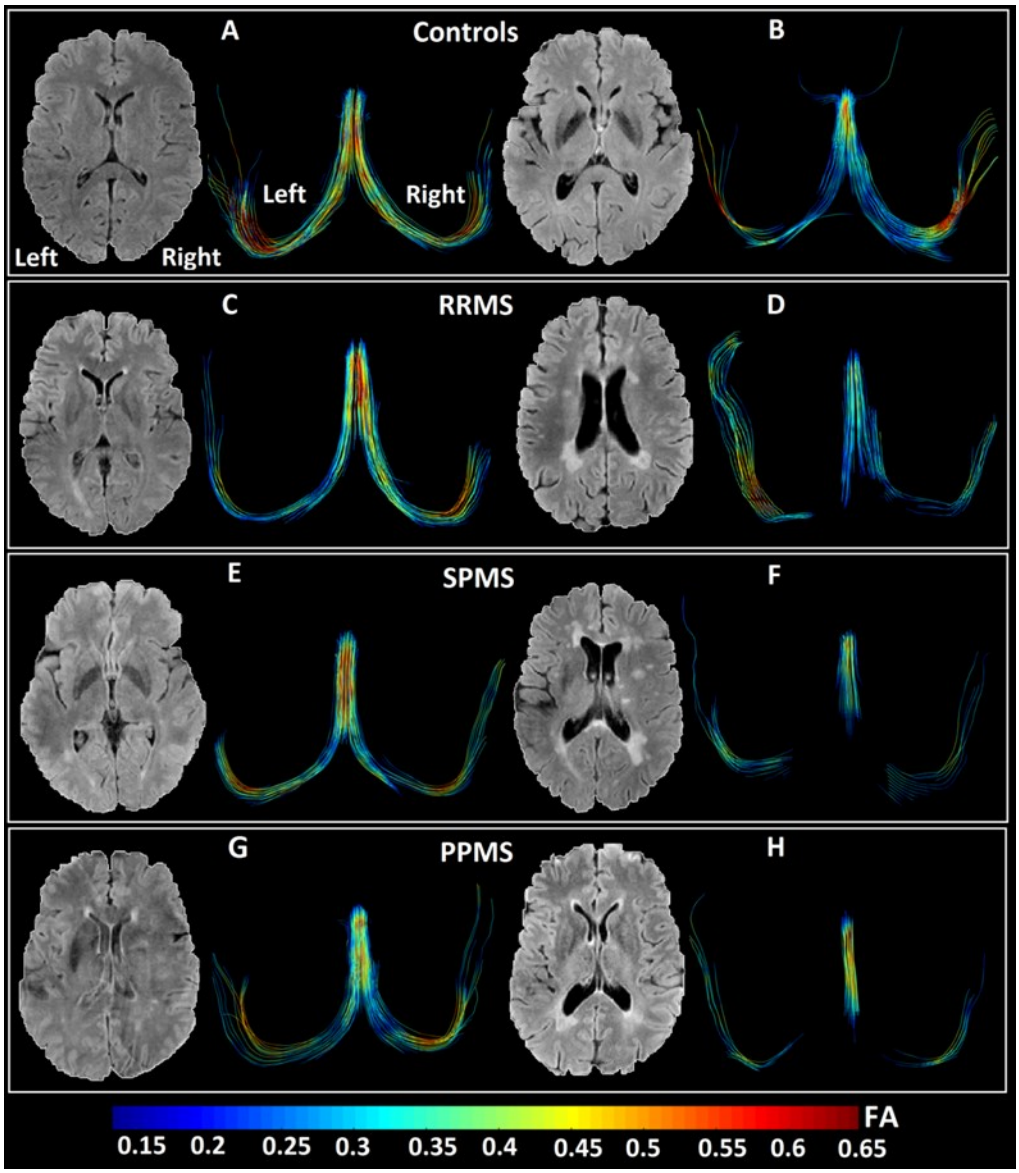

Figure 2.3: Two more examples of each subgroup including an axial FLAIR slice and the fornix for controls (A - 21 years old, female; B - 62 years old, female), RRMS (C - 41 years old, female, EDSS=2.5, time since diagnosis 1 year, TLV= 0.23 cm^3; D - 38 years old, female, EDSS=1.5, time since diagnosis 10 years, TLV= 4.3 cm^3), SPMS (E - 45 years old, female, EDSS=4.5, time since diagnosis 18 years, TLV= 0.19 cm^3; F - 66 years old, female, EDSS=6.5, time since diagnosis 34 years, TLV= 27.9 cm^3), and PPMS (G - 65 years old, female, EDSS=6.0, time since diagnosis 17 years, TLV= 0.83 cm^3; H - 59 years old, male, EDSS=4.0, time since diagnosis 4 years, TLV= 7.5 cm^3). MS participants with greater total lesion volume (F, H) have more disrupted fornix with lower volume and lower FA. The MS participants with a less disrupted fornix (C, E, G) have very low TLV (less than 1 cm^3) and their age range and EDSS scores are quite variable.

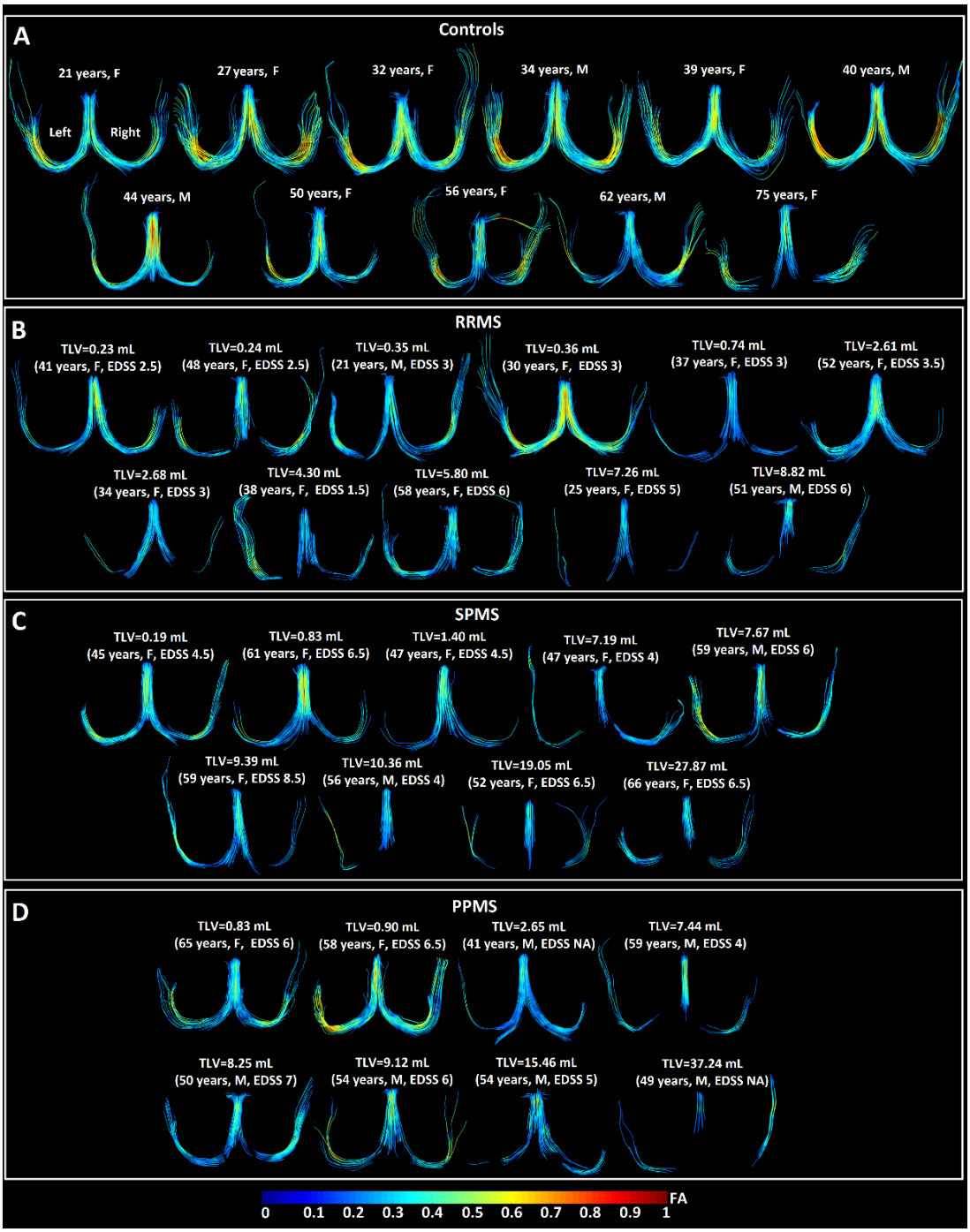

Figure 2.4: Tractography of the fornix for the entire cohort**:** (A) controls – ordered by age, (B) RRMS, (C) SPMS, (D) PPMS participants – ordered by total lesion volume (TLV) for each phenotype. The progressive nature of the fornix degradation and FA decrease is associated with global brain lesion progression in each of the RRMS, SPMS, and PPMS subgroups as shown by tractography here.

2.3.3. Tract Diffusion Metrics and Volumes

The whole 28 MS cohort versus the 11 controls showed significant lower FA in the fornix (-16%, $p<0.001$), the cingulum (-5%, $p<0.05$) and the uncinate fasciculus (-7%, $p=0.001$). The fornix and the uncinate fasciculus also showed smaller volume (-53%, $p<0.001$; -25%, $p=0.023$), greater MD (18%, $p<0.001$; 5%, $p=0.006$) and RD (24%, $p<0.001$; 8%, $p=0.004$) respectively, and higher AD (11%, $p=0.002$) in the case of the fornix. Regarding the MS subgroups individually, the fornix showed significant group differences that were similar across all of them, including smaller fornix volume (RRMS -49%, SPMS -60%, PPMS -53%), lower FA (RRMS -18%, SPMS -15%, PPMS -15%), greater MD (RRMS 17%, SPMS 18%, PPMS 19%) and higher RD (RRMS 24%, SPMS 25%, PPMS 26%) relative to controls (Figure 2.5). The cingulum did not show any differences in any of the three MS subgroups versus controls. The uncinate fasciculus showed significantly smaller FA (10%) in the SPMS group only. The along the tract analysis of the left and right fornix body, which is the superior region that is consistently tracked in all participants, showed significantly lower FA in the posterior portion of the left fornix and in the middle-posterior portion of the right fornix for all three MS subgroups compared to controls (Figure 2.6).

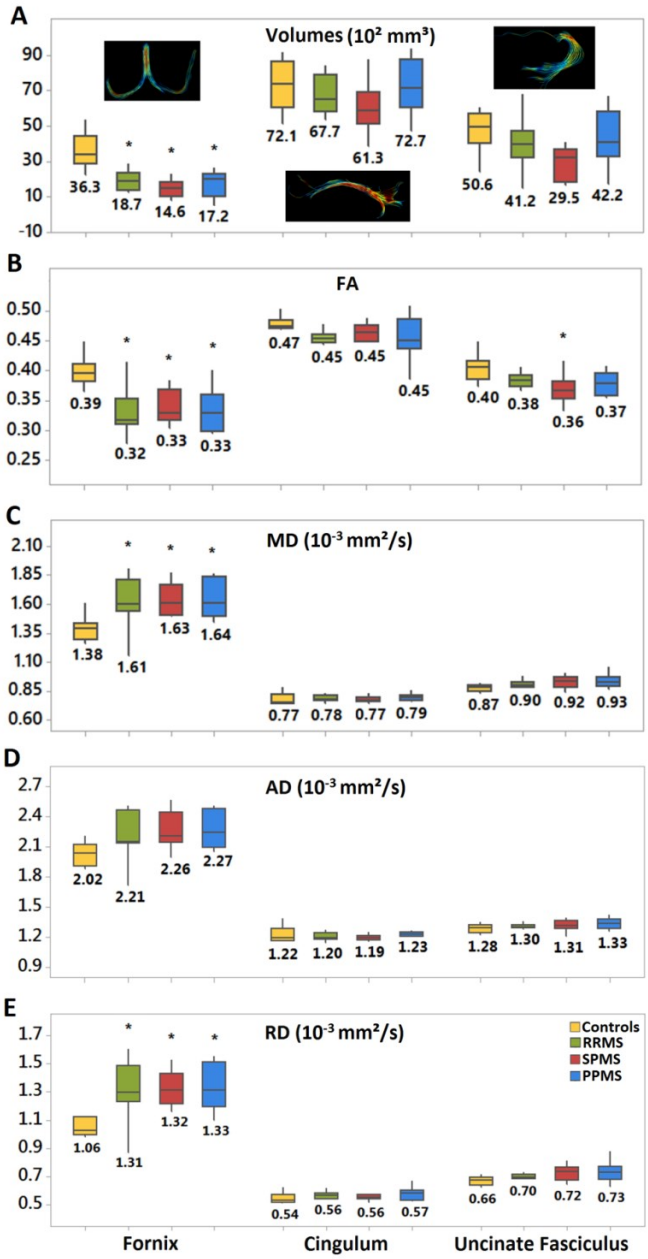

Figure 2.5: (A) Bilateral tract volumes, (B) FA, (C) MD, (D) AD and (E) RD mean values are shown for controls, RRMS, SPMS and PPMS subgroups for the fornix, cingulum and uncinate fasciculus tracts. The central boxes show the median and interquartile range while the whiskers above and below the boxes show the minimum and maximum values. The fornix shows significant differences between the controls and each MS subgroup for the volumes and all the diffusion metrics except AD. The cingulum did not show any differences. The uncinate fasciculus shows FA differences between the SPMS subgroup and the controls. *$p \leq 0.011$ (FDR corrected for multiple comparisons).

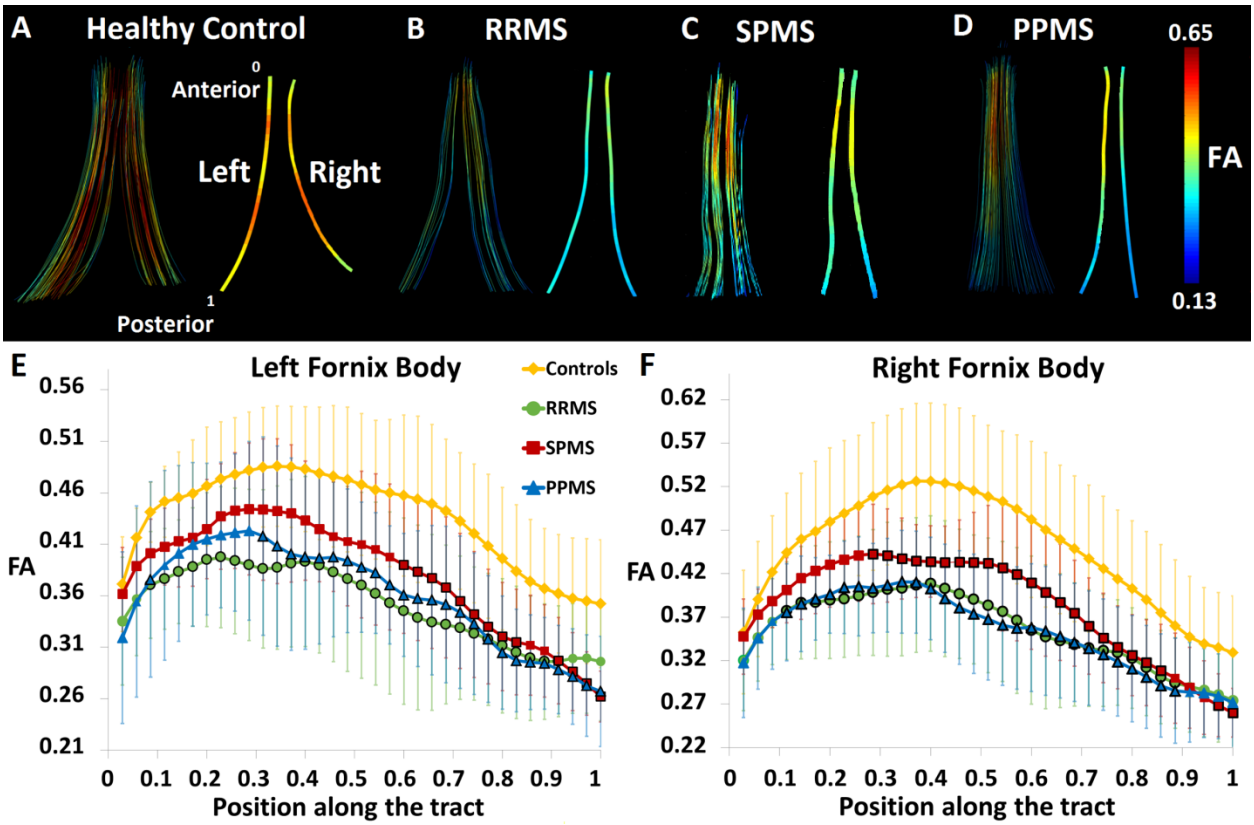

Figure 2.6: Between-groups along the tract analysis in the left and right fornix body, a region which is identified in all 11 controls and 28 MS participants. The corresponding resampled-averaged fornix body fibers are shown along 35 points (0 anterior to 1 posterior) in a healthy control (A, 40 years old, male), a RRMS (B, 41 years old, female), a SPMS (C, 47 years old, female) and a PPMS participant (D, 41 years old, male). (E, F) The along the tract FA profiles averaged over all participants in each group (mean +/- SD shown) are significantly lower than the controls from 0.6-0.83 tract location area in the left fornix (E) and from 0.29-0.86 in the right fornix (F) for all three MS subgroups. All the statistically significant tract points are encircled with a dark black line for each MS subgroup compared to the controls ($p \leq 0.032$ for the left fornix body, $p \leq 0.029$ for the right fornix body, FDR corrected for multiple comparisons). Note that along the tract analysis was not possible in the bilateral crus of the fornix given so many 'disconnections' in the tractography.

Even if a lower FA threshold of 0.13 is applied in the entire healthy and MS cohort, which yields fewer "disconnections", larger volumes, higher MD, and lower FA due to the inclusion of more voxels with low FA contributing to the tractography metrics, the main observations regarding

group comparisons are similar to the previously reported comparisons for the FA=0.2 threshold. The fornix volume/FA are still consistently abnormal in all three MS phenotypes compared with the controls; whereas MD/RD values were only significantly higher after the FDR correction for the SPMS subgroup ($p \leq 0.008$) (Figure 2.7).

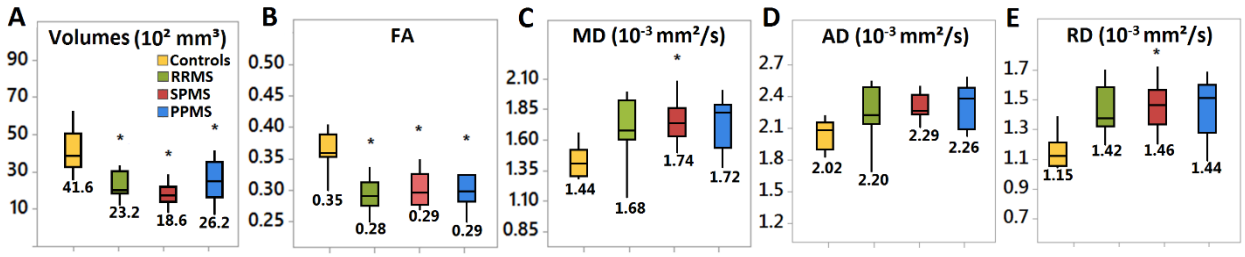

Figure 2.7: (A) Fornix tract derived volumes, (B) FA, (C) MD, (D) AD and (E) RD mean values calculated with an FA threshold of 0.13 are shown for controls, RRMS, SPMS and PPMS subgroups. The fornix volume/FA metrics (A,B) were significantly smaller in each MS subgroup compared to the controls. MD/RD values (C, E) were higher only in the SPMS subgroup versus the controls and AD values did not show any group differences (*$p \leq 0.008$, FDR corrected for multiple comparisons).

2.3.4. Fractional Anisotropy and Tract Volumes versus Clinical/Cognitive Scores

FA correlated positively with tract volume for the left and right fornix as well as the left uncinate fasciculus (Table 2.2). Notably, total lesion volume throughout the brain correlated negatively with several measures of FA and tract volume primarily for the fornix and uncinate fasciculus; namely, left FA and left/right volume of the fornix, left volume of the cingulum, and left/right FA and left volume of the uncinate fasciculus (Fig. 2.8, Table 2.2). There are 4 participants (2 SPMS, 2 PPMS) with total lesion volumes each greater than 15 cm^3 that appear to be driving the negative correlations. Lower FA values in the right cingulum correlated with more severe depression in the entire MS cohort (Fig. 2.9, Table 2.2). There are 7 participants (1 RRMS, 3 SPMS, 3 PPMS) that

appear to be driving the correlations with depression. They all similarly showed high fatigue scores and 5 of them (2 SPMS, 3 PPMS) also showed lesion volumes greater than 7 cm^3.

Table 2.2: Partial Pearson correlation coefficients between right and left FA and volumes in the fornix (Fx), cingulum (Cg) and uncinate fasciculus (UF), total lesion volume (TLV), total lesion number (TLN), time since diagnosis and clinical/cognitive scores over the entire MS cohort.

Tract	Metric	Right/Left	Tract Volume		TLV	TLN	Time since diagnosis	Clinical/Cognitive Tests				
			R	L				EDSS	BVMT-R	MFIS	FSS	BDI-II
Fx	**FA**	**R**	**0.50 (0.0064)**	_	-0.44 (0.01)	**-0.57 (0.0015)**	-0.22 (0.25)	-0.06 (0.73)	0.18 (0.35)	-0.01 (0.92)	-0.06 (0.74)	-0.24 (0.2)
		L	_	**0.61 (0.0004)**	**-0.49 (0.0068)**	-0.48 (0.0094)	-0.46 (0.01)	-0.08 (0.66)	0.08 (0.67)	-0.01 (0.94)	-0.09 (0.63)	-0.27 (0.15)
	Vol	**R**	_	_	**-0.60 (0.0006)**	-0.48 (0.0095)	-0.17 (0.37)	0.02 (0.92)	0.36 (0.06)	0.08 (0.68)	0.04 (0.80)	-0.21 (0.27)
		L	_	_	**-0.59 (0.0007)**	**-0.51 (0.0055)**	-0.41 (0.02)	0.01 (0.92)	0.34 (0.07)	-0.10 (0.58)	-0.19 (0.32)	-0.45 (0.01)
Cg	**FA**	**R**	0.26 (0.17)	_	-0.36 (0.06)	-0.48 (0.0095)	-0.18 (0.34)	0.30 (0.12)	0.39 (0.04)	-0.45 (0.01)	-0.35 (0.06)	**-0.49 (0.0069)**
		L	_	0.46 (0.01)	-0.43 (0.01)	-0.49 (0.008)	-0.25 (0.19)	0.46 (0.01)	0.32 (0.09)	-0.26 (0.17)	-0.27 (0.16)	-0.30 (0.11)
	Vol	**R**	_	_	-0.44 (0.01)	-0.42 (0.026)	-0.43 (0.01)	-0.04 (0.83)	0.23 (0.23)	0.03 (0.87)	-0.09 (0.62)	0.17 (0.37)
		L	_	_	**-0.55 (0.0019)**	-0.18 (0.35)	-0.18 (0.34)	-0.02 (0.9)	0.12 (0.51)	-0.04 (0.82)	-0.06 (0.74)	0.09 (0.63)
UF	**FA**	**R**	0.29 (0.12)	_	**-0.67 (0.0001)**	-0.45 (0.016)	-0.44 (0.01)	0.02 (0.92)	0.28 (0.14)	-0.04 (0.83)	-0.15 (0.44)	-0.37 (0.04)
		L	_	**0.52 (0.0039)**	**-0.53 (0.0038)**	-0.21 (0.29)	-0.32 (0.09)	-0.06 (0.73)	0.18 (0.36)	0.11 (0.55)	0.18 (0.34)	-0.15 (0.44)
	Vol	**R**	_	_	-0.41 (0.02)	-0.01 (0.94)	-0.28 (0.14)	-0.45 (0.02)	-0.10 (0.62)	0.24 (0.21)	-0.04 (0.82)	-0.04 (0.82)
		L	_	_	**-0.58 (0.0012)**	-0.41 (0.032)	-0.33 (0.07)	-0.28 (0.16)	-0.13 (0.51)	0.44 (0.01)	0.28 (0.14)	0.00 (0.99)
_	**TLV**	_	_	_	_	0.39 (0.04)	0.41 (0.02)	0.26 (0.19)	-0.33 (0.08)	-0.10 (0.59)	0.08 (0.67)	0.14 (0.46)
_	**TLN**	_	_	_	_	_	0.38 (0.047)	-0.01 (0.97)	-0.24 (0.22)	0.14 (0.48)	0.16 (0.42)	0.26 (0.17)

Correlation coefficients are controlled for age and sex in the 28 MS participants.
Bold values are False Discovery Rate (FDR) corrected ($p \leq 0.0073$).

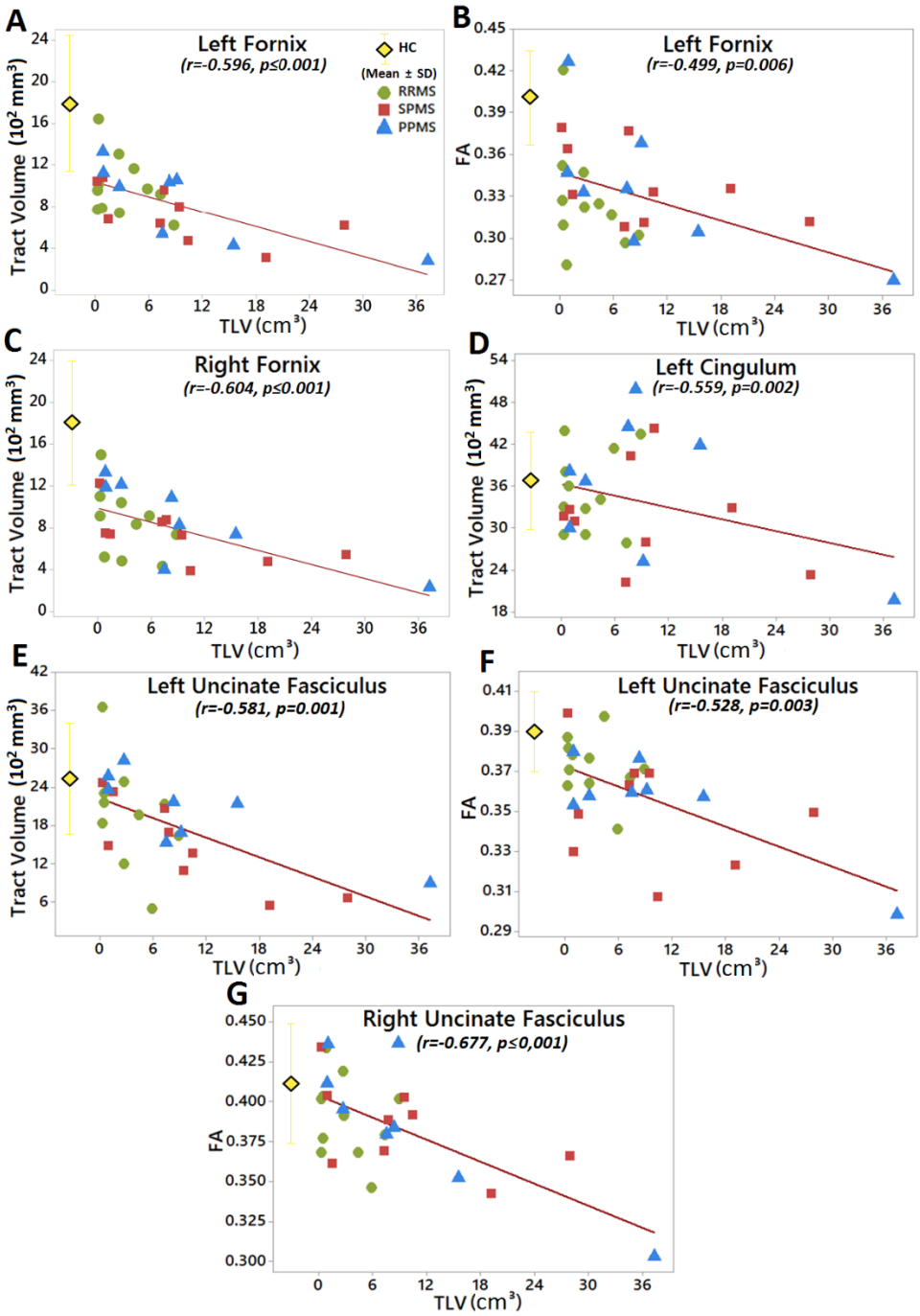

Figure 2.8: Correlations with total lesion volumes (TLV). Greater TLV were correlated to smaller tract volumes for left/right fornix (A, C), left cingulum (D), and left uncinate fasciculus (E), as well as with lower FA values of the left fornix (B), and left/right uncinate fasciculus (F,G) ($p \leq 0.0086$) for all three subgroups of MS (color legend) combined. The mean and the standard deviation of the healthy controls group are shown as reference.

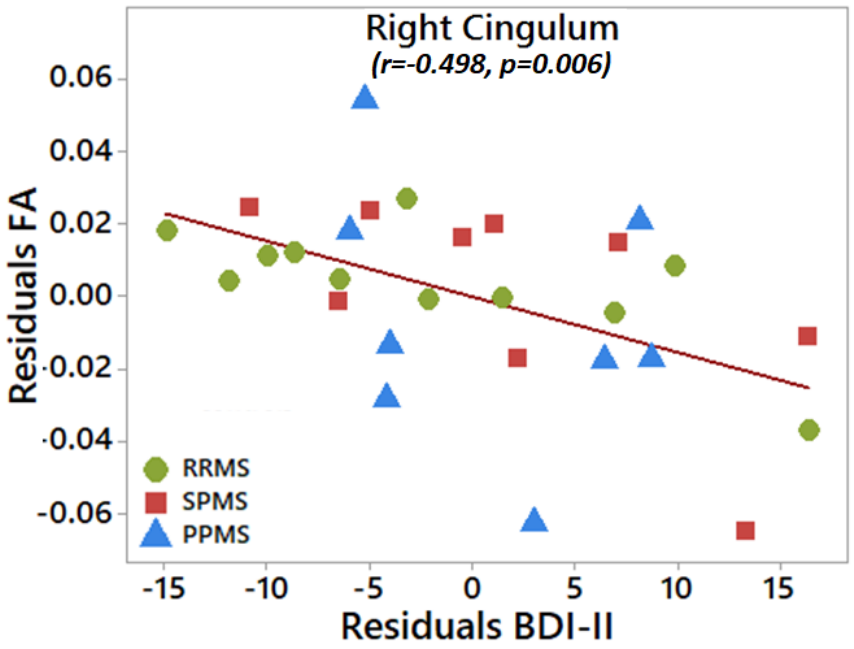

Figure 2.9: Lower FA of the right cingulum correlated with more depression (i.e., higher BDI-II) scores, both corrected for age and sex, over all 28 MS participants.

2.4. Discussion

In agreement with previous MS DTI studies primarily focused on RRMS that have implicated fornix injury [125], [209], [255], [256], [260], [281]–[283], tractography of the fornix acquired with 1.7 mm isotropic resolution showed markedly lower volume (by ~54%) and FA (by ~16%), as well as higher MD (by ~ 18%) and RD (by ~25%) to a similar extent in RRMS, SPMS and PPMS relative to controls. The fornix DTI abnormalities were present in all three MS cohorts despite the disparate ranges of 21-66 years of age, 1-34 years since diagnosis, or 1.5-8.5 EDSS, implying its widespread occurrence early on in the disease course. The three following DTI studies on SPMS and/or PPMS have implicated the fornix, but this tract was not their focus nor was its 3D trajectory identified and measured using tractography [272], [273], [286]. Whole-brain TBSS

analysis yielded lower FA and higher RD of the fornix in SPMS with and without cognitive impairment, with the former showing greater changes [272]. Fornix FA was reduced in PPMS, but data was not specific for this region [273]. One of the few studies to report DTI changes in all three MS diagnostic subpopulations published voxel-based statistical significance figures that suggest fornix anomalies in SPMS and PPMS as well, and the fornix appeared to have reduced FA in PPMS versus healthy controls and in SPMS versus benign MS [286].

It is unclear why all three MS subtypes would yield similar changes to the fornix. Histopathologic studies have reported comparable axon damage across the different subtypes, such as in the corticospinal tract in SPMS and PPMS [289] or in demyelinating and active lesions [290]. The clinical presentation does not always allow an accurate differentiation between relapsing and progressive phases in the disease spectrum [291]. Over the entire MS group, however, the left/right fornix volume and left fornix FA were negatively correlated with total lesion volume suggesting a link between the degree of visible whole brain lesion pathology and fornix integrity. Periventricular lesions are common in MS and are suggestive that inflammatory factors in the CSF may be involved [292]. The fornix would be greatly exposed to such factors since it is bathed in CSF as it passes through the lateral ventricles which could explain the abnormal fornix tractography findings even in those with brief time since MS diagnosis. WM fornix integrity has been linked to Alzheimer's Disease-related CSF factors in normal adults [293]. Active and chronic inactive lesions of the fornix have been observed on histology in 9/16 and 7/16 mostly RRMS participants, respectively [294]. One MRI study only reported 2.6% of 156 RRMS participants with fornix lesions on FLAIR [295], but it was limited by low resolution of the co-registered FA

color maps used to confirm lesion location and potential linear registration algorithm errors. Demyelination of the hippocampus has been reported in brain tissue histological sections of 12/22 progressive MS participants (9 SPMS, 3 PPMS) [296] and this could be reflected in Wallerian degeneration to axons in its major primary efferent fiber bundle, the fornix, although the relationship is still unclear and needs further investigation. The fornix diffusion MRI metrics did not correlate with any of the clinical or cognitive measures, unlike earlier studies [125], [255]–[257], [260], [282], [283].

TBSS mentioned above in many MS DTI studies is a commonly used voxel-based analysis method that involves skeletonization of the white matter and projection of maximal FA values nearby to the skeleton, but it has been shown to have difficulties in the assessment of a small, curvy tract such as the fornix [143]. Tractography has its advantages since it is performed in native space which allows anatomical variations in shape and location and does not require spatial normalization of the images to a common template. However, a limitation of tractography is that it can lead to discontinuities of tract streamlines when the voxel FA or eigenvector angle thresholds are not met, thereby not identifying voxels that are the most severely affected. For the fornix, which is an isolated bundle without other crossing fibers, this tracking stoppage usually occurs when a voxel falls below the set threshold due to partial volume effects with isotropic CSF in the bilateral crus and leads to these apparent discontinuities even in healthy controls [104]. None of the previous fornix DTI papers of MS used any CSF suppression methods – acquisition or post-processing. Furthermore, the implementation of FLAIR-DTI, was not possible at 4.7 T and the single shell DTI data used here is not suitable for post-processing “free water elimination (FWE)”

CSF correction algorithms that require two shells [297]. These FWE algorithms are not still the optimal approach, compared to FLAIR-DTI, to further reduce the standard deviation of diffusion metrics for tracts with high partial volume effects with CSF, such as the fornix [298].

Certainly, fornix tractography is susceptible to stopping its tracking for the above-mentioned reasons but this is not necessarily detrimental. Even if one assumes that the fewer tracts are just due to CSF contamination, then this would imply smaller actual fornix that would increase CSF partial volume and stop tracking. If the fornix volumes were the same, then the error ought to remain consistent in MS as in controls; but it is not the same. Thus, there will be a link between the actual volume and that which is underestimated with tractography. The lower tracking FA threshold of 0.13 yields larger fornix tracts, smaller FA, and higher MD/AD/RD for all four subgroups (controls, RRMS, SPMS, PPMS). The group differences of the fornix hold for all three MS subgroups relative to controls for FA and volume with this lower FA threshold, but only the SPMS group remains significantly different for MD and RD relative to controls. Since the same DTI acquisition and post-processing algorithms with the exact same tracking ROIs and thresholds were applied in all MS participants and controls, these discontinuities indicate markedly reduced FA in these areas of the fornix within the MS patients and any tractography differences are still indicative of group differences of the underlying fornix. This could be due either to actual microstructural differences of the residual fornix in the crus, small demyelinating lesions going undetected due low FLAIR resolution, Wallerian degeneration from potentially damaged hippocampal areas, or simply greater partial volume effect with adjacent CSF if the fornix has undergone greater atrophy (“normal” microstructure but smaller volume). Table 2.2 shows a

positive correlation of left and right fornix FA with tractography-derived fornix volume. Studies are currently underway here to evaluate the fornix in MS using FLAIR-DTI to suppress the CSF, minimize partial volume effects, and yield more complete tracking of the fornix even in the case of atrophy [104]. However, the "along the tracts" analysis of the consistently tracked superior body of the fornix in all controls and MS participants suggests that there are microstructural fornix differences, since the body is not as susceptible as the crus to partial volume errors with CSF.

The uncinate fasciculus had lower FA only for SPMS when compared to controls, consistent with a previous study focused on that phenotype [272]. Others have reported lower FA of the uncinate fasciculus in RRMS [259], [274], [283] or mixed MS cohorts [125], [209], [258], [286]. The uncinate fasciculus tractography was quite variable in our MS participants; for example, in 1 RRMS, 2 SPMS and 1 PPMS participant, it did not show frontal lobe projections, unlike all the healthy controls. These variations may be related either to lesions in frontal cortex areas that this tract connects [273] or to other parts of its pathway that could affect the tracking. The uncinate fasciculus volume and FA also showed significant correlations with total lesion volume.

The cingulum did not show any group diffusion differences relative to controls in agreement with prior work [281], [282] although several other MS studies have reported cingulum differences, mainly FA [209], [255], [258], [260], [274], [283], [285], [286]. In our study, lower FA in the right cingulum correlated with higher depression scores, possibly due to interactions between the anterior cingulate and the amygdala [299]. This finding is consistent with lower cingulum FA in young women at risk of depression [300], and lower FA in the right parahippocampal cingulum in those with catechol-O-methyltransferase gene polymorphisms in major depressive disorder [301].

Lower FA in cingulum has correlated with deficits of episodic and working memory [255], [258], [260], [283] and subjective fatigue [259] in MS, but these studies did not measure depression. A TBSS study showed lower FA of the left cingulum in depressed MS patients [285] and DTI metrics in NAWM have been related to depression in MS [302].

The main technical limitation of our study is the lack of a CSF suppressed DTI sequence; therefore, the fornix tractography may have been altered by partial volume effects from CSF in the ventricles making the DTI metrics and tractography prone to errors and harder to interpret. The authors are currently utilizing high resolution FLAIR-DTI at lower magnetic field strength (3 T) in new MS cohorts in order to diminish the CSF confounding effects in the DTI metrics. While FLAIR-DTI works fine at these lower magnetic field strengths, there are specific absorption rate (SAR) constraints at higher fields such as 4.7 T used here which have resulted in the development of alternative strategies to minimize the influence of CSF in DTI [303], but this was not used in the present study. Furthermore, the small sample size of this study, particularly when looking at each RRMS, SPMS, and PPMS subgroup separately, is another limitation to consider when making inferences about differences between these clinical groups and it should be addressed in future studies. The heterogeneity of the MS subgroups, the high participant variability of the cognitive, depression and fatigue test scores, and the burden of cognitive impairment altogether with the small sample size of the MS cohort may have contributed to the inability to find more cognitive and clinical associations with the DTI findings.

2.5. Conclusions

In summary, high resolution diffusion MRI tractography identified abnormalities in the fornix that were similar across all three primary MS phenotypes of RRMS, SPMS, and PPMS regardless of EDSS, time since diagnosis, or cognitive scores. The fornix FA and tract volumes were more affected with greater total whole brain lesion volumes suggesting a link to other brain pathology that needs further investigation.

3. Diffusion Imaging of Fornix and Interconnected Limbic Deep Grey Matter is Linked to Cognitive Impairment in Multiple Sclerosis[2]

Abstract

Diffusion tensor imaging (DTI) and volumetric magnetic resonance imaging (MRI) have shown white matter (WM) and deep grey matter (GM) abnormalities in the limbic system of multiple sclerosis (MS) participants. Structures like the fornix have been associated with cognitive impairment (CI) in MS, but the diffusion metrics are often biased by partial volume effects from cerebrospinal fluid (CSF) due to its small bundle size and intraventricular location. These errors in DTI parameter estimation worsen with atrophy in MS. The goal here was to evaluate DTI parameters and volumes of the fornix, as well as associated deep GM structures like the thalamus and hippocampus, with high resolution fluid-attenuated inversion recovery (FLAIR)-DTI at 3 T in 43 MS patients, with and without CI, versus 43 controls. The fornix, thalamus and hippocampus displayed atrophy and/or abnormal diffusion metrics, with the fornix showing the most extensive changes within the structures studied here, mainly in CI MS. The affected fornix volumes and diffusion metrics were associated with thalamic atrophy and atypical diffusion metrics in interconnected limbic GM, larger total lesion volume and global brain atrophy. Lower fractional anisotropy (FA) and higher mean and radial diffusivity in the fornix, lower hippocampus FA and lower thalamus volume were strongly correlated with CI in MS. Hippocampus FA and thalamus

[2] Published as: Valdés Cabrera, D., Smyth, P., Blevins, G., Emery, D., & Beaulieu, C. Diffusion imaging of fornix and interconnected limbic deep grey matter is linked to cognitive impairment in multiple sclerosis. European Journal of Neuroscience 2022, 55(1), 277– 294. https://doi.org/10.1111/ejn.15539.

atrophy were negatively correlated with fatigue and longer time since MS symptoms onset, respectively. FLAIR-DTI and volumetric analyses provided methodologically superior evidence for microstructural abnormalities and extensive atrophy of the fornix and interconnected deep GM in MS that were associated with cognitive deficits.

3.1. Introduction

Cognitive impairment (CI) is prevalent in multiple sclerosis (MS), predominantly presenting as deficits in episodic memory, executive functions, attention and information processing speed. This occurs in 40% to 65% of MS patients across all phenotypic classifications [208] and frequently overlaps with other clinical variables such as fatigue [304], [305] and depression [305], [306]. As MS progresses, multifocal white matter (WM) damage ranging from demyelination to axonal loss may result in disconnection between cortical and subcortical grey matter (GM) areas, involving key structures for cognitive and memory processes even early in the disease course [255], [278]. The limbic system includes crucial WM and GM regions that are involved in aspects of emotions and cognition [26], [261], such as the fornix, which is the major efferent WM pathway from the hippocampus with indirect connections to the thalamic nuclei [26], [30]. The fornix as a part of this extended hippocampal–diencephalic system (i.e., hippocampus, fornix, mamillary bodies and anterior thalamus) [23], [261] is crucial for effective encoding, and therefore, new episodic information recalling [26], [261] and its damage as well as any other components of this system can cause anterograde amnesia or related memory impairments [307].

Conventional magnetic resonance imaging (MRI) volumetric studies focusing on limbic structures have consistently reported thalamus and hippocampus atrophy in all MS phenotypes [233], [308]–[311] being associated with deficits in memory encoding and retrieval [211], [233], [308], [309], [311]. Diffusion tensor imaging (DTI) of the limbic WM has been used to further differentiate microstructural tissue changes in relapsing-remitting (RRMS) and progressive (primary [PPMS] and secondary [SPMS]) MS phenotypes, reporting mainly fornix [125], [209], [255], [260], [274], [312] and cingulum [258] diffusion changes including lower fractional anisotropy (FA) and/or higher mean (MD) and radial diffusivity (RD). These altered WM DTI metrics have shown associations with visuospatial memory [255], [257], [272] and processing speed deficits [209], [258]. Moreover, the fornix, as the main isolated WM output of the hippocampus, has been considered essential for multimodal cognitive functions [26], [30], [210], and previous MS DTI studies showed relationships between lower FA and poorer performance in visuospatial memory [256] and between higher RD and worse delayed recall in verbal learning and memory [125]. DTI metrics in the thalamus and the hippocampus have also been studied to explore additional relationships with MS cognitive deficits [267], [269]–[271] reporting either higher MD/RD and/or lower FA in the thalamus [269], [313] and the hippocampus [313], [314], higher thalamic FA [267], [271] or no diffusion changes in these two structures [270] between MS and healthy controls. A full list of all limbic WM and deep GM studies in MS (sorted chronologically to the date) is in Appendix C.

However, most previous limbic MS studies have used low spatial resolution DTI protocols (voxel volume > 8 mm^3) which could contribute to the aforementioned diffusion metric inconsistencies

across studies. Errors can occur from either misregistration between the structures typically identified on higher resolution, undistorted T1-weighted scans that are transferred to coregistered diffusion images, as well as from deleterious partial volume effects with adjacent structures, such as isotropic, rapidly diffusing cerebrospinal fluid (CSF). The study of small WM tracts like the fornix and deep GM near the ventricles by using fluid-attenuated inversion recovery (FLAIR) DTI techniques at higher resolution than previously applied in MS would improve tractography of the fornix [104] and diffusion parameter quantification by minimizing CSF partial volume effects [277]. To our knowledge, this technique has never been applied to the study of MS before. The purpose of this MS study was to (a) use high resolution ($1.2 \times 1.2 \times 2 = 2.9\ mm^3$) CSF-suppressed FLAIR-DTI to probe microstructural damage in fornix WM and interconnecting thalamus/hippocampus GM, (b) evaluate the relation of these fornix diffusion values with global/regional brain volumes and lesion load and (c) assess their correlations to the main cognitive functions affected in MS (information processing speed and visual working memory) as well as probe links to depression, fatigue, disability and time since MS symptom onset.

3.2. Methods

3.2.1. Participants

All 86 participants provided written informed consent including 43 diagnosed with MS (35 RRMS, 8 SPMS), as well as 43 HCs with no self-reported history of neurological/psychiatric disorders or brain injury and similar age and sex distribution as the MS cohort. MS participants were recruited from the University of Alberta Neurosciences Clinic, and controls were recruited by advertising

on campus and in local community venues. The MS participants were recruited consecutively if they fulfilled the inclusion/exclusion criteria, and there was no bias in how they were enlisted in the study (e.g., all phenotypes, EDSS scores, cognitive status and ages were included). This study was approved by the University of Alberta Health Research Ethics Board and all research protocols were conducted according to the World Medical Association Declaration of Helsinki.

Regarding the MS cohort, the only inclusion criteria for eligibility to participate in the study was a clinically definite RRMS, SPMS or PPMS diagnosis not accounting for age or disease duration; and the exclusion criteria was no history of clinically documented relapse or a high dose steroid treatment in a year prior to MRI scan. There were no patients excluded from the study due to these criteria. Two RRMS and six SPMS participants were not receiving MS medications or treatments, but the remaining cohort was on different disease-modifying therapies (dimethyl fumarate, fingolimod, teriflunomide, interferon beta-1a, glatiramer acetate, natalizumab, ocrelizumab and alemtuzumab). Twelve participants (nine RRMS, three SPMS) were on antidepressant medications (escitalopram, duloxetine, amitriptyline, nortriptyline, fluoxetine, desvenlaflaxine, venlafaxine and quetiapine). The demographic and clinical data are summarized in Table 3.1 in the Results.

3.2.2. Cognitive assessment

Cognitive and clinical tests were administered to the MS participants by MS neurologists (Kurtzke Expanded Disability Status Scale, EDSS, only) and a trained user (DVC) to evaluate different aspects of memory, fatigue, depression and disability, as features that could also be related to cognition, and to establish the degree of CI within the MS group. The tests consisted of EDSS for

overall disability in MS, Brief Visual Memory Test—Revised (BVMT-R) for visuospatial learning and memory (age corrected, total recall scores only), Symbol Digit Modalities Test (SDMT) for information processing speed and visual scanning/learning (corrected for age and education level, z scores), Modified Fatigue Impact Scale (MFIS) for effects of fatigue in terms of physical and cognitive functioning and Beck Depression Inventory-II (BDI-II) for depression. The combination of BVMT-R and SDMT was selected as a shortened version of the Brief International Cognitive Assessment for MS (BICAMS), which has been shown to be as reliable as the whole BICAMS battery for detecting CI in MS patients [315], [316]. Cut-off scores for CI classification were set as z scores of SDMT lower than −1.67 standard deviations (SD) [315] and percentage scores of BVMT-R lower than 12% (~1.17 SD) [317]. Patients were classified as CI when at least one out of the two test scores was below clinical cut-off (Table 3.1).

3.2.3. MRI protocol

Brain MRI was acquired on a 3 T Siemens Prisma with a 64-channel head/neck radio frequency (RF) coil. Whole brain 3D T1-weighted magnetization-prepared rapid acquisition with gradient echo (MPRAGE) used a field of view (FOV) 250×250 mm^2, 0.85-mm isotropic voxels, TR = 1800 ms, TE = 2.37 ms and scan time of 3:39 minutes. Whole brain 3D sampling perfection with application-optimized contrasts using different flip angle evolution (SPACE) FLAIR was performed with FOV 230×230 mm^2, 1.2 mm isotropic voxels, TR = 5000 ms, TE = 385 ms, TI = 1800 ms and scan time of 3:07 minutes (SPACE FLAIR was not acquired in one RRMS participant; thus, lesion volume was calculated from a supplementary echo-planar imaging (EPI) FLAIR scan and was not included in the lesion probability maps qualitative analysis). FLAIR-DTI

was acquired over 35 slices from the top of the corpus callosum oriented along the bicommissural line (anterior commissure–posterior commissure [AC-PC]) to allow full coverage of the fornix, 5 b0, 20 diffusion directions with b=1000 s/mm^2, 1.2×1.2×2 mm^3 voxel resolution 2× zero-fill interpolated to 0.64×0.64 mm^2 in-plane resolution, TR = 9000 ms, TE = 69 ms, TI = 2300 ms (to null CSF) and scan time of 4:11 minutes. Prescan normalize filter was applied to minimize B1 inhomogeneity through the slice and to improve ventricular visualization/registration between scans with no detrimental effects on DTI parameters.

3.2.4. MPRAGE brain volume and FLAIR lesion volume analysis

Total and regional brain volumes and total MS lesion volumes were calculated as supplementary information to the main fornix diffusion metrics analysis. For the volumetric analyses and segmentation of brain structures and MS lesions, T1-weighted and FLAIR images were processed by using the VolBrain and LesionBrain pipelines of the volBrain software [318], respectively. For both pipelines, images were denoised with an adaptive non-local mean filter, affine registered to the Montreal Neurological Institute (MNI) space, corrected for image inhomogeneities, intensity normalized and then yielded brain tissue maps (i.e., WM, GM and CSF). The T1-weighted images utilized by VolBrain to segment the brain tissue maps in the MS cohort were lesion filled in FSL with their respective lesion binary masks calculated with LesionBrain pipeline before entering the VolBrain pipeline. Both pipelines are described in detail below.

3.2.4.1. VolBrain pipeline (T1-weighted)

T1-weighted images were used to segment several anatomical structures. First, the intracranial cavity (ICC), brainstem and cerebellum were extracted, and lateral ventricles and subcortical structures were segmented (lateral ventricles definition did not include choroid plexuses), and hippocampi were segmented following the European Alzheimer's Disease Consortium—Alzheimer's Disease Neuroimaging Initiative (EADC-ADNI) Harmonized Hippocampal Protocol (HarP). The following brain tissue and deep GM volumes were calculated: WM, GM, CSF, lateral ventricles, total right and left hippocampus, thalamus, putamen and caudate. All volumes were reported in cm^3 for the group analyses.

3.2.4.2. LesionBrain pipeline (T1-weighted + FLAIR)

Lesion segmentation was only performed on brain areas marked as lesion candidates because either they were above a threshold value calculated from GM FLAIR intensities or included voxels at locations with probability higher than 20% to contain a lesion on the MNI atlas of lesions from this pipeline dataset. Lesions were first segmented using an extension of the Rotation-invariant multi-contrast non-local means (RI-NLM) and patch-wise NLM regularization methods, followed by a systematic error correction step using the Patch-based Ensemble Corrector (PEC) to obtain the final segmentation [319]. The total lesion volume (TLV) was reported in cm^3.

3.2.5. FLAIR-DTI Diffusion Metric Analysis

Gibbs ringing removal, masking, eddy current, subject motion, EPI correction and tensor fitting using Robust estimation of tensors by outlier rejection (RESTORE) were performed in ExploreDTI (v4.8.6) [287].

3.2.5.1. Fornix Tractography

Deterministic tractography was performed in ExploreDTI with an FA threshold of 0.15, a turning angle of 35˚, step size of 0.64 mm, minimum fiber length of 10 mm, and seed point resolution matching the voxel size (0.64×0.64×2 mm^3) [104], [209], [260], [312]. Tractography was performed by the first author (DVC), who was blinded to group classification only for the fornix tracking. Regions of interest (ROIs) were placed similarly to previous lab published protocols for the limbic system tracts [104], [288], [312]: SEED ROIs in fornix columns (axial) and body (coronal, ~5 mm before crura), AND ROI in fornix body (coronal, ~12 mm anterior to SEED ROI) to assure that fornix streamlines are passing through ventricles as expected, and NOT ROIs as needed to remove anterior commissure, callosal and thalamic radiation streamlines. Left and right portions of the fornix were kept together here to reduce multiple comparisons. Volume, FA, MD, AD, and RD were calculated over the entire fornix tract.

3.2.5.2. Thalamus and Hippocampus DTI

Averaged right and left thalamus and hippocampus DTI analyses were performed in ITK-SNAP (v3.8.0) [320]. The mean diffusion weighted image (DWI) was registered to MPRAGE with an

affine transformation model by using mutual information as the image similarity metric, and resliced to MPRAGE resolution with trilinear interpolation. The same transformation matrix was applied to the diffusion parameter maps. FA, MD, axial diffusivity (AD), and RD mean values from the 3D volume for the right and left combined hippocampus and thalamus were calculated from the previously segmented VolBrain Pipeline corresponding labels.

3.2.6. Statistical Analysis

Statistical analyses were performed in Minitab v20 and MatLab R2020b. Total lesion volume was assessed with two-sample t-tests between MS patients sub classified according to their cognitive status as either not cognitively impaired (not CI) or CI. Fornix, thalamus and hippocampus volume, FA, MD, AD and RD were evaluated with One-way Analysis of variance (ANOVA) between MS participants and controls. WM, GM, CSF, lateral ventricle, caudate and putamen volumes were also supplementary assessed with corresponding ANOVA tests. Age was added as a covariate when significant. T1-weighted derived volumes were additionally adjusted for intracranial size by adding the intracranial volume as a covariate. Post-hoc Dunnett's test to control the family-wise error rate was used to calculate differences between not CI and CI MS patients in each one of these brain structures/areas versus healthy controls. The population corrected Hedges's effect size g_s [321] and statistical power derived from our sample size (1-β) were calculated and reported for the fornix, thalamus and hippocampus volume and diffusion metrics between all MS groups and controls.

Pearson correlations between fornix volume and diffusion metrics with age were calculated separately for the MS and healthy cohorts. If correlations were significant for any cohort, stepwise linear regression analyses were performed with age as a continuous predictor, group type as a categorical predictor and an interaction effect between age and group type to test whether these metrics differed between controls and MS or if there were interaction effects versus age in these cohorts.

As the fornix (and other total brain areas, i.e., GM, CSF) metrics show age correlations in the MS cohort, Partial Pearson correlation coefficients, corrected for age, were calculated for the fornix, hippocampus and thalamus volume/diffusion metrics, total brain volumes, total lesion volume, and clinical/cognitive variables (EDSS, BVMT-R, SDMT, MFIS – physical and cognitive, BDI-II, and time since MS symptoms onset (years)).

Ordinal logistic regression models were conducted to investigate the relationships between the volume and diffusion limbic metrics that were significantly different between the MS subgroups and healthy controls while controlling for age as a potential confounder, if significant. The model with the best discriminating power was used to generate receiver operating characteristic (ROC) curves in MatLab R2020b. These curves and their prognostic capabilities were compared by assessing the area under the curve (AUC), accuracy, sensitivity, and specificity metrics.

Previous statistical tests were corrected for multiple comparisons by using the Benjamini–Hochberg false discovery rate (FDR-BH) method using a MatLab R2020b in-house written script

to provide a q-value≤0.05. FDR adjusted p-values were set up as follow: One-way ANOVAs, p≤0.021; full Pearson correlations with age, p≤0.025; and partial Pearson correlations, p≤0.017.

3.3. Results

3.3.1. MS Subgroup Characteristics and Lesions

The control group and the entire MS cohort were similar in sex (p=0.21) with 70%(controls)/81%(MS) females and age (p=0.93) covering 32-71 years both with a mean/SD of 48 +/- 10 years (see Table 3.1 for all demographics). There were 23/43 MS patients classified with cognitive impairment (CI), but both CI and not CI groups had similar sex (p=0.83), age (p=0.41), and time since MS symptom onset (p=0.65). When compared to not CI MS, the CI MS subgroup had higher EDSS scores and higher fatigue levels on both the physical and cognitive subscales and greater depression scores. Compared to RRMS, the SPMS patients were older (SPMS 58 ± 7 years, RRMS 46 ± 9 years), had longer times since MS symptom onset (SPMS 27 ± 10 years, RRMS 13 ± 8 years), had higher EDSS scores (SPMS 5 ± 1, RRMS 3 ± 1.5) and higher fatigue on the physical subscale of the modified fatigue test (SPMS 24 ± 4, RRMS 19 ± 9) (not reported in Table 3.1).

Table 3.1: Demographics and global brain metrics for controls, full MS cohort, not cognitively impaired (not CI) and CI MS subgroups with range and mean ± standard deviation where appropriate (*p<0.05 for differences between the MS cohort and MS subgroups or controls).

	Controls (n=43)	***MS cohort (n=43)***	***Not CI MS (n=20)***	***CI MS (n=23)***
Sex (M/F)	13/30	8/35	4/16	4/19
Age (years)	32-70 48 ± 10	32-71 48 ± 10	32-71 47 ± 10	34-70 49 ± 10
Education level (> 12 years education) †	38/40	16/42	8/20	8/22
WM+GM (cm^3)	1249 ± 125	1143 ± 127*	1184 ± 129*	1106 ± 115*
Lateral Ventricles (cm^3)	13.9 ± 7.2	21.8 ± 11.3*	17.9 ± 10.6*	25.2 ± 11.1*
Total Lesion Volume (cm^3)ƒ	-	0.03-44.2 7.9 ± 11.4	0.14-16.3 2.8 ± 4.6	0.03-44.2 12.4 ± 13.5*
Time since MS symptom onset (years)	-	1-41 16 ± 10	2-41 15 ± 11	1-34 16 ± 10
EDSS ‡	-	0-6.5 3.5 ± 2	0-6.5 3.0 ± 2.0	2-6 4.5 ± 1.0*
BVMT-R (total recall)	-	8-35 21 ± 7	19-35 27 ± 5	8-27 16 ± 5*
SDMT (z-scores)	-	(-3.33)-2.22 -0.80 ± 1.4	(-1.18)-2.22 0.06 ± 0.9	(-3.33)-0.77 -1.55 ± 1.3*
MFIS (physical)	-	3-33 20 ± 8	5-29 16 ± 7	3-33 24 ± 7*
MFIS (cognitive)	-	1-40 19 ± 9	1-29 16 ± 8	4-40 22 ± 9*
BDI-II	-	1-41 13 ± 9	1-21 9 ± 6	4-41 16 ± 10*
RRMS	-	35/43	17/20	18/23
SPMS	-	8/43	3/20	5/23

Abbreviation: EDSS, Expanded Disability Status Scale; BVMT-R, Brief Visual Memory Test-Revised; SDMT, Symbol Digit Modalities Test; MFIS, Modified Fatigue Impact Scale; BDI-II, Beck Depression Inventory-II; RRMS, relapsing-remitting MS; SPMS, secondary progressive MS.

† Education level was not obtained in three healthy participants and one RRMS (CI) participant.

ƒ Total Lesion Volume was not calculated in a RRMS (CI) participant (no FLAIR).

‡ EDSS was not obtained in two cognitively impaired (RRMS) participants.

Lesion probability maps of the entire MS cohort showed the typical periventricular regions (Figure 3.1A). The lesion probability spatial patterns were similar between not CI and CI groups, but with higher proportions of overlapping lesions in the CI group (Figure 3.1B, C). Total lesion volume (Table 3.1) was significantly higher (mean by ~4.5x) in CI MS relative to not CI MS participants ($t(27)=3.21$, $p=0.003$).

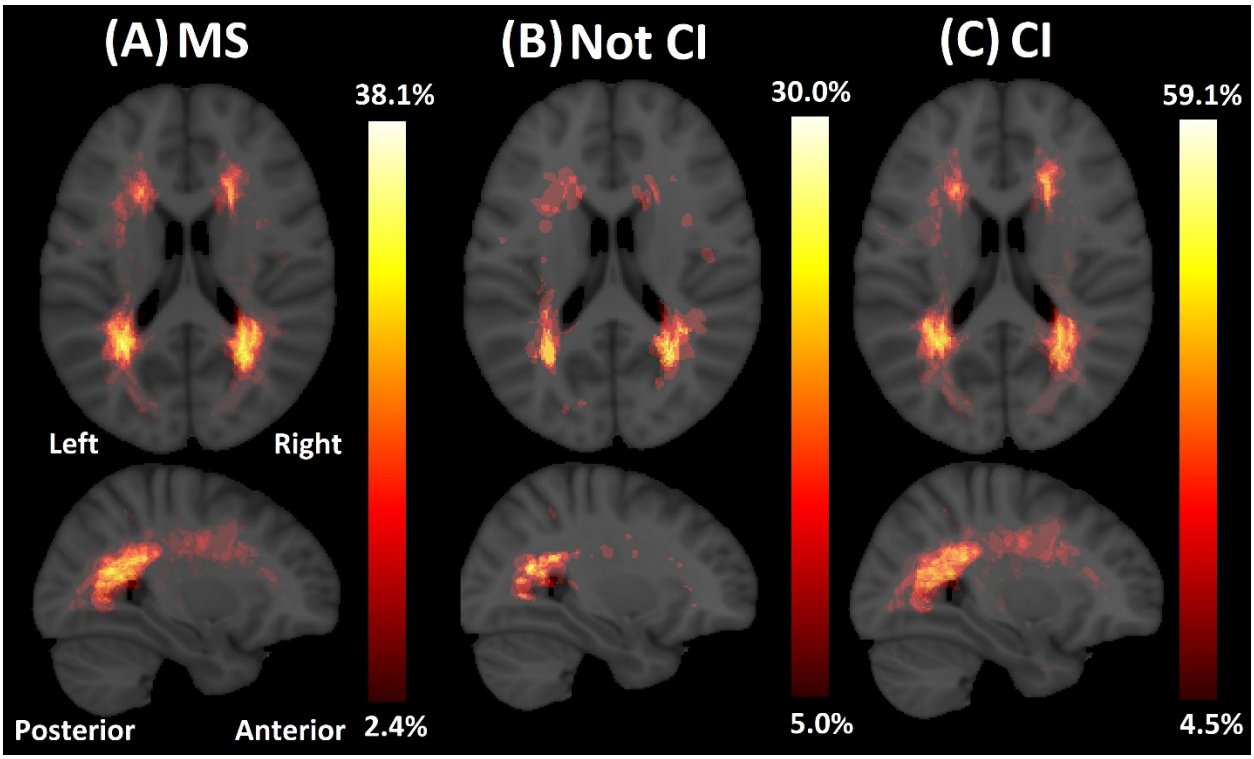

Figure 3.1: Heat color-coded lesion probability maps derived from FLAIR in the (A) entire MS group (n=42), (B) not cognitively impaired – not CI (n=20) and (C) cognitively impaired – CI (n=22; one person was missing FLAIR) overlaid on the MNI152 T1 standard brain. The maximum local probability for lesions were in the classic periventricular regions and was higher in CI patients (~59% peak) compared to the not CI MS subgroup (~30% peak).

3.3.2. Diffusion Tractography Qualitative Analysis of the Fornix

High resolution (1.2x1.2x2=2.9 mm^3) CSF suppressed FLAIR-DTI tractography yielded mostly full fornix tracts for all 43 healthy controls (Figure D.1 in Appendix D displays all fornix tracts color coded by FA and healthy participants ordered by age) and ~91% (39/43) of the MS cohort (Figure D.2 in Appendix D displays all fornix tracts color coded by FA and MS participants ordered by total lesion volume). Most of these MS participants also showed equivalent well delineated fornix tracts although there were examples (at least 6) with thin streamlines uni- or bilaterally, more evident in MS patients with higher total lesion volume (TLV), despite using the exact same tractography pipeline/parameters as the controls. Fornix tracts (classic "W" shape as viewed from above) with FA, MD, AD and RD color encoding from representative examples per group are shown in Figure 3.2 (A- healthy control, B- RRMS not CI, C- SPMS not CI, D- RRMS CI, and E- SPMS CI). Relative to the illustrative healthy control, these four MS examples show smaller fornix volume in three of four cases (23-55%), and all four show lower FA (4-22%) and higher diffusivities of MD (6-17%), AD (4-10%), and RD (9-31%).

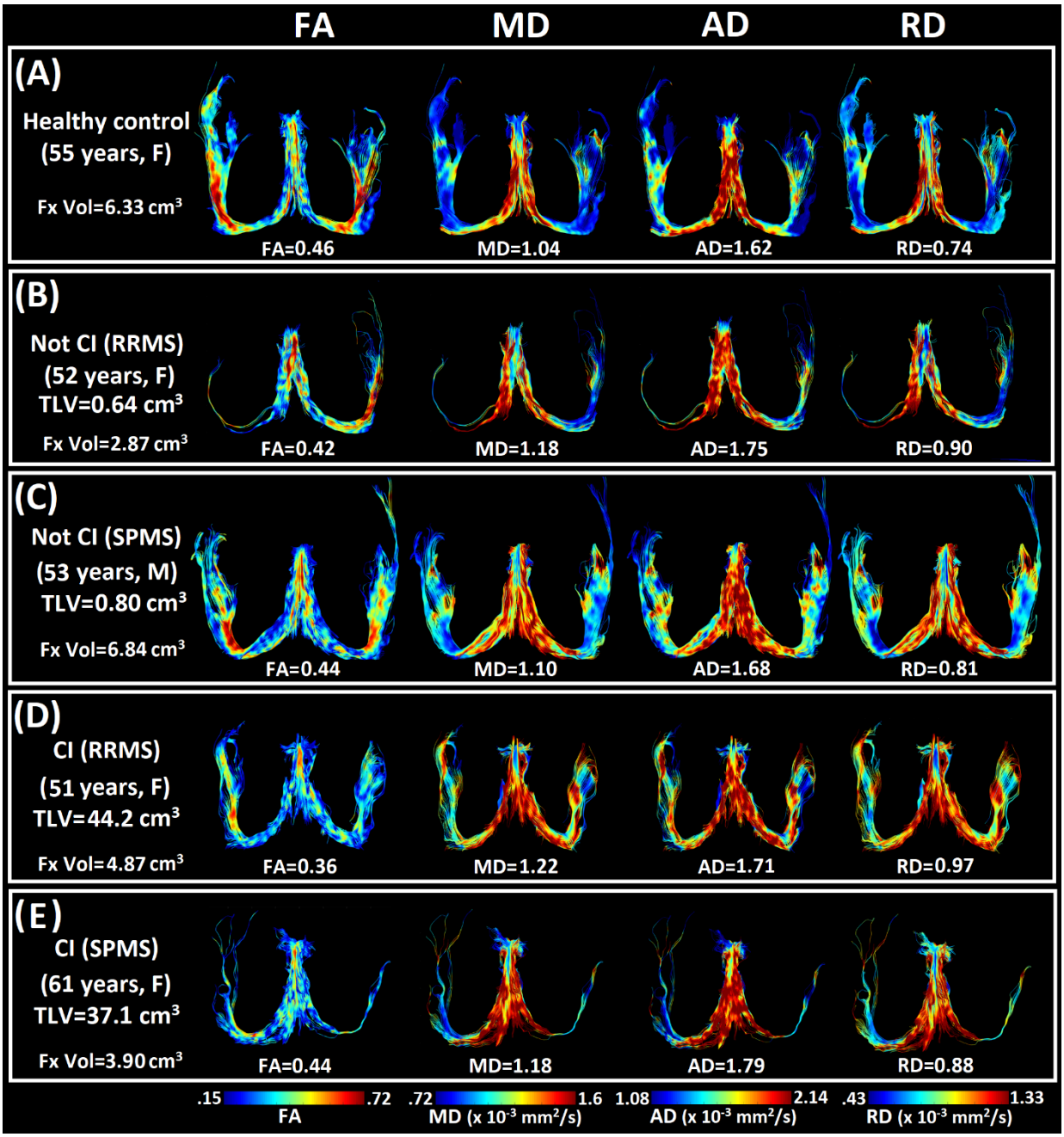

Figure 3.2: Fornix DTI tractography (neurological view from top) with FA, MD, AD and RD color encoding scale in five representative participants: (A) 55 year old female healthy participant, (B) 52 year old not cognitively impaired RRMS female (EDSS 2.0, onset 14 years), (C) 53 year old not cognitively impaired SPMS male (EDSS 6.5, onset 16 years), (D) 51 year old cognitively impaired RRMS female (EDSS 3.5, onset 25 years), and (E) 61 year old cognitively impaired SPMS female (EDSS 6.0, onset 32 years). Three of four MS patients have a much smaller fornix tract volume. All four MS patients showed lower FA and higher MD, AD and RD.

3.3.3. Diffusion Quantitative Analysis of the Fornix

Fornix tractography-derived volumes were 26% lower in the full MS cohort when compared to the healthy controls ($F(1, 83)=12.47$, $p\leq0.0001$, $1-\beta=0.99$) (Figure 3.3A). This appears to be driven by the CI MS subgroup whose fornix volume was 36% smaller than controls ($t(64)=-4.93$, $p\leq0.0001$, $1-\beta=0.97$) although the not CI MS subgroup also showed 16% smaller fornices ($t(61)=-2.35$, $p=0.021$, $1-\beta=0.94$). The fornix displayed 7% lower FA ($F(1, 83)=13.3$, $p\leq0.0001$, $1-\beta=0.99$) (Figure 3.3B), 9% higher MD ($F(1, 83)=22.87$, $p\leq0.0001$, $1-\beta=0.99$) (Figure 3.3C), 6% higher AD ($F(1, 83)=10.88$, $p\leq0.0001$, $1-\beta=0.97$) (Figure 3.3D), and 12% higher RD ($F(1, 83)=27.72$, $p\leq0.0001$, $1-\beta=0.99$) (Figure 3.3E) in the MS group versus controls. As with volume, this was driven by the CI MS participants (-8% FA — $t(64)=-5.15$, $p\leq0.0001$, $1-\beta=0.99$; 12% MD — $t(64)=6.72$, $p\leq0.0001$, $1-\beta=0.99$; 7% AD — $t(64)=4.63$, $p\leq0.0001$, $1-\beta=0.94$; 17% RD — $t(64)=7.40$, $p\leq0.0001$, $1-\beta=0.99$; Figure 3.3B-E and Figure 3.4). It is interesting to note that the fornix DTI parameter most affected was RD, mainly in the CI MS subgroup (Figure 3.4), and MD and RD were the only DTI parameters to differ in the not CI MS subgroup (5% MD — $t(61)=2.57$, $p=0.024$, $1-\beta=0.99$; 7% RD — $t(61)=2.83$, $p=0.011$, $1-\beta=0.99$); albeit to a lesser extent compared to controls (Figure 3.3C, E and Figure 3.4). All fornix volume and diffusion analyses, apart from FA, were adjusted for age.

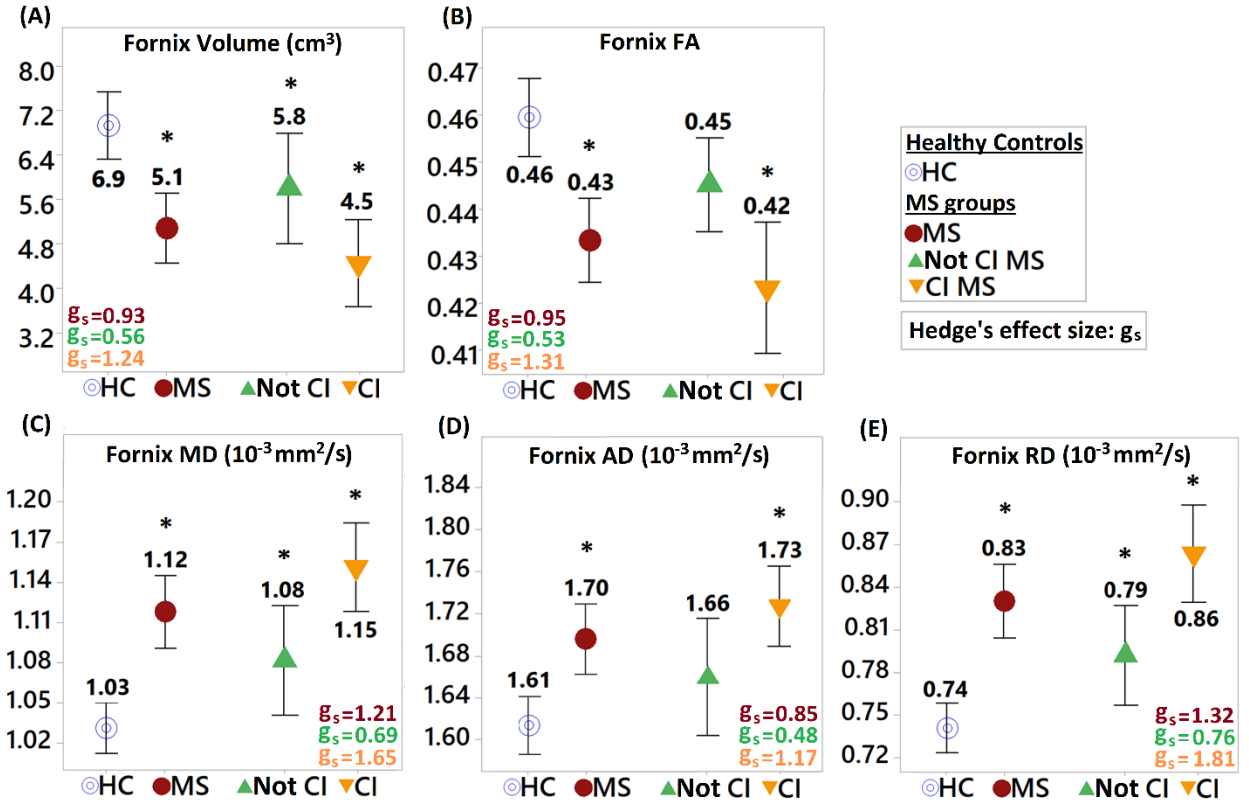

Figure 3.3: Tractography-derived parameters of the fornix (A) volume, (B) FA, (C) MD, (D) AD, and (E) RD for controls (HC), all MS combined, not cognitively impaired (not CI), and cognitively impaired (CI) MS groups. The interval plots show the mean and a 95% confidence interval for the mean of each group with the population corrected Hedges's effect size g_s and statistical differences in the MS groups versus healthy controls (FDR corrected *p<0.021). Volume and FA in the full MS cohort and CI MS were lower than in healthy participants. All diffusivities in the full MS cohort and CI MS were higher than in healthy subjects. Not CI MS showed lower volume and higher MD and RD when compared to healthy controls. In all volume and diffusion metrics, the largest effect sizes were reported in CI MS (g_s=1.17-1.81) when compared to medium effect sizes in not CI MS (g_s=0.48-0.76).

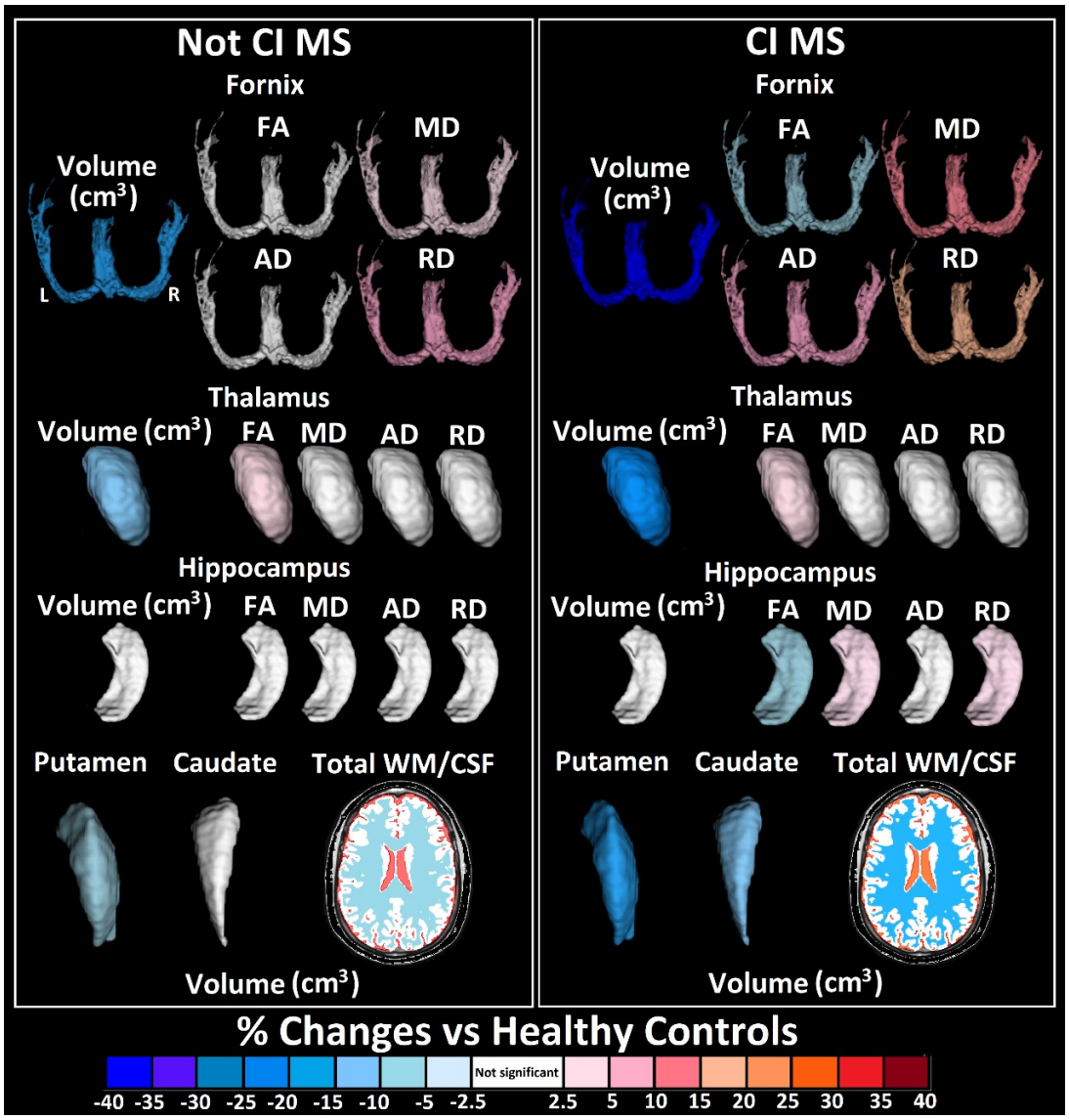

Figure 3.4: Percentage MRI metrics changes in fornix and deep GM in not CI and CI MS versus healthy controls. Neurological view from top of 3D rendered fornix, thalamus, hippocampus, putamen, caudate, and total WM and CSF segmentations in not CI and CI MS subgroups that show significant percentage changes when compared to healthy controls. Volumes were reported for all brain structures/areas and diffusion metrics only for the fornix, thalamus and hippocampus. The color changes in terms of percentage reduction (blue) / increases (red) from all the brain structures/areas analyzed here showed the greatest % volume reductions in the fornix for the CI MS subgroup and the greatest diffusion metrics % differences also in the fornix, mainly MD and RD for both not CI and CI MS subgroups versus controls. Fornix FA and AD were also different when compared to controls only in the CI MS subgroup. (FDR corrected $p<0.021$).

3.3.4. Deep Grey Matter Volume/Diffusion Analyses

Volume and diffusion metrics for the thalamus and the hippocampus are reported in Table 3.2. After the fornix, the thalamus was the limbic structure reported here that showed the greatest MS atrophy with both the not CI ($t(61)=-3.19$, $p=0.002$, $1-\beta=0.99$, $g_s=0.85$) and CI ($t(64)=-6.63$, $p\leq0.0001$, $1-\beta=0.99$, $g_s=1.69$) MS subgroups showing 11% and 23% lower volumes than the healthy controls, respectively. The thalamus FA was 4% higher in the not CI ($t(61)=3.65$, $p=0.001$, $1-\beta=0.78$, $g_s=0.98$) and 3% higher in the CI ($t(64)=2.66$, $p=0.018$, $1-\beta=0.84$, $g_s=0.68$) MS subgroups relative to the controls. As opposed to the thalamus, the hippocampus volume showed no differences between MS and control groups. However, it did show 6% lower FA ($t(64)=-3.2$, $p=0.004$, $1-\beta=0.68$, $g_s=0.82$) and 3-5% higher MD ($t(64)=3.34$, $p=0.002$, $1-\beta=0.74$, $g_s=0.85$) and RD ($t(64)=4.01$, $p\leq0.0001$, $1-\beta=0.87$, $g_s=1.02$) in CI MS versus controls.

Fornix, thalamus and hippocampus volume and diffusion metrics and other brain tissue (total WM, CSF) and structure (putamen and caudate) volumes showing significant changes in the not CI or the CI MS subgroup when compared to healthy controls are pictorially described in Figure 3.4 (FDR corrected $p<0.021$). From all the limbic structures under study here, the fornix showed the greatest volume reductions and diffusion metrics differences for the CI MS subgroup versus healthy controls. Putamen and caudate volumes are additionally shown in Table 3.2 (DTI metrics not shown). Putamen volume was significantly lower (9-15%) in both not CI and CI MS and the caudate volume was 14% lower only in CI MS compared to healthy participants. Combined total WM+GM volume was 5-11% lower in not CI and CI MS versus controls; and it was driven by lower WM volume (8-16%, Figure 3.4) in both MS subgroups as GM did not show any significant

volume changes in MS. Lateral ventricle volume (29-82%) and CSF volume (12-23%, Figure 4) were greater again in both not CI and CI MS when compared to healthy participants. Total WM+GM and lateral ventricle volumes for every group are reported in Table 3.1.

Table 3.2: Deep GM MRI group metrics. Right and left combined thalamus and hippocampus volumes (cm^3, right and left added) and diffusion metrics (average of mean ± standard deviation for FA – no units, MD, AD, RD – 10^{-3} mm^2/s) and caudate and putamen volumes for controls versus the full MS cohort, not cognitively impaired (CI) and CI MS subgroups (FDR corrected *p<0.021).

Right and Left Combined Deep GM Structure		***Controls (n=43)***	***MS cohort (n=43)***	***Not CI MS (n=20)***	***CI MS (n=23)***
Thalamus	**Vol**	12.0 ± 1.5	9.9 ± 1.7*	10.7 ± 1.6*	9.2 ± 1.5*
	FA	0.34 ± 0.02	0.36 ± 0.02*	0.36 ± 0.02*	0.35 ± 0.02*
	MD	0.76 ± 0.02	0.76 ± 0.02	0.76 ± 0.02	0.77 ± 0.02
	AD	1.03 ± 0.03	1.04 ± 0.04	1.04 ± 0.04	1.04 ± 0.04
	RD	0.63 ± 0.02	0.63 ± 0.02	0.62 ± 0.02	0.63 ± 0.02
Hippocampus	**Vol**	8.2 ± 0.9	7.6 ± 0.8	7.8 ± 0.8	7.5 ± 0.8
	FA	0.27 ± 0.02	0.26 ± 0.02*	0.28 ± 0.02	0.26 ± 0.02*
	MD	0.85 ± 0.03	0.87 ± 0.03*	0.86 ± 0.03	0.88 ± 0.04*
	AD	1.08 ± 0.05	1.10 ± 0.04	1.10 ± 0.03	1.10 ± 0.05
	RD	0.73 ± 0.03	0.75 ± 0.04*	0.74 ± 0.03	0.76 ± 0.04*
Putamen	**Vol**	8.4 ± 1.0	7.4 ± 1.0*	7.6 ± 1.0*	7.2 ± 1.0*
Caudate	**Vol**	7.1 ± 0.8	6.4 ± 1.0*	6.8 ± 1.0	6.1 ± 0.9*

Abbreviation: MD, mean diffusivity; AD, axial diffusivity; RD, radial diffusivity; FA, fractional anisotropy; Vol, volume.

3.3.5. Linear Relationships between Fornix Metrics and Age in MS and Healthy Controls

For the fornix, volume (Figure 3.5A) and diffusivities (Figure 3.5C-E), but not FA (Figure 3.5B), showed significant correlations with age in either MS and/or healthy controls (FDR corrected $p<0.033$). The fornix volume correlated negatively ($r=-0.46$, $p=0.002$), and AD correlated positively ($r=0.38$, $p=0.013$) with age only in the MS cohort. Fornix MD (MS – $r=0.37$, $p=0.014$; HC – $r=0.43$, $p=0.004$) and RD (MS – $r=0.34$, $p=0.025$; HC – $r=0.47$, $p=0.001$) displayed significantly positive correlations over the age span under study here (32 to 71 years) for both MS and controls. The fornix MD and RD showed similar slopes between MS and controls, but the Y intercepts were significantly different for the two diffusion metrics (MD — $F(1, 83)= 32.87$, $p\leq0.0001$; RD — $F(1, 83)= 38.87$, $p\leq0.0001$) demonstrating that mean and radial diffusivities within the fornix were higher with age in both cohorts but were consistently higher in MS compared to healthy controls over the age span studied here.

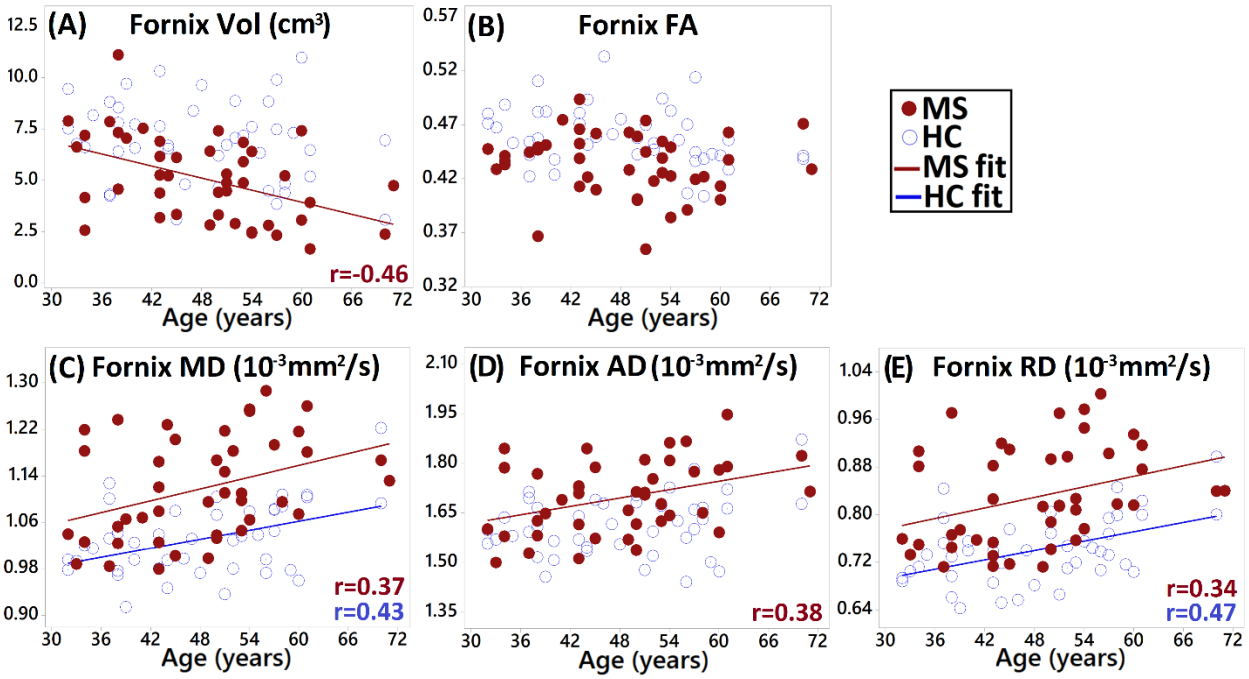

Figure 3.5: The fornix (A) volume, (B) FA, (C) MD, (D) AD, and (E) RD scatterplots versus age for the entire MS cohort (red filled circles) and controls (open blue circles**)** with linear regression fits if significant (FDR corrected $p<0.025$). Fornix volume inversely correlated with age and AD positively correlated with age only in the MS cohort. Fornix MD and RD also showed positive correlations with age in MS and healthy participants. The MD and RD had similar positive slopes with age in both cohorts although both diffusion metrics are consistently higher in MS versus controls over the age span.

3.3.6. Fornix Volume and DTI Metric Correlations with Thalamus/Hippocampus Volume and DTI Metrics, Total WM/GM/CSF/Lateral Ventricles Volumes and TLV in MS

Partial Pearson correlations corrected for age between all the fornix volume and diffusion metrics versus thalamus and hippocampus volume and diffusion metrics, total WM/GM/CSF/lateral ventricles volumes and total lesion volume are shown in Table 3.3. For the thalamus, the fornix volume and diffusion parameters were all correlated to the thalamus volume but not to FA.

Thalamus MD and RD correlated with all fornix metrics but FA, and thalamus AD correlated with fornix MD and RD. In contrast, for the hippocampus, there were no fornix correlations with hippocampal volume, but all fornix metrics correlated with hippocampus FA and RD. Hippocampus MD and AD both showed correlations with all fornix diffusivities and with fornix volume for hippocampus MD only. Total WM volume correlated with fornix MD and RD and total GM volume did not show any fornix correlations. Total CSF and lateral ventricles volumes correlated with fornix volume and all diffusivities but not with fornix FA. Total lesion volume correlated with fornix volume and all diffusion metrics.

Table 3.3: Partial Pearson correlation coefficients of fornix volume / diffusion metrics versus SDMT – information processing speed, thalamus and hippocampus volume / diffusion metrics, and volumes of WM, GM, CSF, lateral ventricles, and total lesions over the entire MS cohort (p-values in brackets, FDR corrected *p<0.017).

Cognitive/Brain Metric	*Fornix Volume*	*Fornix FA*	*Fornix MD*	*Fornix AD*	*Fornix RD*
SDMT z-scores	0.24 (0.110)	0.40* (0.008)	-0.37* (0.013)	-0.25 (0.103)	-0.42* (0.005)
Thalamus Volume	0.48* (0.001)	0.61* (<0.001)	-0.68* (<0.001)	-0.53* (<0.001)	-0.73* (<0.001)
Thalamus FA	-0.02 (0.89)	0.01 (0.95)	0.08 (0.60)	0.08 (0.62)	0.08 (0.62)
Thalamus MD	-0.42* (0.005)	-0.31 (0.044)	0.55* (<0.001)	0.49* (<0.001)	0.54* (<0.001)
Thalamus AD	-0.27 (0.08)	-0.24 (0.12)	0.42* (0.005)	0.36 (0.02)	0.42* (0.005)
Thalamus RD	-0.47* (0.002)	-0.31 (0.045)	0.55* (<0.001)	0.50* (<0.001)	0.53* (<0.001)
Hippocampus Volume	0.11 (0.501)	0.20 (0.19)	-0.18 (0.24)	-0.13 (0.40)	-0.20 (0.20)
Hippocampus FA	0.40* (0.009)	0.54* (<0.001)	-0.58* (<0.001)	-0.44* (0.003)	-0.62* (<0.001)
Hippocampus MD	-0.41* (0.006)	-0.32 (0.038)	0.66* (<0.001)	0.62* (<0.001)	0.63* (<0.001)
Hippocampus AD	-0.18 (0.25)	-0.03 (0.83)	0.36* (0.017)	0.39* (0.010)	0.32 (0.040)
Hippocampus RD	-0.48* (0.001)	-0.42* (0.005)	0.72* (<0.001)	0.65* (<0.001)	0.71* (<0.001)
Total WM Volume	0.32 (0.037)	0.34 (0.028)	-0.41* (0.006)	-0.33 (0.03)	-0.43* (0.004)
Total GM Volume	-0.03 (0.86)	0.21 (0.18)	0.01 (0.96)	0.09 (0.55)	-0.05 (0.76)
Total CSF Volume	-0.52* (<0.001)	-0.13 (0.42)	0.62* (<0.001)	0.66* (<0.001)	0.54* (<0.001)
Lateral Ventricles Volume	-0.40* (0.008)	-0.16 (0.31)	0.64* (<0.001)	0.66* (<0.001)	0.57* (<0.001)
Total Lesion Volume	-0.43* (0.004)	-0.57* (<0.001)	0.66* (<0.001)	0.50* (<0.001)	0.71* (<0.001)

Abbreviation: SDMT, Symbol Digit Modalities Test; FA, fractional anisotropy; MD, mean diffusivity; AD, axial diffusivity; RD, radial diffusivity.

3.3.7. Cognitive and Clinical MS Correlations

Information processing speed given by SDMT, as one of the memory traits severely affected in MS and used here for cognitive impairment classifications, showed linear relationships mainly with the fornix but also with its interconnecting deep GM. Slower information processing speed given by lower SDMT scores correlated with lower FA and higher MD and RD in the fornix (Table 3.3, Figure 3.6A-C). Lower thalamus volume and lower hippocampus FA additionally correlated with slower information processing speed (Figure 3.6D, E). There were no significant correlations of EDSS or visual working memory (BVMT-R) with fornix, thalamus or hippocampus volume/diffusion metrics, global brain volumes, or total lesion volume. Lower thalamus volume correlated with longer MS symptom onset times (Figure 3.7A) with no apparent differences between CI and not CI groups. Higher FA values in the hippocampus correlated with lower physical fatigue (Figure 3.7B), with most of the CI MS participants (83% of total CI MS) displaying the highest fatigue scores with low hippocampus FA.

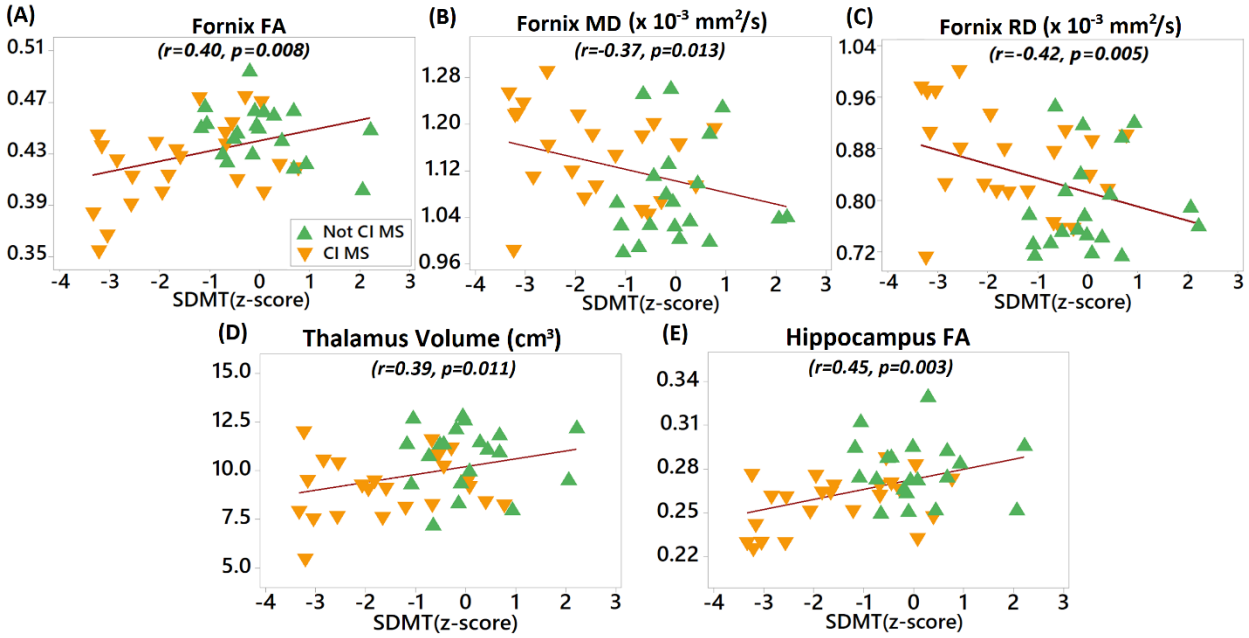

Figure 3.6: MRI correlations with information processing speed. Lower SDMT (z-scores) reflecting slower information processing speed were correlated with (A) lower FA, (B) higher MD and (C) higher RD in the fornix over the entire MS cohort. (D) Lower volume in the thalamus and (E) lower FA in the hippocampus were also related with slower information processing speed (FDR corrected p≤0.017). For visualization, MS participant symbols reflect not cognitively impaired (Not CI – green triangles) or cognitively impaired (CI – orange flipped triangles).

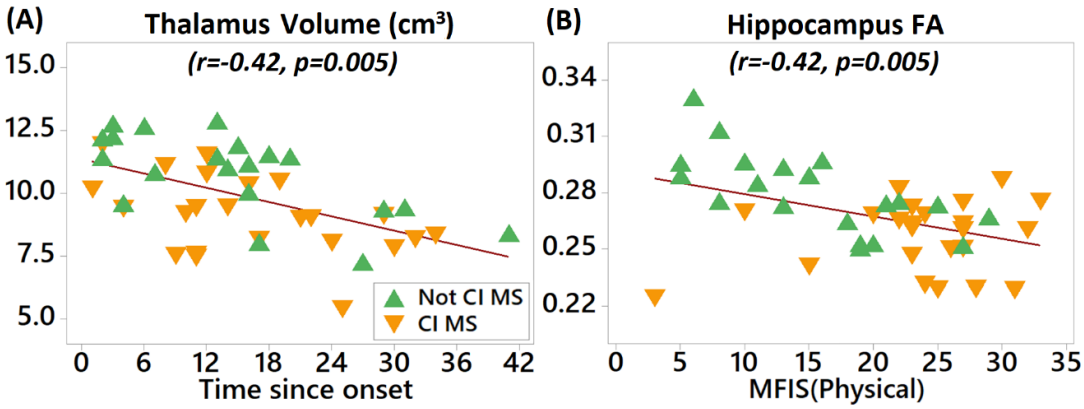

Figure 3.7: Other clinical correlations. (A) Longer times since MS symptom onset correlated with lower thalamus volume for the entire MS cohort and (B) lower physical fatigue (MFIS) was correlated with higher FA in the hippocampus (FDR corrected p≤0.017). For visualization, MS participant symbols reflect not cognitively impaired (Not CI) or cognitively impaired (CI).

3.3.8. Performance of Fornix and Limbic Deep GM Diffusion/Volume Metrics in Discriminating CI in MS

The volume and diffusion metrics considered as prospective predictors to discriminate between the controls and MS groups were the fornix volume, MD and RD, and the thalamus and putamen volumes as these were the limbic metrics/structures that previously differed between all MS groups and healthy participants. The fornix MD and RD were assessed as predictors in separate models to avoid multicollinearity. The ordinal logistic regression model that best fitted the data and showed the greatest measures of association included high fornix RD and low thalamus volume, controlled for age, as predictors of CI in MS. ROC curves (Figure 3.8, Table 3.4) showed a good diagnostic capability (AUC=87.8%, accuracy=81.4%) in differentiating between all MS patients and healthy individuals with high sensitivity and specificity (Table 3.4). The highest predictive statistics were obtained for the CI MS patients (AUC=89.1%, accuracy=87.2%) when compared to not CI MS participants and controls. The lowest predictive performance was achieved for the not CI MS group (AUC=69.2%, accuracy=80.2%). All ROC curves statistics are reported in Table 3.4.

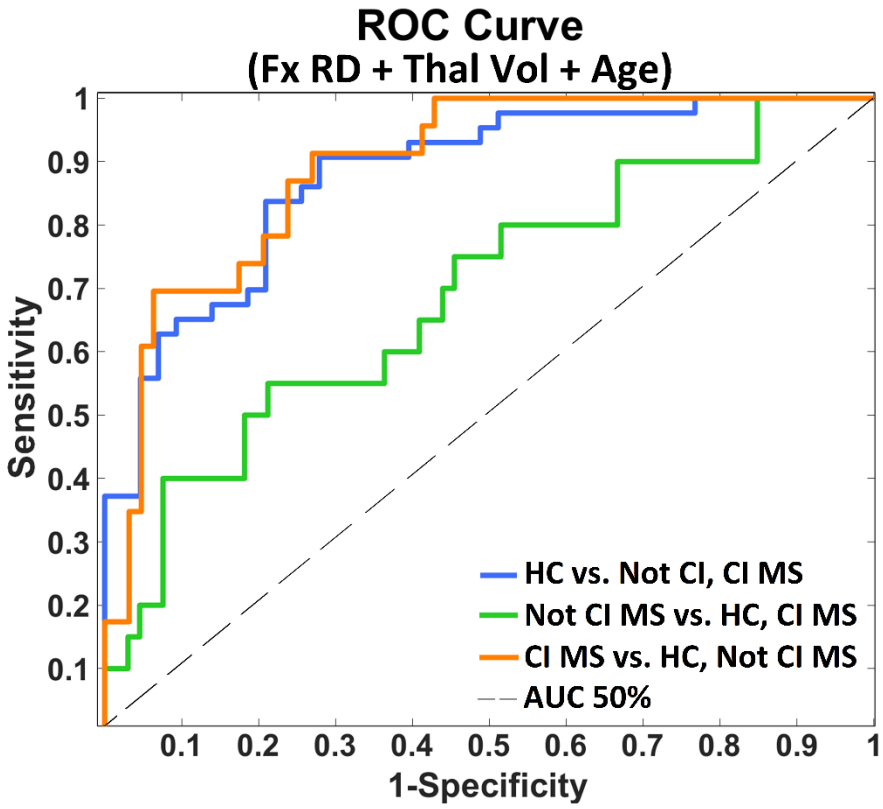

Figure 3.8: Receiver operating characteristic (ROC) curves that best discriminate between CI status in MS and healthy controls. ROC was generated for the ordinal logistic regression model that best discriminated between the MS cohort, not CI MS, CI MS groups and healthy controls. Fornix radial diffusivity, thalamus volume, and age were the main parameters that contributed significantly to the predicting capability of the model. The ROC curves showed the relationship between sensitivity (true positives; y axis) and 1−specificity (false positives; x axis) of these limbic brain metrics to identify each of these MS groups versus the others. The dashed diagonal line represents ROC curves with area under the curve (AUC)=0.5. The CI MS group (orange) followed by the full MS cohort (blue) curves displayed the highest AUC when compared to the not CI MS group (green).

Table 3.4: Receiver operating characteristic (ROC) statistics. ROC Area under the curve (AUC), accuracy (calculated from the optimal operating cut-off point of the receiver operating characteristic, ROC, curve), sensitivity and specificity statistics computed from the ROC curves showing the logistic regression model capability to discriminate between the MS cohort, not CI MS, CI MS groups and healthy controls (HC). The 95% confidence intervals for each ROC metric are shown in brackets.

ROC Curves	***AUC (95% CI)***	***Accuracy (95% CI)***	***Sensitivity (95% CI)***	***Specificity (95% CI)***
HC vs. Not CI, CI MS	87.8% (78.3-93.4)	81.4% (67.9-91.4)	83.7% (69.3-92.9)	79.1% (66.4-90.0)
Not CI MS vs. HC, CI MS	69.2% (54.0-80.8)	80.2% (69.0-89.3)	60.0% (38.1-81.8)	63.6% (49.6-74.6)
CI MS vs. HC, Not CI MS	89.1% (80.2-95.0)	87.2% (76.4-95.3)	87.0% (63.3-96.2)	76.2% (65.5-85.7)

3.4. Discussion

This MS study is the first to use high resolution FLAIR-DTI as a more accurate method to investigate volume and diffusion metrics of the fornix in MS. The CSF suppression and higher spatial resolution suggest that prior lower resolution, non-CSF suppressed findings of diffusion abnormalities of the fornix in MS are reflective of changes in axonal/myelin microstructure and not driven simply by partial volume effects from atrophy of the fornix [125], [209], [210], [256], [260], [274], [312]. Furthermore, robust tractography of the fornix demonstrates that this tract's volume is the most affected percentagewise in cognitively impaired MS (36% reduction), more than any other volume/diffusion measurement, including deep grey matter, in our study. Likewise, the fornix showed the greatest diffusion differences in the MS cohort relative to the thalamus and the hippocampus. These DTI alterations were also all more abnormal in CI MS than in not CI MS compared to the controls suggesting a critical role for the fornix (the major efferent tract of the

hippocampus) and highlighting its early and selective degradation in relation to cognitive impairment that may precede hippocampal atrophy as previously reported in mild cognitive impairment and early stages of Alzheimer's disease [322], [323]. Also, fornix RD displayed higher values in MS regardless of CI classifications which could be interpreted as demyelination [121], [324] and seemed to specifically increase with cognitive deterioration.

Relative to healthy controls, the thalamus volume and the hippocampus DTI metrics were also more altered in CI than not CI MS, extending upon previous DTI findings in these regions in MS [210], [267], [271], [313], [314]. Following the fornix, the thalamus showed the greatest degree of atrophy [233], [270], [309], [313] mostly in CI MS (23%), but also displayed higher FA in the MS cohort, which agreed with previous DTI studies [240], [267], [271]. Thalamic atrophy could be explained by neuronal losses due to various pathological processes such as CSF excitotoxic elements [292], [325], [326], activated microglia [271], [327], or antero- or Wallerian degeneration from thalamic radiations or WM pathways like the mammillary bodies and the fornix. Elevated FA in the thalamus could be partially explained directly from structural reorganization of fiber tracts [267], [328] and cell swelling [271] within the thalamic nuclei, or indirectly from increased coherence due to adjacent/interconnecting crossing fiber loss [240]. However, neither the thalamic radiations nor WM tracts other than the fornix were measured here. In agreement with a previous MS DTI study [329], the hippocampus showed significant although moderate diffusion differences (lower FA, higher MD/RD) in CI MS versus controls suggesting that microstructural changes precede atrophy. It is possible that the hippocampus microstructural injury (e.g. demyelination) is

driven by periventricular WM [330], likely the fornix, given the more extensive changes in that connected tract.

The main fornix cognitive finding was a linear relationship of lower FA or greater MD/RD with slower information processing speed, measured by the SDMT in MS. The thalamus volume and hippocampus FA also correlated with SDMT, being worse in the CI MS patients. These findings were equally supported by the good accuracy of high fornix RD values and thalamus atrophy to correctly classify MS patients, particularly CI participants, and they suggest a link between limbic brain structures such as the fornix and cognitive decline in MS [210], [256], [260], [329]. Slow processing speed appears to be a core cognitive process underlying memory acquisition deficits in MS [331]. The SDMT has been recognized as a highly sensitive test for cognitive change in MS, and it is not only specific to deficits in processing speed, but is also affected by deficits in other cognitive domains, including visual memory, attention, recall and consolidation [331]–[333]. The thalamus atrophy additionally showed a negative relationship with longer MS duration. This cumulative thalamic atrophy over time agrees with a volumetric longitudinal study which focused on thalamus volume in MS [334]. Lower hippocampus FA was associated with greater physical fatigue, which is consistent with a recent volumetric study reporting a link between sustained fatigue and hippocampus/striatal/deep GM atrophy in MS [335]. Fatigue review studies primarily in MS [336], but also in other related neurological disorders [337], have suggested that imbalance in dopamine levels and cognitive dysfunction in hippocampal, striatal and prefrontal cortex areas with reduced functional connectivity between them could lead to effort–reward imbalance, causing fatigue and vice versa.

There were several limitations in our study. The relatively small size of the SPMS group and lack of PPMS compared to the RRMS patients in our MS cohort should be addressed in the future to make inferences regarding relapsing and progressive clinical phenotypes. The application of an automatic segmentation procedure/labels identified on 3D T1-weighted MPRAGE for the DTI metrics calculation in the thalamus and hippocampus, instead of manual segmentation, could cause errors, but the accuracy of the coregistered ROIs were checked in each individual and the same procedure was applied to all. The added inversion pulse for FLAIR-DTI made the scan length longer (relative to regular DTI) which limited the number of slices and brain coverage to keep the scan time to a reasonable 4 minutes, thereby limiting the study of other potentially relevant WM tracts. The cross-sectional design of our study limited conclusions regarding the temporal relationships of the mechanisms involved with fornix damage in MS, necessitating future longitudinal studies.

4. High Resolution Diffusion Tensor Imaging and T2 Mapping Detect Regional Changes within the Hippocampus with Links to Cognitive Impairment in Multiple Sclerosis[3]

Abstract

Hippocampus atrophy as measured by volumetric magnetic resonance imaging (MRI) is well documented in multiple sclerosis (MS). Pathological studies report regional microstructural changes (e.g., demyelination) across the hippocampus that are heterogeneous over MS patients. Diffusion tensor imaging (DTI) and T2 mapping could potentially detect such regional changes in vivo if acquired with sufficient spatial resolution. The goal here was to evaluate the hippocampus in 43 MS patients (35 relapsing-remitting, 8 secondary progressive) with and without cognitive impairment (CI) versus 43 controls using high resolution 1 mm isotropic DTI, as well as complementary methods of T2-weighted and T2 mapping at 3 T. When compared to controls, averaged left/right whole-hippocampus mean diffusivity (MD) was higher in both MS groups, while lower fractional anisotropy (FA) and volumes, and higher T2 relaxometry and T2-weighted signal values were only significant in CI MS. The hippocampal MD and T2 images/maps were not uniformly affected and regions of elevated MD/T2 were more frequent and extensive in MS patients. These were often located along the lateral/medial borders of the hippocampus, specifically in the dentate gyrus and the Cornu Ammonis 1 regions, extending mainly from

[3] Submitted to NeuroImage as: Valdés Cabrera, D., Blevins, G., Smyth, P., Emery, D., & Beaulieu, C. High Resolution Diffusion Tensor Imaging and T2 Mapping Detect Regional Changes within the Hippocampus with Links to Cognitive Impairment in Multiple Sclerosis.

periventricular lesions and perihippocampal/cerebrospinal fluid adjacent areas. Both CI and not CI MS groups showed greater proportional areas of the hippocampus with elevated MD, whereas only the CI group showed greater proportional area of elevated T2 relaxation times or T2-weighted signal. Higher T2 relaxometry and T2-weighted signal values of elevated regions correlated with greater disability (EDSS) and whole-hippocampus FA negatively correlated with physical fatigue. High resolution hippocampus DTI and T2 mapping showed whole hippocampus abnormalities with regional elevations of MD/T2 in MS, likely indicators of demyelination, which overall were more extensive in patients with larger total brain lesion volumes and cognitive impairment.

4.1. Introduction

There is a high incidence of cognitive impairment (CI) in multiple sclerosis (MS) [338], [339]. These deficits are predominantly in episodic and working memory, but also information processing speed [208], [340], all of which often overlap with fatigue and depression that are also prevalent in MS [304], [341]. The anatomical and pathological substrates of cognitive impairment are not fully understood in MS. However, there is a growing body of evidence pointing to the involvement of the hippocampus either directly or as a part of networks with interconnected structures such as the thalamus [342], [343]. The hippocampus is a temporal lobe structure that plays a crucial role in memory, regulation of mood and emotional response [344], [345]. The importance of further quantitative imaging studies of deep grey matter (GM) (including hippocampus) injury in MS has been recently highlighted in a consensus statement by the North American Imaging in MS Cooperative [278].

Demyelinating lesions have been observed in histopathological studies of the hippocampus in about 60% of MS patients postmortem, mostly secondary (SPMS) and primary progressive (PPMS) with disease durations on average ~25-28 years with mean ages of 58-66 years [190], [296], [346]–[348]. For example, in a study of 45 progressive MS patients, demyelinating lesions were observed in 24 of them with 1-4 lesions per case; the demyelination covered on average 30% of the hippocampus albeit with a large range of 2-95% [347]. Demyelinated areas often displayed preserved axons with reductions in synaptic density [190], [296] although significant neuronal loss has also been reported [347]. Most of this damage appeared to be located within the dentate gyrus (DG) [190], [346] and the Cornu Ammonis 1 (CA1) [190], [347], in addition to all the remaining CA subfields (CA2-4) in one study [347]. Other work mentioned CA2 and DG hilus sparing in isolated intra-hippocampal lesions [190]. The residual hippocampus on a coronal slice of pathology has also been reported to have 22% smaller area in MS [347].

GM lesions in MS often cannot be visualized with T2-weighted images due to poor contrast with the surrounding normal appearing GM and CSF [349]. Lesions in the hippocampus have been observed using 3D double inversion recovery (DIR) sequences (T1 based contrast) in 14 out of 16 MS patients (11 relapsing remitting MS - RRMS, 5 SPMS) with an average of 2.6 such lesions per patient which was related to visuospatial memory score [350]. Numerous conventional magnetic resonance imaging (MRI) volumetric studies have reported marked atrophy of the whole hippocampus [211], [213], [274], [311], [351]–[359] by ~8% (range 4-24%) in different MS populations with some of these showing links to cognitive impairment [211], [353], [355], [356], [358]. In these previous studies, atrophy of the hippocampus was often greater than reductions in

overall GM [211], [353], white matter (WM) [211], [213] or total brain volume [311], [353], [357], [359]. Subfield volumetric studies on high resolution T2-weighted coronal images of MS report smaller DG, CA1, and subiculum [311], [355]–[359], and CA2-3 less frequently [311], [357], [358]. Other MRI sequences such as functional MRI and MR spectroscopy have detected hippocampal disconnections with other brain regions [213], [351] and metabolic changes [360], respectively, in MS.

Diffusion tensor imaging (DTI) is sensitive, albeit not specific, to changes in neural microstructure (e.g. axon/cell loss, demyelination, edema) [97], but its poor spatial resolution has led to limited application to the study of the atrophied hippocampus in MS. Nearly all of the few DTI studies of the hippocampus in MS have thus evaluated diffusion metrics averaged over the entire hippocampus demonstrating higher mean diffusivity (MD) [213], [313], [329], [361] and lower fractional anisotropy (FA) [313], [329], [361] versus healthy cohorts. For example, in one study using better than normal 1.6 mm isotropic DTI resolution (also the only previous work actually displaying diffusion maps of the hippocampus) MS showed higher hippocampal MD and lower FA with no difference in hippocampus volume [329]. In this study, higher hippocampus MD correlated with worse long-term episodic verbal memory recall in clinically isolated syndrome (CIS) patients and with information processing speed in MS, and MD had 90% sensitivity in discriminating memory-impaired from memory-preserved CIS patients [329]. Higher MD of the hippocampus has correlated with worse visuospatial skills and slower information processing speed in MS [210]. A separate study using CSF-suppressed DTI showed that lower hippocampal FA correlated with greater fatigue in MS [361]. A recently developed high resolution, 1 mm

isotropic, axial-oblique DTI protocol of the hippocampus at 3 T, with slices aligned along its long axis and acquired under 6 minutes, has demonstrated a marked improvement in visualization and contrast of the hippocampal borders and internal architecture (Figure 4.1A, D) [136]. This has facilitated its segmentation directly in DTI native space without co-registration to anatomical scans while also minimizing partial volume effects and improving accuracy of diffusion metrics. This novel protocol has been able to detect unique patterns of focal diffusion abnormalities throughout the hippocampus of patients with temporal lobe epilepsy [362], but it has never been applied in MS before. As a complement to diffusion MRI, quantitative T2 relaxometry of the hippocampus has also been shown to detect T2 differences reflecting microstructural damage in epilepsy [363] and Alzheimer's disease [364]; high resolution T2 relaxometry has not been applied to the hippocampus in MS to our knowledge. Longer T2 relaxation times have been considered an indicator of neuronal damage, caused by demyelination and increased water content due to inflammation/edema, as seen in normal appearing WM beyond lesions in MS [78].

The aims of this study were (a) to use high resolution (voxel volume 1 mm^3) DTI of the hippocampus to evaluate whole and regional diffusion abnormalities in MS with and without cognitive impairment, (b) to evaluate the utility of high resolution (voxel volume 1.2 mm^3) T2 relaxometry from multi-echo spin echo acquisitions of the hippocampus for the same purpose as DTI and even higher resolution (voxel volume 0.25 mm^3) T2-weighted imaging for signal evaluation, and (c) to assess correlations between the hippocampal MRI metrics and cognitive functions affected in MS (visual working memory, information processing speed), fatigue, depression, and disability.

4.2. Methods

4.2.1. Participants

Study participants included 43 patients diagnosed with MS (35 RRMS, 8 SPMS), in addition to 43 healthy controls with no self-reported neurological/psychiatric disorders or brain injuries and similar age and sex distribution as the MS cohort. MS participants were enrolled from the University of Alberta MS Clinic and controls were selected from a larger normative study on healthy brain development (n=32) or were recruited from advertising (n=11). This study was approved by the University of Alberta Health Research Ethics Board and all protocols were conducted according to the Declaration of Helsinki with written informed consent from all participants. The MS participants were consecutively recruited during the study enrollment period if they fulfilled the inclusion/exclusion criteria (all phenotypes, disability scores, cognitive status and ages were included). The only inclusion criteria for eligibility to participate in the study as a MS participant was a clinically definite RRMS, SPMS or PPMS diagnosis. The exclusion criteria were no history of clinically documented relapse or a high dose steroid treatment in a year prior to MRI scan. Two RRMS and six SPMS participants were not receiving MS medications or treatments, but the remaining cohort were on different disease-modifying therapies. Twelve participants (9 RRMS, 3 SPMS) were on antidepressant medications. The demographic and clinical data are shown in Table 4.1.

4.2.2. Cognitive Assessment

Most of the MS cognitive and clinical tests were performed by the first author (DVC) to evaluate disability, facets of memory (visuospatial abilities, processing speed), depression and fatigue which is known to be interrelated to cognition in MS. The tests consisted of the Kurtzke Expanded Disability Status Scale (EDSS) for overall disability in MS (provided by MS neurologists, coauthors GB and PS); Brief Visual Memory Test-Revised (BVMT-R) for visuospatial learning and memory (age corrected z-scores, total recall scores only); Symbol Digit Modalities Test (SDMT) for information processing speed and visual scanning/learning (corrected for age and education level, z-scores); Modified Fatigue Impact Scale (MFIS) for effects of fatigue in terms of physical and cognitive functioning; and Beck Depression Inventory-II (BDI-II) for depression. The combination of BVMT-R and SDMT was utilized for detecting CI in MS patients with cut-off scores similar to what was applied in previous work [361], although only total recall BVMT-R scores were considered here. Patients were classified as CI when at least one of the two test scores were below the established clinical cut-off (Table 4.1). Patients were additionally classified as fatigued by applying a MFIS cut-off score of 38 [365].

4.2.3. MRI Protocol

Brain MRI was acquired on a 3 T Siemens Prisma with a 64-channel head/neck RF coil. Diffusion MRI data of the hippocampus was acquired over 20 1 mm isotropic resolution axial-oblique slices with no gap, no interpolation and prescan normalization filter on, with single shot 2D echo planar imaging (EPI) (GRAPPA R=2; 6/8 PPF; A/P phase encode), FOV 220×216 mm^2, matrix 220×216, TE 72 ms, TR 2800 ms, b=500 s/mm^2 with 10 monopolar gradient directions, 10 averages and 10

non diffusion-weighted images (DWI) for a scan time of 5:18 min (Figure 1A, D) [136]. The slices were aligned to the long axis of the hippocampus using a whole brain high resolution 3D T1-weighted magnetization-prepared rapid acquisition with gradient echo (MPRAGE) for reference (0.85 mm isotropic; 3:39 min). Whole brain 3D sampling perfection with application optimized contrasts using different flip angle evolution (SPACE) fluid-attenuated inversion recovery (FLAIR) was also performed (1.2 mm isotropic, 3:07 min) in the MS cohort to yield total WM lesion volumes (TLV) [361]. T2 relaxometry and higher in-plane resolution T2-weighted imaging were acquired for the same 20 1 mm axial oblique slices as the DTI and included: (a) T2 multi-echo spin echo with 16 echoes (TE=10.7-171.2 ms with 10.7 ms inter-echo spacing), TR=3560 ms, 1.1×1.1×1 mm^3, 20 slices in 5:47 min, and (b) 0.5×0.5×1 mm^3 T2-weighted images with TE=52 ms, TR=5440 ms, 20 slices in 4:39 min. The T2 multi-echo spin echo sequence was only acquired in 11 of the 43 controls (51 ± 11 years) as many of the controls were part of a larger normative study on healthy brain development which did not have this MRI sequence, and T2 mapping data was discarded in one RRMS not CI patient due to artifacts.

4.2.4. Image Processing

Total brain volumes from MPRAGE and TLV from FLAIR (Table 4.1) were taken from a previous publication focused on FLAIR-DTI of the fornix in this same MS cohort [361]. All ROIs were segmented in ITK-SNAP (v3.8.0) [320].

4.2.4.1. Hippocampus DTI

Denoising, Gibbs-ringing, eddy current, subject motion correction, B1 field inhomogeneity correction, and tensor parameter estimation were performed in MRtrix3 [366]. Hippocampus regions-of-interest (ROIs) [367] were manually segmented to yield whole hippocampal volumes, MD, and FA of right and left separately. The whole hippocampus was segmented in the axial-oblique plane of native space mean DWIs, checking the coronal and sagittal structure boundaries, by a single user (author DVC), who was blinded to participant age and group classification. The entire hippocampus was segmented in accordance with the European Alzheimer's Disease Consortium (EADC) and Alzheimer's Disease Neuroimaging Initiative (ADNI) Harmonized Protocol (HarP) [368], including the fimbria/alveus and whole tail but excluded the subiculum (Figure 4.1B, E). Dice similarity and intraclass correlation coefficients for interrater reliability of authors DVC and KGS was 0.80 and 0.86 respectively for the whole hippocampus ROIs, as measured in a subsample of the healthy cohort (n=38). An MD threshold of 2.2×10^{-3} mm^2/s was set from values calculated from ROIs placed on ventricular cerebrospinal fluid (CSF), excluding the choroid plexus, in 10 representative healthy controls and 10 age matched MS patients (32 to 70 years), and it was used to exclude voxels containing primarily CSF from the whole hippocampus volume and diffusion measurements. To evaluate regional elevated MD areas, histogram analysis was performed in each subject's segmented hippocampus ROIs. Standard deviations (SD) were calculated over all the individual voxels in the healthy control group (n=43), and a threshold set as 2 SD over the group mean value (mean MD of $0.80 \pm$ SD 0.21×10^{-3} mm^2/s led to 1.22×10^{-3} mm^2/s) was defined as hyperintense. The ratio or percentage area relative to the

number of voxels of the total hippocampus that displayed MD values above the defined threshold and the mean MD value in this area was calculated in each subject. No regional analyses were performed for FA which is quite low in the hippocampus.

4.2.4.2. Hippocampus T2 Relaxometry

T2 relaxometry maps were calculated from multi-echo spin echo images using extended phase graph (EPG)-based stimulated echo compensation [89] modified to use slice profiles approximated using the Shinnar-Le Roux algorithm [93]. Whole hippocampus ROIs from the diffusion scans were utilized as a guidance to segment similar ROIs in the T2 relaxometry maps. A threshold of 200 ms was applied to the segmented T2 relaxometry maps to remove voxels with excessive partial volume effects with CSF in agreement with previous work [362], [369]. To evaluate regional elevated T2 relaxometry values within the hippocampus, an analysis similar to that for DTI was performed here. T2 relaxometry values above a threshold were calculated as 2 SD over the healthy control group (n=11) mean value (mean T2 of 74 ± SD 16 ms led to 106 ms threshold) and were defined as hyperintense. The ratio or percentage area of the total hippocampus that displayed T2 relaxometry values above the defined threshold and the mean T2 value in this area was calculated in each subject.

4.2.4.3. Hippocampus T2-weighted Signal

T2-weighted sequences are used for lesion detection in clinical practice and have been used as a comparison in a previous hippocampus DIR study in MS [350]. Whole hippocampus ROIs from the diffusion scans were utilized as guidance to segment similar ROIs in T2-weighted images

(higher 0.5 x 0.5 mm^2 in-plane resolution than the T2 maps above to aid in visualizing small GM lesions) and voxels with pure CSF in the vicinity of the hippocampus were excluded from the ROIs. The T2-weighted signal intensities were calculated for the whole hippocampus and then normalized to ventricular CSF values within the same scan from ROIs carefully placed on ventricular CSF avoiding any visible pulsation artifacts. To evaluate regional hyperintense T2-weighted signal areas within the hippocampus, similar analysis to that performed with DTI and T2 relaxometry was performed here. CSF-normalized T2-weighted signal values above a threshold were calculated as 2 SD over the healthy control group (n=43) mean value (mean relative T2 signal hippocampus/CSF of 0.64 ± SD 0.09 led to 0.82 threshold) and were defined as hyperintense. The ratio or percentage area of the total hippocampus that displayed T2-weighted signal intensities above the defined threshold and the mean value in this area was calculated in each subject.

4.2.5. Statistical Analysis

Statistical analyses were performed in Minitab v20 and MatLab R2020b. There were no hemispheric differences (paired t-test) for hippocampus volume, MD or T2 in the MS cohort and to reduce the number of multiple comparisons, all metrics were left/right averaged for further analyses. Group effects (healthy controls, not CI MS and CI MS) were examined with analysis of covariance tests (ANCOVA, with age as a covariate when significant) for whole hippocampus MD, FA, T2 relaxometry, and T2-weighted signal metrics and regional elevated MD, T2 relaxometry and T2-weighted signal percentage areas and values. Post-hoc Tukey pairwise comparisons, controlling the family-wise error rate, were used to test further differences between not CI and CI MS subgroups and healthy controls. Linear associations between all the whole and

regional hippocampus MRI metrics were tested with Pearson's correlations against TLV and clinical/cognitive variables (EDSS, BVMT-R, SDMT, MFIS – physical and cognitive, BDI-II, MS symptoms onset) in the entire MS cohort. All statistical tests were corrected for multiple comparisons with the Benjamini–Hochberg false discovery rate (FDR-BH) method using a MatLab R2020b in-house written script to provide a q-value≤0.05. FDR adjusted p-values were set up as follows: ANCOVAs, p≤0.027; Pearson correlations, p≤0.008.

4.3. Results

4.3.1. MS Subgroup Characteristics

The control group and the entire MS cohort were similar in sex (p=0.31) with 72%(controls)/81%(MS) females and age (p=0.97) covering 32-71 years both with a mean/SD of 48 +/- 10 years (see Table 4.1 for all demographics). There were 22/43 MS patients classified with cognitive impairment (CI), but both CI and not CI groups had similar sex (p=0.80), age (p=0.59), and time since MS symptom onset (p=0.99). When compared to not CI MS, the CI MS subgroup had higher EDSS scores (p=0.03) and higher fatigue levels on both the physical (p=0.001) and cognitive (p=0.007) subscales, with 16/22 CI individuals scoring as fatigued on MFIS scale. The CI MS group likewise displayed 2.7x higher lesion volumes on average than the not CI MS subgroup (p=0.003).

Table 4.1: Demographics and global brain metrics for controls, full MS cohort, not cognitively impaired (not CI) and CI MS subgroups with range and mean ± standard deviation where appropriate (*p<0.05 for differences between the MS cohort/subgroups and controls).

	Controls (n=43)	***MS Cohort (n=43)***	***Not CI MS (n=21)***	***CI MS (n=22)***
Sex (M/F)	12/31	8/35	4/17	4/18
Age (years)	32-70 48 ± 10	32-71 48 ± 10	32-71 48 ± 10	34-70 49 ± 10
WM+GM (cm^3)	1259 ± 111	1143 ± 127*	1182 ± 126*	1105 ± 118*
Total Lesion Volume (cm^3)[†]	-	0.03-44.2 7.9 ± 11.4	0.14-37.1 4.4 ± 8.7	0.03-44.2 11.8 ± 12.8*
Time since MS Symptom Onset (years)	-	1-41 16 ± 10	2-41 16 ± 11	1-34 16 ± 9
EDSS[‡]	-	0-6.5 3.5 ± 2	0-6.5 3.0 ± 2.0	2-6 4.0 ± 1.0*
BVMT-R (total recall, z-scores)	-	(-3.75)-2.11 -0.56 ± 1.5	(-0.97)-2.11 0.41 ± 1.0	(-3.75)-1.75 -1.48 ± 1.3*
SDMT (z-scores)	-	(-3.33)-2.22 -0.80 ± 1.4	(-1.18)-2.22 0.02 ± 0.9	(-3.33)-0.77 -1.59 ± 1.3*
Fatigued MS (MFIS≥38)	-	22/43	6/21	16/22*
MFIS (physical)	-	3-33 20 ± 8	5-29 16 ± 7	3-33 24 ± 7*
MFIS (cognitive)	-	1-40 19 ± 9	1-29 16 ± 8	4-40 22 ± 9*
BDI-II	-	1-41 13 ± 9	1-21 9 ± 6	4-41 16 ± 11*
RRMS/SPMS	-	35/8	17/4	18/4

Abbreviation: WM, White matter; GM, Grey matter; EDSS, Expanded Disability Status Scale; BVMT-R, Brief Visual Memory Test-Revised; SDMT, Symbol Digit Modalities Test; MFIS, Modified Fatigue Impact Scale; BDI-II, Beck Depression Inventory-II; RRMS, relapsing-remitting MS; SPMS, secondary progressive MS.

[†] Total Lesion Volume was not calculated in a RRMS (CI) participant (no FLAIR).

[‡] EDSS was not obtained in two cognitively impaired (RRMS) participants.

4.3.2. Qualitative Image Assessment

The 1 mm isotropic mean DWI in both healthy (Figure 4.1A, 4.2A, C, E, 4.3A) and MS (Figure 4.1D, 4.2B, D, F, 4.3B-D) participants yielded excellent contrast of the exterior surface of the hippocampus, facilitating its segmentation, and of the internal anatomy and digitations, better than the even higher in-plane resolution T2-weighted images (Figure 4.1C, F, Figure 4.2). When the mean DWIs were visually assessed for all subjects, the participants in both cohorts displayed similar internal architecture such as the presence of the dark band of the stratum lacunosum moleculare (SLM).

FLAIR images reoriented along the long axis of the hippocampus were used in the MS cohort, together with the T2-weighted images, as guidance to assess regional hyperintensities in the hippocampus. FLAIR was only acquired in 5 healthy controls, but hyperintensities were not evident (Figure 4.2A, C, E). Twenty out of 43 MS participants displayed some degree of FLAIR hyperintensity within the hippocampus, widespread or at least one hyperintense area, yet these hyperintensities were not as visible/bright as the typical WM lesions (Figure 4.2B, D, F); this leads to the necessity of quantitative MD/T2 assessment of the hippocampus discussed later to identify lesions. Furthermore, they were not limited by anatomical borders or specific hippocampus subfields, and many were adjacent to the ventricles or the hippocampus sulcus and the perihippocampal fissures (Figure 4.2B, D, F). From the 20 patients displaying hyperintensities, 19 of them were bilateral and one of them was in the left hippocampus tail only. Notably, 15 of these 20 patients were classified as CI MS; thus 15/22 (68%) of CI patients had hippocampal hyperintensities, as opposed to 5/21 (24%) of the not CI MS cohort.

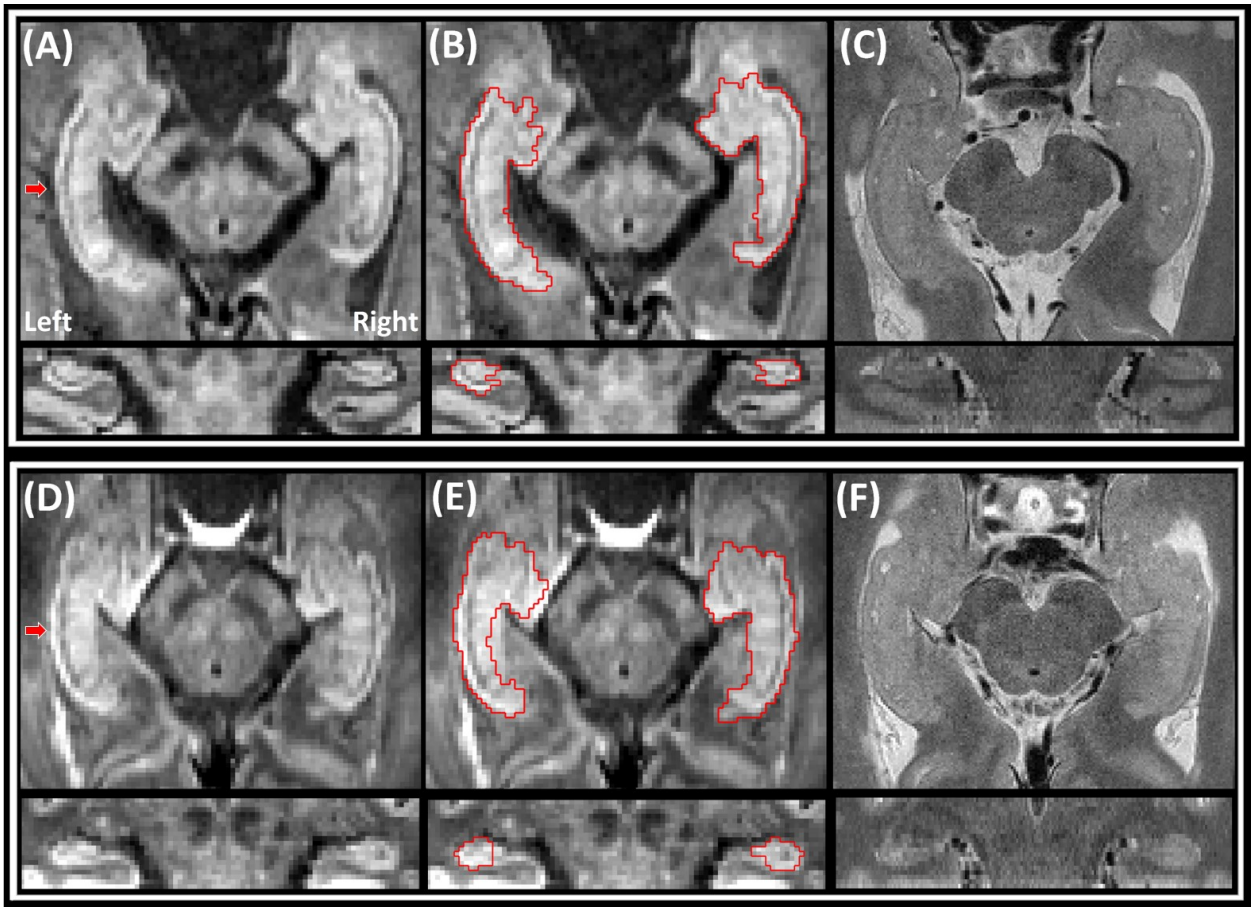

Figure 4.1: High resolution (A, D) mean diffusion-weighted images (1 mm isotropic, b=500 s/mm2) with the (B, E) manual hippocampus outlines and (C, F) same slice T2-weighted images ($0.5 \times 0.5 \times 1$ mm^3) acquired axial-oblique along the long axis of the hippocampus and coronal reconstruction with slice position indicated by red arrows. (A-C) The top row are images from a 53-year-old male healthy control and (D-F) the bottom row is from a 53-year-old male cognitively impaired RRMS participant. High resolution mean DWI provides excellent visualization of the hippocampus structure, shape, and internal architecture, as well as good demarcation from surrounding cerebrospinal fluid (CSF). The coronal DWI of the control shows the typical 'jelly-roll' appearance with flat contrast whereas that appearance is not as evident in the MS patient where the coronal DWI has regions of hyperintensity.

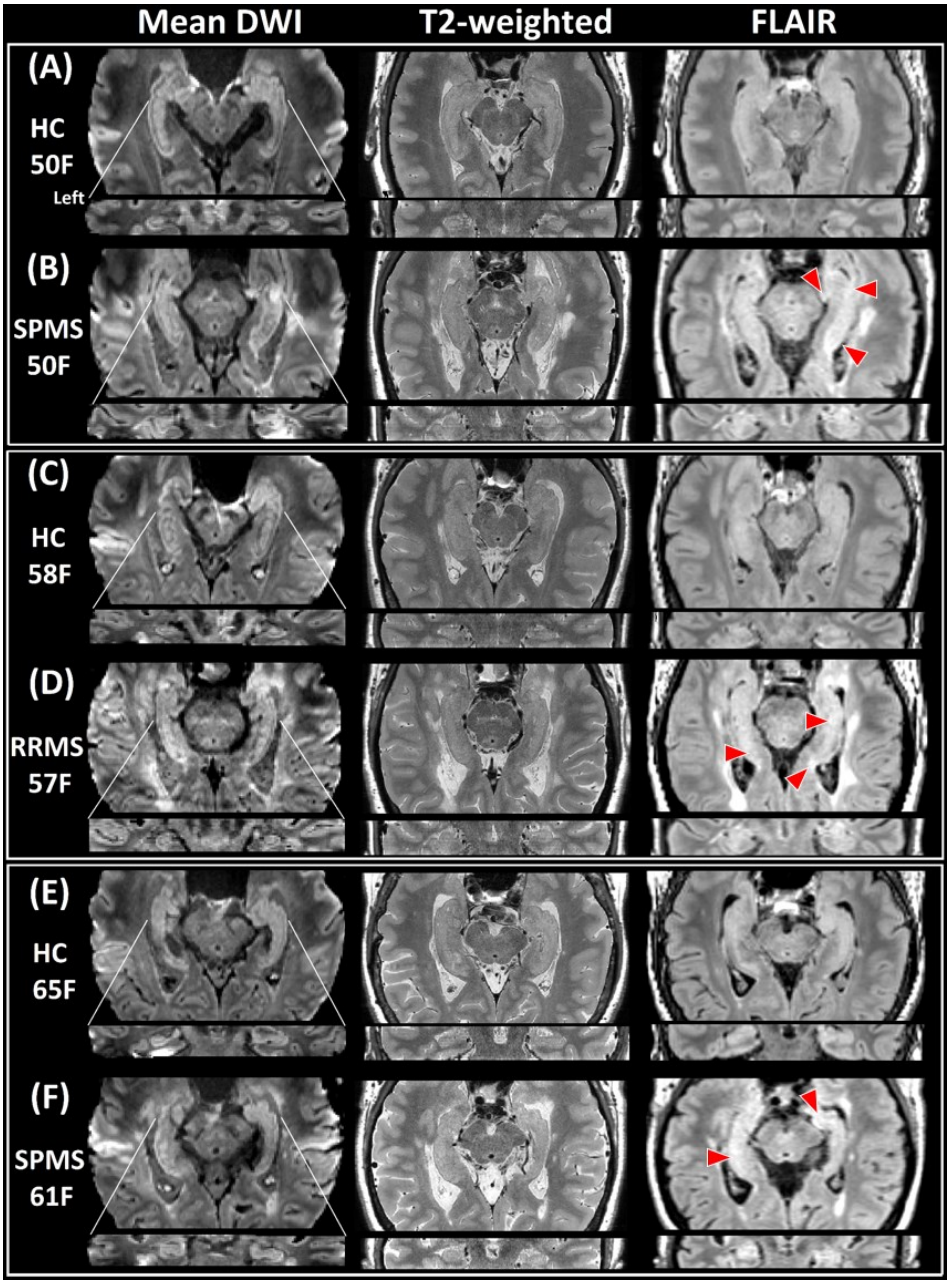

Figure 4.2: Same single slice axial-oblique (top) and coronal (bottom) mean DWI b=500 s/mm^2 (first column), T2-weighted (second column), and FLAIR scans (third column) with visible hyperintense lesions of the hippocampus (red arrowheads) in (B, D, F) three representative MS patients versus (A, C, E) three similarly aged healthy participants. Note that lesions in the WM are far more apparent. (B, D, F) are images from female MS participants with (B) CI, Total lesion volume — TLV=11.9 cm^3, EDSS=4.5, onset 29 years; (D) CI, TLV=19.5 cm^3, EDSS=4.5, onset 17 years; and (F) not CI, TLV=10.1 cm^3, EDSS=6.0, onset 31 years.

The 1 mm image resolution appears to demonstrate more small regions of elevated MD and T2 values on central slices of the hippocampus in three MS patients (Figure 4.3B, C, D) relative to a control (Figure 4.3A). In MS, areas of elevated MD and T2 corresponded to similar regions and they frequently extended along the A-P axis, near the lateral or medial borders (Figure 4.3) in proximity with the lateral ventricles and the perihippocampal fissure. Recall that the maps excluded voxels with high MD and T2 values for CSF. The FA maps show a low degree of anisotropy throughout the hippocampus, as expected, for all cases. Notably, WM lesions in periventricular and perihippocampal areas were extensive and visualized as hyperintense signal on mean DWI (b=500 s/mm^2) and higher MD in several MS patients (Figure 4.3C, D), suggesting WM edema/inflammation as this combination implies T2 shine-through on the DWI.

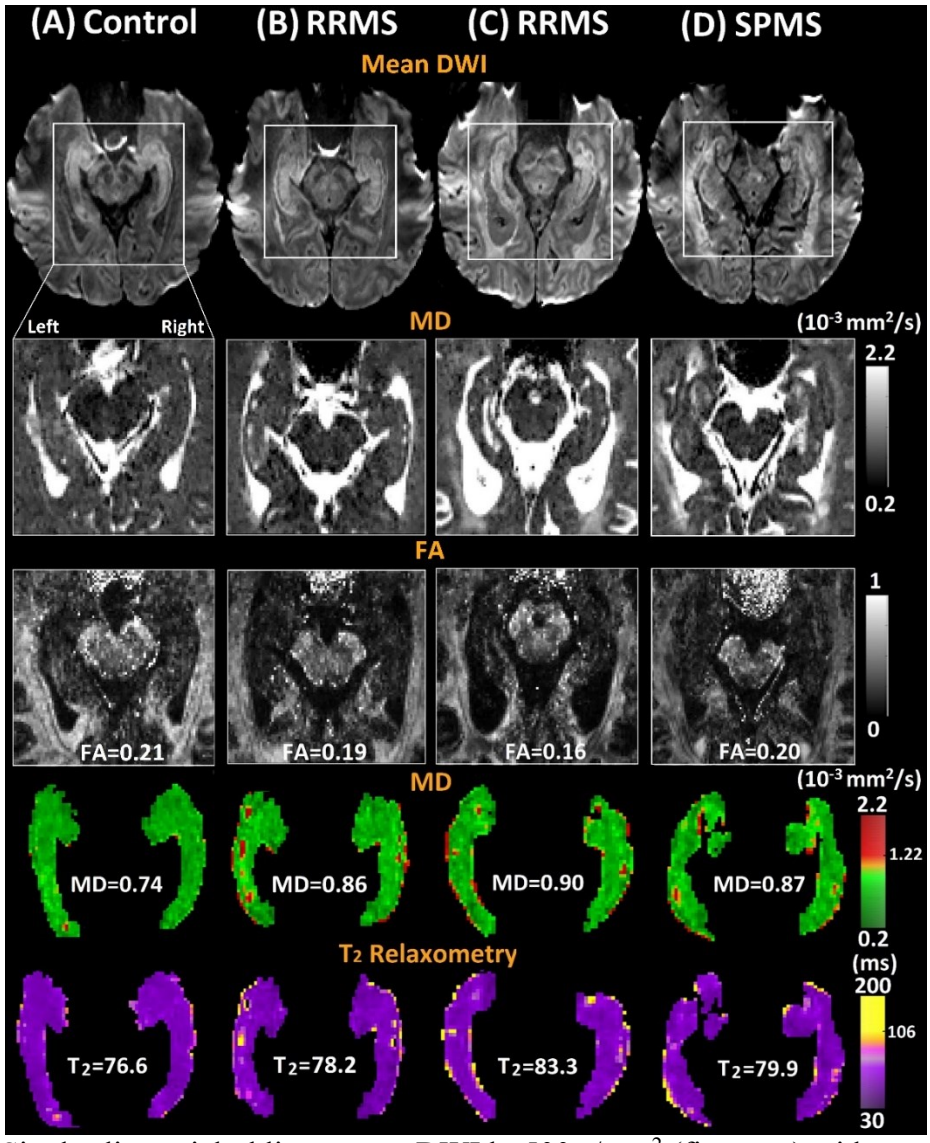

Figure 4.3: Single slice axial-oblique mean DWI b=500 s/mm^2 (first row) with mean diffusivity (MD, second row) and fractional anisotropy (FA, third row) maps of the areas enclosed in white boxes in DWI and their corresponding manually segmented hippocampus MD (fourth row) and T2 relaxometry (fifth row) color maps from (A) a 59-year-old female healthy control, (B) a 53-year-old male RRMS CI patient (TLV=0.7 cm^3, EDSS=3.5, onset 19 years), (C) a 56-year-old female RRMS CI patient (TLV=34.2 cm^3, EDSS=NA, onset 11 years), and (D) a 61-year-old female SPMS not CI patient (TLV=37.1 cm^3, EDSS=6, onset 32 years). Averaged over the entire hippocampus (including slices not shown), the MD and T2 values were higher and FA lower in the three MS patients relative to this control. There are more focal regions of higher MD/T2 values visible in the MS patients. Note the bi-color scales were chosen to highlight voxels above the mean + 2SD thresholds derived from controls and all voxels related to CSF (defined as MD>2.2x10^{-3} mm^2/s or T2>200 ms) have been blacked out.

4.3.3. Whole Hippocampus Quantitative Analysis

Figure 4.3 shows three representative MS patients who had higher MD, higher T2, and lower FA of the whole hippocampi relative to three controls. Overall, there were significant group differences between the MS cohort and the healthy controls for all MRI whole-left/right averaged hippocampus measurements (Figure 4.4), with only FA and T2 relaxometry values displaying age effects for both cohorts: MD ($F(2,86)=16.2$, $p\leq0.0001$), FA ($F(2,86)=3.8$, $p=0.027$; age — $F=6.2$, $p=0.015$), volume ($F(2,86)=5.8$, $p=0.004$), T2 relaxometry ($F(2,53)=6.3$, $p=0.004$; age — $F=8.7$, $p=0.005$), and T2-weighted signal ($F(2,86)=7.1$, $p=0.001$). MD was 5% higher similarly in all MS groups despite their cognitive classifications when compared to heathy controls (Figure 4.4A). FA (-5%, Figure 4.4B) and DTI-derived volumes (-14%, Figure 4.4C) in MS were lower than the controls although only in the CI MS group, with volumes exhibiting the greatest percentage group difference versus controls for the whole hippocampus. T2 relaxometry (5%, Figure 4.4D) and T2-weighted signal values (4%, Figure 4.4E) were higher than the controls, again only in the CI MS group.

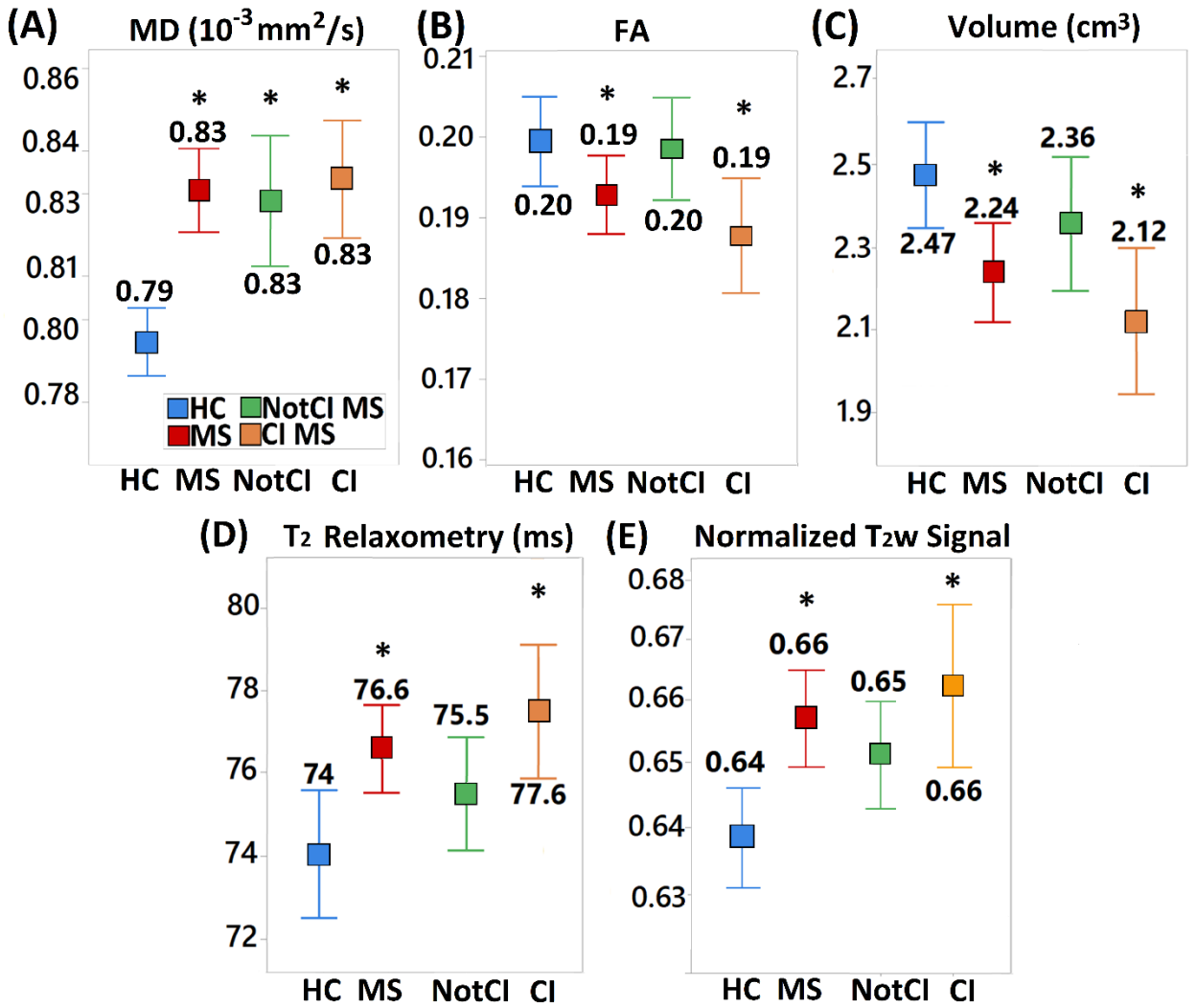

Figure 4.4: Whole hippocampus mean and 95% confidence intervals for left/right averaged (A) MD, (B) FA, (C) volume, (D) T2 relaxometry, and (E) CSF-normalized T2-weighted signal values in healthy controls (HC, n=43), all MS patients combined (n=43), not cognitively impaired MS (not CI, n=21), and cognitively impaired MS (CI, n=22) groups. The entire MS cohort showed significantly greater MD (+5%), T2 (+3.5%), and T2-weighted signal (+3%), and lower FA (-5%) and volume (-9%). MD was elevated in both not CI and CI groups, but the other four whole hippocampal parameters were different from controls only in the CI group with the largest percentage difference being the 14% lower volume derived from the mean DWI scan (FDR corrected *$p<0.027$).

4.3.4. Regional Hippocampus Analyses

MD and T2 relaxometry maps displaying regions of elevated values within the hippocampus of three more MS patients are shown in Figures 4.5, 4.6 and 4.7 for single slices, along with their mean DWI (b=500 s/mm^2), T2-weighted and realigned FLAIR images for reference. In several cases the hippocampus lesions appeared to be part of periventricular lesions involving the temporal horns of the lateral ventricle (e.g., see FLAIR axial and coronal planes in MS examples shown in Figures 4.6C and 4.7C). Preferential locations of elevated MD and T2 relaxation time values were mainly in the DG and the CA1 subfield. They were scattered all over the head, body and tail, although frequently located in the superior portion of head (Figure 4.6) or as a bright lateral/medial rim along the hippocampus borders (Figure 4.7). Elevated MD and T2 values were also evident near the hippocampus sulcus (although CSF voxels were blacked out if the voxels met MD and T2 thresholds) and seemed to affect the SLM area (Figures 4.3B and 4.5).

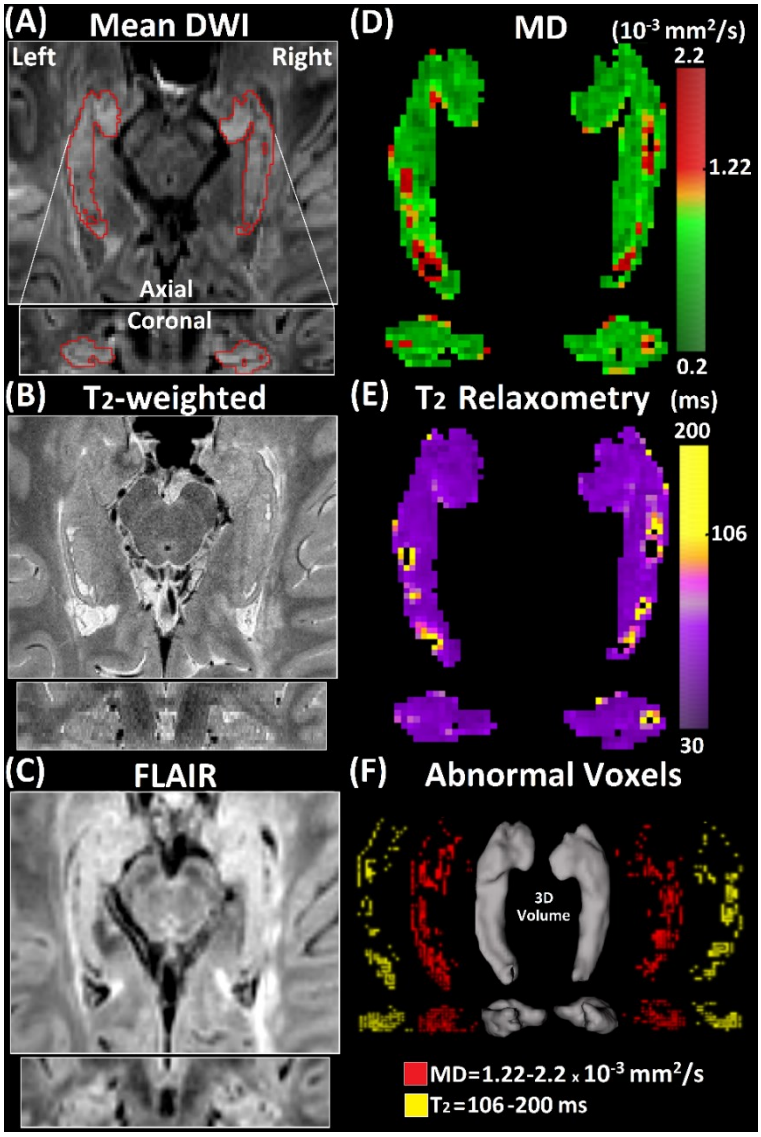

Figure 4.5: Axial-oblique (top) and coronal (bottom) single slice images for (A) mean DWI b=500 s/mm^2, (B) T2-weighted and (C) realigned FLAIR images showing the hippocampus (average left/right hippocampus volume of 1.9 cm^3) in a 38-year-old female RRMS CI patient (TLV=7.0 cm^3, EDSS=4.5, onset 11 years). The color-coded hippocampus (D) MD and (E) T2 relaxometry maps from the same slice (note ROI enclosed in red in A) displayed hyperintense areas (2 standard deviations higher than the mean MD and T2 relaxometry values in controls) that extended mainly across the SLM and near CSF pockets of the hippocampal sulcus in this slice, with good agreement between MD and T2 locations. (F) Voxels across all hippocampal slices (only 1 slice was shown in A-E) that are beyond the MD/T2 threshold are projected onto a single plane demonstrating widespread abnormal values in the lateral borders of the CA1 region and the DG along the entire hippocampus A-P axis. The abnormal MD values comprised 11% and T2 values 8% of the entire hippocampi.

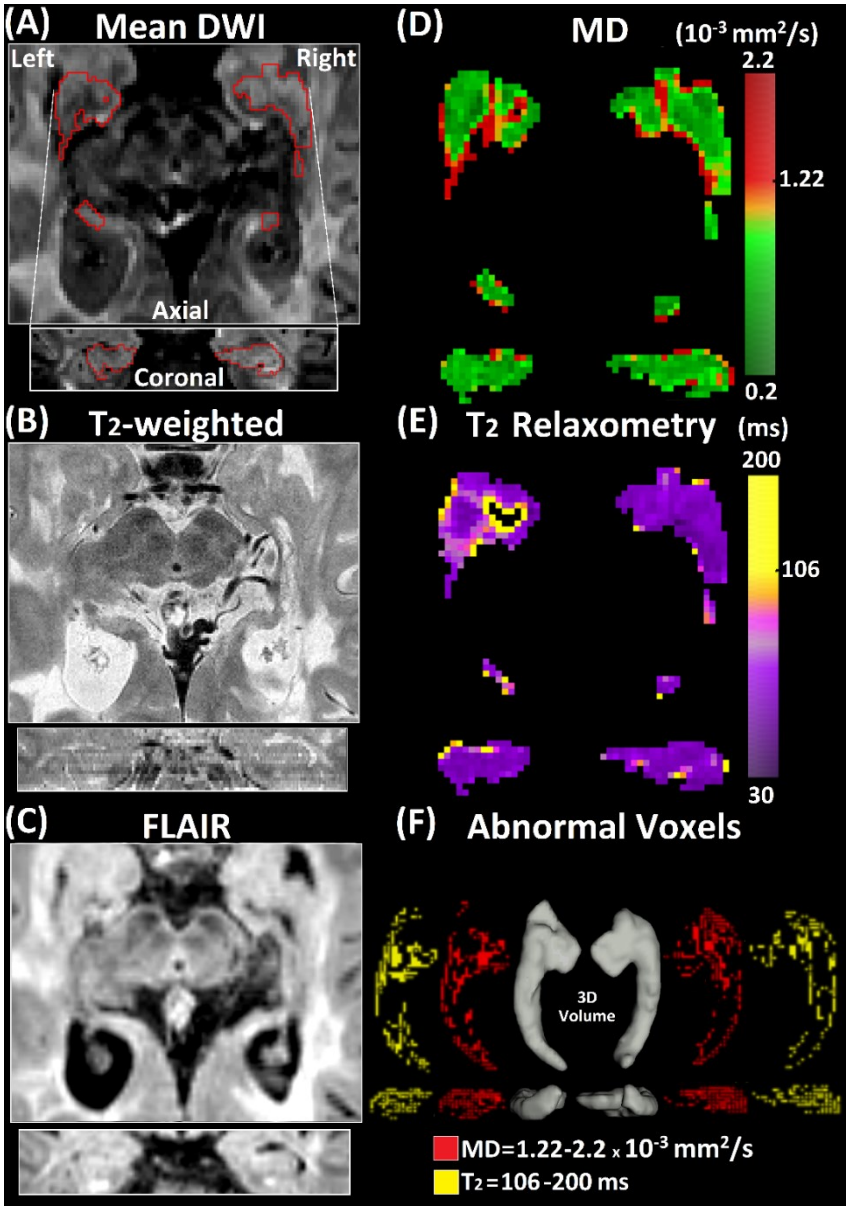

Figure 4.6: Axial-oblique (top) and coronal (bottom) single slice images for (A) mean DWI b=500 s/mm^2, (B) T2-weighted and (C) realigned FLAIR images showing the hippocampus (average left/right hippocampus volume of 2.0 cm^3) in a 51-year-old female RRMS CI patient (TLV=44.2 cm^3, EDSS=3.5, onset 25 years). The color-coded hippocampus (D) MD and (E) T2 relaxometry maps from the same slice displayed hyperintense areas that extended mainly across the DG followed by the CA1 regions in the head and tail in this slice. (F) Voxels across all hippocampal slices that are beyond the MD/T2 threshold are projected onto a single plane demonstrating widespread abnormal values in the lateral and often medial borders of the CA1 region and the DG along the entire hippocampus A-P axis. The abnormal MD values comprised 12% and T2 values 10% of the entire hippocampi.

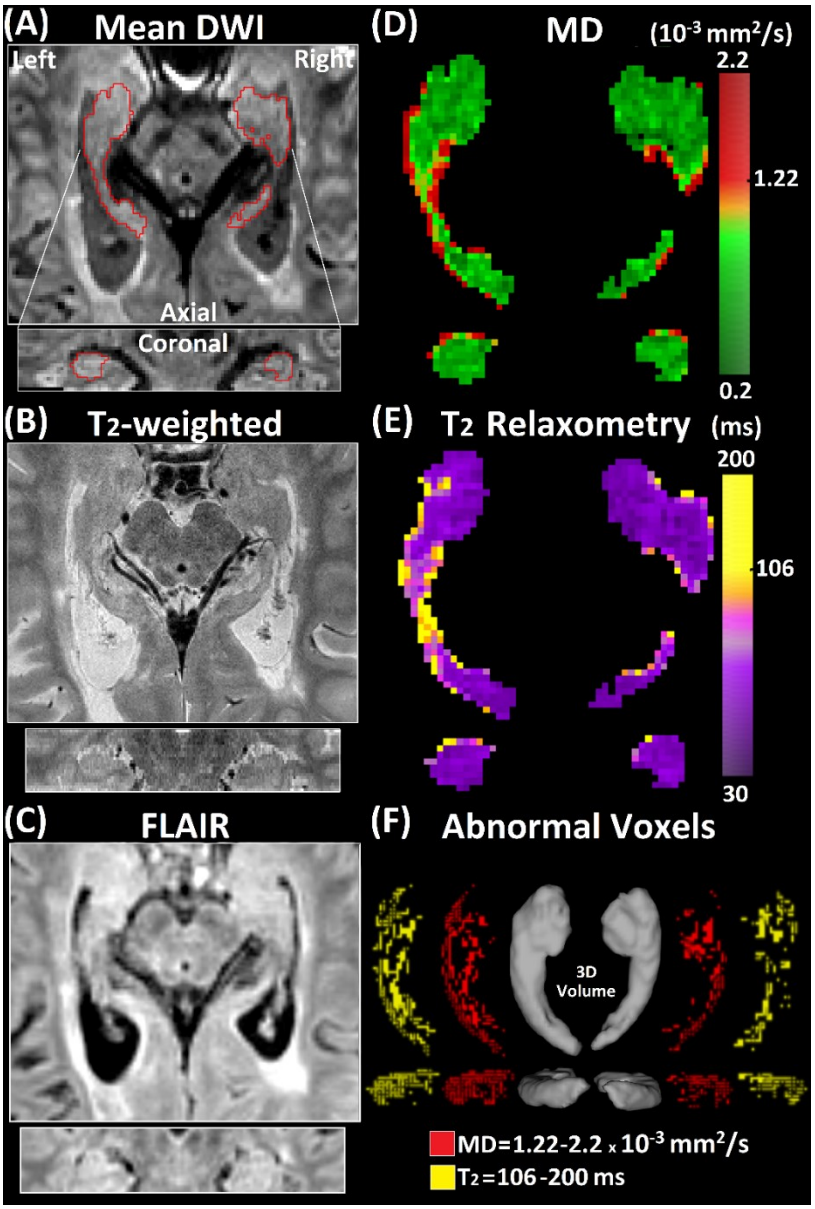

Figure 4.7: Axial-oblique (top) and coronal (bottom) single slice images for (A) mean DWI b=500 s/mm^2, (B) T2-weighted and (C) realigned FLAIR images showing the hippocampus (average left/right total hippocampus volume of 2.7 cm^3) in a 60-year-old female SPMS CI patient (TLV=31.0 cm^3, EDSS=5, onset 21 years). The color-coded hippocampus (D) MD and (E) T2 relaxometry maps from the same slice displayed hyperintense areas that extended mainly across the lateral and medial borders of the CA1 and DG regions areas all over the A-P axis of the hippocampus in this slice. (F) Voxels across all hippocampal slices that are beyond the MD/T2 threshold are projected onto a single plane demonstrating widespread abnormal values mainly in CA1/DG areas along the entire hippocampus A-P axis, which comprised 9% of the hippocampus for both MD and T2 values.

The percentage areas (first row in Figure 4.8), relative to the number of voxels of the total hippocampus, that displayed MD ($p<0.0001$), T2 relaxometry ($p=0.008$), or T2-weighted signal intensity ($p<0.0001$) above the defined thresholds, were greater in the MS cohort when compared to controls. Percentage areas of elevated MD ranged from 1.5-7.6% in the healthy controls and 3.1-12.4% in the MS cohort, with only 2/43 controls displaying areas greater than ~7.3% (2 SD above the control mean group) as opposed to 20/43 MS patients. The percentage area of elevated MD was 1.8 to 1.9 times greater in the not CI and the CI MS groups versus controls (Figure 4.8A), while MD values in those areas were 3.4% higher in the not CI MS and 5% higher in the CI MS group when compared to heathy controls (data not shown). Percentage areas of elevated T2 relaxation times ranged from 2.8-5.9% in the healthy controls and 2.0-12.8% in the MS patients, with none of the 11 controls displaying areas greater than ~6.4% (2 SD above the control mean group) as opposed to 14/42 MS patients. The percentage area of elevated T2 was 1.6 times greater than the controls only in CI MS (Figure 4.8B). Percentage areas of T2-weighted hyperintense signal ranged from 0.6-8.2% in the controls and 1-20% in the MS group, with only 3/43 controls displaying areas greater than ~5.1% (2 SD above the control mean group) versus 8/43 MS patients. The percentage area of elevated T2-weighted signal was 2.2 times greater than the controls only in CI MS (Figure 4.8C).

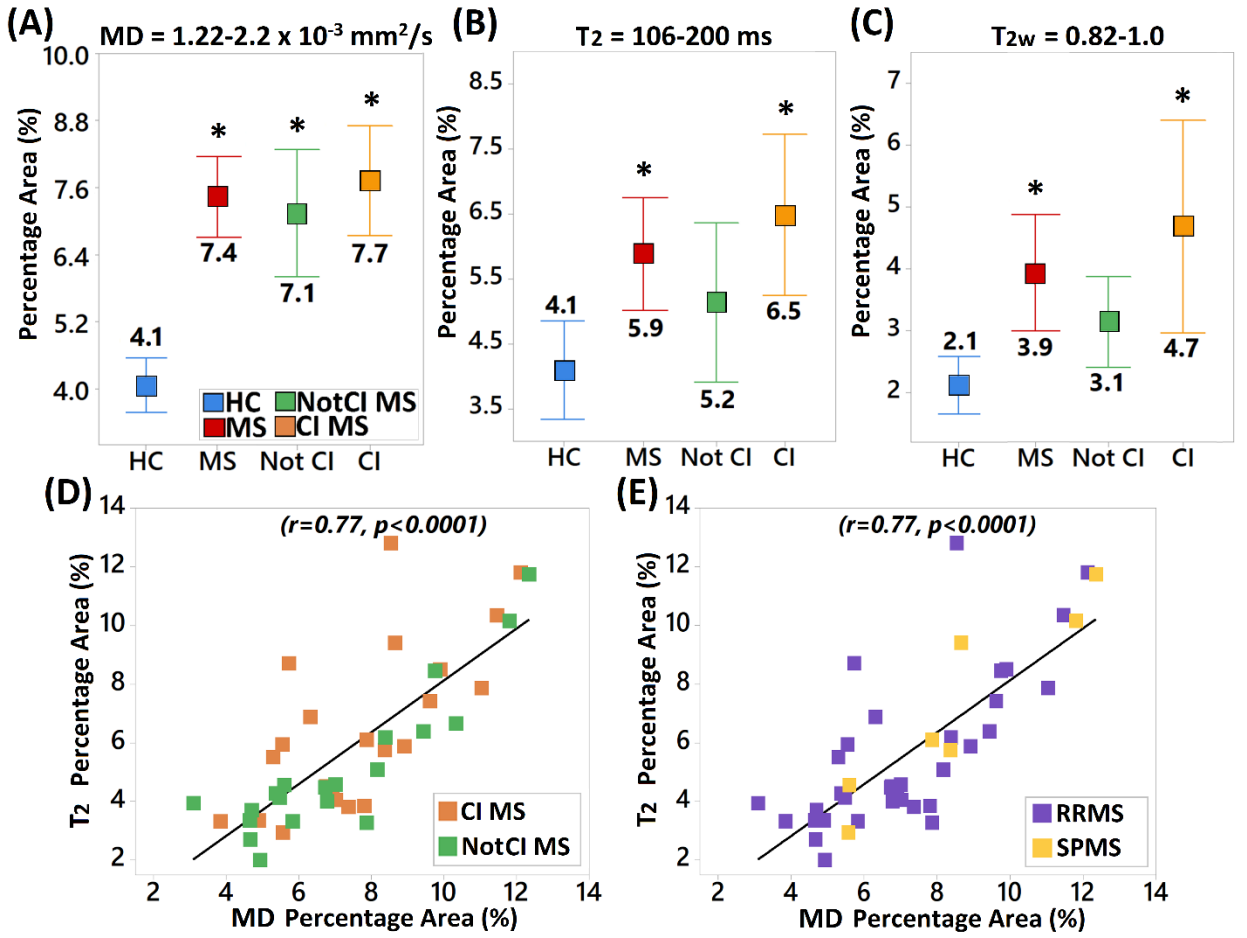

Figure 4.8: The percentage area of the hippocampus that was beyond 2 standard deviations of control values (but below values defined for CSF) for (A) MD, (B) T2 relaxation time, and (C) T2-weighted signal normalized to CSF was 1.8x, 1.4x, and 1.9x greater in the MS cohort than controls (mean and 95% confidence intervals). The CI MS group had on average nearly 8% (range 3.9-12.1%) of the residual hippocampus with elevated MD. The values in these thresholded elevated regions for the MS cohort were MD=1.53 ± 0.05 x 10^{-3} mm^2/s, T2=133.7 ± 2.9 ms, and T2W signal=0.87 ± 0.04. (D-E) The percentage hippocampal area with elevated MD was correlated linearly with the percentage hippocampal area with elevated T2 over all the MS cohort (n=42) – same data but separated into (D) with/without cognitive impairment and (E) RRMS/SPMS.

The percentage hippocampal area with elevated MD strongly correlated with the percentage area with elevated T2 over all the MS cohort (r=0.77, p<0.0001; Figure 8D, E). Notably in these plots

(Figure 4.8D, E), the span of percentage abnormal MD or T2 area did not appear to be dominated by subgroup classification, either cognitive impaired or not MS, or subtype (RRMS vs SPMS). Twelve patients (~29% of the MS cohort) displayed the largest extent of areas of elevated values in both MD/T2 relaxometry analyses (ranging from 6.4-12.4%), with six of these MS subjects shown in Figures 4.3, 4.5, 4.6 and 4.7. Seven of these 12 patients (~58%, 6 RRMS) had cognitive impairment, while six of them (50%, 3 also with cognitive impairment) had high total lesion volume (TLV>10 cm^3), as evident in periventricular areas near the hippocampus (Figures 4.2F, 4.3C, D, 4.6, 4.7). Five of these 12 patients (3 with cognitive impairment) additionally displayed similar extensive areas of elevated values on the T2-weighted signal analysis (ranging from 6.2-7.5%), and 3 of them (one with cognitive impairment) had high TLV.

4.3.5. Whole and Regional Hippocampus MRI Metrics versus Total Lesion Volume and Clinical/Cognitive Scores

Linear correlations of total and regional hippocampus MRI metrics versus TLV, clinical and cognitive scores, and time since MS symptoms onset yielded 13 correlations (6 whole and 7 regional measures) at $p<0.05$ with 7 of these surviving FDR correction at $p\leq0.008$ (Figure 4.9A, B). Of the 13 correlations at $p<0.05$, 5 were with whole brain TLV, 3 with visual memory, 4 with EDSS and 1 with physical fatigue. It is notable that 4 correlations with TLV survived FDR correction with whole hippocampus MD and T2 relaxometry values and greater percentage areas of the hippocampus with regional elevated MD (Figure 4.9C) or T2 values (Figure 4.9D). The T2 relaxometry and the T2-weighted values of thresholded hippocampal regions correlated positively with EDSS (Figure 4.9E, F). Greater levels of physical fatigue (MFIS-Phys) correlated with lower

whole hippocampus FA (Figure 4.9H). It is interesting to note that lower whole hippocampus volumes (Figure 4.9G) and higher whole hippocampus T2-weighted signal ($r=-0.36$, $p=0.018$) and T2-weighted signal values of thresholded hippocampal regions ($r=-0.38$, $p=0.011$) correlated with worse visuospatial working memory, although these correlations were below the FDR correction threshold.

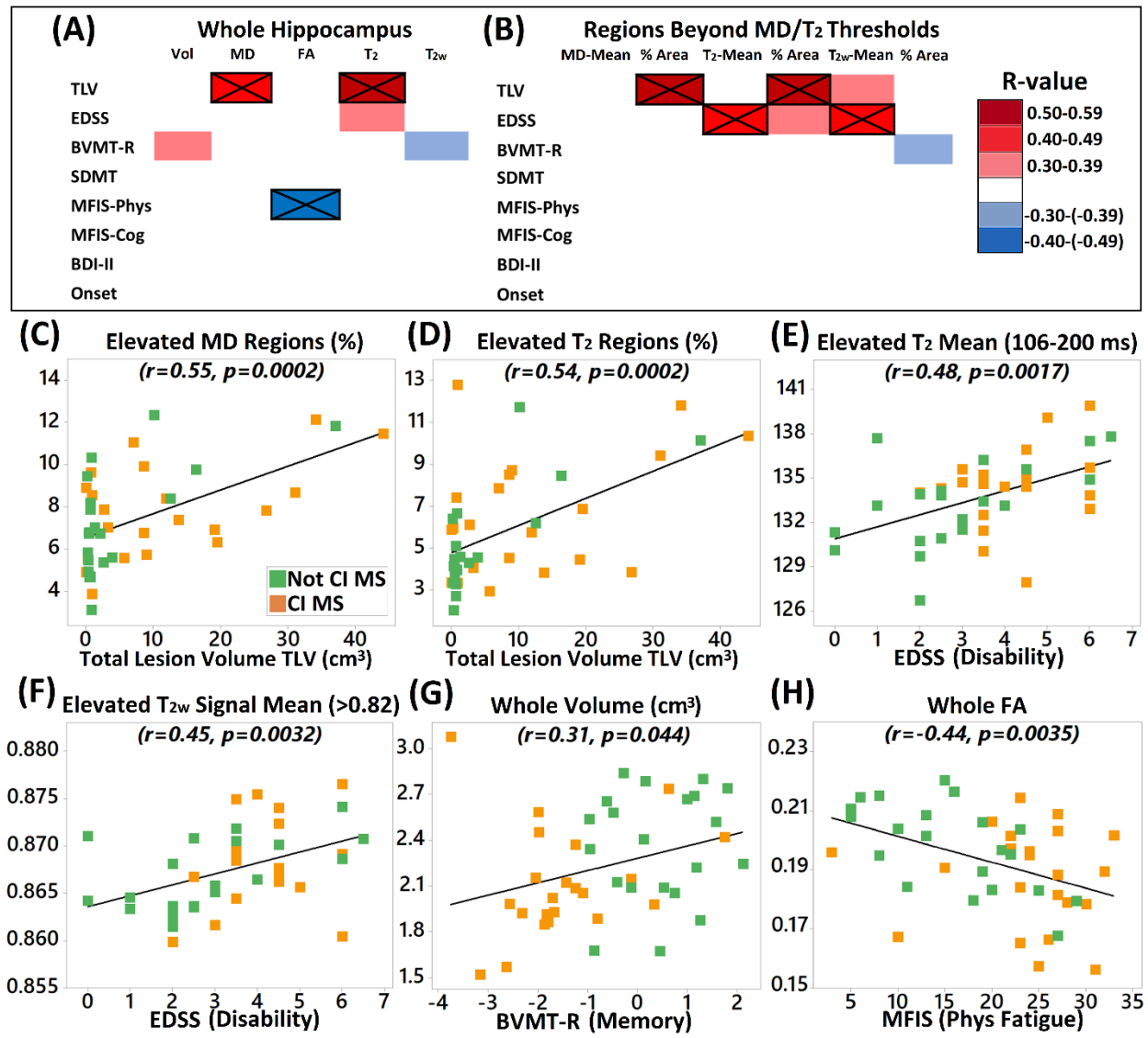

Figure 4.9: Linear correlations ($p<0.05$; X mark indicates FDR corrected at $p<0.008$) between (A) whole and (B) regional hippocampus MRI metrics (left/right averaged) in the entire MS cohort versus total lesion volume (TLV), disability (EDSS), memory (BVMT-R z-scores reflecting visual working memory), information processing speed (SDMT z-scores) and physical (MFIS-Phys) and cognitive fatigue (MFIS-Cog), depression (BDI-II), and time since MS symptoms onset (some example plots in C-H). Greater TLV was correlated with greater percentage areas of elevated (C) MD and (D) T2 values. (E, F) Higher regional T2 relaxometry and T2W signal values in the thresholded regions correlated with greater disability by EDSS. (G) Worse visual working memory correlated with lower whole hippocampus volumes (not FDR corrected). (H) Lower whole hippocampus FA correlated with higher physical fatigue.

4.4. Discussion

Most quantitative MRI studies of MS are on WM, but there is a more recent focus on detecting relevant changes in deep GM, albeit still quite limited in the hippocampus beyond volumetric analyses [278]. Although histopathological studies have demonstrated demyelinating lesions in the hippocampus that are prevalent but quite variable across MS patient's post-mortem [190], [296], [346]–[348], there has been little evidence from in vivo imaging studies. This is partly due to the limited spatial resolution of previous quantitative scans, such as diffusion MRI, but also the poor contrast and small size of GM lesions on typical FLAIR and T2-weighted images, which go frequently undetected [349], with low interobserver agreement for hippocampus lesion scoring, even when applying 3D double inversion recovery (DIR) sequences [350]. This is the first study to apply high resolution (1 mm isotropic) DTI and T2 mapping of the hippocampus in MS which confers five advantages: 1) sufficient spatial resolution to depict regional abnormalities within such a small, convoluted brain structure, 2) yields quantitative diffusion and T2 metrics for unbiased identification of voxels beyond control values (also thresholded out CSF voxels with high MD and T2), 3) manual outlining of the hippocampus and direct diffusion/T2 measurements on the quantitative maps without the need to coregister to anatomical images such as 3D T1-weighted to delineate the hippocampal border, which is commonly done and fraught with potential errors, 4) limits partial volume effects thereby yielding more accurate MRI metrics less biased by atrophy, and 5) provides complementary measures of the underlying microstructure. These methods showed here that the hippocampus is markedly affected in MS, as a whole and with evident regional changes, notably more so in those patients with cognitive impairment (CI).

The core findings on whole hippocampus were that MD was elevated in both CI and not CI MS, but that lower volume and FA and higher T2 relaxation time and normalized T2-weighted signal were different from controls only in the CI MS cohort. Although these MRI metrics are sensitive to neurodegeneration and gliosis [238], this could maybe suggest the greater sensitivity of MD to reflect demyelination (see Table 6.2 in [370] that shows MD elevation in genetic animal models without myelin versus wild type with myelin), while atrophy, FA, and T2 values could be further influenced by additional pathology (e.g., neuronal/axonal loss, inflammatory activity, edema, gliosis), potentially present in some types of MS hippocampal lesions in histology [296], [347]. The 9% reduction of hippocampus volume in the entire MS cohort agrees with the mean from previous volumetric studies [211], [213], [274], [311], [351]–[359]. However, when the MS group was split into CI and not CI, only the CI group yielded a 14% smaller hippocampus, in agreement with earlier work showing its link to cognitive impairment in MS [211], [353], [355], [356], [358], even in the absence of abnormal diffusion metrics in one DTI study [270]. Despite the CI MS group differences above, whole hippocampal volume did not show any FDR-corrected correlations with clinical scores over the entire MS cohort, but there was an uncorrected positive correlation with visual working memory (given by BVMT-R). This aligns with studies implicating whole hippocampus atrophy cross-sectionally [353] and CA1 atrophy longitudinally [356] with worse visual memory.

The high 1 mm spatial resolution and excellent contrast enabled the outlining of the hippocampus directly on the DWI. These manual segmentations on DWI here showed significant group differences whereas automatic segmentations on T1-weighted images previously reported in the

exact same MS cohort were not significant [361]. Automatic volumes always appear to overestimate the hippocampus size relative to manual volumes, partly due to the inclusion of the subiculum in the former [361], [367], [371]. MD and FA measurements were higher and lower, respectively, in the combined MS group compared to controls, confirming previous lower resolution findings where voxel sizes were ~3 to 33 times larger than what was acquired here [213], [313], [329], [361].

New to the study of MS was the high resolution quantitative T2 relaxometry (1.2 mm^3 voxel volume) and T2-weighted signal (0.25 mm^3 voxel volume) measurements of whole hippocampus that showed T2 relaxation time and T2-weighted signal elevations in CI MS, but not in not CI MS, relative to controls. This is consistent with a positron emission tomography study of the hippocampus in MS that showed links of elevated hippocampal neuroinflammation and microglial activation in MS patients with depression [372]; notably depression is higher in our CI MS cohort. Whole hippocampus MD and T2 were positively correlated with total lesion volume (TLV) throughout the brain, which suggests a relationship between retrograde/anterograde degeneration affecting interconnected WM pathways and hippocampus microstructural injury [342], whereas macroscopic hippocampal volume did not correlate with TLV. The correlation between whole hippocampus lower FA and greater fatigue matched our earlier finding in this cohort using a different FLAIR-DTI protocol with lower spatial resolution but with CSF suppression [361]. This is also consistent with a volumetric study reporting a link between sustained fatigue and hippocampus/striatal/deep GM atrophy in MS [335] and supports the involvement of the basal ganglia and deep GM networks in the pathogenesis of fatigue in MS [373]–[375].

Regional analyses revealed that on average ~4-7% of the residual hippocampus in MS had voxels with elevated MD, T2 relaxation time, and T2-weighted signal values (beyond 2 SD of control values); 4-7% translates to a mean of ~90-160 mm^3 volume. These results mirrored the whole hippocampus findings where the mean MD was similar between CI and not CI MS whereas mean T2 relaxometry was only greater in CI MS. Notably, the hippocampal area with abnormal MD correlated highly with the abnormal area identified on T2 and had a large range of ~2-13%, but there was no evident relationship with MS subtype (CI vs not CI or RRMS vs SPMS). Pathology studies have demonstrated demyelination to various degrees from small punctate lesions to nearly the entire hippocampus in 63/101 or 62% of MS patients over four separate papers [190], [296], [347], [348]. Most studies don't report the volumes of the demyelinated region, but one identified a percentage area of demyelination of ~30%, albeit with a huge range of 2-95%, of the hippocampus (excluding subiculum and fimbria) with 1-4 lesions per case in 45 progressive MS patients (note: they also reported that the gross hippocampus cross-sectional area was 22% smaller) [347]. DIR MRI (1.3 x 1.2 x 1.2 mm^3 resolution in 10 min at 1.5T) that nulls CSF and WM is more sensitive to GM lesions than other contrast like T2-weighting and has also shown hippocampal lesions in 14/16 MS patients with ~3 lesions per patient (note: the hippocampal lesion volume was not reported) [350]. DIR has also identified demyelinating lesions in the hippocampus as the region most affected in RRMS with concurrent epileptic seizures [376]. DIR was not acquired here, but it should be compared in future to our high resolution DTI and T2 mapping.

Elevated MD and T2 areas from regional analyses within the hippocampus were reported in 47% and 33% MS participants, respectively. These areas were greater in several patients with higher

TLV, such as in periventricular locations, and were more frequent in CI MS patients (60-64%). The percentage area of MD and T2 relaxometry elevations correlated positively with TLV reflecting a link between the degree of whole brain pathology and that observed in the hippocampus. However, pathological studies have yielded a higher incidence of demyelinated lesions from 53 to 80% of the MS cohorts [190], [296], [347], [348] although one of these studies included 14/37 lesions in close proximity to the hippocampus but not in the structure as such [190]. The lower incidence of MD/T2 elevations and the limited area affected in our study could be due to the fact that by definition histopathological studies are of deceased patients, as opposed to our in vivo MRI study. These histopathological studies were mainly on fully progressive MS cohorts with a mean age of 58-66 years and mean disease duration 18-28 years, and mean EDSS scores of 8.5 in one study [296] and EDSS above 7 in other study [347], as opposed to mainly RRMS patients here (35 RRMS and 8 SPMS) that were 10 years younger, with lower mean disease duration of 16 years, and with EDSS scores≤6.5 with a mean of 3.5. However, the DIR MRI study where 88% of MS patients had hippocampal lesions were composed of 11 RRMS and 5 PPMS patients with younger age ~40 years and shorter disease duration of 10 years [350].

The histopathological studies in post-mortem MS brain have identified lesions all throughout the hippocampus but more frequently in the CA1 and DG subfields locations [190], [296], [347], [348], which agrees with the regions observed here with elevated MD or T2. The lesions often extended from the hippocampus to adjacent WM and GM or were smaller and confined within the hippocampus. CA1 and DG damage appears to emanate from interfaces with CSF which supports the CSF humoral factor hypothesis of subpial cortical demyelination [347], [377], as these areas

are respectively lined by ependyma and pia matter. While demyelination seemed to be the main lesion pathology in histology [190], [296], [347], [348], some mild inflammatory activity was also observed in the boundaries of both hippocampal-perihippocampal lesions [190] and in a number of lesions in the alveus/fimbria and perforant pathway in the SLM together with axonal loss [347]. It is probable that demyelination and increased water content due to vasogenic edema increase the MD and T2 relaxation times in the regions that were often seen as a bright rim or pockets extending from perihippocampal/periventricular lesion areas and CSF in our study here. A decrease in neuronal density/count by 10-30% could also increase MD/T2 [296], [347]. A reduced density of synaptic terminals mainly in the DG and CA1 in demyelinated versus myelinated hippocampi and gene expression profile changes associated with hippocampal demyelination that negatively impacts axonal transport, synaptic integrity, glutamate homeostasis, synaptic plasticity and memory/learning have also been reported with histology in progressive MS [296].

Neuronal degeneration caused by axonal transection due to lesions in the fornix, which is the major efferent WM pathway from the hippocampus, could also trigger diffuse neuronal loss in the hippocampus. A previous CSF suppressed DTI study in the same MS cohort reported marked fornix atrophy (~26%) and microstructural diffusion abnormalities (6-12%) in MS which were greater in the CI group and correlated with hippocampus volume, diffusion and T2 relaxometry abnormalities reported here (not shown) [361]. As the extent of fornix atrophy and diffusion abnormalities are greater than hippocampus atrophy, diffusion and T2 relaxometry differences when compared to controls in this MS cohort, we hypothesize that fornix injury could be inducing hippocampus damage here.

There were several limitations of this study. First, our patients did not have DIR sequences, and thus hippocampal lesions may have been missed in the T2-weighted and FLAIR scans. Second, T2 multi-echo spin echo sequences were only acquired in 11/43 controls, which could decrease the statistical power of the T2 mapping group analysis. Third, our MS cohort was mainly RRMS and had only a small representation of progressive MS phenotypes (8 SPMS) which should be addressed in the future particularly given that all MS hippocampus pathology studies of demyelinated regions were nearly exclusively on progressive MS [190], [296], [347], [348]. Fourth, the diffusion and T2 metrics were not measured in subfields, but this could be an avenue of future study, although that is more suited for the hippocampal body than the head or tail (see Figure 7 in [136]). Fifth, it is possible that some of the MD/T2 findings are due to CSF partial volume as a result of greater atrophy, but this is unlikely since stringent MD/T2 thresholds were used to remove voxels attributed to CSF. Sixth, left and right hippocampal metrics were averaged together to minimize the already large number of comparisons. Separate left and right analyses showed similar findings (data not shown) and most previous studies have shown similar left and right atrophy in MS [213], [352], [355] or have analyzed left and right metrics together [211], [274], [311], [354], [357], including DTI studies [270], [313], [329], [361]. Seventh, our MS study was cross-sectional and as such there was a fair amount of inter-subject variability. Longitudinal studies have shown ~6-7% reductions of hippocampus whole volume over 1 year in PPMS [378] and CIS [356]. Eighth, the DTI model was used here since the acquisition included only one low b-value shell of 500 s/mm^2 with 10 directions (and 10 averages), chosen to minimize signal loss given the high 1 mm isotropic resolution; note this protocols works well for DTI of the

hippocampus as shown in our original paper [136], as well as its application to healthy development [367] and temporal lobe epilepsy [362]. Future studies could attempt multi-shell, higher b-value acquisitions albeit challenging at 1 mm resolution while maintaining a clinically friendly scan time like the 5.5 min used in the current study. In summary high resolution DTI and T2 mapping identified hippocampal abnormalities, whole and regional, in vivo that are related to cognitive and clinical impairment in MS.

5. Multidimensional/b-Tensor Diffusion MRI to Evaluate Microscopic Anisotropy and Diffusional Variance Heterogeneity in Multiple Sclerosis

Abstract

Multiple sclerosis (MS) lesions and additional microstructural damage in normal appearing white matter (NAWM) have been previously detected with diffusion tensor imaging (DTI). DTI metrics such as fractional anisotropy (FA) are sensitive to demyelination, axonal degeneration, and other pathologies triggering MS damage, but are also susceptible to various white matter (WM) tissue characteristics and fiber orientation dispersion. This lack of specificity confounds the pathological interpretation in complex WM fiber arrangements which have previously shown inconsistent FA results. Novel b-tensor encoding strategies for diffusion MRI, which utilize the signals prepared with directional and isotropic diffusion encoding respectively achieved with standard pulse sequences and with magic angle spinning of the q-vector, are capable to discriminate tissue micro- from macrostructure by yielding diffusion metrics unbiased by regional variations within a voxel. Specifically, a diffusional variance decomposition (DIVIDE) method that takes advantage of b-tensor encoding strategies can disentangle the effects of microscopic diffusion anisotropy from the orientation dispersion, as well as the diffusional heterogeneity that originates from isotropic and anisotropic tissue structures. DIVIDE can yield novel diffusion metrics such as microscopic FA (μFA), analogous to FA without the confound of orientation dispersion, and the anisotropic (MK_a) and isotropic (MK_i) diffusional variances or mean kurtosis, which are tentatively linked to cell eccentricity and density. The goal here was to evaluate diffusion metrics (both DTI and DIVIDE) in a cohort of 43 MS participants and 15 healthy controls with b-tensor diffusion MRI. Diffusion

metrics were calculated in regions of interests that included: MS lesions identified on FLAIR, total WM volume (excluding lesions for MS patients) segmented on MPRAGE, both of which were coregistered to diffusion scans and eroded, as well as four normal appearing WM (NAWM) areas with diverse fiber orientation and lesion incidence outlined in the first eigenvector FA map (splenium of the corpus callosum, bilateral posterior limb of the internal capsula, periventricular anterior crossing WM, superior corona radiata). Their correlations were assessed versus total lesion volume and clinical parameters. All diffusion metrics showed differences between lesion and total WM in MS and controls, as well as in the coherent NAWM in the splenium of the corpus callosum. However, DTI and b-tensor yielded different results in crossing NAWM regions, wherein FA did not change but MK_a and μFA were lower in MS versus controls. DTI and b-tensor metrics in MS lesions and several brain areas displayed correlations with total lesion volume, and MK_a within MS lesions positively correlated with better arm and hand dexterity. When compared to DTI, b-tensor metrics overall improved the qualitative and quantitative evaluation of lesions in MS although their utility was limited in this study due to lower spatial resolution precluding a more accurate total NAWM group assessment. Furthermore, MK_a and μFA seemed to have added value as they could depict group differences in discrete crossing fiber regions where standard FA showed no changes.

5.1. Introduction

MS is an autoimmune neurological disorder with inflammation and demyelination as its key pathologic markers [206]. MS is mainly characterized by focal WM lesions, followed by further NAWM damage as the disease progresses [185]. Conventional MRI, due to its sensitivity to visualize WM lesions, has been widely used for detecting and monitoring MS evolution, however it lacks specificity to quantify and to understand the microstructural pathological mechanisms of the disease, fundamentally outside WM plaques [379]–[381]. Over the last two decades, DTI, a quantitative MRI method which surveys tissue microstructure by measuring the Gaussian approximation of water diffusion, has been regularly applied in NAWM in MS [120], [255], [258], [281], [286], [328], [382], [383]. DTI yields macroscopic diffusion parameters for each voxel under study [98], [119], such as FA (unitless) which describes the degree of anisotropy of the diffusion tensor, and MD (mm^2/s) which depicts the average voxel diffusivity in all directions. These DTI parameters are determined in most previous work by applying single diffusion encoding (SDE) sequences [100]. High FA values result from microscopic sources of diffusion anisotropy, but only if there is also macroscopic coherent orientation of the structures within a voxel [99] because it is sensitive to other factors such as their orientation coherence [98], [124] and calculated under the assumption of gaussian WM diffusion [124], [276]. Like all DTI metrics, FA arises from macroscopic voxels, and it is not able to disentangle axon integrity/loss from changes in fiber coherence and crossing, both of which cause similarly lower apparent diffusion anisotropy [130], [170], [384].

In neurodegenerative diseases such as MS, FA changes can indeed come from any of these above mentioned sources but can also be interpreted as several pathological mechanisms [122], [276] which add more uncertainty when analyzing crossing or fanning fiber environments with one or more fiber bundles either being degenerated or displaying WM hyperintense lesions, as described in Figure 1 of [172]. Subsequently, DTI tractography, Tract-based spatial statistics (TBSS) or region of interest (ROI) DTI results are inconclusive, reporting mainly lower FA and higher MD throughout brain WM in different MS phenotypes [255], [258], [280], [281], [286], [312], [361] but also higher FA in some NAWM tracts [280], [281], or no regional FA differences versus controls [312], [385], [386].

The relationship between diffusion MRI metrics and tissue microstructure has been previously studied with complex diffusion encoding pulse sequences and brain data modelling. Advanced techniques beyond DTI such as High Angular Resolution Diffusion Imaging (HARDI) [150], [387] and Diffusion kurtosis imaging (DKI) [152], both based on SDE acquisitions, can identify subtle tissue changes [388], [389] by applying biophysical models based on non-Gaussian water diffusion, a high number of gradient diffusion directions and higher b-values. However, they are still unable to fully disentangle the factors causing those changes as they cannot separate size, shape nor orientation variation of the diffusion microenvironments within a voxel without prior tissue information [390], [391]. Several b-tensor diffusion encoding approaches have been further developed with the aim to discriminate these tissue microenvironments by separating microscopic anisotropy from isotropic heterogeneity [163], [164], [170], [392], [393]. These alternative encoding methods reveal additional microstructural information by modifying the shape of the b-

tensor before the image readout with, for example, multiple pairs of pulsed field gradients, where each pair performs a measurement in a certain direction [162], [392], [394], or by applying time-varying gradients that are not pulsed, such as oscillating gradients [395]. There are such approaches based on double diffusion encoding (DDE) pulse sequences [162], [170], [392], [396] that enable linear (LTE) and planar tensor encoding, and on isotropic time-varying diffusion encoding gradient waveforms (as opposed to typical trapezoid gradients) [164], [169], [393], such as q-space trajectory encoding (QTI) [160]. The latter allows several b-tensor shapes such as linear and spherical tensor encoding (STE), as well as prolate and oblate encoding. These methods allow for the calculation of invariant microscopic diffusion parameters by diffusion tensor distribution (DTD) data models based on the previously mentioned encoding trajectories [397], [398]. One of these proposed DTD frameworks, namely the diffusional variance decomposition (DIVIDE) [161], can disentangle the isotropic (MK_i) and anisotropic (MK_a) components of the total diffusional variance (MK_t), which is equivalent to the mean kurtosis (MK) from DKI [152], and estimate novel microscopic diffusion metrics. These include the MK_i and MK_a contributions of the diffusional variance that appear to be respectively related with cell density variance and cell eccentricity [161], as well as the microscopic fractional anisotropy (μFA) which is indicative of the microscopic diffusion anisotropy, independent from the orientation coherence [163], [169]. These b-tensor diffusion encoding approaches are technically demanding of the gradient system but are feasible on clinical MRI systems [166] and have been successfully applied to the study of healthy subjects [161], [169], brain tumor discrimination [161], [169], breast cancer [399], and WM age related lesions in elderly healthy subjects and patients with Parkinson's disease [400].

Additionally, two previous diffusion studies [162], [172] have also applied different b-tensor encoding strategies in MS, nominally DDE [162] and LTE/STE (based on QTI) [172], to assess microscopic diffusion anisotropy in lesions [162], NAWM, and several WM ROIs with μFA (corpus callosum, internal capsula, centrum semi-ovale and frontal subcortical WM in [162]; corticospinal tract, superior longitudinal fasciculus and cingulum in [172]) and GM (thalamus and putamen in [162]). When DDE was applied with 3 mm isotropic voxel resolution in a small sample of 6 RRMS and 8 controls [162], μFA showed group differences only for the T1-hypointense and T2-hyperintense lesions, but not for the NAWM, or any WM or GM ROIs; while FA calculated from DTI at a higher 2 mm isotropic resolution displayed NAWM group differences but only T1-hypointense lesion group differences. The LTE/STE study [172] was acquired with 2.5 mm isotropic voxels in a bigger sample of 26 RRMS, 14 PPMS and 27 controls although only in a NAWM slab (36.3 mm) covering the corpus callosum where lesions typically are to be found. This latter work reported NAWM differences between MS and controls with μFA as well as correlations between higher total lesion load, higher disability, and slower information processing speed with lower μFA. However, no group μFA differences were reported for discrete WM ROIs, only FA for the corticospinal tract.

The purpose of this tensor-valued diffusion MS study was to (a) apply an optimized QTI whole brain protocol and corresponding DIVIDE analysis on a group of MS participants and healthy controls, (b) demonstrate the efficacy of this method to improve the measurement specificity of tissue microstructure in MS lesions, NAWM, healthy WM, and different WM fiber configurations in both healthy and MS cohorts, and (c) assess the relationships of the aforementioned measures

with total lesion volume, and overall disability, motor, dexterity and cognitive functions affected in MS, as well as depression, fatigue, and time since disease onset.

5.2. Methods

5.2.1. Participants

This study involved 43 participants diagnosed with MS (35 relapsing-remitting MS – RRMS, 8 secondary progressive MS – SPMS; the same as in Chapters 3 and 4) and 15 healthy controls with no neurological/psychiatric disorders or brain injury. MS participants had no history of clinically documented relapse or a high dose steroid treatment in a year prior to MRI scan, and they were recruited from the University of Alberta MS Clinic. Healthy controls were recruited by online and on-campus advertising. All participants provided written informed consent and the study was approved by the University of Alberta Human Research Ethics Board. The demographic and clinical data are summarized in Table 5.1 in the Results.

5.2.2. Cognitive Assessment

Clinical and cognitive tests were administered to the MS participants by a trained user (DVC) to evaluate global disability, memory, fatigue, depression, leg function/ambulation, and arm/hand function (Table 5.1). The tests consisted of Kurtzke Expanded Disability Status Scale (EDSS) for overall disability in MS; Brief Visual Memory Test Revised (BVMT-R) for visuospatial learning and memory (Total Recall scores only); Symbol Digit Modalities Test (SDMT) for information processing speed and visual scanning/learning; Modified Fatigue Impact Scale (MFIS) for effects of fatigue in terms of physical and cognitive functioning; Beck Depression Inventory-II

(BDI-II) for depression; Timed 25-Foot Walk (T25-FW) for quantitative mobility and leg function performance; 9-Hole Peg Test (9-HPT) as a quantitative measure of arm and hand function.

5.2.3. MRI Protocol

Three different protocols with whole brain coverage were acquired on a 3 T Siemens Prisma (80 mT/m gradient strength per axis) and a 64-channel Head/Neck RF coil:

(i) 3D T1-weighted Magnetization-prepared rapid acquisition with gradient echo (MPRAGE) with field of view (FOV) 250×250 mm^2, 0.85 mm isotropic voxels, TR=1800 ms, TE=2.37 ms, scan time of 3:39 minutes (Figure 5.1A) for total WM segmentation, improving lesion conspicuity and ROI selection;

(ii) 3D Sampling Perfection with Application optimized Contrasts using different flip angle Evolution (SPACE) Fluid-attenuated inversion recovery (FLAIR) was performed with FOV 230×230 mm^2, 1.2 mm isotropic voxels, TR=5000 ms, TE=385 ms, TI=1800 ms, scan time of 3:07 minutes (Figure 5.1B) for WM lesion segmentation (FLAIR was not acquired in one RRMS participant);

(iii) Tensor-valued diffusion MRI [166] (see Figure 1.15B, C in the Introduction section): used a prototype echo-planar imaging sequence with 40 3 mm slices, 2×2 mm^2 resolution, GRAPPA R=2, TR=4300 ms, TE=89 ms, A-P phase encoding directions and total scan time of 6:36 minutes to yield the diffusion metrics. The STE (Figure 1.15B) was acquired with custom asymmetric gradient waveforms using isotropic diffusion encoding based on the magic angle spinning of the q-vector (qMAS) [160],

[164] and 6 averages each of b=100, 500, 1000, 1500, 2000 s/mm^2. The LTE (Figure 1.15C) used the gradient shape corresponding to the x-direction of the STE, with 6 directions at b=100 s/mm^2, 12 directions at b=1000 s/mm^2 and 22 directions at b=2000 s/mm^2.

(iv)

5.2.5. Structural MRI Postprocessing

Total WM volumes from MPRAGE (segmented with volBrain) and total lesion volumes (TLV) from FLAIR (Table 5.1) were taken from Chapter 3. For each subject, MPRAGE and its volBrain segmented WM regions, and FLAIR and its derived binarized WM lesions were manually aligned to μFA maps in ITK-SNAP (v3.8.0) [320] and then registered with an affine transformation model by using mutual information. For each MS participant, ROIs for NAWM were calculated by subtracting the WM lesion maps from the total WM. WM lesions, NAWM, and WM ROIs were resliced to the diffusion image space and eroded by one voxel to reduce partial volume effects with adjacent CSF, WM lesions and/or GM voxels. Lesions that did not survive the eroding process (at least one lesion voxel) were not included in the total lesion metrics to avoid inaccurate results due to partial volume effects. Three RRMS participants with very small lesions and low TLV (< 0.15 cm^3) were excluded from the lesion analysis

5.2.6. b-tensor Diffusion MRI Postprocessing and ROI Selection

Diffusion MRI data were corrected for motion and eddy currents in Elastix [134] with reference volumes extrapolated from low b-value images [401] and smoothed with a Gaussian filter (1.18

mm FWHM, σ=0.5 voxels). The average diffusion tensor and the tensor covariance were fitted to the data with linear least squares fitting and corrected for heteroscedasticity [384]. A covariance DTD model for QTI data analysis [160] available in the Multidimensional Diffusion MRI toolbox (https://github.com/lubosvojtisek/markus-nilssonmd-dmri) [397] was utilized to yield standard diffusion parameters (MD, FA) and μFA, MK_a, MK_i, and MK_t maps.

All the diffusion metrics of MS patients and healthy controls were assessed in the above-mentioned total WM lesions and NAWM in MS patients and total WM ROIs in controls, as well as in four 2D axial WM ROIs enclosing different complexity in brain tissue microstructure, which were manually delineated on the first eigenvector FA (FEFA) maps. Two of the latter ROIs were axially positioned at the midline on the splenium of the corpus callosum and the bilateral posterior limb of the internal capsula as instances of straight coherent WM with similar axon sizes [402] but different degrees of MS lesion incidence (the corpus callosum has the highest incidence). One bilateral ROI was placed on the anterior crossing WM adjacent to the lateral ventricles (at least one voxel from the lateral ventricles to avoid partial volume effects with CSF) where the frontal fibers from the genu of the corpus callosum and the anterior corona radiata intersect. Another bilateral ROI was located on the fanning WM enclosing the superior area of the corona radiata at the level of the centrum semiovale. All ROIs were placed in comparable slices for each subject, showing the largest portion of the selected areas. Voxels displaying FLAIR hyperintense, or T1-weighted hypointense MS lesions were excluded from the WM ROIs outlined on the FEFA maps, as well as all peripheral voxels within the ROIs showing potential partial volume effects with CSF

(MD threshold of 2.2×10^{-3} mm^2/s). When applicable, left and right ROI metrics per structure were averaged bilaterally to reduce multiple comparisons.

5.2.7. Statistical Analysis

MD, FA, μFA, MK_a, MK_i, and MK_t between lesions and total NAWM of MS patients were compared with paired t-tests by using Minitab v20. Two-sample t-tests were performed to compare lesions in MS vs total WM in controls, total NAWM in MS vs total WM in controls, as well as the four WM regions with different fiber configurations and lesion incidence between MS and controls. Pearson correlations between diffusion metrics and age were calculated separately for the MS and healthy cohorts and scatterplots were visually assessed. If correlations were significant between any diffusion metric and age for both cohorts, stepwise linear regression analyses were performed with age as a continuous predictor, group type as a categorical predictor and an interaction effect between age and group type to test whether these metrics differed between controls and MS or if there were interaction effects versus age in these cohorts. Pearson correlations, age-corrected for any metric that displayed age correlations, were calculated between all diffusion metrics and total lesion volume, EDSS, BVMT-R, SDMT (age corrected z-scores), MFIS (physical, cognitive), BDI-II, T25-FW, and 9-HPT to assess microstructural relationships with disability, cognition, fatigue, depression, and upper/lower limb mobility in the full MS cohort. T-tests ($p \leq 0.01$) and Pearson correlations ($p \leq 0.017$) were corrected for multiple comparisons by using the Benjamini–Hochberg false discovery rate (FDR-BH) method with an in-house written script (MatLab R2020b).

5.3. Results

5.3.1. MS Subgroup Demographics

The control group and the full MS cohort did not show any sex (p=0.51) differences with 73%(controls) and 81%(MS) females, or age (p=0.97) differences with controls covering 24-70 years and the MS group 32-71 years. All demographics are shown in Table 5.1 below.

Table 5.1: Demographics for controls and the full MS cohort with mean ± SD and range in brackets when applicable (*p≤0.05 for differences between groups).

	Controls (n=15)	***MS cohort (n=43)***
Sex (M/F)	4/11	8/35
Age (years)	48 ± 14 (24-70)	48 ± 10 (32-71)
WM+GM (cm^3)	1230 ± 125	1143 ± 127*
Total lesion volume (cm^3)	-	7.9 ± 11.4 (0.03-44.2)
Time since onset (years)	-	16 ± 10 (1-41)
EDSS[a]	-	3.5 ± 2 (0-6.5)
BVMT-R (total recall)	-	21 ± 7 (8-35)
SDMT (z-scores)	-	-0.80 ± 1.4 ((-3.33)-2.22)
MFIS (physical)	-	20 ± 8 (3-33)
MFIS (cognitive)	-	19 ± 9 (1-40)
BDI-II	-	13 ± 9 (1-41)
T25-FW (secs)[b]	-	6.81 ± 2.94 (4.01-18.19)
9-HPT[c]	-	0.042 ± 0.011 (0.024-0.066)

[a] EDSS was not obtained in two RRMS participants.
[b] T25-FW was not obtained in four RRMS and in three SPMS participants.
[c] 9-HPT was not obtained in four RRMS and in two SPMS participants.

5.3.2. Qualitative Evaluation of Diffusion Metrics Changes in WM Lesions, Total NAWM in MS Patients and Total WM in Healthy Controls

Example MPRAGE, FLAIR, and diffusion images/maps for a younger RRMS male participant and an elder SPMS female participant both displaying different loads of the typical periventricular MS lesion are shown in Figure 5.1 and 5.2, respectively. In our MS cohort, most of the large WM lesions appeared consistently hyperintense on FLAIR (Figure 5.1B, Figure 5.2B) and on the MD maps (Figure 5.1C, Figure 5.2C) and they corresponded to T1 "black holes" (Figure 5.1A) or hypointensities mainly on μFA, MK_a, and MK_t (Figure 5.1E, F, H; Figure 5.2E, F, H). The pattern and range of hypointensities in the μFA, MK_a and MK_t maps more accurately mirrored the lesion distribution on FLAIR when compared to FA (Figure 5.1D, Figure 5.2D). MK_i didn't display any apparently 'high' hyperintensities associated with greater isotropic variance, which reflects its specific sensitivity to interfaces between brain matter and CSF due to partial volume effects. However, in the SPMS subject the intensity values within the posterior periventricular lesions in the MK_i map appeared similar in value to the CSF areas and to the hypointensities displayed in the MK_a map within the same lesions (Figure 5.2). In regions with crossing WM fibers, FA intensity variations (e.g., left posterior crossing WM lesion versus contralateral 'normal appearing' crossing WM in Figure 5.1, and posterior crossing WM lesions versus anterior 'normal appearing' crossing WM partially mixed with smaller lesions in Figure 5.2) were more difficult to depict and interpret as FA hypointense values may be caused not only by lesions but also by contributions from different crossing fiber populations.

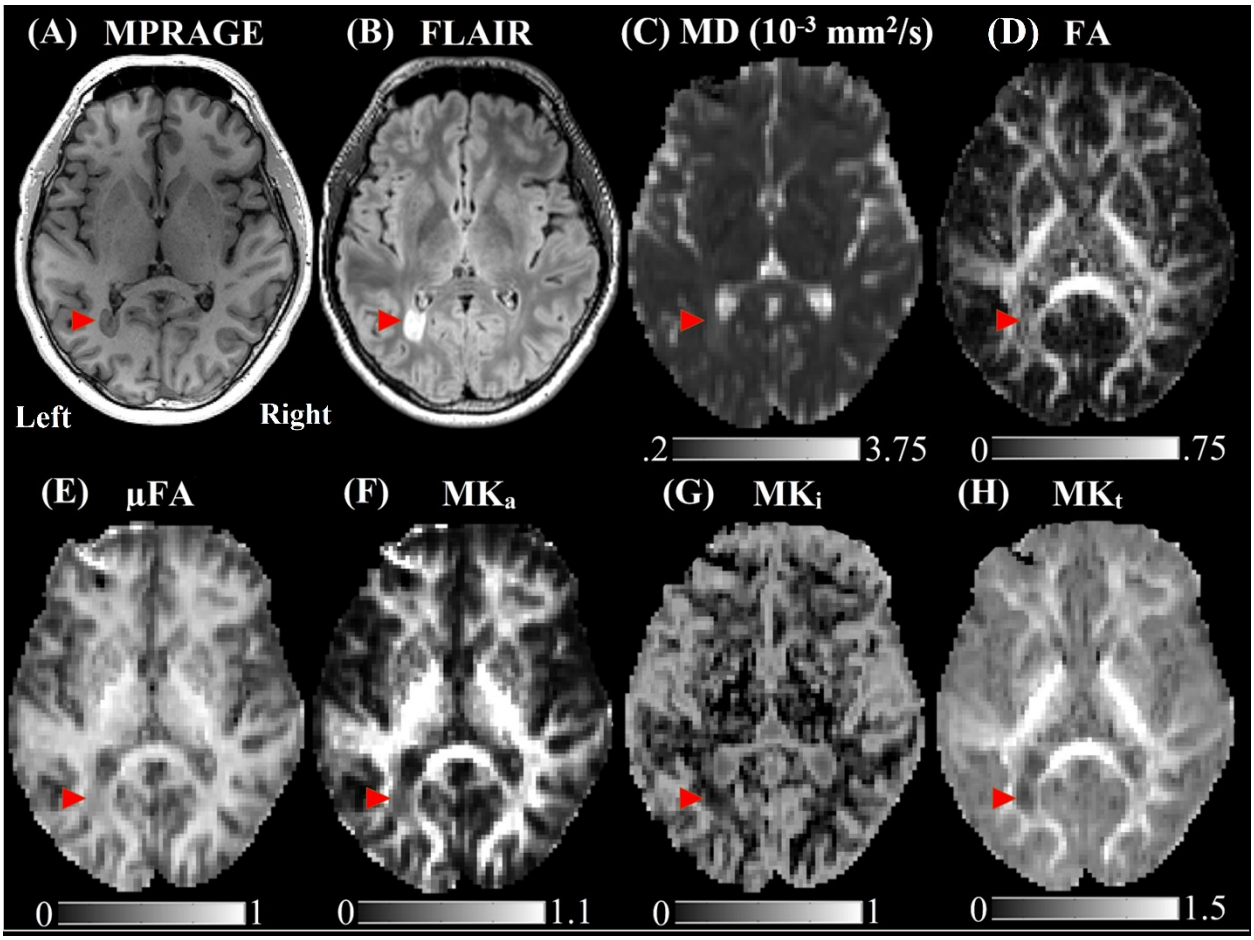

Figure 5.1: Axial (A) MPRAGE, (B) FLAIR, (C, D) DTI and (E-H) DIVIDE diffusion maps in a 38-year-old RRMS male (EDSS 2.0, total lesion volume - TLV=3.3 cm^3). Note the T1 hypointense/FLAIR hyperintense lesion next to the posterior left ventricle horn (red arrowheads), which is hyperintense in MD and clearly hypointense in µFA, MK_a and MK_t maps. This lesion was not evident in FA, when compared to contralateral 'normal appearing' crossing WM, due to the contribution of different crossing fiber populations to the calculation of this metric.

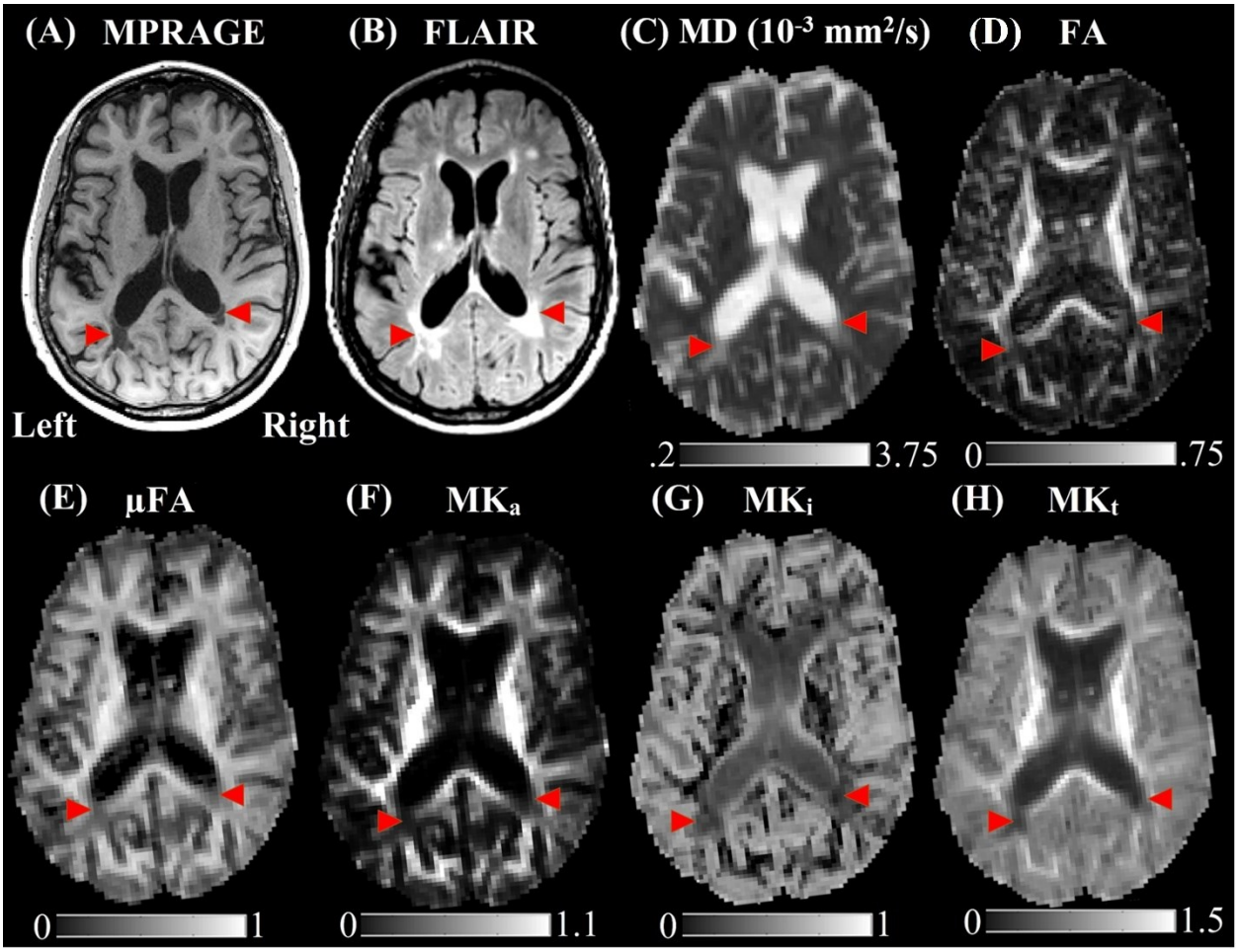

Figure 5.2: Axial (A) MPRAGE, (B) FLAIR, (C, D) DTI and (E-H) DIVIDE diffusion maps in a 60-year-old SPMS female (EDSS 5.0, TLV=31.0 cm^3). Note the large T1 hypointense/FLAIR hyperintense bilateral lesions next to the posterior left ventricle horn (red arrowheads), which are hyperintense in MD and clearly hypointense in µFA, MK_a and MK_t maps. These lesions were not as evident in FA, when compared to contralateral 'normal appearing' crossing WM, due to the contribution of different crossing fiber populations to the calculation of this metric.

From the LTE signal decay analysis, lesions (Figure 5.3A) appeared to have a lower normalized diffusional variance (MK_t), when compared to NAWM (Figure 5.3B) or to WM (Figure 5.3C). By adding the isotropic STE, the proper microstructural features could be differentiated in terms of isotropic and anisotropic microenvironments. In the MS lesions, almost half of the diffusional

variance came from MK_i, which seemed higher in lesions when assessed in NAWM and WM. The remaining diffusional variance within the MS lesions resulted from MK_a values comparable to MK_i, which seemed lower in lesions when compared to NAWM and WM. These two isotropic and anisotropic variance contributions made up for the overall apparently higher MK_t in both NAWM and WM when compared to lesions.

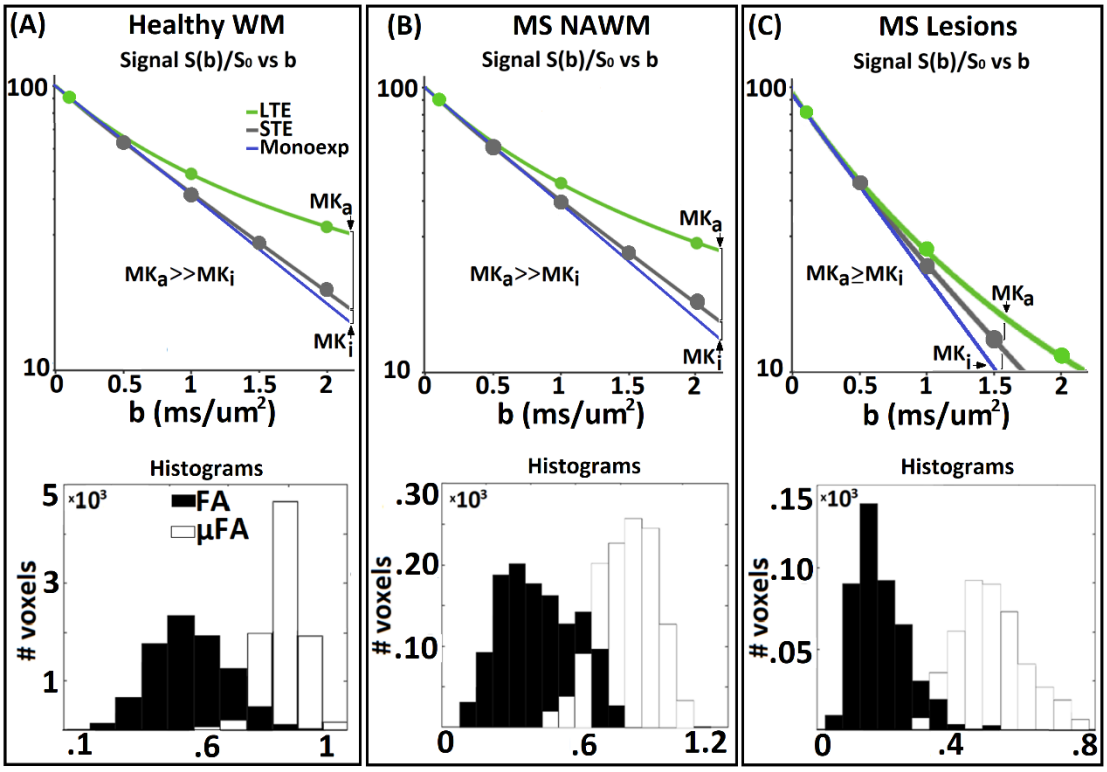

Figure 5.3: Signal vs b-value curves (first row) and FA/μFA histograms (second row) within (A) total healthy WM in a 50-year-old female healthy participant, and (B) total NAWM and (C) lesions in a 51-year-old RRMS female (EDSS 3.5, TLV=44.2 cm^3). LTE and STE signals are shown as green and grey solid lines, respectively. Mono-exponential signal decay is shown with a blue solid line only for visual reference. When applying STE, the signal curvature relative to the mono-exponential signal decay is related to the degree of isotropic diffusional variance (MK_i). Adding the isotropic encoding STE acquisition allowed for separation of the anisotropic diffusional variance (MK_a) from the total variance (MK_t) calculated with conventional/linear diffusion encoding – LTE. FA and μFA histogram distributions showed differences between these two metrics and μFA was higher than FA for the three tissues demonstrating how μFA is still sensitive to the anisotropic diffusion even in MS lesions.

5.3.3. Group Analysis of Diffusion Metrics in WM Lesions vs Total NAWM in MS, WM Lesions in MS vs Total WM in Healthy Controls, and Total NAWM in MS vs Total WM in Healthy Controls

MS lesions, total NAMW, and total WM diffusion metrics in the MS and the healthy cohorts are displayed in Figure 5.4. There were no significant diffusion differences between the total NAWM in MS patients and the total WM in the healthy controls.

Lesions versus Total NAWM in MS: Within lesions, MD (Figure 5.4A) and MK_i (Figure 5.4E) were 64% and 35% respectively higher than in NAWM. Within lesions, FA (Figure 5.4B) and μFA (Figure 5.4C) were -47% and -32% respectively lower and MK_a (Figure 5.4D) and MK_t (Figure 5.4F) were -65% and -49% respectively lower than in NAWM.

Lesions versus Total WM in Healthy Controls: Lesion MD (Figure 5.4A) and MK_i (Figure 5.4E) were 66% and 35%, respectively, higher than in healthy WM in controls. Within lesions, FA (Figure 5.4B) and μFA (Figure 5.4C) were -48% and -32%, respectively, lower and MK_a (Figure 5.4D) and MK_t (Figure 5.4F) were -66% and -50%, respectively, lower than in total WM in healthy controls.

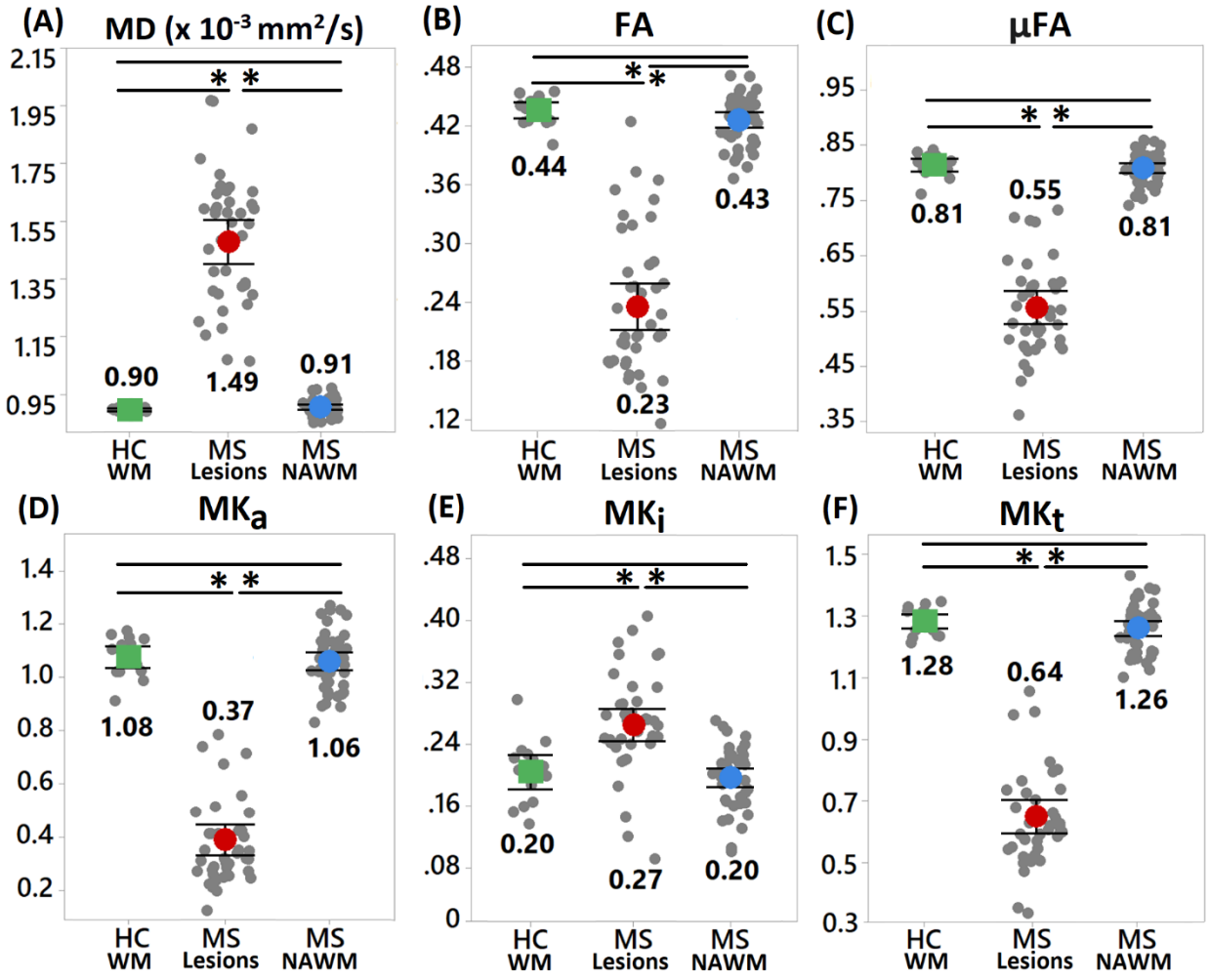

Figure 5.4: Interval plots of diffusion metrics for lesions and NAWM in MS and healthy WM in controls. Interval plots showed the mean and its 95% confidence interval, as well as individual participant values of the (A) MD, (B) FA, (C) µFA, (D) MK_a, (E) MK_i, and (F) MK_t metrics in lesions and NAWM for the full MS cohort, and in healthy WM for control participants (HC) with their corresponding symbols legend (FDR-corrected *p<0.01).

5.3.4. Qualitative Evaluation of Diffusion Metrics Changes in Different WM Configurations in MS Patients and Healthy Controls

T1-weighted MPRAGE, T2-weighted FLAIR images, and diffusion maps are shown for a 50-year-old healthy control and a 50-year-old RRMS patient (Figure 5.5). The RRMS patient displayed slightly enlarged ventricles when compared with a similarly aged healthy control despite having an MS onset from only 4 years ago, a low total lesion volume and EDSS=0. MD seemed very homogeneous all over the WM in both examples (Figure 5.5C). FA appeared to be higher in highly coherent WM such as the splenium of corpus callosum and posterior limb of internal capsula and lower in the anterior crossing WM in controls and MS when compared to coherent WM (Figure 5.5D); wherein μFA was more homogeneous all over the WM reflecting high anisotropy (Figure 5.5E), in both participants. MK_a and MK_t maps appeared brightest in the highly anisotropic coherent WM within the corpus callosum and the internal capsula when compared to crossing WM areas (Figure 5.5F, H), while MK_i displayed high intensity only in voxels with partial volume with CSF (Figure 5.5G).

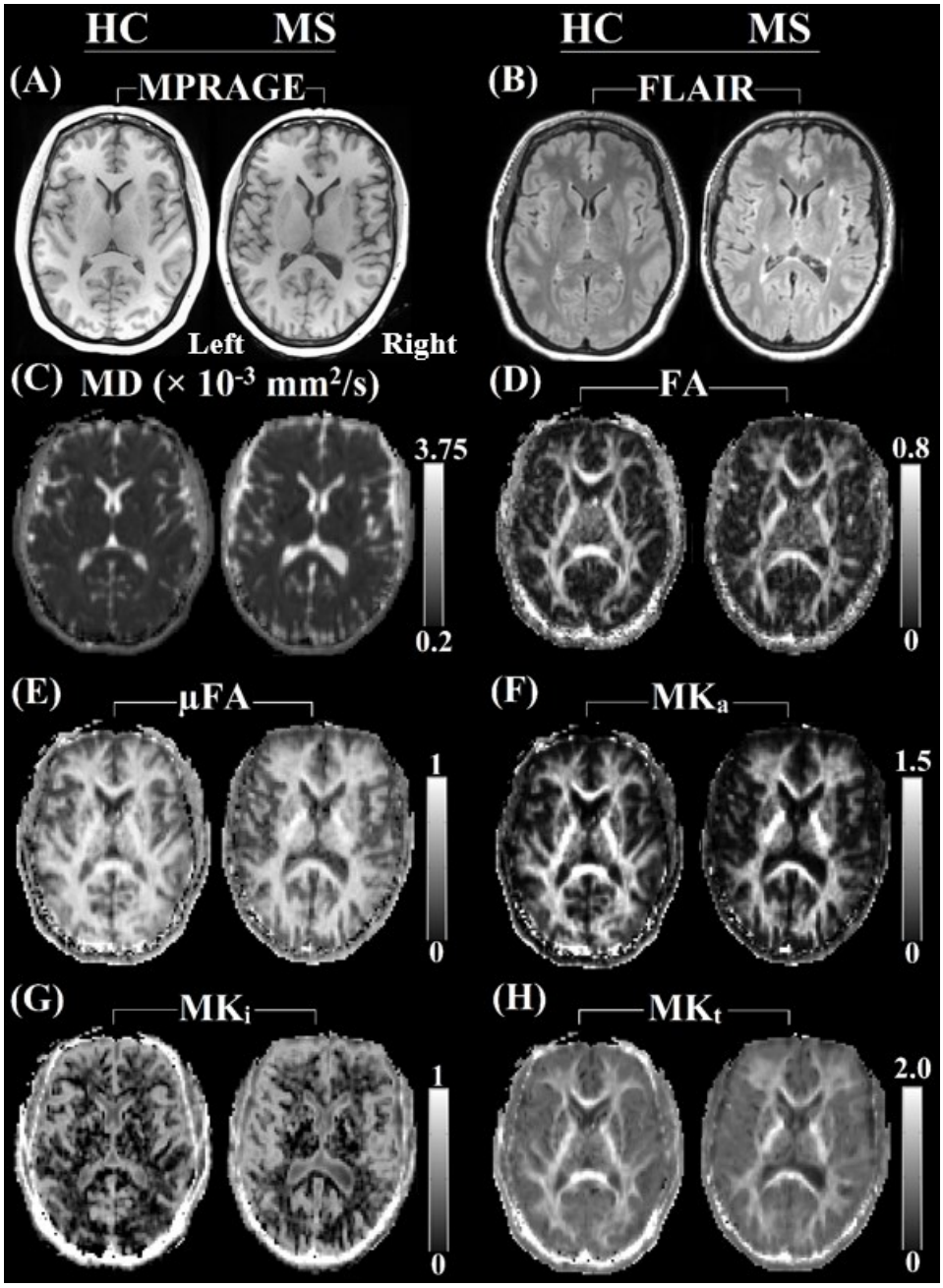

Figure 5.5: (A) MPRAGE, (B) FLAIR, (C, D) DTI and (E-H) DIVIDE diffusion maps in a 50-year-old healthy female (first column) and in a 50-year-old RRMS female (second column, EDSS 0.0, TLV=0.7 cm^3).

Figure 5.6 displays an SPMS example with high lesion load (shown in the first row on FLAIR) and the four WM ROIs enclosing regions with different WM fiber configurations under study here, which were depicted on the FEFA map (second row in Figure 5.6). Among the regions inspected within the same individual with MS, MK_a (fourth row in Figure 5.6) and MK_t (sixth row in Figure 5.6) brightest areas were in the highly coherent WM (Figure 5.6A, B) and the lowest values in crossing WM (Figure 5.6C). MK_i (fourth row in Figure 5.6) was generally low all over the brain showing the highest values in periventricular areas with high lesion incidence and near CSF such as the corpus callosum and the anterior crossing WM. The MK_t values were the highest in the posterior limb of the internal capsula when compared to the corpus callosum, with the former also displaying higher anisotropic variance MK_a and lower to nearly zero isotropic variance MK_i when compared to the latter (Figure 5.6A, B). This could be reflecting the higher incidence of MS lesions in callosal WM versus the internal capsula, although it could also be influenced by partial volume effects with CSF near the lateral ventricles. In fanning WM, MK_t values were higher than in crossing WM, with MK_a being twice higher and MK_i twice lower in the former than in the latter (Figure 5.6C, D). Both fanning and crossing WM ROIs had heavy lesion incidence, however Mk_i values were higher in the crossing WM; again they are likely more greatly influenced by partial volume effects with ventricular CSF and not only by inflammatory MS lesions.

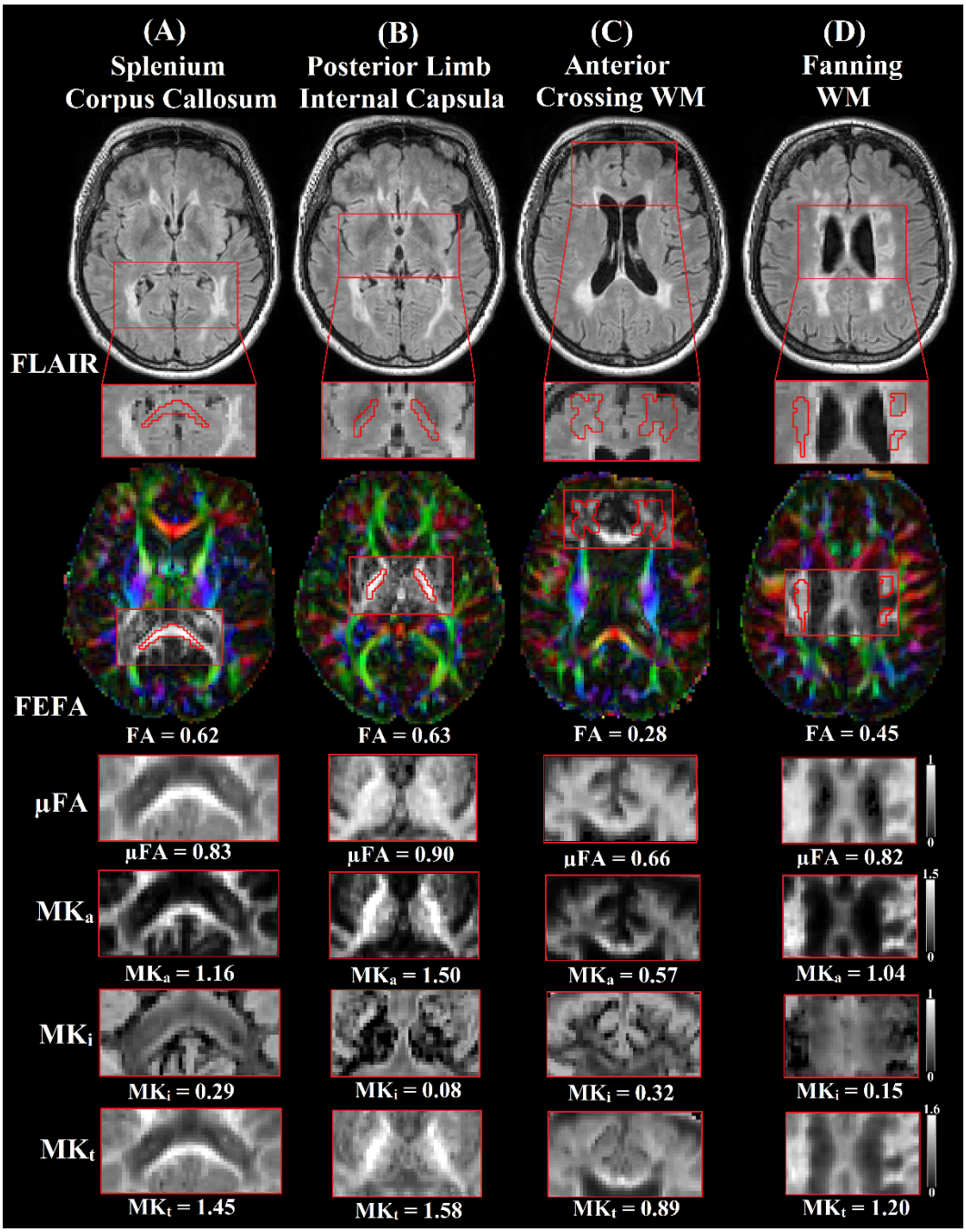

Figure 5.6: DTI and b-tensor derived diffusion metrics in 4 different types of WM regions. Regions included (A, B) coherent, (C) crossing, and (D) fanning WM in a 61-year-old SPMS female (EDSS 6.0, TLV=37.1 cm^3). μFA was high for all WM regions reflecting WM anisotropy while FA was heterogeneous within the enclosed crossing WM region reflecting its sensitivity to orientation dispersion. MK_a and MK_t were the highest in highly coherent WM regions while MK_i was slightly elevated near CSF interfaces.

5.3.5. Group Analysis of Diffusion Metrics in Different WM Configurations in MS Patients and Healthy Controls

Diffusion metrics extracted from the ROIs enclosing different WM configurations that displayed significant group differences between the MS cohort and the healthy controls are shown in Table 5.2. The splenium of the corpus callosum, coherent WM with high lesion incidence in MS ($p \leq 0.001$, Figure 5.6A), the anterior crossing in frontal WM ($p \leq 0.015$, Figure 5.6C) and the fanning WM of the corona radiata ($p \leq 0.029$, Figure 5.6D), each showed abnormally higher MD and lower μFA, MK_a, and MK_t in MS when compared with controls. FA was lower only in the splenium of the corpus callosum ($p=0.001$) and the fanning WM ($p=0.019$), but not in the crossing WM, and MK_i was higher only in the corpus callosum splenium ($p=0.001$) in MS patients versus healthy participants. The posterior limb of the internal capsula showed no diffusion differences (Controls: FA=0.63 ± 0.03, MD=0.87 ± 0.02 x 10^{-3} mm^2/s, μFA=0.90 ± 0.03, $MK_{a=}$1.52 ± 0.15, $MK_{i=}$0.1 ± 0.08, $MK_{t=}$1.61 ± 0.09; MS: FA=0.64 ± 0.03, MD=0.86 ± 0.04 x 10^{-3} mm^2/s, μFA=0.91 ± 0.03, $MK_{a=}$1.57 ± 0.20, $MK_{i=}$0.05 ± 0.11, $MK_{t=}$1.61 ± 0.11).

Table 5.2: Diffusion metrics for controls (HC) versus the MS cohort in different WM/NAWM regions (FDR corrected *p≤0.01)

		Mean ± SD (MD – 10^{-3} mm^2/s, FA, µFA, MK_a, MK_i, MK_t – no units)		***% Differences vs HC (p-value)***
		HC (n=15)	***MS (n=43)***	
Coherent WM (Corpus Callosum Splenium)	**MD**	0.89 ± 0.03	0.99 ± 0.12*	11% (p<0.0001)
	FA	0.76 ± 0.05	0.68 ± 0.07*	-11% (p<0.0001)
	µFA	0.92 ± 0.03	0.86 ± 0.07*	-6.5% (p<0.0001)
	MK_a	1.73 ± 0.21	1.36 ± 0.33*	-21% (p<0.0001)
	MK_i	0.16 ± 0.08	0.26 ± 0.10*	62% (p=0.001)
	MK_t	1.89 ± 0.14	1.62 ± 0.26*	-14% (p<0.0001)
Anterior Crossing (Frontal WM)	**MD**	0.93 ± 0.02	0.97 ± 0.06*	4% (p=0.002)
	FA	0.36 ± 0.03	0.34 ± 0.05	Not significant
	µFA	0.76 ± 0.02	0.73 ± 0.05*	-4% (p=0.002)
	MK_a	0.85 ± 0.07	0.75 ± 0.15*	-12% (p=0.002)
	MK_i	0.28 ± 0.04	0.30 ± 0.05	Not significant
	MK_t	1.13 ± 0.04	1.05 ± 0.11*	-7% (p<0.0001)
Fanning WM (Corona Radiata)	**MD**	0.87 ± 0.02	0.92 ± 0.10*	6% (p=0.001)
	FA	0.46 ± 0.04	0.42 ± 0.05*	-9% (p=0.01)
	µFA	0.88 ± 0.02	0.84 ± 0.06*	-5% (p<0.0001)
	MK_a	1.31 ± 0.09	1.15 ± 0.22*	-12% (p<0.0001)
	MK_i	0.08 ± 0.06	0.12 ± 0.07	Not significant
	MK_t	1.39 ± 0.05	1.26 0.15*	-9% (p<0.0001)

5.3.6. Linear Relationships Between Diffusion Metrics and Age in MS Patients and Healthy Controls

In the MS cohort, lesion MD and anterior crossing WM MK_i increased with age (Figure 5.7A, E), while anterior crossing WM FA, µFA and WM MK_a decreased with age (Figure 5.7B-D). Anterior crossing WM FA also decreased with age in the healthy cohort (Figure 5.7B). For anterior crossing WM FA there were age effects for both cohorts ($F(1, 55)=13.96$, $p\leq0.0001$) which differed per group ($F(1, 55)=5.61$, $p=0.02$). This was evident from the different slopes between MS and controls in the age scatterplot, where FA decreases with age were steeper in the MS cohort (Figure 5.7B).

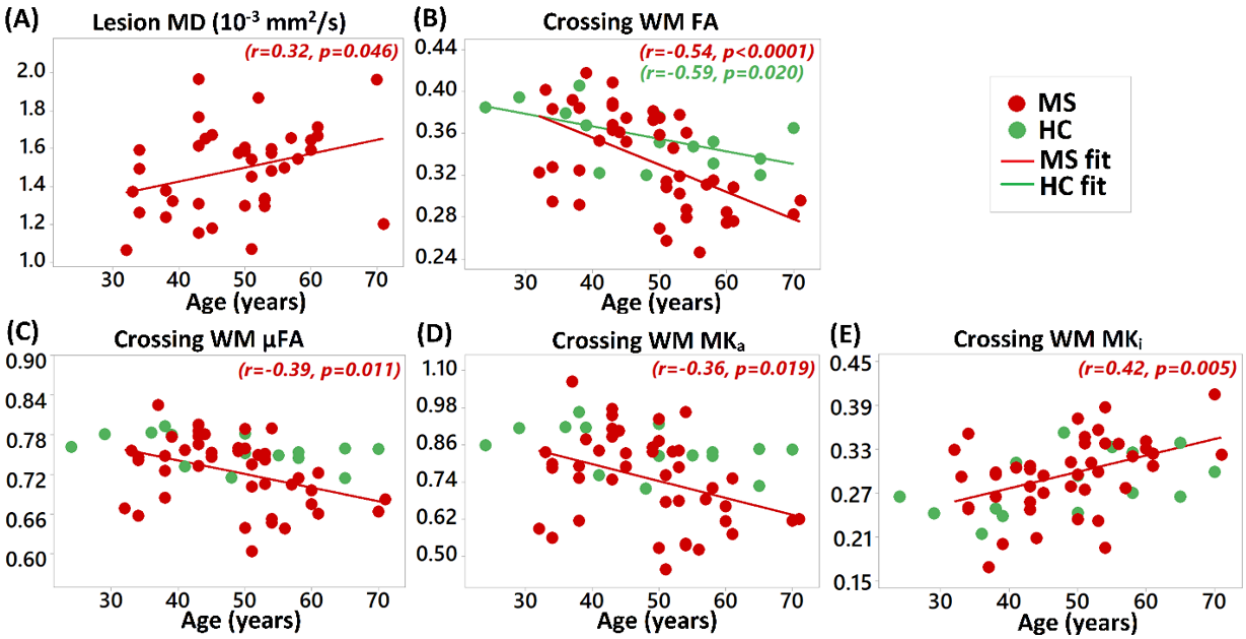

Figure 5.7: (A) Lesion MD, and anterior crossing WM (B) FA, (C) µFA, (D) MK_a and (E) MK_i scatterplots versus age for the entire MS cohort (red circles) and controls (green circles) with linear regression fits when significant ($p<0.05$). The anterior crossing WM FA showed a negative relationship with age in MS and healthy participants, with FA decreasing faster with age in the MS cohort.

5.3.7. Correlations between Brain Diffusion Metrics with Total Lesion Volume, Clinical and Cognitive Scores in MS

Statistically significant correlations (FDR-corrected, $p<0.017$) are shown in Figure 5.8. The strongest correlations with total lesion volume (TLV, Figure5.8A) were found in the splenium of the corpus callosum ((-0.73)-0.69) and in the superior corona radiata which reflects fanning WM ((-0.80)-0.86), followed by the anterior crossing WM ((-0.64)-0.68), which is consistent with the high incidence of lesions in these WM areas. Higher MK_a (Figure 5.7B, n=35) within the WM lesions positively correlated with greater hand and arm dexterity (9-HPT - higher values). Three RRMS participants (all female and 45 years old or younger) were driving the correlations, displaying both high 9-HPT scores and high lesion MK_a values. Several correlations between EDSS, BVMT-R, SDMT and 9-HPT with diffusion metrics in MS lesions, the splenium of the corpus callosum, as well as anterior crossing frontal WM and fanning WM in the superior corona radiata were found (not shown) although they did not reach the FDR correction threshold.

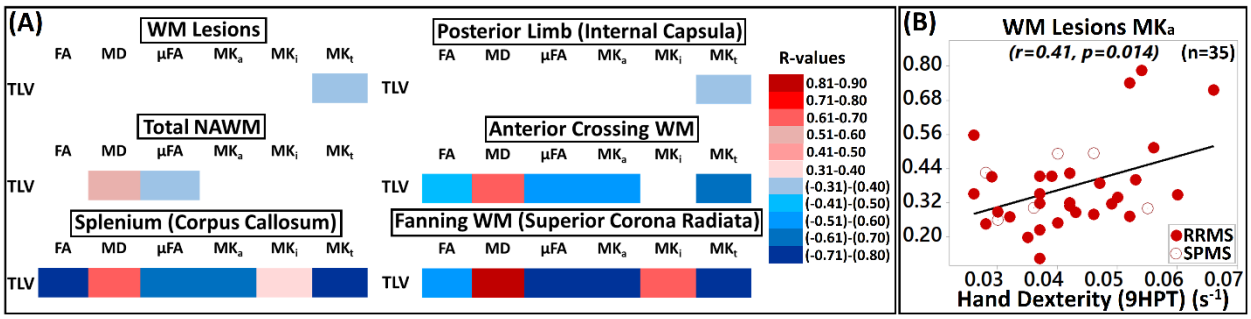

Figure 5.8: (A) Linear correlations (pink—positive; blue—negative) between diffusion metrics in lesions, total NAWM, and discrete WM regions excluding lesions in the entire MS cohort versus total lesion volume (TLV). (B) Greater hand and arm dexterity positively correlated with higher MK_a within the lesions. (FDR-corrected, $p\leq0.017$).

5.4. Discussion

This is one of the first studies to apply b-tensor diffusion MRI in MS pathology to better understand the underlying tissue microstructure in MS lesions and different WM fiber orientations, as well as to compare novel diffusion metrics obtained from the b-tensor acquisition between MS and healthy participants. In advantage over the two previous MS diffusion studies that only quantified the microscopic diffusion anisotropy in terms of μFA, here we reported several novel diffusion metrics, which are related to the diffusional variance that arise from different diffusion microenvironments within a macroscopic voxel (MK_a, MK_i, MK_t). Furthermore, by disentangling the anisotropic (MK_a) and isotropic ($MK_{i)}$ components of this diffusional variance we were able to quantify them in different WM fiber configurations in MS for the first time and to compare them with healthy volunteers.

When comparing MS lesions with NAWM in patients and versus healthy WM in controls the standard diffusion metrics and the b-tensor diffusion metrics were all different between lesions and 'normal appearing' WM in both cohorts, although not within the 'normal appearing' WM regions in MS when compared to healthy WM in controls. Moreover, from the qualitative assessments, the μFA, MK_a and MK_t maps demarcated lesions within crossing/fanning fiber regions and periventricular regions more accurately than FA, and these maps appeared to better overlap with both hypointense T1- and hyperintense T2-weighted lesion anomalies in MS as opposed to FA which seemed to be mostly related with T1-weighted "black holes", which are indicators of more severe tissue destruction and axonal loss [403], [404]. These results were in

agreement with one of the two previous studies which reported differences for T2- and T1-weighted lesion areas between MS and controls but not for NAWM [162]. The other previous study reported μFA group differences for 'normal appearing' WM between MS patients and healthy controls although this group difference was also reported with FA [172]. More than a third of the MS patients in this previous study were primary progressive; this is a more severe MS outcome with quicker worsening when compared to RRMS patients, which were the bulk (81%) of our study. Moreover, 'normal appearing' WM in that study was only measured in a slab that covered the corpus callosum, which is an area known for its high incidence of extensive WM periventricular lesions in MS which could be the reason why they found group differences with both DTI and b-tensor derived metrics as opposed to our results here [172].

We propose that perhaps the stringent voxel eroding performed here to deal with partial volume with CSF, that was applied twice (once for the lesion mask and once for the WM mask) could be the reason why no group differences were found in the 'normal appearing' WM. For our voxel size, each voxel removed in the eroding process would effectively remove 12 mm^3 from the lesion and NAWM mask contours. This leaves the lesion masks with only the core of the bigger lesions and removes the adjacent voxels located in the vicinity of the WM lesions from the NAWM masks, which could effectively remove many areas with the greatest WM damage from the NAWM masks in MS as previously shown in a magnetization transfer study [405]. Additionally, this would dramatically change the total number of voxels that we are assessing in many patients, mainly in those with high TLV (note the number of voxels on the FA/μFA histograms in Figure 5.3B, C which were performed in the RRMS patient with the highest TLV in our cohort, compared to a

heathy control in Figure 5.3A) and will bias the contribution of the different WM structures to the total WM. Still, lower μFA values in WM lesions when compared to total NAWM values in the MS cohort quantitively agreed with previous tensor-valued diffusion MS studies [162], [172]. Global healthy WM μFA values in controls were also consistent with one of these studies (μFA~0.81) [162], but they were slightly lower than what reported in the other previous work (μFA~0.83) [172], perhaps due to their assessment of a slab positioned around the corpus callosum as previously mentioned.

In our study, although all diffusion metrics differed between lesions and WM in both cohorts, in Figure 5.4 one can notice some degree of overlapping of the FA lesion values in individual subjects (~8% of lesion values – 3/40 in MS) with NAWM (~49% overlapped values – 21/43 in MS) and healthy WM (~33% overlapped values – 5/15 in controls). This was contrasted with no overlapping in μFA, MK_a and MK_t individual subject values from the same participant's ROIs, and demonstrates their complementary value to DTI metrics if there is a loss of anisotropy in the tissue microstructure and/or a comparatively large water (edema) component [161] as in MS lesions. Regarding the total diffusional variance MK_t as a probe of tissue heterogeneity and its respective anisotropic and isotropic contributions, MK_a was the diffusion measurement from all the standard and the tensor-valued diffusion metrics that showed the greatest quantitative differences between lesions and total WM for both cohorts. MK_t almost numerically doubled its values in total NAWM and WM when compared to lesion values. These lesion values were in good agreement with WM lesion values in elderly healthy subjects and patients with Parkinson's disease from a comparable b-valued diffusion study [400]. Other MS DKI studies [158], [406] comparing MK in MS lesions

versus NAWM/WM have also reported lower values in different type of lesions consistent with our results here, although their numerical values were expected to be different relative to ours due to variations in signal parameterization [169], [407]. These previous DKI studies agreed with results here which provided evidence that MK_t is a robust indicator of lesion tissue architecture and heterogeneity, and that it has been associated with diffuse WM damage in terms of demyelination and axonal degeneration in MS patients. Still, MK_t itself is sensitive to both variable cell eccentricity and density but lacks specificity regarding these their precise contributions to MS lesion microstructure characteristics.

On the other hand, when the STE was added to the LTE in the diffusion signal acquisition stage, these contributions were further disentangled, indicating that low MK_t values within MS lesions were explained by 58% MK_a and 42% MK_i contributions as opposed to NAWM/WM which both showed that 84% of MK_t occurred from MK_a and only 16% from MK_i. In MS lesions the MK_i values were not negligible and they were higher than in NAWM and in healthy WM, potentially due to different degrees of inflammation/edema in active lesion states due to the migration of inflammatory cells combined with demyelination [403]. This together with partial volume effects with CSF, largely on the lesion areas which are near to the lateral ventricles, could be the cause of MK_i displaying relatively scattered values, with low accuracy and some overlap with NAWM and healthy WM. MK_a values in NAWM and healthy WM were almost three times higher than in lesions and appeared sensitive to different degrees of microstructural anisotropy in NAWM/WM. The brightest hyperintense WM areas were found in the corpus callosum and the internal capsule

reflecting MK_a sensitivity to highly coherent and highly myelinated fibers and to anisotropic diffusion in the extracellular space [400].

Neither of the other two previous DDE [162] and b-tensor [172] MS studies reported group diffusion differences in specific WM regions, three of which were investigated here (e.g., corpus callosum, internal capsula, frontal subcortical WM). In our study, for outside lesion areas that could indeed encompass variable cell density due to inflammation, MK_i only differed in the corpus callosum genu between MS and healthy cohorts. This metric showed the greatest percentage wise group difference in the corpus callosum, followed by MK_a, which could imply variable cell density due to inflammation possibly coming from microscopic lesions (slow isotropic compartments), but also due to CSF (fast isotropic compartments) [169]. MK_i seemed to be very sensitive to partial volume effects with CSF [400], and these effects were greater in MS patients with enlarged ventricles, which together with inflammation and lesions could be one of the reasons behind MK_i differences between MS patients and controls. However, MK_i numerical values are 7-10 times smaller than MK_a, making the impact on results from CSF likely small, although these results should be carefully interpreted. In the fanning WM with high lesion incidence, all metrics but MK_i were different between groups. Interesting to note here, the MK_a displayed the greatest differences, which were supported by lower μFA in MS and could be interpreted mainly as less anisotropy or eccentric cells [169], due to axonal loss resulting from Wallerian degeneration [408] from nearby lesions, which can still be detected at the voxel level. In the anterior periventricular crossing WM, μFA, MK_a and MK_t were able to depict diffusion differences between MS patients and controls while FA did not find any group differences. In both crossing and fanning WM areas, MK_a showed

the greatest group differences (-12%). This demonstrates the added value of microstructural diffusion metrics to depict group differences in WM areas with high fiber orientation dispersion where conventional metrics could fail. Based on these results, if b-tensor protocols are acquired at this voxel resolution we recommend either (i) analyse discrete WM structures directly on diffusion maps and apply MD or even MK_i thresholds to deal with partial volume effects with CSF, or (ii) perform atlas-based or TBSS approaches to analyse specific WM bundles individually as opposed to assessing total NAWM.

Regarding correlations with clinical tests in MS, high MK_a within MS lesions was linearly related to greater hand and arm dexterity. This was possibly due to the higher incidence of these lesions in periventricular WM brain structures such as the corpus callosum, which seemed significantly affected in the MS cohort here, and in which fiber integrity have been previously related to better ability in bimanual motor tasks in MS with standard DTI [409].

One limitation of this study is the poor spatial resolution of the b-tensor protocol (12 mm^3 voxel size) that could create partial volume effects particularly for small regions in the presence of atrophy, as is known in MS, as well as in small lesions. Spatial resolution was kept this low here in order to maintain a feasible SNR at high b-values of 2000 s/mm^2 while keeping a reasonable scan time given the many other MRI protocols performed in this cohort. Another limitation is the small control group of only 15 participants, as only this MS project and another stroke project were utilizing b-tensor protocols which precluded recruiting a greater number of controls, and the fact that not many progressive patients (only 8 SPMS and no PPMS) were scanned here. This limitation could indeed reduce the statistical power of our group comparisons. The last limitation is that we

had no post-Gadolinium T1 scans so we cannot make any interpretations regarding 'active' lesions with blood-brain barrier damage. In summary, b-tensor results obtained here were complementary to DTI results. In MS, where high resolution is key in MRI studies, due to the diversity of lesion sizes, location and pathology as well as patient specific diffuse WM injury, the added value of new b-tensor metrics at this available resolution seems mainly to improve the interpretation of standard DTI metrics. Future studies with better resolution and methodology are needed to achieve superior conclusions regarding its use in MS.

6. Summary & Conclusions

The work presented in this thesis adds extensive knowledge to the field of diffusion MRI and its research applications with a focus on MS pathology. In addition, this manuscript also provides further evidence that cognitive and behavioural functions are correlated with macroscopic and microscopic abnormalities in limbic WM and GM structures. These results were achieved with novel acquisition and postprocessing strategies beyond those used in clinical MRI of MS.

6.1. Fornix

DTI analyses derived from MRI acquisitions in Chapter 2 and Chapter 3 suggested that within the limbic system, the fornix appeared to be severely affected in terms of volume (from -26 to -53%) and diffusion metrics (from -16% to 24%) in MS patients despite their phenotypic classification. Furthermore, these fornix abnormalities persisted with the use of CSF supressed diffusion acquisitions, therefore they cannot be attributed only to an excess of CSF contamination due to the fornix tract intraventricular location and small sizes. In both Chapters 2 and 3, these affected fornix metrics appeared to be consistently worse in MS patients with high lesion load on FLAIR, and in those who were classified as cognitively impaired in Chapter 3.

6.2. Hippocampus

Lower hippocampus FA was reported in MS from the diffusion and volume metrics calculated with FLAIR DTI in Chapter 3. Chapter 4 further focused on the hippocampus as the brain memory center. A high resolution 1 mm isotropic DTI slab acquired along the long axis of the hippocampus was utilized to manually segment the structure directly in mean DWI for the first time in MS, as

opposed to automatic segmentation and T1 coregistration applied in Chapter 3. These DTI hippocampus results were complemented with high resolution T2-weighted and T2 multi-echo spin echo scans acquired on similarly oriented hippocampus slabs. Total hippocampus volume, FA, T2 relaxometry values and T2-weighted signal were significantly abnormal in the MS cohort and the most significantly abnormal values were reported in cognitively impaired MS participants, while MD was elevated in all MS groups regardless of their cognitive status. MD together with T2 relaxometry values were thresholded to assess regional hyperintensities as indicators of demyelination and inflammation, and results were consistent with MS damage seen in previous histologic studies. Furthermore, the proportion of these hyperintense regions were also greater in MS, mainly in patients with cognitive decline for T2-relaxometry and in general in patients with greater lesion volumes. As MD total and regional hippocampus hyperintensities were affected, although to a lesser extent, in cognitively preserved patients, this could indicate that hippocampus demyelination is an early pathological feature of MS, and its worsening could influence irreversible atrophy and cognitive impairment.

6.3. Other Regions Displaying Volume/Diffusion Abnormalities in MS

In Chapter 2, the cingulum did not display any abnormalities in MS but the uncinate fasciculus showed lower FA in SPMS. In Chapter 3, severe atrophy was reported in the thalamus mainly in cognitively impaired patients (-23%). In Chapter 5, MD and FA, and novel diffusion metrics such as μFA, MK_a and MK_t achieved with b-tensor encoding, were found abnormal in lesions when compared to total NAWM in MS and WM in controls, although no differences were reported in 'normal appearing' WM between the two groups. Similar kinds of diffusion encoding analyses

have only been performed in MS twice before, however they have reported only μFA values. Coherent WM in the corpus callosum and the fanning WM in the superior corona radiata were consistently different between MS and controls although the greatest percentagewise differences between groups were reported with diffusional variance metrics such as MK_a and MK_t Additionally, μFA, MK_t and MK_a, but not FA, were significantly lower in MS when assessing anterior periventricular crossing WM excluding lesions.

6.4. Clinical/Cognitive Correlations

In MS, lower cingulum FA (Chapter 2) and lower hippocampus FA (Chapter 3 and Chapter 4) respectively correlated with higher depression and greater physical fatigue. Abnormal fornix diffusion metrics, thalamus volume and hippocampus FA correlated with slower information processing speed in Chapter 3. In Chapter 3, the fornix RD together with thalamic volumes were excellent predictors of cognitive impairment in MS with an accuracy of 87%. In Chapter 4, higher T2 relaxometry values and higher T2-weighted signal in the hippocampus correlated with greater disability. In Chapter 5, higher MK_a within the MS lesions correlated with better hand and arm dexterity.

6.5. Limitations

Several limitations of this work should be noted. First, the sample sizes, mainly in Chapter 2 could be increased to make more robust inferences regarding MS phenotypes. Second, the absence of PPMS and low proportion of SPMS patients in Chapter 3, Chapter 4 and Chapter 5 should be addressed and the numbers of patients classified with these phenotypes could be increased to make

better interpretations in relation to histology work. Third, CSF suppressed acquisitions were not acquired in Chapter 2, due to specific absorption rate (SAR) constraints at 4.7 T, and the lack of multi-shell diffusion acquisition within the same work precluded the application of accurate postprocessing "free water elimination (FWE)" CSF correction algorithms. Fourth, there were no histology analyses available to fully confirm the validity of the imaging results versus a gold standard in the MS cohorts under study here. Fifth, spatial resolution should be increased for the b-tensor diffusion protocol, which along with an optimized methodology, could improve the robustness of results achieved in Chapter 5. Sixth, the long duration of the MS protocols utilized here, which were acquired all together making the total acquisition ~1 hour long which could increase sensitivity to subject motion. The MRI was followed by the cognitive/clinical testing which could potentially make the MS patients prone to overtiredness and fatigue and bias the testing and questionnaire results. Despite these important limitations and many more, this work has advanced the field of diffusion MRI in MS and it has possibly led to more questions than it has answered regarding MS cognitive decline, limbic structures, and diffusion metrics interpretation. Nevertheless, this work has also significantly contributed towards the identification of key structures that were previously poorly studied in MS, and to the better understanding of the pathological processes behind the degradation of these structures and their relationship with clinical and cognitive deficits.

6.5. Future Directions

Longitudinal FLAIR-DTI work in MS, as well as greater and more phenotypically diverse MS cohorts will help to confirm if the fornix could be an early and robust indicator of cognitive

impairment in MS, which could possibly precede abnormalities in other brain deep GM structures related to cognitive functions, particularly considering results shown by our findings. Furthermore, the status of structures like the fornix, hippocampus and thalamus as evaluated by combined high resolution multi-shell diffusion and volume MRI metrics could serve as prospective biomarkers of cognitive impairment in MS, similar to suggested biomarkers of Alzheimer's disease. A high resolution (1.5 mm isotropic) whole brain diffusion MRI protocol was acquired as part of the full set of MRI sequences performed for Chapters 3, 4 and 5. It was acquired in 6 min with a SS-EPI sequence: GRAPPA R=2, 6/8 partial Fourier, 6 b= 0 s/mm^2, 30 directions at b=1000 s/mm^2 and 30 directions at b=2000 s/mm^2, TR=4700 ms, TE=64 ms. Future work in this MS cohort could include expanding the tractography analysis from DTI- to CSD-based tract reconstruction and apply it in a larger number of WM bundles in the brain with a focus on crossing fiber areas such as the thalamic radiation and in regions with high MS lesion incidence and low diffusion anisotropy. Furthermore, the b=1000 s/mm^2 shell of this diffusion MRI protocol could be utilized for examining cortical anisotropy in MS, by applying an automated cortical boundary segmentation method that works directly on FA and mean DWI maps yielded from the aforementioned diffusion acquisition [410]. This method was previously developed by our lab, but it has not yet been applied in MS. Diffusion cortical measures in the MS cohort may complement deep GM diffusion metrics previously calculated in this thesis and further could advance the understanding of GM damage in MS. Finally, additional cross-sectional and longitudinal studies applying b-tensor diffusion MRI in MS and control groups with greater spatial resolution, sample sizes and in conjunction with histological validation, will help to confirm the clinical value of these

novel acquisitions which may be used to improve the interpretation of diffusion metrics regarding pathology.

References

[1] S. Herculano-Houzel, “The human brain in numbers: a linearly scaled-up primate brain,” *Front. Hum. Neurosci.*, vol. 3, p. 31, Nov. 2009, doi: 10.3389/neuro.09.031.2009.

[2] R. W. Guillery, “Observations of synaptic structures: origins of the neuron doctrine and its current status,” *Philos. Trans. R. Soc. Lond. B. Biol. Sci.*, vol. 360, no. 1458, pp. 1281–1307, Jun. 2005, doi: 10.1098/rstb.2003.1459.

[3] B. W. Connors and M. A. Long, “Electrical synapses in the mammalian brain,” *Annu. Rev. Neurosci.*, vol. 27, no. 1, pp. 393–418, 2004, doi: 10.1146/annurev.neuro.26.041002.131128.

[4] B. Stevens, “Glia: much more than the neuron’s side-kick.,” *Curr. Biol.*, vol. 13, no. 12, pp. R469-72, Jun. 2003, doi: 10.1016/s0960-9822(03)00404-4.

[5] S. Jäkel and L. Dimou, “Glial Cells and Their Function in the Adult Brain: A Journey through the History of Their Ablation,” *Frontiers in Cellular Neuroscience*, vol. 11. 2017. Available: https://www.frontiersin.org/article/10.3389/fncel.2017.00024.

[6] S. Aamodt, “Focus on glia and disease,” *Nat. Neurosci.*, vol. 10, no. 11, p. 1349, 2007, doi: 10.1038/nn1107-1349.

[7] F. Deisenhammer, H. Zetterberg, B. Fitzner, and U. K. Zettl, “The Cerebrospinal Fluid in Multiple Sclerosis,” *Frontiers in Immunology*, vol. 10. 2019. Available: https://www.frontiersin.org/article/10.3389/fimmu.2019.00726.

[8] A. Irimia, “Cross-Sectional Volumes and Trajectories of the Human Brain, Gray Matter, White Matter and Cerebrospinal Fluid in 9473 Typically Aging Adults,” *Neuroinformatics*, vol. 19, no. 2, pp. 347–366, 2021, doi: 10.1007/s12021-020-09480-w.

[9] K. Narvacan, S. Treit, R. Camicioli, W. Martin, and C. Beaulieu, “Evolution of deep gray matter volume across the human lifespan,” *Hum. Brain Mapp.*, vol. 38, no. 8, pp. 3771–3790, Aug. 2017, doi: 10.1002/hbm.23604.

[10] J. Sastre-Garriga *et al.*, “Grey and white matter volume changes in early primary progressive multiple sclerosis: a longitudinal study,” *Brain*, vol. 128, no. 6, pp. 1454–1460, Jun. 2005, doi: 10.1093/brain/awh498.

[11] M. Tiberio *et al.*, “Gray and white matter volume changes in early RRMS,” *Neurology*, vol. 64, no. 6, pp. 1001 LP – 1007, Mar. 2005, doi: 10.1212/01.WNL.0000154526.22878.30.

[12] N. Snaidero and M. Simons, “Myelination at a glance,” *J. Cell Sci.*, vol. 127, no. 14, pp. 2999–3004, 2014, doi: 10.1242/jcs.151043.

[13] C. Hildebrand, S. Remahl, H. Persson, and C. Bjartmar, “Myelinated nerve fibres in the CNS,” *Prog. Neurobiol.*, vol. 40, no. 3, pp. 319–384, 1993, doi: 10.1016/0301-0082(93)90015-K.

[14] R. D. Fields and Y. Ni, “Nonsynaptic communication through ATP release from volume-activated anion channels in axons.,” *Sci. Signal.*, vol. 3, no. 142, p. ra73, Oct. 2010, doi:

10.1126/scisignal.2001128.

[15] A. L. MacKay and C. Laule, “Magnetic Resonance of Myelin Water: An in vivo Marker for Myelin,” *Brain Plast.*, vol. 2, no. 1, pp. 71–91, Dec. 2016, doi: 10.3233/BPL-160033.

[16] C. Lebel and S. Deoni, “The development of brain white matter microstructure,” *Neuroimage*, vol. 182, pp. 207–218, Nov. 2018, doi: 10.1016/j.neuroimage.2017.12.097.

[17] K. B. Walhovd, H. Johansen-Berg, and R. T. Káradóttir, “Unraveling the secrets of white matter - Bridging the gap between cellular, animal and human imaging studies,” *Neuroscience*, vol. 276, pp. 2–13, 2014, doi: 10.1016/j.neuroscience.2014.06.058.

[18] C. Serra, L. Guida, V. E. Staartjes, N. Krayenbühl, and U. Türe, “Historical controversies about the thalamus: From etymology to function,” *Neurosurg. Focus*, vol. 47, no. 3, pp. 1–10, 2019, doi: 10.3171/2019.6.FOCUS19331.

[19] N. D. Child and E. E. Benarroch, “Anterior nucleus of the thalamus,” *Neurology*, vol. 81, no. 21, pp. 1869 LP – 1876, Nov. 2013, doi: 10.1212/01.wnl.0000436078.95856.56.

[20] T. Stein, C. Moritz, M. Quigley, D. Cordes, V. Haughton, and E. Meyerand, “Functional connectivity in the thalamus and hippocampus studied with functional MR imaging,” *Am. J. Neuroradiol.*, vol. 21, no. 8, pp. 1397–1401, 2000.

[21] C. M. Bird and N. Burgess, “The hippocampus and memory: Insights from spatial processing,” *Nat. Rev. Neurosci.*, vol. 9, no. 3, pp. 182–194, 2008, doi: 10.1038/nrn2335.

[22] J. Kwon *et al.*, “Label-free nanoscale optical metrology on myelinated axons in vivo,” *Nat. Commun.*, vol. 8, no. 1, p. 1832, 2017, doi: 10.1038/s41467-017-01979-2.

[23] J. W. Papez, “A proposed mechanism of emotion. 1937 [classical article],” *J. Neuropsychiatry Clin. Neurosci.*, vol. 7, no. 1, pp. 103–112, Feb. 1995, doi: 10.1176/jnp.7.1.103.

[24] I. Nakano, “The limbic system: An outline and brief history of its concept,” *Neuropathology*, vol. 18, no. 2, pp. 211–214, Jun. 1998, doi: 10.1111/j.1440-1789.1998.tb00102.x.

[25] Y. J. Choi, E. J. Lee, and J. E. Lee, “The Fornix: Functional Anatomy, Normal Neuroimaging, and Various Pathological Conditions,” *Investig Magn Reson Imaging*, vol. 25, no. 2, pp. 59–75, Jun. 2021, doi: 10.13104/imri.2021.25.2.59.

[26] A. G. Thomas, P. Koumellis, and R. A. Dineen, “The fornix in health and disease: An imaging review,” *Radiographics*, vol. 31, no. 4, pp. 1107–1121, 2011, doi: 10.1148/rg.314105729.

[27] O. Ozdogmus, S. Cavdar, Y. Ersoy, F. Ercan, and I. Uzun, “A preliminary study, using electron and light-microscopic methods, of axon numbers in the fornix in autopsies of patients with temporal lobe epilepsy.,” *Anat. Sci. Int.*, vol. 84, no. 1–2, pp. 2–6, Apr. 2009, doi: 10.1007/s12565-008-0001-2.

[28] R. Pascalau, R. Popa Stănilă, S. Sfrângeu, and B. Szabo, “Anatomy of the Limbic White

Matter Tracts as Revealed by Fiber Dissection and Tractography," *World Neurosurg.*, vol. 113, pp. e672–e689, 2018, doi: 10.1016/j.wneu.2018.02.121.

[29] S. Senova, A. Fomenko, E. Gondard, and A. M. Lozano, "Anatomy and function of the fornix in the context of its potential as a therapeutic target," *J. Neurol. Neurosurg. & Psychiatry*, vol. 91, no. 5, pp. 547 LP – 559, May 2020, doi: 10.1136/jnnp-2019-322375.

[30] F. D. Raslau, J. C. Augustinack, A. P. Klein, J. L. Ulmer, V. P. Mathews, and L. P. Mark, "Memory part 3: The role of the fornix and clinical cases," *Am. J. Neuroradiol.*, vol. 36, no. 9, pp. 1604–1608, 2015, doi: 10.3174/ajnr.A4371.

[31] V. Douet and L. Chang, "Fornix as an imaging marker for episodic memory deficits in healthy aging and in various neurological disorders," *Frontiers in Aging Neuroscience* , vol. 6. 2015. Available: https://www.frontiersin.org/article/10.3389/fnagi.2014.00343.

[32] H. M. Duvernoy, F. Cattin, P.-Y. Risold, J. L. Vannson, and M. Gaudron, "The Human Hippocampus: Functional Anatomy, Vascularization and Serial Sections with MRI," 3rd edition. 2005. AJNR: American Journal of Neuroradiology, 26(10), 2702.

[33] R. Lorente De Nó, "Studies on the structure of the cerebral cortex. II. Continuation of the study of the ammonic system.," *J. für Psychol. und Neurol.*, vol. 46, pp. 113–177, 1934.

[34] K. S. Anand and V. Dhikav, "Hippocampus in health and disease: An overview," *Ann. Indian Acad. Neurol.*, vol. 15, no. 4, pp. 239–246, Oct. 2012, doi: 10.4103/0972-

2327.104323.

[35] T. G. Ohm, “The dentate gyrus in Alzheimer’s disease,” *Prog. Brain Res.*, vol. 163, pp. 723–740, 2007.

[36] L. Su *et al.*, “Hippocampal Stratum Radiatum, Lacunosum, and Moleculare Sparing in Mild Cognitive Impairment.,” *J. Alzheimers. Dis.*, vol. 61, no. 1, pp. 415–424, 2018, doi: 10.3233/JAD-170344.

[37] K. Christiansen, J. P. Aggleton, G. D. Parker, M. J. O’Sullivan, S. D. Vann, and C. Metzler-Baddeley, “The status of the precommissural and postcommissural fornix in normal ageing and mild cognitive impairment: An MRI tractography study,” *Neuroimage*, vol. 130, pp. 35–47, 2016, doi: 10.1016/j.neuroimage.2015.12.055.

[38] A. D. H. *et al.*, “Characterizing the human hippocampus in aging and Alzheimer’s disease using a computational atlas derived from ex vivo MRI and histology,” *Proc. Natl. Acad. Sci.*, vol. 115, no. 16, pp. 4252–4257, Apr. 2018, doi: 10.1073/pnas.1801093115.

[39] Ackerman S. Discovering the Brain. Washington (DC): National Academies Press (US); 1992. PMID: 25121239..

[40] F. Vargha-Khadem, D. G. Gadian, K. E. Watkins, A. Connelly, W. Van Paesschen, and M. Mishkin, “Differential effects of early hippocampal pathology on episodic and semantic memory,” *Science*, vol. 277, no. 5324, pp. 376–380, 1997, doi: 10.1126/science.277.5324.376.

[41] T. Hartley, C. Lever, N. Burgess, and J. O'Keefe, "Space in the brain: how the hippocampal formation supports spatial cognition," *Philos. Trans. R. Soc. Lond. B. Biol. Sci.*, vol. 369, no. 1635, p. 20120510, Dec. 2013, doi: 10.1098/rstb.2012.0510.

[42] J. R. Binder, R. H. Desai, W. W. Graves, and L. L. Conant, "Where Is the Semantic System? A Critical Review and Meta-Analysis of 120 Functional Neuroimaging Studies," *Cereb. Cortex*, vol. 19, no. 12, pp. 2767–2796, Dec. 2009, doi: 10.1093/cercor/bhp055.

[43] K. Dharani, "The biology of thought: A neuronal mechanism in the generation of thought - A new molecular model". Academic Press, 2014.

[44] I. S. Edelman and J. Leibman, "Anatomy of body water and electrolytes.," *Am. J. Med.*, vol. 27, pp. 256–277, 1959.

[45] F. Bloch, "Nuclear Induction," *Phys. Rev.*, vol. 70, no. 7–8, pp. 460–474, Oct. 1946, doi: 10.1103/PhysRev.70.460.

[46] W. R. Nitz and P. Reimer, "Contrast mechanisms in MR imaging," *Eur. Radiol.*, vol. 9, no. 6, pp. 1032–1046, 1999, doi: 10.1007/s003300050789.

[47] E. L. Hahn, "Spinechoes," *Phys Rev Lett*, vol. 80, no. 4. pp. 580–594, 1950.

[48] P. C. Lauterbur, "Image Formation by Induced Local Interactions: Examples Employing Nuclear Magnetic Resonance," *Nature*, vol. 242, no. 5394, pp. 190–191, 1973, doi: 10.1038/242190a0.

[49] P. Mansfield, “Multi-planar image formation using NMR spin echoes,” *J. Phys. C Solid State Phys.*, vol. 10, no. 3, pp. L55–L58, 1977, doi: 10.1088/0022-3719/10/3/004.

[50] B. D. C. Group, “Total and Regional Brain Volumes in a Population-Based Normative Sample from 4 to 18 Years: The NIH MRI Study of Normal Brain Development,” *Cereb. Cortex*, vol. 22, no. 1, pp. 1–12, Jan. 2012, doi: 10.1093/cercor/bhr018.

[51] R. I. Scahill, C. Frost, R. Jenkins, J. L. Whitwell, M. N. Rossor, and N. C. Fox, “A Longitudinal Study of Brain Volume Changes in Normal Aging Using Serial Registered Magnetic Resonance Imaging,” *Arch. Neurol.*, vol. 60, no. 7, pp. 989–994, Jul. 2003, doi: 10.1001/archneur.60.7.989.

[52] N. M. Armstrong *et al.*, “Associations between cognitive and brain volume changes in cognitively normal older adults,” *Neuroimage*, vol. 223, p. 117289, 2020, doi: 10.1016/j.neuroimage.2020.117289.

[53] A. Brodtmann, M. S. Khlif, N. Egorova, M. Veldsman, L. J. Bird, and E. Werden, “Dynamic Regional Brain Atrophy Rates in the First Year After Ischemic Stroke,” *Stroke*, vol. 51, no. 9, pp. e183–e192, Sep. 2020, doi: 10.1161/STROKEAHA.120.030256.

[54] M. S. Byun *et al.*, “Heterogeneity of Regional Brain Atrophy Patterns Associated with Distinct Progression Rates in Alzheimer’s Disease,” *PLoS One*, vol. 10, no. 11, p. e0142756, Nov. 2015, doi: 10.1371/journal.pone.0142756.

[55] J. L. Whitwell *et al.*, “Rates of cerebral atrophy differ in different degenerative

pathologies," *Brain*, vol. 130, no. 4, pp. 1148–1158, Apr. 2007, doi: 10.1093/brain/awm021.

[56] J. Fujimori, K. Fujihara, R. Ogawa, T. Baba, M. Wattjes, and I. Nakashima, "Patterns of regional brain volume loss in multiple sclerosis: a cluster analysis.," *J. Neurol.*, vol. 267, no. 2, pp. 395–405, Feb. 2020, doi: 10.1007/s00415-019-09595-4.

[57] E. C. Klawiter, "Current and new directions in MRI in multiple sclerosis," *Continuum*, vol. 19, no. 4 Multiple Sclerosis, pp. 1058–1073, Aug. 2013, doi: 10.1212/01.CON.0000433283.00221.37.

[58] J. V. Hajnal *et al.*, "High signal regions in normal white matter shown by heavily t2-weighted csf nulled ir sequences," *Journal of Computer Assisted Tomography*, vol. 16, no. 4. pp. 506–513, 1992, doi: 10.1097/00004728-199207000-00002.

[59] À. Rovira *et al.*, "MAGNIMS consensus guidelines on the use of MRI in multiple sclerosis—clinical implementation in the diagnostic process," *Nat. Rev. Neurol.*, vol. 11, no. 8, pp. 471–482, 2015, doi: 10.1038/nrneurol.2015.106.

[60] A. Montagne, A. W. Toga, and B. V Zlokovic, "Blood-Brain Barrier Permeability and Gadolinium: Benefits and Potential Pitfalls in Research," *JAMA Neurol.*, vol. 73, no. 1, pp. 13–14, Jan. 2016, doi: 10.1001/jamaneurol.2015.2960.

[61] A. Crombé *et al.*, "MS lesions are better detected with 3D T1 gradient-echo than with 2D T1 spin-echo gadolinium-enhanced imaging at 3T," *Am. J. Neuroradiol.*, vol. 36, no. 3,

pp. 501–507, 2015.

[62] À. Rovira, C. Auger, and J. Alonso, “Magnetic resonance monitoring of lesion evolution in multiple sclerosis,” *Ther. Adv. Neurol. Disord.*, vol. 6, no. 5, pp. 298–310, May 2013, doi: 10.1177/1756285613484079.

[63] J. P. Mugler, “Rapid 3D T1-w MRI with MP-RAGE sequence,” *Journal of Magnetic Resonance Imaging*, vol. 1, no. 561–567. 1991.

[64] J. P. Mugler and J. R. Brookeman, “Three-dimensional magnetization-prepared rapid gradient-echo imaging (3D MP RAGE),” *Magn. Reson. Med.*, vol. 15, no. 1, pp. 152–157, 1990, doi: 10.1002/mrm.1910150117.

[65] J. Hennig, A. Nauerth, and H. Friedburg, “RARE imaging: A fast imaging method for clinical MR,” *Magn. Reson. Med.*, vol. 3, no. 6, pp. 823–833, 1986, doi: 10.1002/mrm.1910030602.

[66] M. P. Wattjes *et al.*, “2021 MAGNIMS–CMSC–NAIMS consensus recommendations on the use of MRI in patients with multiple sclerosis,” *Lancet Neurol.*, vol. 20, no. 8, pp. 653–670, 2021, doi: 10.1016/S1474-4422(21)00095-8.

[67] J. G. Adams and E. R. Melhem, “Clinical usefulness of T2-weighted fluid-attenuated inversion recovery MR imaging of the CNS.,” *Am. J. Roentgenol.*, vol. 172, no. 2, pp. 529–536, Feb. 1999, doi: 10.2214/ajr.172.2.9930818.

[68] K. Y. Wang, T. A. Uribe, and C. M. Lincoln, “Comparing lesion detection of

infratentorial multiple sclerosis lesions between T2-weighted spin-echo, 2D-FLAIR, and 3D-FLAIR sequences," *Clin. Imaging*, vol. 51, pp. 229–234, 2018, doi: 10.1016/j.clinimag.2018.05.017.

[69] P. Polak, C. Magnano, R. Zivadinov, and G. Poloni, "3D FLAIRED: 3D fluid attenuated inversion recovery for enhanced detection of lesions in multiple sclerosis.," *Magn. Reson. Med.*, vol. 68, no. 3, pp. 874–881, Sep. 2012, doi: 10.1002/mrm.23289.

[70] K. P. Whittall, A. L. MacKay, D. A. Graeb, R. A. Nugent, D. K. Li, and D. W. Paty, "In vivo measurement of T2 distributions and water contents in normal human brain.," *Magn. Reson. Med.*, vol. 37, no. 1, pp. 34–43, Jan. 1997, doi: 10.1002/mrm.1910370107.

[71] A. MacKay, C. Laule, I. Vavasour, T. Bjarnason, S. Kolind, and B. Mädler, "Insights into brain microstructure from the T2 distribution," *Magn. Reson. Imaging*, vol. 24, no. 4, pp. 515–525, 2006, doi: 10.1016/j.mri.2005.12.037.

[72] C. Laule *et al.*, "Long T2 water in multiple sclerosis: What else can we learn from multi-echo T2 relaxation?," *J. Neurol.*, vol. 254, no. 11, pp. 1579–1587, 2007, doi: 10.1007/s00415-007-0595-7.

[73] C. Laule *et al.*, "Water content and myelin water fraction in multiple sclerosis. A T2 relaxation study.," *J. Neurol.*, vol. 251, no. 3, pp. 284–293, Mar. 2004, doi: 10.1007/s00415-004-0306-6.

[74] J. Oh, E. T. Han, D. Pelletier, and S. J. Nelson, "Measurement of in vivo multi-component

T2 relaxation times for brain tissue using multi-slice T2 prep at 1.5 and 3 T.," *Magn. Reson. Imaging*, vol. 24, no. 1, pp. 33–43, Jan. 2006, doi: 10.1016/j.mri.2005.10.016.

[75] D. J. Tozer, G. R. Davies, D. R. Altmann, D. H. Miller, and P. S. Tofts, "Correlation of apparent myelin measures obtained in multiple sclerosis patients and controls from magnetization transfer and multicompartmental T2 analysis.," *Magn. Reson. Med.*, vol. 53, no. 6, pp. 1415–1422, Jun. 2005, doi: 10.1002/mrm.20479.

[76] T. D. Faizy *et al.*, "Heterogeneity of Multiple Sclerosis Lesions in Multislice Myelin Water Imaging," *PLoS One*, vol. 11, no. 3, p. e0151496, Mar. 2016, doi: 10.1371/journal.pone.0151496.

[77] I. M. Vavasour *et al.*, "Longitudinal changes in myelin water fraction in two MS patients with active disease.," *J. Neurol. Sci.*, vol. 276, no. 1–2, pp. 49–53, Jan. 2009, doi: 10.1016/j.jns.2008.08.022.

[78] M. Neema *et al.*, "3 T MRI relaxometry detects T2 prolongation in the cerebral normal-appearing white matter in multiple sclerosis.," *Neuroimage*, vol. 46, no. 3, pp. 633–641, Jul. 2009, doi: 10.1016/j.neuroimage.2009.03.001.

[79] T. M. Shepherd *et al.*, "New rapid, accurate T(2) quantification detects pathology in normal-appearing brain regions of relapsing-remitting MS patients," *NeuroImage. Clin.*, vol. 14, pp. 363–370, Feb. 2017, doi: 10.1016/j.nicl.2017.01.029.

[80] E. Papadaki *et al.*, "T2 Relaxometry Evidence of Microstructural Changes in Diffusely

Abnormal White Matter in Relapsing–Remitting Multiple Sclerosis and Clinically Isolated Syndrome: Impact on Visuomotor Performance," *J. Magn. Reson. Imaging*, vol. 54, no. 4, pp. 1077–1087, Oct. 2021, doi: 10.1002/jmri.27661.

[81] K. P. Whittall, A. L. MacKay, D. K. B. Li, I. M. Vavasour, C. K. Jones, and D. W. Paty, "Normal-appearing white matter in multiple sclerosis has heterogeneous, diffusely prolonged T(2).," *Magn. Reson. Med.*, vol. 47, no. 2, pp. 403–408, Feb. 2002, doi: 10.1002/mrm.10076.

[82] R. M. Gracien *et al.*, "Assessment of cortical damage in early multiple sclerosis with quantitative T2 relaxometry," *NMR Biomed.*, vol. 29, no. 4, pp. 444–450, Apr. 2016, doi: 10.1002/nbm.3486.

[83] R. M. Lebel, A. Eissa, P. Seres, G. Blevins, and A. H. Wilman, "Quantitative high-field imaging of sub-cortical gray matter in multiple sclerosis," *Mult. Scler. J.*, vol. 18, no. 4, pp. 433–441, Oct. 2011, doi: 10.1177/1352458511428464.

[84] A. Burgetova, Z. Seidl, J. Krasensky, D. Horakova, and M. Vaneckova, "Multiple Sclerosis and the Accumulation of Iron in the Basal Ganglia: Quantitative Assessment of Brain Iron Using MRI T_2 Relaxometry," *Eur. Neurol.*, vol. 63, no. 3, pp. 136–143, 2010, doi: 10.1159/000279305.

[85] H. Y. Carr and E. M. Purcell, "Effects of Diffusion on Free Precession in Nuclear Magnetic Resonance Experiments," *Phys. Rev.*, vol. 94, no. 3, pp. 630–638, May 1954, doi: 10.1103/PhysRev.94.630.

[86] S. Meiboom and D. Gill, “Modified Spin_Echo Method for Measuring Nuclear Relaxation Times,” *Rev. Sci. Instrum.*, vol. 29, pp. 688–691, 1958.

[87] P. Röschmann, “Radiofrequency penetration and absorption in the human body: limitations to high-field whole-body nuclear magnetic resonance imaging.,” *Med. Phys.*, vol. 14, no. 6, pp. 922–931, 1987, doi: 10.1118/1.595995.

[88] J. M. Jin, J. Chen, W. C. Chew, H. Gan, R. L. Magin, and P. J. Dimbylow, “Computation of electromagnetic fields for high-frequency magnetic resonance imaging applications.,” *Phys. Med. Biol.*, vol. 41, no. 12, pp. 2719–2738, Dec. 1996, doi: 10.1088/0031-9155/41/12/011.

[89] R. M. Lebel and A. H. Wilman, “Transverse relaxometry with stimulated echo compensation,” *Magn. Reson. Med.*, vol. 64, no. 4, pp. 1005–1014, Oct. 2010, doi: 10.1002/mrm.22487.

[90] M. N. Uddin, R. Marc Lebel, and A. H. Wilman, “Transverse relaxometry with reduced echo train lengths via stimulated echo compensation,” *Magn. Reson. Med.*, vol. 70, no. 5, pp. 1340–1346, Nov. 2013, doi: 10.1002/mrm.24568.

[91] N. Ben-Eliezer, D. K. Sodickson, and K. T. Block, “Rapid and accurate T2 mapping from multi–spin-echo data using Bloch-simulation-based reconstruction,” *Magn. Reson. Med.*, vol. 73, no. 2, pp. 809–817, 2015.

[92] J. Pauly, P. Le Roux, D. Nishimura, and A. Macovski, “Parameter relations for the

Shinnar-Le Roux selective excitation pulse design algorithm [NMR imaging].," *IEEE Trans. Med. Imaging*, vol. 10, no. 1, pp. 53–65, 1991, doi: 10.1109/42.75611.

[93] K. C. McPhee and A. H. Wilman, "Transverse relaxation and flip angle mapping: Evaluation of simultaneous and independent methods using multiple spin echoes," *Magn. Reson. Med.*, vol. 77, no. 5, pp. 2057–2065, May 2017, doi: 10.1002/mrm.26285.

[94] A. B. Einstein, "Über die von der molekularkinetischen theorie der wärme geforderte bewegung von in ruhenden flüssigkeiten suspendierten teilchen," 1905.

[95] D. Le Bihan, "Apparent diffusion coefficient and beyond: what diffusion MR imaging can tell us about tissue structure.," *Radiology*, vol. 268, no. 2. United States, pp. 318–322, Aug. 2013, doi: 10.1148/radiol.13130420.

[96] P. J. Basser, J. Mattiello, and D. LeBihan, "MR diffusion tensor spectroscopy and imaging.," *Biophys. J.*, vol. 66, no. 1, pp. 259–267, Jan. 1994, doi: 10.1016/S0006-3495(94)80775-1.

[97] C. Beaulieu, "The basis of anisotropic water diffusion in the nervous system – a technical review," *NMR Biomed.*, vol. 15, no. 7–8, pp. 435–455, Nov. 2002, doi: 10.1002/nbm.782.

[98] C. Pierpaoli, P. Jezzard, P. J. Basser, A. Barnett, and G. Di Chiro, "Diffusion tensor MR imaging of the human brain.," *Radiology*, vol. 201, no. 3, pp. 637–648, Dec. 1996, doi: 10.1148/radiology.201.3.8939209.

[99] S. Mori and J. Zhang, "Principles of Diffusion Tensor Imaging and Its Applications to

Basic Neuroscience Research," *Neuron*, vol. 51, no. 5, pp. 527–539, 2006, doi: 10.1016/j.neuron.2006.08.012.

[100] E. O. Stejskal and J. E. Tanner, "Spin Diffusion Measurements: Spin Echoes in the Presence of a Time-Dependent Field Gradient," *J. Chem. Phys.*, vol. 42, no. 1, pp. 288–292, Jan. 1965, doi: 10.1063/1.1695690.

[101] D. V. Cabrera, J. O. D. García, and G. Sarty, "Diffusion-weighted magnetic resonance imaging attenuation factors and their selection for cancer diagnosis and monitoring," *Crit. Rev. Biomed. Eng.*, vol. 43, no. 2–3, pp. 201–212, 2015, doi: 10.1615/critrevbiomedeng.2015013734.

[102] K. K. Kwong, R. C. McKinstry, D. Chien, A. P. Crawley, J. D. Pearlman, and B. R. Rosen, "CSF-suppressed quantitative single-shot diffusion imaging.," *Magn. Reson. Med.*, vol. 21, no. 1, pp. 157–163, Sep. 1991, doi: 10.1002/mrm.1910210120.

[103] J. C. Falconer and P. A. Narayana, "Cerebrospinal fluid-suppressed high-resolution diffusion imaging of human brain," *Magn. Reson. Med.*, vol. 37, no. 1, pp. 119–123, Jan. 1997, doi: 10.1002/mrm.1910370117.

[104] L. Concha, D. W. Gross, and C. Beaulieu, "Diffusion tensor tractography of the limbic system," *Am. J. Neuroradiol.*, vol. 26, no. 9, pp. 2267–2274, 2005.

[105] P. Mansfield and I. L. Pykett, "Biological and medical imaging by NMR," *J. Magn. Reson.*, vol. 29, no. 2, pp. 355–373, 1978, doi: 10.1016/0022-2364(78)90159-2.

[106] J. Pipe, “Chapter 2 - Pulse sequences for diffusion-weighted MRI”. In: Diffusion MRI, pp. 11-35, 2009. Elsevier Inc. doi:10.1016/B978-0-12-374709-9.00002-XEds. San Diego: Academic Press, 2009, pp. 11–35.

[107] A. L. Alexander, J. S. Tsuruda, and D. L. Parker, “Elimination of eddy current artifacts in diffusion-weighted echo-planar images: The use of bipolar gradients,” *Magn. Reson. Med.*, vol. 38, no. 6, pp. 1016–1021, Dec. 1997, doi: 10.1002/mrm.1910380623.

[108] N. G. Papadakis, T. Smponias, J. Berwick, and J. E. W. Mayhew, “k-space correction of eddy-current-induced distortions in diffusion-weighted echo-planar imaging.,” *Magn. Reson. Med.*, vol. 53, no. 5, pp. 1103–1111, May 2005, doi: 10.1002/mrm.20429.

[109] J. C. Haselgrove and J. R. Moore, “Correction for distortion of echo-planar images used to calculate the apparent diffusion coefficient.,” *Magn. Reson. Med.*, vol. 36, no. 6, pp. 960–964, Dec. 1996, doi: 10.1002/mrm.1910360620.

[110] J. L. R. Andersson and S. N. Sotiropoulos, “An integrated approach to correction for off-resonance effects and subject movement in diffusion MR imaging.,” *Neuroimage*, vol. 125, pp. 1063–1078, Jan. 2016, doi: 10.1016/j.neuroimage.2015.10.019.

[111] M. Blaimer, F. Breuer, M. Mueller, R. M. Heidemann, M. A. Griswold, and P. M. Jakob, “SMASH, SENSE, PILS, GRAPPA: how to choose the optimal method.,” *Top. Magn. Reson. Imaging*, vol. 15, no. 4, pp. 223–236, Aug. 2004, doi: 10.1097/01.rmr.0000136558.09801.dd.

[112] J. F. Glockner, H. H. Hu, D. W. Stanley, L. Angelos, and K. King, “Parallel MR imaging: a user’s guide.,” *Radiogr. a Rev. Publ. Radiol. Soc. North Am. Inc*, vol. 25, no. 5, pp. 1279–1297, 2005, doi: 10.1148/rg.255045202.

[113] J. G. Pipe, “Motion correction with PROPELLER MRI: Application to head motion and free-breathing cardiac imaging,” *Magn. Reson. Med.*, vol. 42, no. 5, pp. 963–969, 1999, doi: 10.1002/(SICI)1522-2594(199911)42:5<963::AID-MRM17>3.0.CO;2-L.

[114] C. B. Ahn, J. H. Kim, and Z. H. Cho, “High-speed spiral-scan echo planar NMR imaging-I.,” *IEEE Trans. Med. Imaging*, vol. 5, no. 1, pp. 2–7, 1986, doi: 10.1109/TMI.1986.4307732.

[115] P. W. Schaefer, P. E. Grant, and R. G. Gonzalez, “Diffusion-weighted MR imaging of the brain.,” *Radiology*, vol. 217, no. 2, pp. 331–345, Nov. 2000, doi: 10.1148/radiology.217.2.r00nv24331.

[116] P. J. Basser, “Inferring microstructural features and the physiological state of tissues from diffusion-weighted images.,” *NMR Biomed.*, vol. 8, no. 7–8, pp. 333–344, 1995, doi: 10.1002/nbm.1940080707.

[117] K. M. Curran, L. Emsell, and A. Leemans, “Quantitative DTI Measures BT” - In: “Diffusion Tensor Imaging: A Practical Handbook,” W. Van Hecke, L. Emsell, and S. Sunaert, Eds. New York, NY: Springer New York, 2016, pp. 65–87.

[118] L. Emsell, W. Van Hecke, and J.-D. Tournier, “Introduction to Diffusion Tensor Imaging”

- In: “Diffusion Tensor Imaging: A Practical Handbook,” W. Van Hecke, L. Emsell, and S. Sunaert, Eds. New York, NY: Springer New York, 2016, pp. 7–19.

[119] P. J. Basser and C. Pierpaoli, “Microstructural and Physiological Features of Tissues Elucidated by Quantitative-Diffusion-Tensor MRI,” *J. Magn. Reson. Ser. B*, vol. 111, no. 3, pp. 209–219, 1996, doi: 10.1006/jmrb.1996.0086.

[120] M. Filippi, M. Cercignani, M. Inglese, M. A. Horsfield, and G. Comi, “Diffusion tensor magnetic resonance imaging in multiple sclerosis.,” *Neurology*, vol. 56, no. 3, pp. 304–311, Feb. 2001, doi: 10.1212/wnl.56.3.304.

[121] S. K. Song, S. W. Sun, W. K. Ju, S. J. Lin, A. H. Cross, and A. H. Neufeld, “Diffusion tensor imaging detects and differentiates axon and myelin degeneration in mouse optic nerve after retinal ischemia,” *Neuroimage*, vol. 20, no. 3, pp. 1714–1722, 2003, doi: 10.1016/j.neuroimage.2003.07.005.

[122] E. Sbardella, F. Tona, N. Petsas, and P. Pantano, “DTI Measurements in Multiple Sclerosis: Evaluation of Brain Damage and Clinical Implications,” *Mult. Scler. Int.*, vol. 2013, p. 671730, 2013, doi: 10.1155/2013/671730.

[123] D. K. Jones, “Studying connections in the living human brain with diffusion MRI,” *Cortex*, vol. 44, no. 8, pp. 936–952, 2008, doi: 10.1016/j.cortex.2008.05.002.

[124] D. K. Jones, T. R. Knösche, and R. Turner, “White matter integrity, fiber count, and other fallacies: The do’s and don’ts of diffusion MRI,” *Neuroimage*, vol. 73, pp. 239–254, 2013,

doi: 10.1016/j.neuroimage.2012.06.081.

[125] F. Fink *et al.*, "The association between California Verbal Learning Test performance and fibre impairment in multiple sclerosis: evidence from diffusion tensor imaging," *Mult. Scler. J.*, vol. 16, no. 3, pp. 332–341, Feb. 2010, doi: 10.1177/1352458509356367.

[126] A. Klistorner *et al.*, "Diffusivity in the core of chronic multiple sclerosis lesions," *PLoS One*, vol. 13, no. 4, p. e0194142, Apr. 2018, doi: 10.1371/journal.pone.0194142.

[127] S. K. Song, S. W. Sun, M. J. Ramsbottom, C. Chang, J. Russell, and A. H. Cross, "Dysmyelination revealed through MRI as increased radial (but unchanged axial) diffusion of water," *Neuroimage*, vol. 17, no. 3, pp. 1429–1436, 2002, doi: 10.1006/nimg.2002.1267.

[128] J. D. Tournier, S. Mori, and A. Leemans, "Diffusion tensor imaging and beyond," *Magn. Reson. Med.*, vol. 65, no. 6, pp. 1532–1556, Jun. 2011, doi: 10.1002/mrm.22924.

[129] D. C. Alexander, G. J. Barker, and S. R. Arridge, "Detection and modeling of non-Gaussian apparent diffusion coefficient profiles in human brain data," *Magn. Reson. Med.*, vol. 48, no. 2, pp. 331–340, 2002, doi: 10.1002/mrm.10209.

[130] B. Jeurissen, A. Leemans, J.-D. Tournier, D. K. Jones, and J. Sijbers, "Investigating the prevalence of complex fiber configurations in white matter tissue with diffusion magnetic resonance imaging.," *Hum. Brain Mapp.*, vol. 34, no. 11, pp. 2747–2766, Nov. 2013, doi: 10.1002/hbm.22099.

[131] S. Mohammadi, H. E. Möller, H. Kugel, D. K. Müller, and M. Deppe, “Correcting eddy current and motion effects by affine whole-brain registrations: evaluation of three-dimensional distortions and comparison with slicewise correction.,” *Magn. Reson. Med.*, vol. 64, no. 4, pp. 1047–1056, Oct. 2010, doi: 10.1002/mrm.22501.

[132] G. K. Rohde, A. S. Barnett, P. J. Basser, S. Marenco, and C. Pierpaoli, “Comprehensive approach for correction of motion and distortion in diffusion-weighted MRI,” *Magn. Reson. Med.*, vol. 51, no. 1, pp. 103–114, Jan. 2004, doi: 10.1002/mrm.10677.

[133] A. Leemans and D. K. Jones, “The B-matrix must be rotated when correcting for subject motion in DTI data,” *Magn. Reson. Med.*, vol. 61, no. 6, pp. 1336–1349, Jun. 2009, doi: 10.1002/mrm.21890.

[134] S. Klein, M. Staring, K. Murphy, M. A. Viergever, and J. P. W. Pluim, “elastix: a toolbox for intensity-based medical image registration.,” *IEEE Trans. Med. Imaging*, vol. 29, no. 1, pp. 196–205, Jan. 2010, doi: 10.1109/TMI.2009.2035616.

[135] D. Perrone, J. Aelterman, A. Pižurica, B. Jeurissen, W. Philips, and A. Leemans, “The effect of Gibbs ringing artifacts on measures derived from diffusion MRI,” *Neuroimage*, vol. 120, pp. 441–455, 2015, doi: 10.1016/j.neuroimage.2015.06.068.

[136] S. Treit, T. Steve, D. W. Gross, and C. Beaulieu, “High resolution in-vivo diffusion imaging of the human hippocampus.,” *Neuroimage*, vol. 182, pp. 479–487, Feb. 2018, doi: 10.1016/j.neuroimage.2018.01.034.

[137] J. Veraart, E. Fieremans, and D. S. Novikov, “Diffusion MRI noise mapping using random matrix theory,” *Magn. Reson. Med.*, vol. 76, no. 5, pp. 1582–1593, Nov. 2016, doi: 10.1002/mrm.26059.

[138] H.-H. Lee, D. S. Novikov, and E. Fieremans, “Removal of partial Fourier-induced Gibbs (RPG) ringing artifacts in MRI.,” *Magn. Reson. Med.*, vol. 86, no. 5, pp. 2733–2750, Nov. 2021, doi: 10.1002/mrm.28830.

[139] S. A. Sarra, “Digital total variation filtering as postprocessing for Chebyshev pseudospectral methods for conservation laws,” *Numer. Algorithms*, vol. 41, no. 1, pp. 17–33, 2006, doi: 10.1007/s11075-005-9003-5.

[140] R. L. Lagore and R. L. Lagore, “University of Alberta,” *Neurosurgery*, vol. 5, no. 1, p. 182, 2013, doi: 10.1227/00006123-197907010-00116.

[141] N. J. Tustison *et al.*, “N4ITK: improved N3 bias correction.,” *IEEE Trans. Med. Imaging*, vol. 29, no. 6, pp. 1310–1320, Jun. 2010, doi: 10.1109/TMI.2010.2046908.

[142] S. M. Smith *et al.*, “Tract-based spatial statistics: Voxelwise analysis of multi-subject diffusion data,” *Neuroimage*, vol. 31, no. 4, pp. 1487–1505, 2006, doi: 10.1016/j.neuroimage.2006.02.024.

[143] M. Bach *et al.*, “Methodological considerations on tract-based spatial statistics (TBSS),” *Neuroimage*, vol. 100, pp. 358–369, 2014, doi: 10.1016/j.neuroimage.2014.06.021.

[144] M. Wilson, C. R. Tench, P. S. Morgan, and L. D. Blumhardt, “Pyramidal tract mapping by

diffusion tensor magnetic resonance imaging in multiple sclerosis: improving correlations with disability," *J. Neurol. Neurosurg. & Psychiatry*, vol. 74, no. 2, pp. 203–207, Feb. 2003, doi: 10.1136/jnnp.74.2.203.

[145] K. C. Kern, J. Sarcona, M. Montag, B. S. Giesser, and N. L. Sicotte, "Corpus callosal diffusivity predicts motor impairment in relapsing–remitting multiple sclerosis: A TBSS and tractography study," *Neuroimage*, vol. 55, no. 3, pp. 1169–1177, 2011, doi: 10.1016/j.neuroimage.2010.10.077.

[146] S. Mori, B. J. Crain, V. P. Chacko, and P. C. M. Van Zijl, "Three-dimensional tracking of axonal projections in the brain by magnetic resonance imaging," *Ann. Neurol.*, vol. 45, no. 2, pp. 265–269, Feb. 1999, doi: 10.1002/1531-8249(199902)45:2<265::AID-ANA21>3.0.CO;2-3.

[147] J.-D. Tournier, F. Calamante, M. D. King, D. G. Gadian, and A. Connelly, "Limitations and requirements of diffusion tensor fiber tracking: An assessment using simulations," *Magn. Reson. Med.*, vol. 47, no. 4, pp. 701–708, 2002, doi: 10.1002/mrm.10116.

[148] B. Jeurissen, M. Descoteaux, S. Mori, and A. Leemans, "Diffusion MRI fiber tractography of the brain," *NMR Biomed.*, vol. 32, no. 4, p. e3785, Apr. 2019, doi: 10.1002/nbm.3785.

[149] P. J. Basser, S. Pajevic, C. Pierpaoli, J. Duda, and A. Aldroubi, "In vivo fiber tractography using DT-MRI data," *Magn. Reson. Med.*, vol. 44, no. 4, pp. 625–632, 2000, doi: 10.1002/1522-2594(200010)44:4<625::AID-MRM17>3.0.CO;2-O.

[150] D. S. Tuch, T. G. Reese, M. R. Wiegell, N. Makris, J. W. Belliveau, and V. J. Wedeen, "High angular resolution diffusion imaging reveals intravoxel white matter fiber heterogeneity.," *Magn. Reson. Med.*, vol. 48, no. 4, pp. 577–582, Oct. 2002, doi: 10.1002/mrm.10268.

[151] J.-D. Tournier, F. Calamante, and A. Connelly, "Robust determination of the fibre orientation distribution in diffusion MRI: Non-negativity constrained super-resolved spherical deconvolution," *Neuroimage*, vol. 35, no. 4, pp. 1459–1472, 2007, doi: 10.1016/j.neuroimage.2007.02.016.

[152] J. H. Jensen, J. A. Helpern, A. Ramani, H. Lu, and K. Kaczynski, "Diffusional kurtosis imaging: the quantification of non-gaussian water diffusion by means of magnetic resonance imaging.," *Magn. Reson. Med.*, vol. 53, no. 6, pp. 1432–1440, Jun. 2005, doi: 10.1002/mrm.20508.

[153] J. H. Jensen and J. A. Helpern, "MRI quantification of non-Gaussian water diffusion by kurtosis analysis," *NMR Biomed.*, vol. 23, no. 7, pp. 698–710, 2010.

[154] J.-D. Tournier, F. Calamante, D. G. Gadian, and A. Connelly, "Direct estimation of the fiber orientation density function from diffusion-weighted MRI data using spherical deconvolution," *Neuroimage*, vol. 23, no. 3, pp. 1176–1185, 2004, doi: 10.1016/j.neuroimage.2004.07.037.

[155] H. Zhang, T. Schneider, C. A. Wheeler-Kingshott, and D. C. Alexander, "NODDI: Practical in vivo neurite orientation dispersion and density imaging of the human brain,"

Neuroimage, vol. 61, no. 4, pp. 1000–1016, 2012, doi: 10.1016/j.neuroimage.2012.03.072.

[156] H. Zhang, P. L. Hubbard, G. J. M. Parker, and D. C. Alexander, "Axon diameter mapping in the presence of orientation dispersion with diffusion MRI," *Neuroimage*, vol. 56, no. 3, pp. 1301–1315, 2011, doi: 10.1016/j.neuroimage.2011.01.084.

[157] T. Schneider, W. Brownlee, H. Zhang, O. Ciccarelli, D. H. Miller, and C. G. Wheeler-Kingshott, "Sensitivity of multi-shell NODDI to multiple sclerosis white matter changes: a pilot study.," *Funct. Neurol.*, vol. 32, no. 2, pp. 97–101, 2017, doi: 10.11138/fneur/2017.32.2.097.

[158] S. De Santis *et al.*, "Characterizing Microstructural Tissue Properties in Multiple Sclerosis with Diffusion MRI at 7 T and 3 T: The Impact of the Experimental Design," *Neuroscience*, vol. 403, pp. 17–26, 2019, doi: 10.1016/j.neuroscience.2018.03.048.

[159] T. Granberg *et al.*, "In vivo characterization of cortical and white matter neuroaxonal pathology in early multiple sclerosis," *Brain*, vol. 140, no. 11, pp. 2912–2926, Nov. 2017, doi: 10.1093/brain/awx247.

[160] C. F. Westin *et al.*, "Q-space trajectory imaging for multidimensional diffusion MRI of the human brain," *Neuroimage*, vol. 135, pp. 345–362, 2016, doi: 10.1016/j.neuroimage.2016.02.039.

[161] F. Szczepankiewicz *et al.*, "The link between diffusion MRI and tumor heterogeneity: Mapping cell eccentricity and density by diffusional variance decomposition (DIVIDE),"

Neuroimage, vol. 142, pp. 522–532, 2016, doi: 10.1016/j.neuroimage.2016.07.038.

[162] G. Yang, Q. Tian, C. Leuze, M. Wintermark, and J. A. McNab, "Double diffusion encoding MRI for the clinic," *Magn. Reson. Med.*, vol. 80, no. 2, pp. 507–520, 2018, doi: 10.1002/mrm.27043.

[163] S. Lasič, F. Szczepankiewicz, S. Eriksson, M. Nilsson, and D. Topgaard, "Microanisotropy imaging: quantification of microscopic diffusion anisotropy and orientational order parameter by diffusion MRI with magic-angle spinning of the q-vector ," *Frontiers in Physics* , vol. 2. 2014. Available: https://www.frontiersin.org/article/10.3389/fphy.2014.00011.

[164] S. Eriksson, S. Lasic, and D. Topgaard, "Isotropic diffusion weighting in PGSE NMR by magic-angle spinning of the q-vector.," *J. Magn. Reson.*, vol. 226, pp. 13–18, Jan. 2013, doi: 10.1016/j.jmr.2012.10.015.

[165] D. Topgaard, "Isotropic diffusion weighting in PGSE NMR: Numerical optimization of the q-MAS PGSE sequence," *Microporous Mesoporous Mater.*, vol. 178, pp. 60–63, 2013, doi: 10.1016/j.micromeso.2013.03.009.

[166] F. Szczepankiewicz, J. Sjölund, F. Ståhlberg, J. Lätt, and M. Nilsson, "Tensor-valued diffusion encoding for diffusional variance decomposition (DIVIDE): Technical feasibility in clinical MRI systems," *PLoS One*, vol. 14, no. 3, pp. 1–20, 2019, doi: 10.1371/journal.pone.0214238.

[167] F. Szczepankiewicz, “Imaging diffusional variance by MRI: The role of tensor-valued diffusion encoding and tissue heterogeneity”, Lund University, Faculty of Science, Department of Medical Radiation Physics, 2016.

[168] P. P. Mitra, “Multiple wave-vector extensions of the NMR pulsed-field-gradient spin-echo diffusion measurement,” *Phys. Rev. B*, vol. 51, no. 21, pp. 15074–15078, Jun. 1995, doi: 10.1103/PhysRevB.51.15074.

[169] F. Szczepankiewicz *et al.*, “Quantification of microscopic diffusion anisotropy disentangles effects of orientation dispersion from microstructure: Applications in healthy volunteers and in brain tumors,” *Neuroimage*, vol. 104, pp. 241–252, 2015, doi: 10.1016/j.neuroimage.2014.09.057.

[170] S. N. Jespersen, H. Lundell, C. K. Sønderby, and T. B. Dyrby, “Orientationally invariant metrics of apparent compartment eccentricity from double pulsed field gradient diffusion experiments.,” *NMR Biomed.*, vol. 26, no. 12, pp. 1647–1662, Dec. 2013, doi: 10.1002/nbm.2999.

[171] J. H. Jensen, E. S. Hui, and J. A. Helpern, “Double-pulsed diffusional kurtosis imaging,” *NMR Biomed.*, vol. 27, no. 4, pp. 363–370, Apr. 2014, doi: 10.1002/nbm.3094.

[172] K. W. Andersen *et al.*, “Disentangling white-matter damage from physiological fibre orientation dispersion in multiple sclerosis,” *Brain Commun.*, vol. 2, no. 2, Jun. 2020, doi: 10.1093/braincomms/fcaa077.

[173] Multiple Sclerosis International Federation, “Atlas of MS 3rd edition,” *Mult. Scler. Int. Fed. (MSIF)*, Sept. 2020, pp. 1–37.

[174] B. Kjetil *et al.*, “Longitudinal analysis reveals high prevalence of Epstein-Barr virus associated with multiple sclerosis,” *Science*, vol. 375, no. 6578, pp. 296–301, Jan. 2022, doi: 10.1126/science.abj8222.

[175] F. D. Lublin *et al.*, “Defining the clinical course of multiple sclerosis: The 2013 revisions,” *Neurology*, vol. 83, no. 3, pp. 278–286, Jul. 2014, doi: 10.1212/WNL.0000000000000560.

[176] M. Hosseiny, S. D. Newsome, and D. M. Yousem, “Radiologically Isolated Syndrome: A Review for Neuroradiologists,” *Am. J. Neuroradiol.*, vol. 41, no. 9, pp. 1542 LP – 1549, Sep. 2020, doi: 10.3174/ajnr.A6649.

[177] D. Miller, F. Barkhof, X. Montalban, A. Thompson, and M. Filippi, “Clinically isolated syndromes suggestive of multiple sclerosis, part I: natural history, pathogenesis, diagnosis, and prognosis.,” *Lancet. Neurol.*, vol. 4, no. 5, pp. 281–288, May 2005, doi: 10.1016/S1474-4422(05)70071-5.

[178] T. L. Neurology, “Setting new standards in multiple sclerosis care and research,” *Lancet Neurol.*, vol. 11, no. 10, p. 835, 2012, doi: 10.1016/S1474-4422(12)70214-4.

[179] M. Rovaris, C. Confavreux, R. Furlan, L. Kappos, G. Comi, and M. Filippi, “Secondary progressive multiple sclerosis: current knowledge and future challenges.,” *Lancet.*

Neurol., vol. 5, no. 4, pp. 343–354, Apr. 2006, doi: 10.1016/S1474-4422(06)70410-0.

[180] D. Ontaneda and R. J. Fox, "Progressive multiple sclerosis," *Curr. Opin. Neurol.*, vol. 28, no. 3, pp. 237–243, Jun. 2015, doi: 10.1097/WCO.0000000000000195.

[181] D. Miljković and I. Spasojević, "Multiple sclerosis: molecular mechanisms and therapeutic opportunities," *Antioxid. Redox Signal.*, vol. 19, no. 18, pp. 2286–2334, Dec. 2013, doi: 10.1089/ars.2012.5068.

[182] B. F. G. Popescu, I. Pirko, and C. F. Lucchinetti, "Pathology of multiple sclerosis: where do we stand?," *Continuum (Minneap. Minn).*, vol. 19, no. 4 Multiple Sclerosis, pp. 901–921, Aug. 2013, doi: 10.1212/01.CON.0000433291.23091.65.

[183] B. D. Trapp and K.-A. Nave, "Multiple sclerosis: an immune or neurodegenerative disorder?," *Annu. Rev. Neurosci.*, vol. 31, pp. 247–269, 2008, doi: 10.1146/annurev.neuro.30.051606.094313.

[184] I. Loma and R. Heyman, "Multiple sclerosis: pathogenesis and treatment.," *Curr. Neuropharmacol.*, vol. 9, no. 3, pp. 409–416, Sep. 2011, doi: 10.2174/157015911796557911.

[185] E. M. Frohman, M. K. Racke, and C. S. Raine, "Multiple sclerosis--the plaque and its pathogenesis.," *N. Engl. J. Med.*, vol. 354, no. 9, pp. 942–955, Mar. 2006, doi: 10.1056/NEJMra052130.

[186] H. Lassmann, "Multiple Sclerosis Pathology.," *Cold Spring Harb. Perspect. Med.*, vol. 8,

no. 3, Mar. 2018, doi: 10.1101/cshperspect.a028936.

[187] L. Bø, C. A. Vedeler, H. I. Nyland, B. D. Trapp, and S. J. Mørk, “Subpial demyelination in the cerebral cortex of multiple sclerosis patients.,” *J. Neuropathol. Exp. Neurol.*, vol. 62, no. 7, pp. 723–732, Jul. 2003, doi: 10.1093/jnen/62.7.723.

[188] M. Pardini, J. W. L. Brown, R. Magliozzi, R. Reynolds, and D. T. Chard, “Surface-in pathology in multiple sclerosis: a new view on pathogenesis?,” *Brain*, vol. 144, no. 6, pp. 1646–1654, Jun. 2021, doi: 10.1093/brain/awab025.

[189] M. Vercellino *et al.*, “Demyelination, inflammation, and neurodegeneration in multiple sclerosis deep gray matter.,” *J. Neuropathol. Exp. Neurol.*, vol. 68, no. 5, pp. 489–502, May 2009, doi: 10.1097/NEN.0b013e3181a19a5a.

[190] J. J. G. Geurts *et al.*, “Extensive hippocampal demyelination in multiple sclerosis.,” *J. Neuropathol. Exp. Neurol.*, vol. 66, no. 9, pp. 819–827, Sep. 2007, doi: 10.1097/nen.0b013e3181461f54.

[191] C. C. Park *et al.*, “Detection of Cortical and Deep Gray Matter Lesions in Multiple Sclerosis Using DIR and FLAIR at 3T.,” *J. neuroimaging Off. J. Am. Soc. Neuroimaging*, vol. 31, no. 2, pp. 408–414, Mar. 2021, doi: 10.1111/jon.12822.

[192] A. Kutzelnigg *et al.*, “Cortical demyelination and diffuse white matter injury in multiple sclerosis.,” *Brain*, vol. 128, no. Pt 11, pp. 2705–2712, Nov. 2005, doi: 10.1093/brain/awh641.

[193] R. Magliozzi, R. Reynolds, and M. Calabrese, “MRI of cortical lesions and its use in studying their role in MS pathogenesis and disease course,” *Brain Pathol.*, vol. 28, no. 5, pp. 735–742, Sep. 2018, doi: 10.1111/bpa.12642.

[194] C. P. Gilmore, L. Bö, T. Owens, J. Lowe, M. M. Esiri, and N. Evangelou, “Spinal Cord Gray Matter Demyelination in Multiple Sclerosis—A Novel Pattern of Residual Plaque Morphology,” *Brain Pathol.*, vol. 16, no. 3, pp. 202–208, Jul. 2006, doi: 10.1111/j.1750-3639.2006.00018.x.

[195] J. Sastre-Garriga *et al.*, “Spinal cord grey matter atrophy in Multiple Sclerosis clinical practice,” *Neurosci. Informatics*, vol. 2, no. 2, p. 100071, 2022, doi: 10.1016/j.neuri.2022.100071.

[196] M. Bussas *et al.*, “Multiple sclerosis lesions and atrophy in the spinal cord: Distribution across vertebral levels and correlation with disability,” *NeuroImage Clin.*, vol. 34, p. 103006, 2022, doi: 10.1016/j.nicl.2022.103006.

[197] R. J. Bevan *et al.*, “Meningeal inflammation and cortical demyelination in acute multiple sclerosis.,” *Ann. Neurol.*, vol. 84, no. 6, pp. 829–842, Dec. 2018, doi: 10.1002/ana.25365.

[198] L. Haider *et al.*, “The topograpy of demyelination and neurodegeneration in the multiple sclerosis brain,” *Brain*, vol. 139, no. Pt 3, pp. 807–815, Mar. 2016, doi: 10.1093/brain/awv398.

[199] S. Luchetti, N. L. Fransen, C. G. van Eden, V. Ramaglia, M. Mason, and I. Huitinga,

"Progressive multiple sclerosis patients show substantial lesion activity that correlates with clinical disease severity and sex: a retrospective autopsy cohort analysis.," *Acta Neuropathol.*, vol. 135, no. 4, pp. 511–528, Apr. 2018, doi: 10.1007/s00401-018-1818-y.

[200] C. Elliott *et al.*, "Chronic white matter lesion activity predicts clinical progression in primary progressive multiple sclerosis.," *Brain*, vol. 142, no. 9, pp. 2787–2799, Sep. 2019, doi: 10.1093/brain/awz212.

[201] M. Absinta *et al.*, "Association of Chronic Active Multiple Sclerosis Lesions With Disability In Vivo," *JAMA Neurol.*, vol. 76, no. 12, pp. 1474–1483, Dec. 2019, doi: 10.1001/jamaneurol.2019.2399.

[202] M. Absinta, H. Lassmann, and B. D. Trapp, "Mechanisms underlying progression in multiple sclerosis," *Curr. Opin. Neurol.*, vol. 33, no. 3, pp. 277–285, Jun. 2020, doi: 10.1097/WCO.0000000000000818.

[203] S. R. Choi *et al.*, "Meningeal inflammation plays a role in the pathology of primary progressive multiple sclerosis.," *Brain*, vol. 135, no. Pt 10, pp. 2925–2937, Oct. 2012, doi: 10.1093/brain/aws189.

[204] G. Giovannoni *et al.*, "Smouldering multiple sclerosis: the 'real MS,'" *Ther. Adv. Neurol. Disord.*, vol. 15, p. 17562864211066752, Jan. 2022, doi: 10.1177/17562864211066751.

[205] S. Singh *et al.*, "Relationship of acute axonal damage, Wallerian degeneration, and clinical disability in multiple sclerosis," *J. Neuroinflammation*, vol. 14, no. 1, p. 57, 2017,

doi: 10.1186/s12974-017-0831-8.

[206] A. Compston and A. Coles, “Multiple sclerosis,” *Lancet*, vol. 372, no. 9648, pp. 1502–1517, 2008, doi: 10.1016/S0140-6736(08)61620-7.

[207] J. M. Gelfand, “Multiple sclerosis: diagnosis, differential diagnosis, and clinical presentation.,” *Handb. Clin. Neurol.*, vol. 122, pp. 269–290, 2014, doi: 10.1016/B978-0-444-52001-2.00011-X.

[208] S. M. Rao, G. J. Leo, L. Bernardin, and F. Unverzagt, “Cognitive dysfunction in multiple sclerosis. I. Frequency, patterns, and prediction.,” *Neurology*, vol. 41, no. 5, pp. 685–691, May 1991, doi: 10.1212/wnl.41.5.685.

[209] Z. Keser *et al.*, “Limbic Pathway Correlates of Cognitive Impairment in Multiple Sclerosis,” *J. Neuroimaging*, vol. 27, no. 1, pp. 37–42, Jan. 2017, doi: 10.1111/jon.12381.

[210] Z. Keser *et al.*, “Quantitative limbic system mapping of main cognitive domains in multiple sclerosis,” *Front. Neurol.*, vol. 9, no. MAR, pp. 1–12, 2018, doi: 10.3389/fneur.2018.00132.

[211] D. Damjanovic *et al.*, “Hippocampal and deep gray matter nuclei atrophy is relevant for explaining cognitive impairment in MS: A multicenter study,” *Am. J. Neuroradiol.*, vol. 38, no. 1, pp. 18–24, 2017, doi: 10.3174/ajnr.A4952.

[212] P. Preziosa *et al.*, “Structural MRI correlates of cognitive impairment in patients with multiple sclerosis: A Multicenter Study,” *Hum. Brain Mapp.*, vol. 37, no. 4, pp. 1627–

1644, Apr. 2016, doi: 10.1002/hbm.23125.

[213] S. D. Roosendaal *et al.*, “Structural and Functional Hippocampal Changes in Multiple Sclerosis Patients with Intact Memory Function,” *Radiology*, vol. 255, no. 2, pp. 595–604, Apr. 2010, doi: 10.1148/radiol.10091433.

[214] L. Bö, S. Mörk, P. A. Kong, H. Nyland, C. A. Pardo, and B. D. Trapp, “Detection of MHC class II-antigens on macrophages and microglia, but not on astrocytes and endothelia in active multiple sclerosis lesions,” *J. Neuroimmunol.*, vol. 51, no. 2, pp. 135–146, 1994, doi: 10.1016/0165-5728(94)90075-2.

[215] B. D. Trapp, J. Peterson, R. M. Ransohoff, R. Rudick, S. Mörk, and L. Bö, “Axonal Transection in the Lesions of Multiple Sclerosis,” *N. Engl. J. Med.*, vol. 338, no. 5, pp. 278–285, Jan. 1998, doi: 10.1056/NEJM199801293380502.

[216] C. Lucchinetti, W. Brück, J. Parisi, B. Scheithauer, M. Rodriguez, and H. Lassmann, “Heterogeneity of multiple sclerosis lesions: Implications for the pathogenesis of demyelination,” *Ann. Neurol.*, vol. 47, no. 6, pp. 707–717, Jun. 2000, doi: 10.1002/1531-8249(200006)47:6<707::AID-ANA3>3.0.CO;2-Q.

[217] P. Van Der Valk and C. J. A. De Groot, “Staging of multiple sclerosis (MS) lesions: pathology of the time frame of MS,” *Neuropathol. Appl. Neurobiol.*, vol. 26, no. 1, pp. 2–10, 2000, doi: 10.1046/j.1365-2990.2000.00217.x.

[218] H. Lassmann, C. S. Raine, J. Antel, and J. W. Prineas, “Immunopathology of multiple

sclerosis: Report on an international meeting held at the Institute of Neurology of the University of Vienna," *J. Neuroimmunol.*, vol. 86, no. 2, pp. 213–217, 1998, doi: 10.1016/S0165-5728(98)00031-9.

[219] T. Kuhlmann, S. Ludwin, A. Prat, J. Antel, W. Brück, and H. Lassmann, "An updated histological classification system for multiple sclerosis lesions," *Acta Neuropathol.*, vol. 133, no. 1, pp. 13–24, 2017, doi: 10.1007/s00401-016-1653-y.

[220] W. I. McDonald *et al.*, "Recommended diagnostic criteria for multiple sclerosis: Guidelines from the international panel on the diagnosis of multiple sclerosis," *Ann. Neurol.*, vol. 50, no. 1, pp. 121–127, Jul. 2001, doi: 10.1002/ana.1032.

[221] A. J. Thompson *et al.*, "Diagnosis of multiple sclerosis: 2017 revisions of the McDonald criteria," *Lancet Neurol.*, vol. 17, no. 2, pp. 162–173, 2018, doi: 10.1016/S1474-4422(17)30470-2.

[222] B. Uitdehaag *et al.*, "Impact of exposure to interferon beta-1a on outcomes in patients with relapsing-remitting multiple sclerosis: exploratory analyses from the PRISMS long-term follow-up study.," *Ther. Adv. Neurol. Disord.*, vol. 4, no. 1, pp. 3–14, Jan. 2011, doi: 10.1177/1756285610391693.

[223] R. Rudick, C. Polman, D. Clifford, D. Miller, and L. Steinman, "Natalizumab: Bench to Bedside and Beyond," *JAMA Neurol.*, vol. 70, no. 2, pp. 172–182, Feb. 2013, doi: 10.1001/jamaneurol.2013.598.

[224] J. A. Cohen *et al.*, “Fingolimod versus intramuscular interferon in patient subgroups from TRANSFORMS.,” *J. Neurol.*, vol. 260, no. 8, pp. 2023–2032, Aug. 2013, doi: 10.1007/s00415-013-6932-0.

[225] S. L. Hauser *et al.*, “Safety of Ocrelizumab in Patients With Relapsing and Primary Progressive Multiple Sclerosis,” *Neurology*, vol. 97, no. 16, p. e1546 LP-e1559, Oct. 2021, doi: 10.1212/WNL.0000000000012700.

[226] A. Traboulsee *et al.*, “Revised Recommendations of the Consortium of MS Centers Task Force for a Standardized MRI Protocol and Clinical Guidelines for the Diagnosis and Follow-Up of Multiple Sclerosis,” *Am. J. Neuroradiol.*, vol. 37, no. 3, pp. 394 LP – 401, Mar. 2016, doi: 10.3174/ajnr.A4539.

[227] P. Eisele *et al.*, “Reduced Diffusion in a Subset of Acute MS Lesions: A Serial Multiparametric MRI Study,” *Am. J. Neuroradiol.*, vol. 33, no. 7, pp. 1369 LP – 1373, Aug. 2012, doi: 10.3174/ajnr.A2975.

[228] P. Sati, I. C. George, C. D. Shea, M. I. Gaitán, and D. S. Reich, “FLAIR*: A Combined MR Contrast Technique for Visualizing White Matter Lesions and Parenchymal Veins,” *Radiology*, vol. 265, no. 3, pp. 926–932, Dec. 2012, doi: 10.1148/radiol.12120208.

[229] M. A. Clarke *et al.*, “Value of 3T Susceptibility-Weighted Imaging in the Diagnosis of Multiple Sclerosis,” *Am. J. Neuroradiol.*, vol. 41, no. 6, pp. 1001– 1008, Jun. 2020, doi: 10.3174/ajnr.A6547.

[230] A. Traboulsee *et al.*, “Disability in multiple sclerosis is related to normal appearing brain tissue MTR histogram abnormalities,” *Mult. Scler. J.*, vol. 9, no. 6, pp. 566–573, Dec. 2003, doi: 10.1191/1352458503ms958oa.

[231] S. H. Kolind *et al.*, “Complementary information from multi-exponential T2 relaxation and diffusion tensor imaging reveals differences between multiple sclerosis lesions.,” *Neuroimage*, vol. 40, no. 1, pp. 77–85, Mar. 2008, doi: 10.1016/j.neuroimage.2007.11.033.

[232] R. Bammer *et al.*, “Magnetic resonance diffusion tensor imaging for characterizing diffuse and focal white matter abnormalities in multiple sclerosis,” *Magn. Reson. Med.*, vol. 44, no. 4, pp. 583–591, Oct. 2000, doi: 10.1002/1522-2594(200010)44:4<583::AID-MRM12>3.0.CO;2-O.

[233] A. Eshaghi *et al.*, “Deep gray matter volume loss drives disability worsening in multiple sclerosis,” *Ann. Neurol.*, vol. 83, no. 2, pp. 210–222, 2018, doi: 10.1002/ana.25145.

[234] H. B. W. Larsson, C. Thomsen, J. Frederiksen, M. Stubgaard, and O. Henriksen, “In vivo magnetic resonance diffusion measurement in the brain of patients with multiple sclerosis,” *Magn. Reson. Imaging*, vol. 10, no. 1, pp. 7–12, 1992, doi: 10.1016/0730-725X(92)90367-9.

[235] M. A. Horsfield *et al.*, “Apparent diffusion coefficients in benign and secondary progressive multiple sclerosis by nuclear magnetic resonance,” *Magn. Reson. Med.*, vol. 36, no. 3, pp. 393–400, Sep. 1996, doi: 10.1002/mrm.1910360310.

[236] M. A. van Walderveen *et al.*, “Histopathologic correlate of hypointense lesions on T1-weighted spin-echo MRI in multiple sclerosis.,” *Neurology*, vol. 50, no. 5, pp. 1282–1288, May 1998, doi: 10.1212/wnl.50.5.1282.

[237] A. Castriota-Scanderbeg *et al.*, “Diffusion of water in large demyelinating lesions: a follow-up study.,” *Neuroradiology*, vol. 44, no. 9, pp. 764–767, Sep. 2002, doi: 10.1007/s00234-002-0806-y.

[238] M. Inglese and M. Bester, “Diffusion imaging in multiple sclerosis: research and clinical implications,” *NMR Biomed.*, vol. 23, no. 7, pp. 865–872, Aug. 2010, doi: 10.1002/nbm.1515.

[239] A. C. Guo, V. L. Jewells, and J. M. Provenzale, “Analysis of Normal-Appearing White Matter in Multiple Sclerosis: Comparison of Diffusion Tensor MR Imaging and Magnetization Transfer Imaging,” *Am. J. Neuroradiol.*, vol. 22, no. 10, pp. 1893 LP – 1900, Nov. 2001.

[240] O. Ciccarelli *et al.*, “Investigation of MS normal-appearing brain using diffusion tensor MRI with clinical correlations.,” *Neurology*, vol. 56, no. 7, pp. 926–933, Apr. 2001, doi: 10.1212/wnl.56.7.926.

[241] L. Testaverde, L. Caporali, E. Venditti, G. Grillea, and C. Colonnese, “Diffusion tensor imaging applications in multiple sclerosis patients using 3T magnetic resonance: a preliminary study,” *Eur. Radiol.*, vol. 22, no. 5, pp. 990–997, 2012, doi: 10.1007/s00330-011-2342-9.

[242] A. Klistorner, C. Wang, C. Yiannikas, S. L. Graham, J. Parratt, and M. H. Barnett, "Progressive Injury in Chronic Multiple Sclerosis Lesions Is Gender-Specific: A DTI Study," *PLoS One*, vol. 11, no. 2, p. e0149245, Feb. 2016, doi: 10.1371/journal.pone.0149245.

[243] M. Filippi, G. Iannucci, M. Cercignani, M. Assunta Rocca, A. Pratesi, and G. Comi, "A Quantitative Study of Water Diffusion in Multiple Sclerosis Lesions and Normal-Appearing White Matter Using Echo-Planar Imaging," *Arch. Neurol.*, vol. 57, no. 7, pp. 1017–1021, Jul. 2000, doi: 10.1001/archneur.57.7.1017.

[244] M. Cercignani, G. Iannucci, M. A. Rocca, G. Comi, M. A. Horsfield, and M. Filippi, "Pathologic damage in MS assessed by diffusion-weighted and magnetization transfer MRI," *Neurology*, vol. 54, no. 5, pp. 1139 LP – 1144, Mar. 2000, doi: 10.1212/WNL.54.5.1139.

[245] M. A. Rocca, M. Cercignani, G. Iannucci, G. Comi, and M. Filippi, "Weekly diffusion-weighted imaging of normal-appearing white matter in MS," *Neurology*, vol. 55, no. 6, pp. 882 LP – 884, Sep. 2000, doi: 10.1212/WNL.55.6.882.

[246] J. Chen *et al.*, "Magnetic resonance diffusion tensor imaging for occult lesion detection in multiple sclerosis," *Exp Ther Med*, vol. 13, no. 1, pp. 91–96, 2017, doi: 10.3892/etm.2016.3950.

[247] S.-H. Kim *et al.*, "Diffusion tensor imaging of normal-appearing white matter in patients with neuromyelitis optica spectrum disorder and multiple sclerosis.," *Eur. J. Neurol.*, vol.

24, no. 7, pp. 966–973, Jul. 2017, doi: 10.1111/ene.13321.

[248] M. Rovaris *et al.*, “Assessment of Normal-Appearing White and Gray Matter in Patients With Primary Progressive Multiple Sclerosis: A Diffusion-Tensor Magnetic Resonance Imaging Study,” *Arch. Neurol.*, vol. 59, no. 9, pp. 1406–1412, Sep. 2002, doi: 10.1001/archneur.59.9.1406.

[249] A. Pulizzi *et al.*, “Determinants of Disability in Multiple Sclerosis at Various Disease Stages: A Multiparametric Magnetic Resonance Study,” *Arch. Neurol.*, vol. 64, no. 8, pp. 1163–1168, Aug. 2007, doi: 10.1001/archneur.64.8.1163.

[250] C. A. M. Wheeler-Kingshott and M. Cercignani, “About ‘axial’ and ‘radial’ diffusivities,” *Magn. Reson. Med.*, vol. 61, no. 5, pp. 1255–1260, May 2009, doi: 10.1002/mrm.21965.

[251] A. Asaf, S. Evan, and A. Anat, “Injury to white matter tracts in relapsing-remitting multiple sclerosis: A possible therapeutic window within the first 5 years from onset using diffusion-tensor imaging tract-based spatial statistics,” *NeuroImage. Clin.*, vol. 8, pp. 261–266, Apr. 2015, doi: 10.1016/j.nicl.2015.04.020.

[252] M. E. K. A. ElSayed, M. M. B. El-Toukhy, R. E. Asaad, and O. A. El-Serafy, “Diffusion tensor imaging for assessment of normally appearing white matter of the brain and spinal cord in cases of multiple sclerosis: a multi-parametric correlation in view of patient’s clinical status,” *Egypt. J. Radiol. Nucl. Med.*, vol. 50, no. 1, p. 30, 2019, doi: 10.1186/s43055-019-0031-x.

[253] M. S. Vishwas, T. Chitnis, R. Pienaar, B. C. Healy, and P. E. Grant, “Tract-based analysis of callosal, projection, and association pathways in pediatric patients with multiple sclerosis: A preliminary study,” *Am. J. Neuroradiol.*, vol. 31, no. 1, pp. 121–128, 2010, doi: 10.3174/ajnr.A1776.

[254] A. Ozturk *et al.*, “MRI of the corpus callosum in multiple sclerosis: association with disability,” *Mult. Scler.*, vol. 16, no. 2, pp. 166–177, Feb. 2010, doi: 10.1177/1352458509353649.

[255] R. A. Dineen *et al.*, “Disconnection as a mechanism for cognitive dysfunction in multiple sclerosis,” *Brain*, vol. 132, no. 1, pp. 239–249, 2009, doi: 10.1093/brain/awn275.

[256] R. A. Dineen, C. M. Bradshaw, C. S. Constantinescu, and D. P. Auer, “Extra-Hippocampal Subcortical Limbic Involvement Predicts Episodic Recall Performance in Multiple Sclerosis,” *PLoS One*, vol. 7, no. 10, 2012, doi: 10.1371/journal.pone.0044942.

[257] K. A. Koenig *et al.*, “High spatial and angular resolution diffusion-weighted imaging reveals forniceal damage related to memory impairment,” *Magn. Reson. Imaging*, vol. 31, no. 5, pp. 695–699, Jun. 2013, doi: 10.1016/j.mri.2012.10.030.

[258] S. Mesaros *et al.*, “Diffusion tensor MRI tractography and cognitive impairment in multiple sclerosis,” *Neurology*, vol. 78, no. 13, pp. 969–975, 2012, doi: 10.1212/WNL.0b013e31824d5859.

[259] M. Pardini, M. Bergamino, G. Bommarito, L. Bonzano, G. Luigi Mancardi, and L.

Roccatagliata, “Structural correlates of subjective and objective memory performance in multiple sclerosis,” *Hippocampus*, vol. 24, no. 4, pp. 436–445, Apr. 2014, doi: 10.1002/hipo.22237.

[260] S. B. Syc, D. M. Harrison, S. Saidha, M. Seigo, P. A. Calabresi, and D. S. Reich, “Quantitative MRI Demonstrates Abnormality of the Fornix and Cingulum in Multiple Sclerosis,” *Mult. Scler. Int.*, vol. 2013, pp. 1–9, 2013, doi: 10.1155/2013/838719.

[261] J. P. Aggleton and M. W. Brown, “Aggleton 1999,” *Behav. Brain Sci.*, vol. 22, no. 3, pp. 425–489, 1999.

[262] A. Ceccarelli *et al.*, “A multiparametric evaluation of regional brain damage in patients with primary progressive multiple sclerosis,” *Hum. Brain Mapp.*, vol. 30, no. 9, pp. 3009–3019, Sep. 2009, doi: 10.1002/hbm.20725.

[263] F. Zhou, C.-S. Zee, H. Gong, M. Shiroishi, and J. Li, “Differential Changes in Deep and Cortical Gray Matters of Patients With Multiple Sclerosis: A Quantitative Magnetic Resonance Imaging Study,” *J. Comput. Assist. Tomogr.*, vol. 34, no. 3, 2010.

[264] M. Bozzali, M. Cercignani, M. P. Sormani, G. Comi, and M. Filippi, “Quantification of Brain Gray Matter Damage in Different MS Phenotypes by Use of Diffusion Tensor MR Imaging,” *Am. J. Neuroradiol.*, vol. 23, no. 6, pp. 985–988, Jun. 2002

[265] A. J. Fabiano *et al.*, “Thalamic Involvement in Multiple Sclerosis: A Diffusion-Weighted Magnetic Resonance Imaging Study,” *J. Neuroimaging*, vol. 13, no. 4, pp. 307–314, Oct.

2006, doi: 10.1111/j.1552-6569.2003.tb00197.x.

[266] R. Natarajan *et al.*, “Diffusion Tensor Imaging in NAWM and NADGM in MS and CIS: Association with Candidate Biomarkers in Sera,” *Mult. Scler. Int.*, vol. 2013, p. 265259, 2013, doi: 10.1155/2013/265259.

[267] F. Tovar-Moll *et al.*, “Thalamic involvement and its impact on clinical disability in patients with multiple sclerosis: A diffusion tensor imaging study at 3T,” *Am. J. Neuroradiol.*, vol. 30, no. 7, pp. 1380–1386, 2009, doi: 10.3174/ajnr.A1564.

[268] C. Oreja-Guevara *et al.*, “Progressive Gray Matter Damage in Patients With Relapsing-Remitting Multiple Sclerosis: A Longitudinal Diffusion Tensor Magnetic Resonance Imaging Study,” *Arch. Neurol.*, vol. 62, no. 4, pp. 578–584, Apr. 2005, doi: 10.1001/archneur.62.4.578.

[269] N. Bergsland, F. Schweser, M. G. Dwyer, B. Weinstock-Guttman, R. H. B. Benedict, and R. Zivadinov, “Thalamic white matter in multiple sclerosis: A combined diffusion-tensor imaging and quantitative susceptibility mapping study,” *Hum. Brain Mapp.*, vol. 39, no. 10, pp. 4007–4017, 2018, doi: 10.1002/hbm.24227.

[270] L. Debernard *et al.*, “Deep grey matter MRI abnormalities and cognitive function in relapsing-remitting multiple sclerosis,” *Psychiatry Res. - Neuroimaging*, vol. 234, no. 3, pp. 352–361, 2015, doi: 10.1016/j.pscychresns.2015.10.004.

[271] S. Hannoun *et al.*, “Diffusion tensor-MRI evidence for extra-axonal neuronal degeneration

in caudate and thalamic nuclei of patients with multiple sclerosis," *Am. J. Neuroradiol.*, vol. 33, no. 7, pp. 1363–1368, 2012, doi: 10.3174/ajnr.A2983.

[272] K. A. Meijer *et al.*, "White matter tract abnormalities are associated with cognitive dysfunction in secondary progressive multiple sclerosis," *Mult. Scler. J.*, vol. 22, no. 11, pp. 1429–1437, Jan. 2016, doi: 10.1177/1352458515622694.

[273] B. Bodini, Z. Khaleeli, M. Cercignani, D. H. Miller, A. J. Thompson, and O. Ciccarelli, "Exploring the relationship between white matter and gray matter damage in early primary progressive multiple sclerosis: An in vivo study with TBSS and VBM," *Hum. Brain Mapp.*, vol. 30, no. 9, pp. 2852–2861, Sep. 2009, doi: 10.1002/hbm.20713.

[274] K. C. Kern *et al.*, "Thalamic-hippocampal-prefrontal disruption in relapsing-remitting multiple sclerosis," *NeuroImage Clin.*, vol. 8, pp. 440–447, 2015, doi: 10.1016/j.nicl.2014.12.015.

[275] C. Louapre *et al.*, "Is the Relationship between Cortical and White Matter Pathologic Changes in Multiple Sclerosis Spatially Specific? A Multimodal 7-T and 3-T MR Imaging Study with Surface and Tract-based Analysis," *Radiology*, vol. 278, no. 2, pp. 524–535, Sep. 2015, doi: 10.1148/radiol.2015150486.

[276] Y. Assaf and O. Pasternak, "Diffusion tensor imaging (DTI)-based white matter mapping in brain research: A review," *J. Mol. Neurosci.*, vol. 34, no. 1, pp. 51–61, 2008, doi: 10.1007/s12031-007-0029-0.

[277] S. B. Vos, D. K. Jones, M. A. Viergever, and A. Leemans, “Partial volume effect as a hidden covariate in DTI analyses,” *Neuroimage*, vol. 55, no. 4, pp. 1566–1576, 2011, doi: 10.1016/j.neuroimage.2011.01.048.

[278] D. Ontaneda *et al.*, “Deep grey matter injury in multiple sclerosis: A NAIMS consensus statement,” *Brain*, no. 2021, 2021, doi: 10.1093/brain/awab132.

[279] C. Bjartmar, J. R. Wujek, and B. D. Trapp, “Axonal loss in the pathology of MS: Consequences for understanding the progressive phase of the disease,” *J. Neurol. Sci.*, vol. 206, no. 2, pp. 165–171, 2003, doi: 10.1016/S0022-510X(02)00069-2.

[280] T. Welton, D. Kent, C. S. Constantinescu, D. P. Auer, and R. A. Dineen, “Functionally relevant white matter degradation in multiple sclerosis: a tract-based spatial meta-analysis.,” *Radiology*, vol. 275, no. 1, pp. 89–96, Apr. 2015, doi: 10.1148/radiol.14140925.

[281] S. D. Roosendaal *et al.*, “Regional DTI differences in multiple sclerosis patients,” *Neuroimage*, vol. 44, no. 4, pp. 1397–1403, 2009, doi: 10.1016/j.neuroimage.2008.10.026.

[282] K. C. Kern *et al.*, “Fornix damage limits verbal memory functional compensation in multiple sclerosis,” *Neuroimage*, vol. 59, no. 3, pp. 2932–2940, 2012, doi: 10.1016/j.neuroimage.2011.09.071.

[283] H. J. Yu *et al.*, “Multiple white matter tract abnormalities underlie cognitive impairment in RRMS,” *Neuroimage*, vol. 59, no. 4, pp. 3713–3722, 2012, doi:

10.1016/j.neuroimage.2011.10.053.

[284] M. Catani and M. T. De Schotten, “Atlas of human brain connections”. Oxford University Press, 2012. ISBN: 9780198729372.

[285] Q. van Geest *et al.*, “Fronto-limbic disconnection in patients with multiple sclerosis and depression,” *Mult. Scler. J.*, 2018, doi: 10.1177/1352458518767051.

[286] P. Preziosa, M. a Rocca, and D. Caputo, “Intrinsic Damage to the Major White Matter Tracts in Patients with Different Clinical Phenotypes of Multiple Sclerosis : A Voxelwise Diffusion Tensor MR Study,” *Radiology*, vol. 260, no. 2, pp. 541–550, 2011, doi: 10.1148/radiol.11110315/-/DC1.

[287] A. Leemans, B. Jeurissen, J. Sijbers, and D. K. Jones, “ExploreDTI: a graphical toolbox for processing, analyzing, and visualizing diffusion MR data,” *Proc. Int. Soc. Magn. Reson. Med.*, vol. 17, no. 2, p. 3537, 2009.

[288] N. Malykhin, L. Concha, P. Seres, C. Beaulieu, and N. J. Coupland, “Diffusion tensor imaging tractography and reliability analysis for limbic and paralimbic white matter tracts,” *Psychiatry Res. - Neuroimaging*, vol. 164, no. 2, pp. 132–142, 2008, doi: 10.1016/j.pscychresns.2007.11.007.

[289] E. C. Tallantyre *et al.*, “Greater loss of axons in primary progressive multiple sclerosis plaques compared to secondary progressive disease,” *Brain*, vol. 132, no. 5, pp. 1190–1199, 2009, doi: 10.1093/brain/awp106.

[290] T. Kuhlmann, “Acute axonal damage in multiple sclerosis is most extensive in early disease stages and decreases over time,” *Brain*, vol. 125, no. 10, pp. 2202–2212, 2002, doi: 10.1093/brain/awf235.

[291] T. Kuhlmann, “Relapsing–remitting and primary progressive MS have the same cause(s)-the neuropathologist’s view: 2,” *Mult. Scler. J.*, vol. 19, no. 3, pp. 268–269, Feb. 2013, doi: 10.1177/1352458513476563.

[292] Z. Matejčíková *et al.*, “Cerebrospinal fluid inflammatory markers in patients with multiple sclerosis: a pilot study,” *J. Neural Transm.*, vol. 122, no. 2, pp. 273–277, 2015, doi: 10.1007/s00702-014-1244-9.

[293] B. T. Gold *et al.*, “White matter integrity is associated with cerebrospinal fluid markers of Alzheimer’s disease in normal adults.,” *Neurobiol. Aging*, vol. 35, no. 10, pp. 2263–2271, Oct. 2014, doi: 10.1016/j.neurobiolaging.2014.04.030.

[294] I. Huitinga, C. J. A. De Groot, P. Van der Valk, W. Kamphorst, F. J. H. Tilders, and D. F. Swaab, “Hypothalamic Lesions in Multiple Sclerosis,” *J. Neuropathol. Exp. Neurol.*, vol. 60, no. 12, pp. 1208–1218, Dec. 2001, doi: 10.1093/jnen/60.12.1208.

[295] N. Sahin, R. Selouan, C. E. Markowitz, E. R. Melhem, and M. Bilello, “Limbic pathway lesions in patients with multiple sclerosis,” *Acta radiol.*, vol. 57, no. 3, pp. 341–347, Apr. 2015, doi: 10.1177/0284185115578689.

[296] R. Dutta *et al.*, “Demyelination causes synaptic alterations in hippocampi from multiple

sclerosis patients.," *Ann. Neurol.*, vol. 69, no. 3, pp. 445–454, Mar. 2011, doi: 10.1002/ana.22337.

[297] A. R. Hoy, C. G. Koay, S. R. Kecskemeti, and A. L. Alexander, "Optimization of a free water elimination two-compartment model for diffusion tensor imaging," *Neuroimage*, vol. 103, pp. 323–333, 2014, doi: 10.1016/j.neuroimage.2014.09.053.

[298] A. R. Hoy, S. R. Kecskemeti, and A. L. Alexander, "Free water elimination diffusion tractography: A comparison with conventional and fluid-attenuated inversion recovery, diffusion tensor imaging acquisitions," *J. Magn. Reson. Imaging*, vol. 42, no. 6, pp. 1572–1581, Dec. 2015, doi: 10.1002/jmri.24925.

[299] E. J. Bubb, C. Metzler-Baddeley, and J. P. Aggleton, "The cingulum bundle: Anatomy, function, and dysfunction," *Neurosci. Biobehav. Rev.*, vol. 92, pp. 104–127, 2018, doi: 10.1016/j.neubiorev.2018.05.008.

[300] P. A. Keedwell, R. Chapman, K. Christiansen, H. Richardson, J. Evans, and D. K. Jones, "Cingulum White Matter in Young Women at Risk of Depression: The Effect of Family History and Anhedonia," *Biol. Psychiatry*, vol. 72, no. 4, pp. 296–302, 2012, doi: 10.1016/j.biopsych.2012.01.022.

[301] J.-H. Seok, S. Choi, H. K. Lim, S.-H. Lee, I. Kim, and B.-J. Ham, "Effect of the COMT val158met polymorphism on white matter connectivity in patients with major depressive disorder," *Neurosci. Lett.*, vol. 545, pp. 35–39, 2013, doi: 10.1016/j.neulet.2013.04.012.

[302] A. Feinstein, P. O'Connor, N. Akbar, L. Moradzadeh, C. J. M. Scott, and N. J. Lobaugh, "Diffusion tensor imaging abnormalities in depressed multiple sclerosis patients," *Mult. Scler. J.*, vol. 16, no. 2, pp. 189–196, Dec. 2009, doi: 10.1177/1352458509355461.

[303] C. A. Baron and C. Beaulieu, "Acquisition strategy to reduce cerebrospinal fluid partial volume effects for improved DTI tractography," *Magn. Reson. Med.*, vol. 73, no. 3, pp. 1075–1084, Mar. 2015, doi: 10.1002/mrm.25226.

[304] K. Hanken, P. Eling, and H. Hildebrandt, "Is there a cognitive signature for MS-related fatigue?," *Mult. Scler. J.*, vol. 21, no. 4, pp. 376–381, Sep. 2014, doi: 10.1177/1352458514549567.

[305] A. Takeda *et al.*, "Impact of depression on mental fatigue and attention in patients with multiple sclerosis," *J. Affect. Disord. Reports*, vol. 5, p. 100143, 2021, doi: 10.1016/j.jadr.2021.100143.

[306] M. Niino *et al.*, "Apathy/depression, but not subjective fatigue, is related with cognitive dysfunction in patients with multiple sclerosis," *BMC Neurol.*, vol. 14, no. 1, p. 3, 2014, doi: 10.1186/1471-2377-14-3.

[307] C. G. Goetz and E. J. Pappert, "Textbook of clinical neurology, " W.B. Saunders, 1999. ISBN: 0721664237.

[308] S. Batista *et al.*, "Basal ganglia, thalamus and neocortical atrophy predicting slowed cognitive processing in multiple sclerosis," *J. Neurol.*, vol. 259, no. 1, pp. 139–146, 2012,

doi: 10.1007/s00415-011-6147-1.

[309] S. Magon *et al.*, “Volume loss in the deep gray matter and thalamic subnuclei: a longitudinal study on disability progression in multiple sclerosis,” *J. Neurol.*, vol. 267, no. 5, pp. 1536–1546, 2020, doi: 10.1007/s00415-020-09740-4.

[310] G. Pontillo *et al.*, “Determinants of deep gray matter atrophy in multiple sclerosis: A multimodal MRI study,” *Am. J. Neuroradiol.*, vol. 40, no. 1, pp. 99–106, 2019, doi: 10.3174/ajnr.A5915.

[311] N. L. Sicotte *et al.*, “Regional hippocampal atrophy in multiple sclerosis,” *Brain*, vol. 131, no. 4, pp. 1134–1141, Apr. 2008, doi: 10.1093/brain/awn030.

[312] D. Valdés Cabrera, R. Stobbe, P. Smyth, F. Giuliani, D. Emery, and C. Beaulieu, “Diffusion tensor imaging tractography reveals altered fornix in all diagnostic subtypes of multiple sclerosis,” *Brain Behav.*, vol. 10, no. 1, pp. 1–16, 2020, doi: 10.1002/brb3.1514.

[313] R. Cappellani *et al.*, “Subcortical deep gray matter pathology in patients with multiple sclerosis is associated with white matter lesion burden and atrophy but not with cortical atrophy: A diffusion tensor MRI study,” *Am. J. Neuroradiol.*, vol. 39, no. 5, pp. 912–919, 2014, doi: 10.3174/ajnr.A3788.

[314] I. Koubiyr *et al.*, “Differential gray matter vulnerability in the 1 year following a clinically isolated syndrome,” *Front. Neurol.*, vol. 9, no. OCT, pp. 1–8, 2018, doi: 10.3389/fneur.2018.00824.

[315] S. J. Baetge, M. Filser, A. Renner, S. Ullrich, C. Lassek, and I. K. Penner, “On the validity of single tests, two-test combinations and the full Brief International Cognitive Assessment for Multiple Sclerosis (BICAMS) in detecting patients with cognitive impairment,” *Mult. Scler. J.*, vol. 26, no. 14, pp. 1919–1928, 2020, doi: 10.1177/1352458519887897.

[316] F. Corfield and D. Langdon, “A Systematic Review and Meta-Analysis of the Brief Cognitive Assessment for Multiple Sclerosis (BICAMS),” *Neurol. Ther.*, vol. 7, no. 2, pp. 287–306, 2018, doi: 10.1007/s40120-018-0102-3.

[317] A. Busse, A. Hensel, U. Gühne, M. C. Angermeyer, and S. G. Riedel-Heller, “Mild cognitive impairment,” *Neurology*, vol. 67, no. 12, pp. 2176 LP – 2185, Dec. 2006, doi: 10.1212/01.wnl.0000249117.23318.e1.

[318] J. V. Manjón and P. Coupé, “Volbrain: An online MRI brain volumetry system,” *Front. Neuroinform.*, vol. 10, no. JUL, pp. 1–14, 2016, doi: 10.3389/fninf.2016.00030.

[319] P. Coupé, T. Tourdias, P. Linck, J. E. Romero, and J. V. Manjón, “LesionBrain: An online tool for white matter lesion segmentation,” *Lect. Notes Comput. Sci. (including Subser. Lect. Notes Artif. Intell. Lect. Notes Bioinformatics)*, vol. 11075 LNCS, pp. 95–103, 2018, doi: 10.1007/978-3-030-00500-9_11.

[320] P. A. Yushkevich *et al.*, “User-guided 3D active contour segmentation of anatomical structures: Significantly improved efficiency and reliability,” *Neuroimage*, vol. 31, no. 3, pp. 1116–1128, 2006, doi: 10.1016/j.neuroimage.2006.01.015.

[321] D. Lakens, “Calculating and reporting effect sizes to facilitate cumulative science: a practical primer for t-tests and ANOVAs,” *Frontiers in Psychology*, vol. 4. p. 863, 2013. Available: https://www.frontiersin.org/article/10.3389/fpsyg.2013.00863.

[322] M. A. Nowrangi and P. B. Rosenberg, “The fornix in mild cognitive impairment and Alzheimer’s disease,” *Front. Aging Neurosci.*, vol. 7, p. 1, Jan. 2015, doi: 10.3389/fnagi.2015.00001.

[323] L. Zhuang *et al.*, “Microstructural white matter changes, not hippocampal atrophy, detect early amnestic mild cognitive impairment,” *PLoS One*, vol. 8, no. 3, pp. e58887–e58887, 2013, doi: 10.1371/journal.pone.0058887.

[324] P. E. C. Klawiter, R. E. Schmidt, K. Trinkaus, H. F. Liang, M. D. Budde, R. T. Naismith, S. K. Song, A. H. Cross, T. L. Benzinger, “Radial diffusivity predicts demyelination in ex vivo multiple sclerosis spinal cords, ” Neuroimage, vol. 55, no. 4, pp. 1454–1460, 2011, doi: 10.1016/j.neuroimage.2011.01.007.

[325] A. Gajofatto, M. Calabrese, M. D. Benedetti, and S. Monaco, “Clinical, MRI, and CSF markers of disability progression in multiple sclerosis,” *Dis. Markers*, vol. 35, no. 6, pp. 687–699, 2013, doi: 10.1155/2013/484959.

[326] K. R. Mahajan, K. Nakamura, J. A. Cohen, B. D. Trapp, and D. Ontaneda, “Intrinsic and Extrinsic Mechanisms of Thalamic Pathology in Multiple Sclerosis,” *Ann. Neurol.*, vol. 88, no. 1, pp. 81–92, 2020, doi: 10.1002/ana.25743.

[327] B. D. Trapp *et al.*, “Evidence for synaptic stripping by cortical microglia,” *Glia*, vol. 55, no. 4, pp. 360–368, 2007.

[328] B. Audoin *et al.*, “Structure of WM bundles constituting the working memory system in early multiple sclerosis: A quantitative DTI tractography study,” *Neuroimage*, vol. 36, no. 4, pp. 1324–1330, 2007, doi: 10.1016/j.neuroimage.2007.04.038.

[329] V. Planche *et al.*, “Hippocampal microstructural damage correlates with memory impairment in clinically isolated syndrome suggestive of multiple sclerosis.,” *Mult. Scler.*, vol. 23, no. 9, pp. 1214–1224, Aug. 2017, doi: 10.1177/1352458516675750.

[330] C. Stadelmann, C. Wegner, and W. Brück, “Inflammation, demyelination, and degeneration - Recent insights from MS pathology,” *Biochim. Biophys. Acta - Mol. Basis Dis.*, vol. 1812, no. 2, pp. 275–282, 2011, doi: 10.1016/j.bbadis.2010.07.007.

[331] N. D. Chiaravalloti, J. Stojanovic-Radic, and J. Deluca, “The role of speed versus working memory in predicting learning new information in multiple sclerosis,” *J. Clin. Exp. Neuropsychol.*, vol. 35, no. 2, pp. 180–191, 2013, doi: 10.1080/13803395.2012.760537.

[332] R. H. Benedict, J. DeLuca, G. Phillips, N. LaRocca, L. D. Hudson, and R. Rudick, “Validity of the Symbol Digit Modalities Test as a cognition performance outcome measure for multiple sclerosis.,” *Mult. Scler.*, vol. 23, no. 5, pp. 721–733, Apr. 2017, doi: 10.1177/1352458517690821.

[333] J. Sandry, M. Zuppichini, J. Rothberg, Z. Valdespino-Hayden, and J. DeLuca, “Poor

Encoding and Weak Early Consolidation Underlie Memory Acquisition Deficits in Multiple Sclerosis: Retroactive Interference, Processing Speed, or Working Memory?," *Arch. Clin. Neuropsychol.*, vol. 34, no. 2, pp. 162–182, 2019, doi: 10.1093/arclin/acy029.

[334] K. Hänninen *et al.*, "Thalamic Atrophy Predicts 5-Year Disability Progression in Multiple Sclerosis ," *Frontiers in Neurology* , vol. 11. p. 606, 2020, doi: 10.3389/fneur.2020.00606.

[335] M. Palotai *et al.*, "History of fatigue in multiple sclerosis is associated with grey matter atrophy," *Sci. Rep.*, vol. 9, no. 1, pp. 1–10, 2019, doi: 10.1038/s41598-019-51110-2.

[336] E. Dobryakova, H. M. Genova, J. DeLuca, and G. R. Wylie, "The dopamine imbalance hypothesis of fatigue in multiple sclerosis and other neurological disorders," *Front. Neurol.*, vol. 6, p. 52, Mar. 2015, doi: 10.3389/fneur.2015.00052.

[337] E. Dobryakova, J. DeLuca, H. M. Genova, and G. R. Wylie, "Neural correlates of cognitive fatigue: Cortico-Striatal circuitry and effort-reward imbalance," *J. Int. Neuropsychol. Soc.*, vol. 19, no. 8, pp. 849–853, 2013, doi: 10.1017/S1355617713000684.

[338] R. H. B. Benedict and R. Zivadinov, "Risk factors for and management of cognitive dysfunction in multiple sclerosis," *Nat. Rev. Neurol.*, vol. 7, no. 6, pp. 332–342, 2011, doi: 10.1038/nrneurol.2011.61.

[339] J. F. Sumowski *et al.*, "Cognition in multiple sclerosis: State of the field and priorities for the future.," *Neurology*, vol. 90, no. 6, pp. 278–288, Feb. 2018, doi:

10.1212/WNL.0000000000004977.

[340] N. D. Chiaravalloti and J. DeLuca, “Cognitive impairment in multiple sclerosis.,” *Lancet. Neurol.*, vol. 7, no. 12, pp. 1139–1151, Dec. 2008, doi: 10.1016/S1474-4422(08)70259-X.

[341] I.-K. Penner, “Evaluation of cognition and fatigue in multiple sclerosis: daily practice and future directions,” *Acta Neurol. Scand.*, vol. 134, no. S200, pp. 19–23, Sep. 2016, doi: 10.1111/ane.12651.

[342] M. A. Rocca *et al.*, “The hippocampus in multiple sclerosis,” *Lancet Neurol.*, vol. 17, no. 10, pp. 918–926, 2018, doi: 10.1016/S1474-4422(18)30309-0.

[343] A. Feinstein, “The hippocampus and behaviour in multiple sclerosis,” *Lancet Neurol.*, vol. 17, no. 10, pp. 837–839, 2018, doi: 10.1016/S1474-4422(18)30324-7.

[344] L. R. Squire, C. E. L. Stark, and R. E. Clark, “The medial temporal lobe.,” *Annu. Rev. Neurosci.*, vol. 27, pp. 279–306, 2004, doi: 10.1146/annurev.neuro.27.070203.144130.

[345] A. J. McDonald and D. D. Mott, “Functional neuroanatomy of amygdalohippocampal interconnections and their role in learning and memory,” *J. Neurosci. Res.*, vol. 95, no. 3, pp. 797–820, Mar. 2017, doi: 10.1002/jnr.23709.

[346] M. Vercellino, F. Plano, B. Votta, R. Mutani, M. T. Giordana, and P. Cavalla, “Grey Matter Pathology in Multiple Sclerosis,” *J. Neuropathol. Exp. Neurol.*, vol. 64, no. 12, pp. 1101–1107, Dec. 2005, doi: 10.1097/01.jnen.0000190067.20935.42.

[347] D. Papadopoulos, S. Dukes, R. Patel, R. Nicholas, A. Vora, and R. Reynolds, “Substantial archaeocortical atrophy and neuronal loss in multiple sclerosis.,” *Brain Pathol.*, vol. 19, no. 2, pp. 238–253, Apr. 2009, doi: 10.1111/j.1750-3639.2008.00177.x.

[348] E.-J. Kooi *et al.*, “Cholinergic imbalance in the multiple sclerosis hippocampus,” *Acta Neuropathol.*, vol. 122, no. 3, pp. 313–322, 2011, doi: 10.1007/s00401-011-0849-4.

[349] M. Filippi and M. A. Rocca, “MR Imaging of Gray Matter Involvement in Multiple Sclerosis: Implications for Understanding Disease Pathophysiology and Monitoring Treatment Efficacy,” *Am. J. Neuroradiol.*, vol. 31, no. 7, pp. 1171–1177, Aug. 2010, doi: 10.3174/ajnr.A1944.

[350] S. D. Roosendaal *et al.*, “In vivo MR imaging of hippocampal lesions in multiple sclerosis,” *J. Magn. Reson. Imaging*, vol. 27, no. 4, pp. 726–731, Apr. 2008, doi: 10.1002/jmri.21294.

[351] M. A. Rocca *et al.*, “Hippocampal-DMN disconnectivity in MS is related to WM lesions and depression,” *Hum. Brain Mapp.*, vol. 36, no. 12, pp. 5051–5063, Dec. 2015, doi: 10.1002/hbm.22992.

[352] V. M. Anderson *et al.*, “Hippocampal atrophy in relapsing-remitting and primary progressive MS: a comparative study.,” *Mult. Scler.*, vol. 16, no. 9, pp. 1083–1090, Sep. 2010, doi: 10.1177/1352458510374893.

[353] K. A. Koenig *et al.*, “Hippocampal volume is related to cognitive decline and fornicial

diffusion measures in multiple sclerosis," *Magn. Reson. Imaging*, vol. 32, no. 4, pp. 354–358, May 2014, doi: 10.1016/j.mri.2013.12.012.

[354] C. A. Bishop *et al.*, "Analysis of ageing-associated grey matter volume in patients with multiple sclerosis shows excess atrophy in subcortical regions," *NeuroImage. Clin.*, vol. 13, pp. 9–15, Nov. 2016, doi: 10.1016/j.nicl.2016.11.005.

[355] G. Longoni *et al.*, "Deficits in memory and visuospatial learning correlate with regional hippocampal atrophy in MS," *Brain Struct. Funct.*, vol. 220, no. 1, pp. 435–444, 2015, doi: 10.1007/s00429-013-0665-9.

[356] V. Planche *et al.*, "Regional hippocampal vulnerability in early multiple sclerosis: Dynamic pathological spreading from dentate gyrus to CA1," *Hum. Brain Mapp.*, vol. 39, no. 4, pp. 1814–1824, Apr. 2018, doi: 10.1002/hbm.23970.

[357] S. M. Gold *et al.*, "Smaller cornu ammonis 2-3/dentate gyrus volumes and elevated cortisol in multiple sclerosis patients with depressive symptoms," *Biol. Psychiatry*, vol. 68, no. 6, pp. 553–559, Sep. 2010, doi: 10.1016/j.biopsych.2010.04.025.

[358] J. A. González Torre, Á. J. Cruz-Gómez, A. Belenguer, C. Sanchis-Segura, C. Ávila, and C. Forn, "Hippocampal dysfunction is associated with memory impairment in multiple sclerosis: A volumetric and functional connectivity study," *Mult. Scler. J.*, vol. 23, no. 14, pp. 1854–1863, Jan. 2017, doi: 10.1177/1352458516688349.

[359] M. A. Rocca *et al.*, "In vivo evidence of hippocampal dentate gyrus expansion in multiple

sclerosis," *Hum. Brain Mapp.*, vol. 36, no. 11, pp. 4702–4713, Nov. 2015, doi: 10.1002/hbm.22946.

[360] J. J. G. Geurts *et al.*, "MR spectroscopic evidence for thalamic and hippocampal, but not cortical, damage in multiple sclerosis," *Magn. Reson. Med.*, vol. 55, no. 3, pp. 478–483, Mar. 2006, doi: 10.1002/mrm.20792.

[361] D. Valdés Cabrera, P. Smyth, G. Blevins, D. Emery, and C. Beaulieu, "Diffusion imaging of fornix and interconnected limbic deep grey matter is linked to cognitive impairment in multiple sclerosis," *Eur. J. Neurosci.*, vol. 55, no. 1, pp. 277–294, Nov. 2021, doi: 10.1111/ejn.15539.

[362] S. Treit *et al.*, "Regional hippocampal diffusion abnormalities associated with subfield-specific pathology in temporal lobe epilepsy.," *Epilepsia open*, vol. 4, no. 4, pp. 544–554, Dec. 2019, doi: 10.1002/epi4.12357.

[363] G. P. Winston, S. B. Vos, J. L. Burdett, M. J. Cardoso, S. Ourselin, and J. S. Duncan, "Automated T2 relaxometry of the hippocampus for temporal lobe epilepsy," *Epilepsia*, vol. 58, no. 9, pp. 1645–1652, 2017, doi: 10.1111/epi.13843.

[364] M. J. Knight, A. Wearn, E. Coulthard, and R. A. Kauppinen, "T2 Relaxometry and Diffusion Tensor Indices of the Hippocampus and Entorhinal Cortex Improve Sensitivity and Specificity of MRI to Detect Amnestic Mild Cognitive Impairment and Alzheimer's Disease Dementia," *J. Magn. Reson. Imaging*, vol. 49, no. 2, pp. 445–455, 2019, doi: 10.1002/jmri.26195.

[365] P. Flachenecker *et al.*, “Fatigue in multiple sclerosis: A comparison of different rating scales and correlation to clinical parameters,” *Mult. Scler.*, vol. 8, no. 6, pp. 523–526, 2002, doi: 10.1191/1352458502ms839oa.

[366] J.-D. Tournier *et al.*, “MRtrix3: A fast, flexible and open software framework for medical image processing and visualisation,” *Neuroimage*, vol. 202, p. 116137, 2019, doi: 10.1016/j.neuroimage.2019.116137.

[367] K. G. Solar, S. Treit, and C. Beaulieu, “High resolution diffusion tensor imaging of the hippocampus across the healthy lifespan,” *Hippocampus*, vol. 31, no. 12, pp. 1271–1284, Oct. 2021, doi: 10.1002/hipo.23388.

[368] G. B. Frisoni *et al.*, “The EADC-ADNI Harmonized Protocol for manual hippocampal segmentation on magnetic resonance: Evidence of validity,” *Alzheimer’s Dement.*, vol. 11, no. 2, pp. 111–125, Feb. 2015, doi: 10.1016/j.jalz.2014.05.1756.

[369] J. M. Spijkerman, E. T. Petersen, J. Hendrikse, P. Luijten, and J. J. M. Zwanenburg, “T (2) mapping of cerebrospinal fluid: 3 T versus 7 T,” *MAGMA*, vol. 31, no. 3, pp. 415–424, Jun. 2018, doi: 10.1007/s10334-017-0659-3.

[370] C. Beaulieu, “The biological basis of diffusion anisotropy - Diffusion MRI ”, Academic Press, 2009, H. Johansen-Berg, T.E. J. Behrens, pp. 105-126. doi: 10.1016/B978-0-12-374709-9.00006-7.

[371] T. N. Akudjedu *et al.*, “A comparative study of segmentation techniques for the

quantification of brain subcortical volume," *Brain Imaging Behav.*, vol. 12, no. 6, pp. 1678–1695, 2018.

[372] A. Colasanti *et al.*, "Hippocampal Neuroinflammation, Functional Connectivity, and Depressive Symptoms in Multiple Sclerosis.," *Biol. Psychiatry*, vol. 80, no. 1, pp. 62–72, Jul. 2016, doi: 10.1016/j.biopsych.2015.11.022.

[373] I. Induruwa, C. S. Constantinescu, and B. Gran, "Fatigue in multiple sclerosis — A brief review," *J. Neurol. Sci.*, vol. 323, no. 1, pp. 9–15, 2012, doi: 10.1016/j.jns.2012.08.007.

[374] N. Téllez *et al.*, "The basal ganglia: a substrate for fatigue in multiple sclerosis.," *Neuroradiology*, vol. 50, no. 1, pp. 17–23, Jan. 2008, doi: 10.1007/s00234-007-0304-3.

[375] G. Niepel, C. R. Tench, P. S. Morgan, N. Evangelou, D. P. Auer, and C. S. Constantinescu, "Deep gray matter and fatigue in MS: a T1 relaxation time study.," *J. Neurol.*, vol. 253, no. 7, pp. 896–902, Jul. 2006, doi: 10.1007/s00415-006-0128-9.

[376] M. Calabrese *et al.*, "Epilepsy in multiple sclerosis: The role of temporal lobe damage," *Mult. Scler. J.*, vol. 23, no. 3, pp. 473–482, Jun. 2016, doi: 10.1177/1352458516651502.

[377] A. Junker *et al.*, "Extensive subpial cortical demyelination is specific to multiple sclerosis," *Brain Pathol.*, vol. 30, no. 3, pp. 641–652, May 2020, doi: 10.1111/bpa.12813.

[378] T. L. Rothstein, "Gray Matter Matters: A Longitudinal Magnetic Resonance Voxel-Based Morphometry Study of Primary Progressive Multiple Sclerosis," *Frontiers in Neurology*, vol. 11. 2020, doi: 10.3389/fneur.2020.581537.

[379] H. Lassmann, W. Brück, and C. Lucchinetti, “Heterogeneity of multiple sclerosis pathogenesis: implications for diagnosis and therapy.,” *Trends Mol. Med.*, vol. 7, no. 3, pp. 115–121, Mar. 2001, doi: 10.1016/s1471-4914(00)01909-2.

[380] A. Kutzelnigg and H. Lassmann, “Pathology of multiple sclerosis and related inflammatory demyelinating diseases.,” *Handb. Clin. Neurol.*, vol. 122, pp. 15–58, 2014, doi: 10.1016/B978-0-444-52001-2.00002-9.

[381] M. Filippi, E. Pagani, P. Preziosa, and M. A. Rocca, “The Role of DTI in Multiple Sclerosis and Other Demyelinating Conditions BT - Diffusion Tensor Imaging: A Practical Handbook,” W. Van Hecke, L. Emsell, and S. Sunaert, Eds. New York, NY: Springer New York, 2016, pp. 331–341.

[382] M. A. Rocca *et al.*, “Altered functional and structural connectivities in patients with MS: a 3-T study.,” *Neurology*, vol. 69, no. 23, pp. 2136–2145, Dec. 2007, doi: 10.1212/01.wnl.0000295504.92020.ca.

[383] K. Schmierer *et al.*, “Diffusion tensor imaging of post mortem multiple sclerosis brain,” *Neuroimage*, vol. 35, no. 2, pp. 467–477, 2007, doi: 10.1016/j.neuroimage.2006.12.010.

[384] D. K. Jones and M. Cercignani, “Twenty-five pitfalls in the analysis of diffusion MRI data.,” *NMR Biomed.*, vol. 23, no. 7, pp. 803–820, Aug. 2010, doi: 10.1002/nbm.1543.

[385] D. S. Reich *et al.*, “Multiparametric magnetic resonance imaging analysis of the corticospinal tract in multiple sclerosis,” *Neuroimage*, vol. 38, no. 2, pp. 271–279, 2007,

doi: 10.1016/j.neuroimage.2007.07.049.

[386] E. Pagani, M. Filippi, M. A. Rocca, and M. A. Horsfield, “A method for obtaining tract-specific diffusion tensor MRI measurements in the presence of disease: application to patients with clinically isolated syndromes suggestive of multiple sclerosis.,” *Neuroimage*, vol. 26, no. 1, pp. 258–265, May 2005, doi: 10.1016/j.neuroimage.2005.01.008.

[387] S. Mori, J. D. Tournier, “Moving Beyond DTI: High Angular Resolution Diffusion Imaging (HARDI),” – In: “Introduction to Diffusion Tensor Imaging”, Academic Press, 2014, pp. 65–78, doi: 10.1016/B978-0-12-398398-5.00008-4.

[388] M. Descoteaux, E. Angelino, S. Fitzgibbons, and R. Deriche, “Apparent diffusion coefficients from high angular resolution diffusion imaging: Estimation and applications,” *Magn. Reson. Med.*, vol. 56, no. 2, pp. 395–410, Aug. 2006, doi: 10.1002/mrm.20948.

[389] E. Fieremans, J. H. Jensen, and J. A. Helpern, “White matter characterization with diffusional kurtosis imaging,” *Neuroimage*, vol. 58, no. 1, pp. 177–188, 2011, doi: 10.1016/j.neuroimage.2011.06.006.

[390] R. Neto Henriques, M. M. Correia, R. G. Nunes, and H. A. Ferreira, “Exploring the 3D geometry of the diffusion kurtosis tensor--impact on the development of robust tractography procedures and novel biomarkers.,” *Neuroimage*, vol. 111, pp. 85–99, May 2015, doi: 10.1016/j.neuroimage.2015.02.004.

[391] G. D. Parker, D. Marshall, P. L. Rosin, N. Drage, S. Richmond, and D. K. Jones, “A

pitfall in the reconstruction of fibre ODFs using spherical deconvolution of diffusion MRI data.," *Neuroimage*, vol. 65, pp. 433–448, Jan. 2013, doi: 10.1016/j.neuroimage.2012.10.022.

[392] E. Özarslan and P. J. Basser, "Microscopic anisotropy revealed by NMR double pulsed field gradient experiments with arbitrary timing parameters," *J. Chem. Phys.*, vol. 128, no. 15, p. 154511, Apr. 2008, doi: 10.1063/1.2905765.

[393] C.-F. Westin *et al.*, "Measurement tensors in diffusion MRI: generalizing the concept of diffusion encoding.," *Med. image Comput. Comput. Interv. MICCAI ... Int. Conf. Med. Image Comput. Comput. Interv.*, vol. 17, no. Pt 3, pp. 209–216, 2014, doi: 10.1007/978-3-319-10443-0_27.

[394] S. Lasič, M. Nilsson, J. Lätt, F. Ståhlberg, and D. Topgaard, "Apparent exchange rate mapping with diffusion MRI.," *Magn. Reson. Med.*, vol. 66, no. 2, pp. 356–365, Aug. 2011, doi: 10.1002/mrm.22782.

[395] M. D. Does, E. C. Parsons, and J. C. Gore, "Oscillating gradient measurements of water diffusion in normal and globally ischemic rat brain.," *Magn. Reson. Med.*, vol. 49, no. 2, pp. 206–215, Feb. 2003, doi: 10.1002/mrm.10385.

[396] N. Shemesh *et al.*, "Conventions and nomenclature for double diffusion encoding NMR and MRI," *Magn. Reson. Med.*, vol. 75, no. 1, pp. 82–87, Jan. 2016, doi: 10.1002/mrm.25901.

[397] T. D. Nilsson M, Szczepankiewicz F, Lampinen B, Ahlgren A, de Almeida Martins JP, Lasič S, Westin C-F, "An open-source framework for analysis of multidimensional diffusion MRI data implemented in MATLAB.," *Proc Intl Soc Mag Reson Med*, no. June, pp. 1–3. 35., 2018.

[398] D. Topgaard, "Multidimensional diffusion MRI," *J. Magn. Reson.*, vol. 275, pp. 98–113, 2017, doi: 10.1016/j.jmr.2016.12.007.

[399] I. D. Naranjo *et al.*, "Multidimensional Diffusion Magnetic Resonance Imaging for Characterization of Tissue Microstructure in Breast Cancer Patients: A Prospective Pilot Study," *Cancers (Basel).*, vol. 13, no. 7, p. 1606, Mar. 2021, doi: 10.3390/cancers13071606.

[400] B. Lampinen *et al.*, "Searching for the neurite density with diffusion MRI: Challenges for biophysical modeling," *Hum. Brain Mapp.*, vol. 40, no. 8, pp. 2529–2545, 2019, doi: 10.1002/hbm.24542.

[401] M. Nilsson, F. Szczepankiewicz, D. van Westen, and O. Hansson, "Extrapolation-Based References Improve Motion and Eddy-Current Correction of High B-Value DWI Data: Application in Parkinson's Disease Dementia," *PLoS One*, vol. 10, no. 11, p. e0141825, Nov. 2015, doi: 10.1371/journal.pone.0141825.

[402] M. Barakovic *et al.*, "Bundle-Specific Axon Diameter Index as a New Contrast to Differentiate White Matter Tracts," *Frontiers in Neuroscience* , vol. 15. 2021, doi: 10.3389/fnins.2021.646034.

[403] A. Bitsch, T. Kuhlmann, C. Stadelmann, H. Lassmann, C. Lucchinetti, and W. Brück, "A longitudinal MRI study of histopathologically defined hypointense multiple sclerosis lesions.," *Ann. Neurol.*, vol. 49, no. 6, pp. 793–796, Jun. 2001, doi: 10.1002/ana.1053.

[404] C. Thaler *et al.*, "T1 Recovery Is Predominantly Found in Black Holes and Is Associated with Clinical Improvement in Patients with Multiple Sclerosis," *Am. J. Neuroradiol.*, vol. 38, no. 2, pp. 264–269, Feb. 2017, doi: 10.3174/ajnr.A5004.

[405] H. Vrenken *et al.*, "Normal-appearing white matter changes vary with distance to lesions in multiple sclerosis," *AJNR. Am. J. Neuroradiol.*, vol. 27, no. 9, pp. 2005–2011, Oct. 2006. Available: https://pubmed.ncbi.nlm.nih.gov/17032884.

[406] C. Thaler *et al.*, "Heterogeneity of multiple sclerosis lesions in fast diffusional kurtosis imaging," *PLoS One*, vol. 16, no. 2, p. e0245844, Feb. 2021, doi: 10.1371/journal.pone.0245844.

[407] J. Lätt *et al.*, "Accuracy of q-space related parameters in MRI: simulations and phantom measurements.," *IEEE Trans. Med. Imaging*, vol. 26, no. 11, pp. 1437–1447, Nov. 2007, doi: 10.1109/TMI.2007.907278.

[408] J. H. Simon, R. P. Kinkel, L. Jacobs, L. Bub, and N. Simonian, "A Wallerian degeneration pattern in patients at risk for MS.," *Neurology*, vol. 54, no. 5, pp. 1155–1160, Mar. 2000, doi: 10.1212/wnl.54.5.1155.

[409] L. Bonzano, A. Tacchino, L. Roccatagliata, G. Abbruzzese, G. L. Mancardi, and M. Bove,

"Callosal contributions to simultaneous bimanual finger movements," *J. Neurosci.*, vol. 28, no. 12, pp. 3227–3233, 2008, doi: 10.1523/JNEUROSCI.4076-07.2008.

[410] G. Little and C. Beaulieu, "Automated cerebral cortex segmentation based solely on diffusion tensor imaging for investigating cortical anisotropy," *Neuroimage*, vol. 237, p. 118105, 2021, doi: 10.1016/j.neuroimage.2021.118105.

[411] K. A. Koenig *et al.*, "The relationship between cognitive function and high-resolution diffusion tensor MRI of the cingulum bundle in multiple sclerosis," *Mult. Scler.*, vol. 21, no. 14, pp. 1794–1801, Dec. 2015, doi: 10.1177/1352458515576983.

[412] R. Woitek *et al.*, "Diffusion tensor imaging of the normal-appearing deep gray matter in primary and secondary progressive multiple sclerosis," *Acta radiol.*, vol. 61, no. 1, pp. 85–92, 2020, doi: 10.1177/0284185119852735.

[413] A.-M. Beaudoin *et al.*, "Modern Technology in Multi-Shell Diffusion MRI Reveals Diffuse White Matter Changes in Young Adults With Relapsing-Remitting Multiple Sclerosis ," *Frontiers in Neuroscience* , vol. 15. 2021,doi: 10.3389/fnins.2021.665017.

[414] Á. Bernabéu-Sanz, S. Morales, V. Naranjo, and Á. P. Sempere, "Contribution of Gray Matter Atrophy and White Matter Damage to Cognitive Impairment in Mildly Disabled Relapsing-Remitting Multiple Sclerosis Patients," *Diagnostics* , vol. 11, no. 3. 2021, doi: 10.3390/diagnostics11030578.

Appendix A: Fornix Tractography

Key FACT deterministic tractography points considered here:

i. The thresholds or tracking conditions under consideration for fornix tractography were the voxel local FA value, the angle of curvature or turning angle, the step size and the minimum fiber length.

ii. The minimum fiber length was set to 10 mm and it was not further modified to avoid noisy contributions from shorter fibers.

iii. The step size and the turning angle are parameters that are coupled together to limit the allowed tract curvature. Then, the turning angle is usually chosen between 30-90° but not higher than 90° to avoid fiber backtracking, which is generally not anatomically plausible.

iv. In ExploreDTI, the turning angle is defined as the half cone of opening. The angle threshold chosen for this analysis was 30°, which is an effective 60° total, and it was not further modified as it did not seem necessary due to the fornix anatomy.

v. Instead, the step size was modified to assess overall tract curvature. The step size or pathway propagation is not recommended to be set higher than the voxel size.

The final deterministic tractography settings to track the fornix in ExploreDTI in Chapter 2 were set up as: FA threshold of 0.2, a turning angle of 30˚, step size of 1 mm (due to zero-filling interpolation) and minimum fiber length of 10 mm. This procedure yielded excellent depictions of the fornix (and the other two tracts) including the bending parts as shown in Chapter 2 and in Figure A.1 below, particularly in controls.

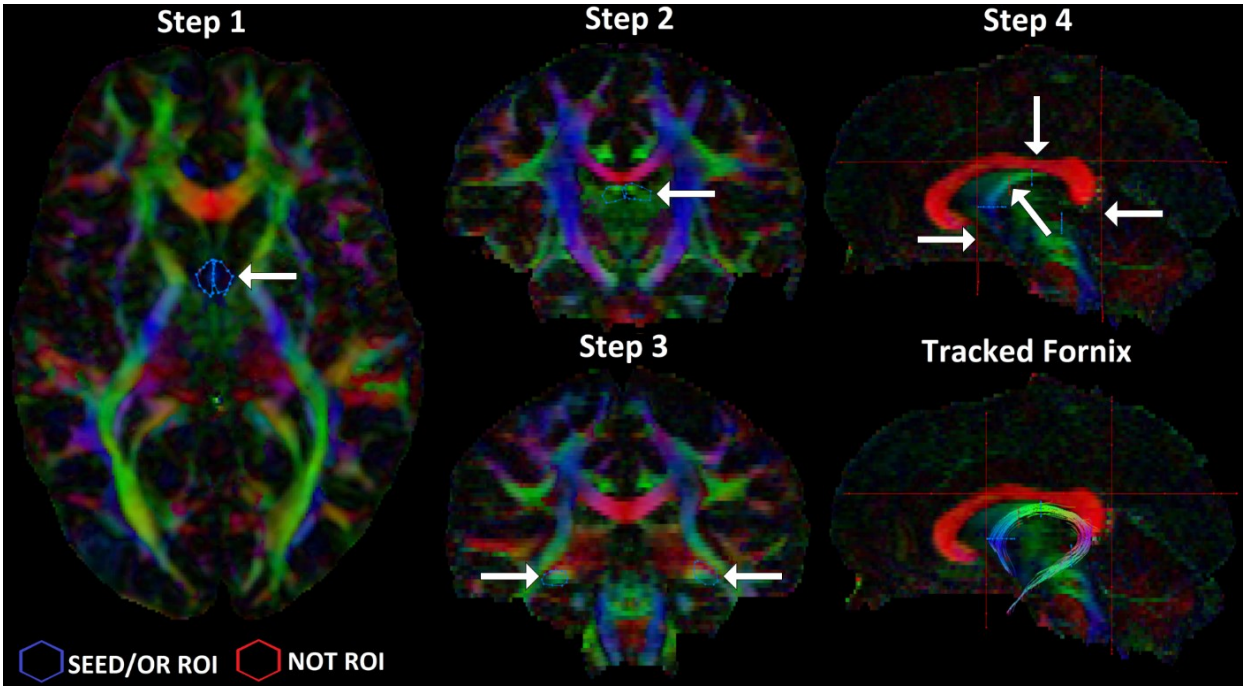

Figure A.1: Fornix tractography steps as described in Chapter 2: "SEED/OR" ROIs were placed on an axial slice around the fornix column above the anterior commissure (Step 1) and in two coronal slices, one in the fornix body (Step 2), and one between the crus and fimbria (Step 3). These ROIs were placed on three distinct portions for the left and right hemispheres separately at first, and then the two fornices were concatenated into one. "NOT" ROIs were placed on axial and coronal slices above, anterior and posterior to the fornix to avoid spurious fibers when necessary (Step 4).

For interest here, fornix tractography settings (FA threshold and step size) were compared between what we presented in Chapter 2 Methods (FA=0.2, step=1 mm) and two other scenarios (FA=0.2, step=0.5 mm; and FA=0.13, step=1 mm) for two controls, two RRMS, two SPMS and two PPMS participants (Figure A.1). A lower FA threshold was chosen for comparisons (FA=0.13, taken from references in Chapter 2) as FA in focal MS lesions is lower than in healthy WM and NAWM. A lower step size was chosen for comparisons as this parameter should not be set higher than

'information size' (voxel size), hence a step size which was half of what we utilized in Chapter 2 was selected here for comparison purposes.

Step sizes comparison (first and second column in Figure A.2): There are no major qualitative or quantitative changes in any of the subgroups if the step size changes from 1 to 0.5 mm; the FA values are very comparable and the changes in MD are no larger than 0.04×10^{-3} mm^2/s.

FA threshold comparisons (first and second column in Figure A.2, also shown in Chapter 2): If the FA threshold is modified from 0.2 to 0.13, qualitative tract differences are observable, primarily in the MS cohort, due to a greater number of streamlines arising from the lower FA threshold. In some participants, this lower FA threshold enables streamlines to connect across the previously "transected" crura and there are fewer disconnections compared to the tracts presented in the main manuscript:

- FA threshold=0.2: Controls – 1/11 transections (1 bilateral), RRMS – 8/11 transections (1 left side, 2 right side, 5 bilateral), SPMS – 6/9 transections (2 right side, 4 bilateral), PPMS – 4/8 transections (1 right side, 3 bilateral).
- FA threshold=0.13: Controls – no transections, RRMS – 4/11 transections (2 left side, 2 right side), SPMS – 5/9 transections (2 left side, 1 right side, 2 bilateral), PPMS – 2/8 transections (1 left side, 1 bilateral).

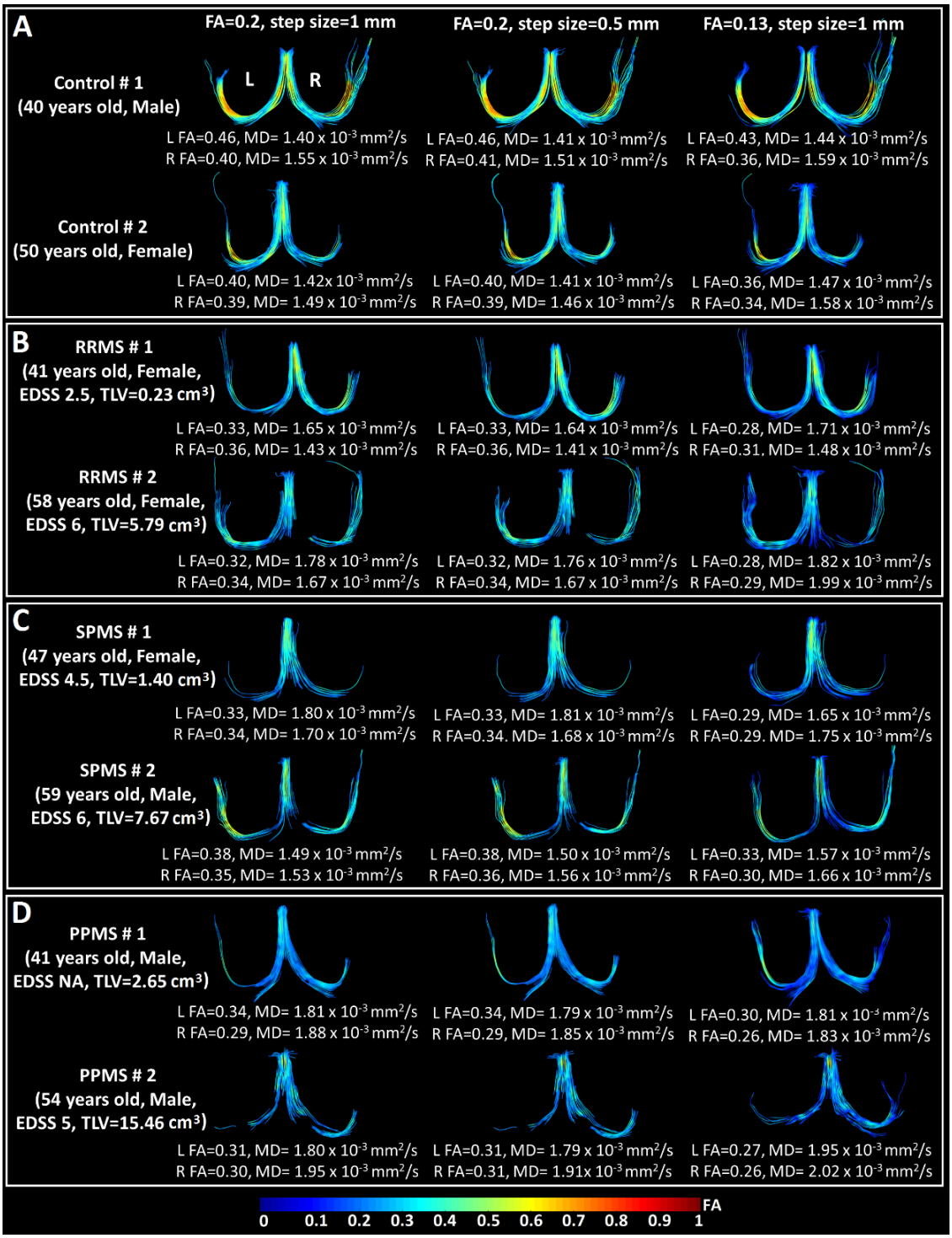

Figure A.2: Comparison of different tracking thresholds (FA and step size) for deterministic fornix tractography in two controls (A), two RRMS (B), two SPMS (C), and two PPMS (D) participants.

The angle threshold was analyzed together with the step size to assess the tract curvature within a voxel. Here, the step size (1 mm) was smaller than the voxel size and the applied angle threshold (30°) allows enough deviation within the voxel to keep tracking the fornix. To demonstrate that this angle threshold was sufficient, the mean ± SD angle deviation per step size over the entire fornix is shown in Table A.1 below for 8 participants where full fornix tracts were achieved (2 healthy controls, 2 RRMS, 2 SPMS, and 2 PPMS). In all these 8 examples, the angle deviation per step size was much less than the 30° threshold.

Table A.1: Average angle deviation per step size (mean ± SD) in the full fornix in 2 healthy controls, 2 RRMS, 2 SPMS, and 2 PPMS examples.

Angle deviation per step size (°)	Controls	RRMS	SPMS	PPMS
Subject 1	4.2 ± 3.1°	3.8 ± 1.9°	4.0 ± 2.5°	3.6 ± 2.2°
Subject 2	3.8 ± 2.2°	4.4 ± 3.0°	3.7 ± 2.2°	4.5 ± 3.0°

Appendix B: Cognitive and Clinical Battery of Tests Performed by the MS Cohorts. Forms and Questionnaires

- **Kurtzke Expanded Disability Status Scale (EDSS, acquired in MS cohort 1[†] and MS cohort 2[‡]).**
- **Brief Visual Memory Test-Revised (BVMT-R, acquired in both MS cohorts).**
- **Symbol Digit Modalities Test (SDMT, acquired in both MS cohorts).**
- **Rey Auditory Verbal Learning Test (RAVLT, acquired only in 29 MS patients from MS cohort 2).**
- **Paced Auditory Serial Addition Test (PASAT, acquired in MS cohort 1).**
- **Fatigue Severity Scale (FSS, acquired in MS cohort 1).**
- **Modified Fatigue Impact Scale (MFIS, acquired in both MS cohorts).**
- **Beck Depression Inventory-II (BDI-II, acquired in both MS cohorts).**
- **Timed 25-Foot Walk (T25-FW, acquired in both MS cohorts).**
- **9-Hole Peg Test (9-HPT, acquired in both MS cohorts).**

[†]MS Cohort 1 included 28 patients (11 RRMS, 9 SPMS, 8 PPMS) and it was acquired for Chapter 2.

[‡] MS Cohort 2 included 43 patients (35 RRMS, 8 SPMS) and it was acquired for Chapters 3, 4, and 5.

Symbol Digit Modalities Test (SDMT): It involves a simple substitution task using a reference key. The MS participant has 90 seconds to pair specific numbers with given geometric figures and to write them in the form below.

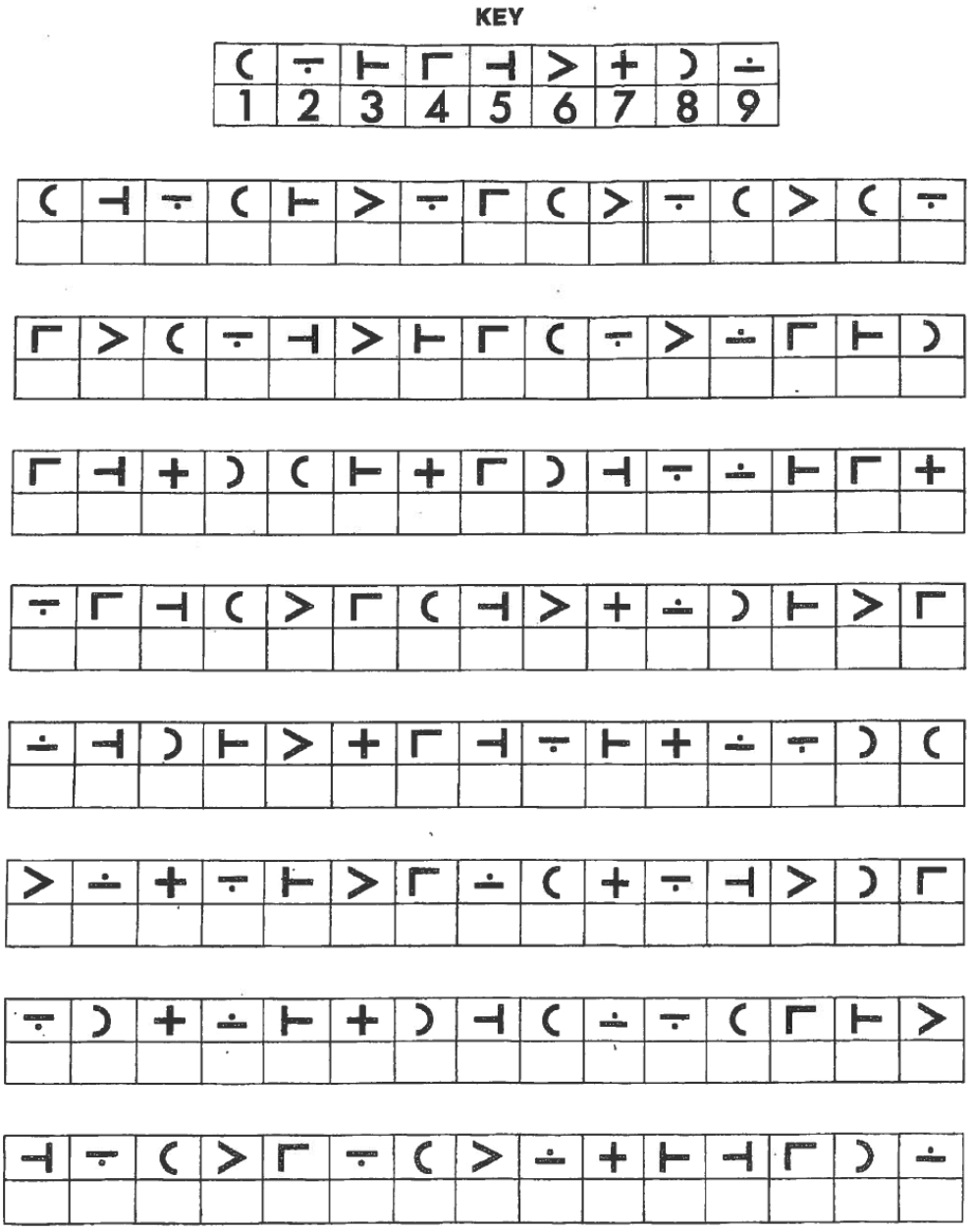

Figure B.1: The Symbol Digit Modalities Test (written version).

Brief Visuospatial Memory Test–Revised (BVMT-R): In three Learning Trials, the respondent views the stimulus page for 10 seconds and is asked to draw as many of the figures as possible in their correct location on a page in the response booklet. A Delayed Recall Trial is administered after a 25-minute delay. The stimulus form below was utilized.

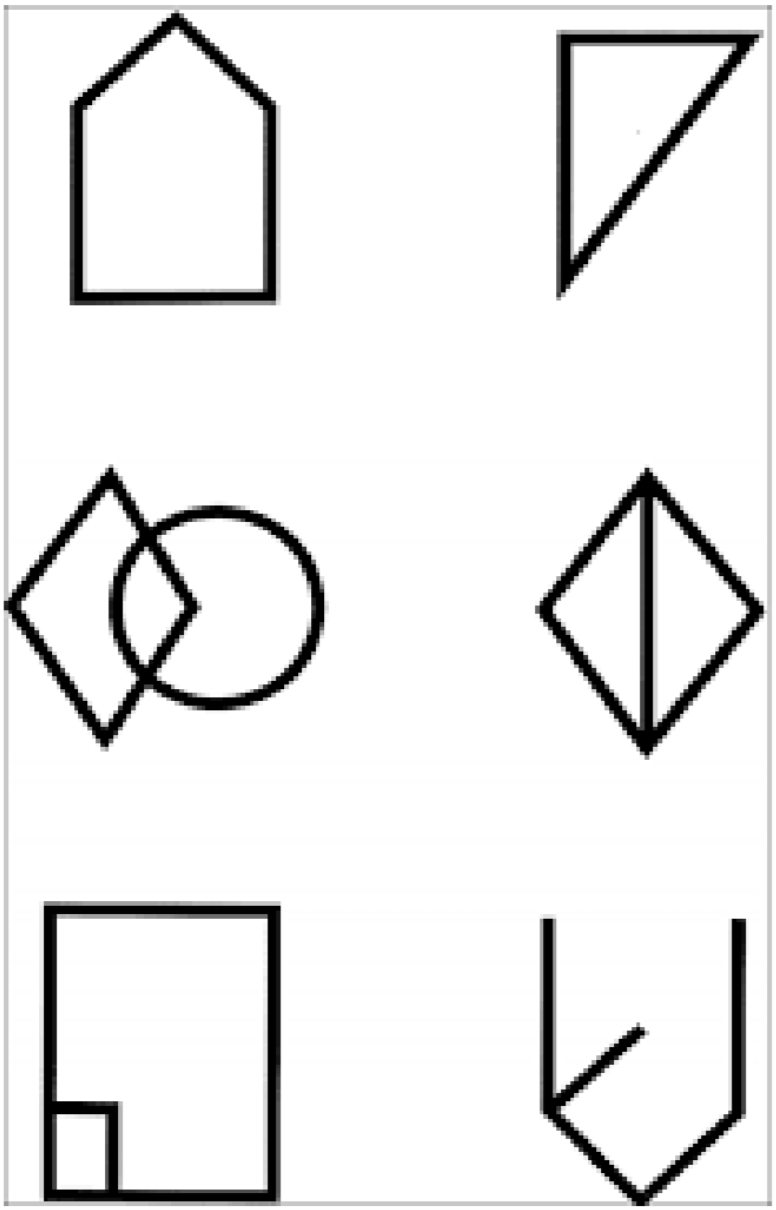

Figure B.2: Test stimuli form utilized in the MS cohorts in this dissertation.

FATIGUE SEVERITY SCALE (FSS)

Date _____ Name _____

Please circle the number between 1 and 7 which you feel best fits the following statements. This refers to your usual way of life within the last week. 1 indicates "strongly disagree" and 7 indicates "strongly agree."

Read and circle a number.	Strongly Disagree → Strongly Agree						
1. My motivation is lower when I am fatigued.	1	2	3	4	5	6	7
2. Exercise brings on my fatigue.	1	2	3	4	5	6	7
3. I am easily fatigued.	1	2	3	4	5	6	7
4. Fatigue interferes with my physical functioning.	1	2	3	4	5	6	7
5. Fatigue causes frequent problems for me.	1	2	3	4	5	6	7
6. My fatigue prevents sustained physical functioning.	1	2	3	4	5	6	7
7. Fatigue interferes with carrying out certain duties and responsibilities.	1	2	3	4	5	6	7
8. Fatigue is among my most disabling symptoms.	1	2	3	4	5	6	7
9. Fatigue interferes with my work, family, or social life.	1	2	3	4	5	6	7

VISUAL ANALOGUE FATIGUE SCALE (VAFS)

Please mark an "X" on the number line which describes your global fatigue with 0 being worst and 10 being normal.

0	1	2	3	4	5	6	7	8	9	10

Figure B.3: Fatigue Severity Scale (FSS) questionnaire.

Modified Fatigue Impact Scale (MFIS)

Fatigue is a feeling of physical tiredness and lack of energy that many people experience from time to time. But people who have medical conditions like MS experience stronger feelings of fatigue more often and with greater impact than others.

Following is a list of statements that describe the effects of fatigue. Please read each statement carefully, the circle the one number that best indicates how often fatigue has affected you in this way during the past 4 weeks. (If you need help in marking your responses, tell the interviewer the number of the best response.) Please answer every question. If you are not sure which answer to select choose the one answer that comes closest to describing you. Ask the interviewer to explain any words or phrases that you do not understand.

Because of my fatigue during the past 4 weeks

		Never	Rarely	Sometimes	Often	Almost Always
1.	I have been less alert.	0	1	2	3	4
2.	I have had difficulty paying attention for long periods of time.	0	1	2	3	4
3.	I have been unable to think clearly.	0	1	2	3	4
4.	I have been clumsy and uncoordinated.	0	1	2	3	4
5.	I have been forgetful.	0	1	2	3	4
6.	I have had to pace myself in my physical activities.	0	1	2	3	4
7.	I have been less motivated to do anything that requires physical effort.	0	1	2	3	4
8.	I have been less motivated to participate in social activities.	0	1	2	3	4
9.	I have been limited in my ability to do things away from home.	0	1	2	3	4
10.	I have trouble maintaining physical effort for long periods.	0	1	2	3	4
11.	I have had difficulty making decisions.	0	1	2	3	4
12.	I have been less motivated to do anything that requires thinking	0	1	2	3	4
13.	My muscles have felt weak	0	1	2	3	4
14.	I have been physically uncomfortable.	0	1	2	3	4
15.	I have had trouble finishing tasks that require thinking.	0	1	2	3	4
16.	I have had difficulty organizing my thoughts when doing things at home or at work.	0	1	2	3	4
17.	I have been less able to complete tasks that require physical effort.	0	1	2	3	4

Figure B.4: Modified Fatigue Impact Scale (MFIS) questionnaire page 1.

		Never	Rarely	Sometimes	Often	Almost Always	
18.	My thinking has been slowed down.	0	1	2	3	4	
19.	I have had trouble concentrating.	0	1	2	3	4	
20.	I have limited my physical activities.	0	1	2	3	4	
21.	I have needed to rest more often or for longer periods.	0	1	2	3	4	

Instructions for Scoring the MFIS

Items on the MFIS can be aggregated into three subscales (physical, cognitive, and psychosocial), as well as into a total MFIS score. All items are scaled so that higher scores indicate a greater impact of fatigue on a person's activities.

Physical Subscale

This scale can range from 0 to 36. It is computed by adding raw scores on the following items: 4+6+7+10+13+14+17+20+21.

Cognitive Subscale

This scale can range from 0 to 40. It is computed by adding raw scores on the following items: 1+2+3+5+11+12+15+16+18+19.

Psychosocial Subscale

This scale can range from 0 to 8. It is computed by adding raw scores on the following items: 8+9.

Total MFIS Score

The total MFIS score can range from 0 to 84. It is computed by adding scores on the physical, cognitive, and psychosocial subscales.

Figure B.5: Modified Fatigue Impact Scale (MFIS) questionnaire page 2.

Beck's Depression Inventory

This depression inventory can be self-scored. The scoring scale is at the end of the questionnaire.

1.
- 0 I do not feel sad.
- 1 I feel sad
- 2 I am sad all the time and I can't snap out of it.
- 3 I am so sad and unhappy that I can't stand it.

2.
- 0 I am not particularly discouraged about the future.
- 1 I feel discouraged about the future.
- 2 I feel I have nothing to look forward to.
- 3 I feel the future is hopeless and that things cannot improve.

3.
- 0 I do not feel like a failure.
- 1 I feel I have failed more than the average person.
- 2 As I look back on my life, all I can see is a lot of failures.
- 3 I feel I am a complete failure as a person.

4.
- 0 I get as much satisfaction out of things as I used to.
- 1 I don't enjoy things the way I used to.
- 2 I don't get real satisfaction out of anything anymore.
- 3 I am dissatisfied or bored with everything.

5.
- 0 I don't feel particularly guilty
- 1 I feel guilty a good part of the time.
- 2 I feel quite guilty most of the time.
- 3 I feel guilty all of the time.

6.
- 0 I don't feel I am being punished.
- 1 I feel I may be punished.
- 2 I expect to be punished.
- 3 I feel I am being punished.

7.
- 0 I don't feel disappointed in myself.
- 1 I am disappointed in myself.
- 2 I am disgusted with myself.
- 3 I hate myself.

8.
- 0 I don't feel I am any worse than anybody else.
- 1 I am critical of myself for my weaknesses or mistakes.
- 2 I blame myself all the time for my faults.
- 3 I blame myself for everything bad that happens.

9.
- 0 I don't have any thoughts of killing myself.
- 1 I have thoughts of killing myself, but I would not carry them out.
- 2 I would like to kill myself.
- 3 I would kill myself if I had the chance.

10.
- 0 I don't cry any more than usual.
- 1 I cry more now than I used to.
- 2 I cry all the time now.
- 3 I used to be able to cry, but now I can't cry even though I want to.

Figure B.6: Beck depression Inventory (BDI-II) questionnaire page 1.

11.

0 I am no more irritated by things than I ever was.
1 I am slightly more irritated now than usual.
2 I am quite annoyed or irritated a good deal of the time.
3 I feel irritated all the time.

12.

0 I have not lost interest in other people.
1 I am less interested in other people than I used to be.
2 I have lost most of my interest in other people.
3 I have lost all of my interest in other people.

13.

0 I make decisions about as well as I ever could.
1 I put off making decisions more than I used to.
2 I have greater difficulty in making decisions more than I used to.
3 I can't make decisions at all anymore.

14.

0 I don't feel that I look any worse than I used to.
1 I am worried that I am looking old or unattractive.
2 I feel there are permanent changes in my appearance that make me look unattractive
3 I believe that I look ugly.

15.

0 I can work about as well as before.
1 It takes an extra effort to get started at doing something.
2 I have to push myself very hard to do anything.
3 I can't do any work at all.

16.

0 I can sleep as well as usual.
1 I don't sleep as well as I used to.
2 I wake up 1-2 hours earlier than usual and find it hard to get back to sleep.
3 I wake up several hours earlier than I used to and cannot get back to sleep.

17.

0 I don't get more tired than usual.
1 I get tired more easily than I used to.
2 I get tired from doing almost anything.
3 I am too tired to do anything.

18.

0 My appetite is no worse than usual.
1 My appetite is not as good as it used to be.
2 My appetite is much worse now.
3 I have no appetite at all anymore.

19.

0 I haven't lost much weight, if any, lately.
1 I have lost more than five pounds.
2 I have lost more than ten pounds.
3 I have lost more than fifteen pounds.

Figure B.7: Beck depression Inventory (BDI-II) questionnaire page 2.

20.

0 I am no more worried about my health than usual.

1 I am worried about physical problems like aches, pains, upset stomach, or constipation.

2 I am very worried about physical problems and it's hard to think of much else.

3 I am so worried about my physical problems that I cannot think of anything else.

21.

0 I have not noticed any recent change in my interest in sex.

1 I am less interested in sex than I used to be.

2 I have almost no interest in sex.

3 I have lost interest in sex completely.

INTERPRETING THE BECK DEPRESSION INVENTORY

Now that you have completed the questionnaire, add up the score for each of the twenty-one questions by counting the number to the right of each question you marked. The highest possible total for the whole test would be sixty-three. This would mean you circled number three on all twenty-one questions. Since the lowest possible score for each question is zero, the lowest possible score for the test would be zero. This would mean you circles zero on each question. You can evaluate your depression according to the Table below.

Total Score	Levels of Depression
1-10	These ups and downs are considered normal
11-16	Mild mood disturbance
17-20	Borderline clinical depression
21-30	Moderate depression
31-40	Severe depression
over 40	Extreme depression

Figure B.8: Beck depression Inventory (BDI-II) questionnaire page 3.

Appendix C: DTI Limbic System WM and Deep GM Studies in MS (chronologically ordered since 2006)

Authors, year *(journal)*	Subjects	Imaging Parameters	Image Analysis	Limbic WM Tracts / Deep GM Structures Findings (R: Right, L: Left, Fx: Fornix, Cg: Cingulum, UF: Uncinate Fasciculus, Th: Thalamus, Hp: Hippocampus)
Fabiano et al. 2006 *(J. Neuroimaging)* [265]	82 MS (63 RR, 17 SP, 1 PP), 43 HC	1.5T, b=1000 s/mm^2,3 xyz axis directions, voxel size 3.75×2.1×5 mm^3	ROI (standardized template Th)	**Th:** ↑ADCs in L Th in MS vs HC and in SP vs RR. ↑ADCs in R Th in SP vs HC.
Dineen et al. 2009 *(Brain)* [255]	37 MS (35 RR, 2 SP) 25 HC	3 T, 15 directions b=1000 s/mm^2, voxel size 2×2×2.5 mm^3	TBSS (FA=0.2)	**Fx:** ↓FA (body & tail) in MS vs HC. ↓FA in L Fx α ↓verbal and episodic memory (CVLT-II, BVRT). **Cg:** ↓FA in L Cg α ↓attention, verbal and episodic memory (PASAT, CVLT-II). **UF:** No differences.
Roosendaal et al. 2009 *(Neuroimage)* [281]	30 MS (5 CIS, 21 RR, 4 SP), 31 HC	1.5T, 60 directions b=700 s/mm^2, 2 mm isotropic voxels	TBSS (FA=0.2, thresholded to FA=0.1 for WM lesions)	**Fx:** ↓FA, ↑RD in MS vs HC. **Cg and UF:** No differences in MS vs HC.
Tovar-Moll et al. 2009 (*Am. J. Neuroradiol,)* [267]	24 MS (13 RR, 11 SP), 24 HC	3 T, 33 directions, b=1000 s/mm^2, 54 slices, voxel size 2.5×2.5×2.4 mm^3	ROI	**Th:** ↑FA and ↑MD in MS vs HC.
Fink et al. 2010 *(Mult. Scler. J.)* [125]	50 MS, 20 HC	1.5T, 30 directions b=1000 s/mm², voxel size 1.98×1.98×2.7 mm³	Tractography (FA=0.2)	**Fx:** ↓FA in L&R Fx, ↑RD in L Fx in MS vs HC. ↓FA in R Fx α ↑ disability (EDSS), ↑symptoms and ↑disease duration. ↑RD in R Fx α ↓verbal performance (RECOG in CVLT).

				Cg: ↑RD in L Cg in MS vs HC. ↑RD in L Cg α ↑disease duration (marginally). **UF:** ↓FA in L UF in MS vs HC. ↑RD in L&R UF. ↑RD in R UF α ↑disease duration, ↓verbal performance.
Roosendaal et al. 2010 *(Radiology)* [213]	25 MS (intact spatial memory) (5 CIS, 18 RR, 2 SP), 30 HC	1.5T, 60 directions b=700 s/mm², 2 mm isotropic voxels (resting-state fMRI also acquired)	Hp T1w manual segmentation corregistered to DTI (FA and MD)	**Hp:** ↑MD in L&R Hp in MS vs HC.
Zhou et al. 2010 *(J. Comput. Assist. Tomogr.)* [263]	50 MS, 25 HC	3 T, b=1,000 s/mm², 15 directions, voxel size 0.94×0.94×5 mm^3	ROI (bilateral Th and other deep GM)	**Th:** No differences in MS vs HC.
Preziosa et al. 2011 *(Radiology)* [286]	172 MS (22 CIS, 20 benign MS, 51 RR, 44 SP, 35 PP), 46 HC	1.5T, b=1000 s/mm², 12 directions, 40 slices, 1.88×1.88×2.5 mm^3)	VBA	**Fx:** ↑MD, ↑AD, ↑RD in CIS vs HC. ↑MD, ↑AD, ↑RD, ↓FA in PPMS vs HC. ↓FA, ↓AD in RRMS vs benign MS. ↑MD, ↑AD, ↑RD in SPMS vs RRMS. ↓FA, ↑MD, ↑AD, ↑RD in SPMS vs benign MS. ↓FA, ↑MD, ↑AD, ↑RD in SPMS vs PPMS. **Cg:** ↑MD, ↑AD, ↑RD in CIS vs HC. ↑MD, ↑AD, ↑RD in PPMS vs HC. ↓FA, ↓AD in RRMS vs benign MS. ↑MD, ↑AD, ↑RD in SPMS vs RRMS. ↓FA, ↑MD (L Cg), ↑AD (L Cg), ↑RD (L Cg) in SPMS vs benign MS. ↓FA, ↑MD, ↑AD, ↑RD in SPMS vs PPMS. **UF:** ↑MD, ↑AD, ↑RD (R UF) in CIS vs HC. ↑MD, ↑AD, ↑RD in PPMS vs HC. ↓FA, ↓AD (R UF) in RRMS vs benign MS. ↑MD, ↑AD, ↑RD in SPMS vs RRMS. ↓FA, ↑MD (R UF), ↑AD (R UF), ↑RD (R UF) in SPMS vs benign MS. ↓FA, ↑MD, ↑AD, ↑RD in SPMS vs PPMS.
Dineen et al. 2012 *(PLoS One)* [256]	34 RRMS, 24 HC	3 T, b=1000 s/mm², 15 directions, voxel size 2×2×2.5 mm^3	ROI	**Fx:** ↓FA, ↑RD in RRMS vs HC. ↓FA α ↓episodic memory (CVLT, BVRT).

Hannoun et al. 2012 *(Am. J. Neuroradiol.)* [271]	41 MS (23 RR, 18 SP), 27 HC	1.5T, b=1000 s/mm², 24 directions, 2.5 mm isotropic voxels	ROI (manual segmentation of Th and caudate in FA maps)	**Th:** ↑FA, ↑MD in MS vs HC (↑SP vs RR) (↑FA in the caudate in MS vs HC). ↓MD in Th α auditory information processing speed (PASAT).
Kern et al. 2012 *(Neuroimage)* [282]	18 RRMS, 16 HC	3 T, b=900 s/mm², 12 directions, 2 mm isotropic voxels	TBSS	**Fx:** ↓FA α ↓verbal memory performance (word-pairs task). **Cg and UF:** No differences in MS vs HC.
Yu et al. 2012 *(Neuroimage)* [283]	37 RRMS, 20 HC	3 T, b=800 s/mm²,15 directions, voxel size 2×2×3 mm³	TBSS (FA=0.2)	**Fx:** ↓FA in R Fx in RRMS vs HC. ↓FA α ↓ visual working and verbal memory (SDMT, RAVLT). **Cg:** ↓FA in L Cg in RRMS vs HC. ↓FA α ↓ information processing speed (SDMT). ↓FA in R Cg α ↓ verbal memory (RAVLT). **UF:** ↓FA in R UF in RRMS vs HC. ↓FA α ↓ information processing speed (SDMT).
Koenig et al. 2013 *(Magn. Reson. Imaging)* [257]	40 MS (38 RR, 2 SP), 20 HC	3 T, b=1000 s/mm², 71 directions, 1 mm isotropic voxels (probably interpolated)	ROI	**Fx:** ↓FA, ↑MD, ↑RD in MS vs HC. ↑MD, ↑RD, ↓FA (L) α ↓episodic memory (BVMT-R).
Natarajan et al. 2013 *(Mult. Scler. Int.)* [266]	110 MS (24 CIS, 36 RR, 19 SP, 21 PP), 10 HC	1.5T, b=1000 s/mm², 12 directions, voxel size 1.8×1.8×5 mm³	ROIs (Th, but also caudate and WM tracts)	**Th:** No differences in MS vs HC. ↑Th FA α worse EDSS scores in RRMS.
Syc et al. 2013 *(Mult. Scler. Int.)* [260]	101 MS (64 RR, 24 SP, 13 PP), 16 HC	3 T, b=700 s/mm², 32 directions, 2.2 mm isotropic voxels	Tractography (FA=0.13, ∢=40˚)	**Fx:** ↓FA, ↑MD, ↑RD, ↑AD in MS vs HC. ↓FA, ↑MD, ↑RD, ↑AD α ↑ disability (EDSS) and ↑disease duration. ↓FA, ↑MD, RD α ↓PASAT-3. ↓FA ↑MD, RD, AD α ↑9-HPT. **Cg:** ↑MD, ↑RD, ↑AD in MS vs HC. ↓FA, ↑RD α ↑EDSS. ↓FA, ↓AD α ↑disease duration. ↓FA, ↓AD, ↑RD (L) α ↑EDSS. ↓FA, ↑RD (L) α ↑disease duration. ↓FA, ↑MD, RD (L) α ↓PASAT-3, ↑9-HPT.
Cappellani et al. 2014 *(Am. J.*	285 MS (210 RR,	3 T, b=800 s/mm², 15	DTI corregistered	**Th:** ↓FA (and ↑ in putamen and nucleus accumbens), ↑MD, ↑RD,

Neuroradiol.) [313]	75 PMS), 110 HC	directions, voxel size 3.33×3.33×3 mm^3)	to T1w manual segmentations (Th, Hp and remaining deep GM).	↑AD (and ↑diffusivities in caudate) in MS vs HC. **Hp:** ↓FA, ↑MD, ↑RD, ↑AD in MS vs HC.
Koenig et al. 2014 (*Magn. Reson. Imaging)* [353]	52 MS, 20 HC	3 T, b=1000 s/mm^2,71 directions, 1 mm isotropic voxels (probably interpolated)	ROI	**Fx:** ↓FA, ↑MD, ↑RD, ↑AD α ↓information processing speed and episodic memory (BVMT-R, SDMT). ↑MD, ↑RD, ↑AD (R) α ↑EDSS. ↑FA, ↓MD, ↓RD, ↓AD α ↑Hp volume.
Pardini et al. 2014 *(Hippocampus)* [259]	25 RRMS (EDSS≤ 3.0), 19 HC	1.5T, b=1000 s/mm^2, 15 directions, 0.94 mm isotropic voxels (probably interpolated)	TBSS (normalized Hp volumes also calculated)	**Cg:** ↓FA in L&R Cg ventral division in MS vs HC. No correlations with lesion load or Hp volumes. ↓FA in L Cg α ↑retrospective memory (PDQ-RM). **UF:** ↓FA in L&R UF in MS vs HC. No correlations with lesion load or Hp volumes. ↓FA in L UF α ↑prospective memory (PDQ-PM).
Debernard et al. 2015 *(Psychiatry Res. Neuroimaging)* [270]	60 RRMS (20-51 years, onset 0-15 years), 30 HC	3 T, b=1000 s/mm^2, 64 directions, voxel size 1.95×1.95×3 mm^3	DTI corregistered to T1w automatic segmentations (Th, Hp and remaining deep GM).	No DTI differences in any deep GM structure in MS vs HC.
Kern et al. 2015 *(Neuroimage Clin.)* [274]	27 RRMS, 20 HC	3 T, b=1000 s/mm^2,30 directions, 2 mm isotropic voxels	Tractography (FA=0.3, ∢=70˚)	**Fx:** ↓FA in RRMS vs HC. **Cg:** ↓FA in RRMS vs HC. **UF:** ↓FA in RRMS vs HC. ↓FA α ↓ information processing speed (SDMT, PASAT) and ↓spatial memory (7/24 spatial-recall tests).
Koenig et al. 2015 *(Mult. Scler. J.)* [411]	57 MS (44 RR, 13 SP), 17 HC	3 T, b=1000 s/mm^2, 71 directions, 1 mm isotropic voxels (probably interpolated)	ROI	**Cg:** ↓FA, ↑MD, ↑RD, ↑AD in MS vs HC. ↓FA, ↑MD, ↑RD α ↓ information processing speed and episodic memory (BVMT-R, SDMT).
Louapre et al. 2016 *(Radiology)*	34 MS, 17 HC	3 T, b=700 s/mm^2, 60 directions,	TBSS (along the tracts)	**Cg:** ↓FA (mainly central area) in MS vs HC. ↑RD (proximal and middle portions) α ↑ information processing

[275]		voxel size 1.85×1.85×1.85 mm^3		speed (SDMT) (and ↑quantitative T2*).
Meijer et al. 2016 *(Mult. Scler. J.)* [272]	30 SPMS, 32 HC	3 T, b=1200 s/mm^2, 61 directions, 2 mm isotropic voxels	TBSS	**Fx:** ↓FA, ↑RD in MS vs HC (and in CI SPMS vs controls and not CI SPMS). ↓FA, ↑RD α ↑CI index. **UF:** ↓FA, ↑RD in MS vs HC (and in CI SPMS vs controls and not CI SPMS). ↓FA, ↑RD α ↑CI index.
Keser et al. 2017 *(J. Neuroimaging)* [209]	46 MS (39 RR, 7 SP)	3 T, b=1000 s/mm^2, 21 directions, voxel size 2×2×3 mm^3	Tractography (FA=0.15, ∢=70˚)	**Fx:** ↓FA, ↑RD in CI MS vs not CI MS. ↓FA, ↑RD α ↑CI index. **Cg:** ↓FA, ↑MD (L) in CI MS vs not CI MS. ↓FA, ↑MD, RD (R). ↓FA, ↑RD (R) α ↑CI index. **UF:** ↓FA (L) in CI MS vs not CI MS.
Planche et al. 2017 *(Mult. Scler. J.)* [329]	32 MS (27 RR, 3 SP, 2 PP), 36 HC	3 T, b=1000 s/mm^2, 20 diffusion directions, 1.6 mm isotropic voxels	DTI corregistered to T1w automatic Hp segmentations	**Hp:** ↓FA, ↑MD in MS (followed by CIS) vs HC. ↓MD α better long-term recall (delayed recall in SRT).
Bergsland et al. 2018 *(Hum. Brain Mapp.)* [269]	45 MS (26 RR, 17 SP, 2 PP), 17 HC	3 T, b=1000 s/mm^2, 21 directions, 2.5 mm isotropic voxels	TBSS (applied to skeletonized thalamic WM)	**Th:** ↓FA, ↑MD in MS vs HC. ↓MD α information processing speed (SDMT) and verbal episodic memory (BVMT-R, CVLT-II).
Keser et al. 2018 *(Front. Neurol.)* [210]	40 MS (36 RR, 4 SP) (30 CI, 10 not CI)	3 T, b=1000 s/mm^2, 21 directions (Icosa21), voxel size 2×2×3 mm^3	Tractography (FA=0.15, ∢=70˚) for Fx, Cg, and UF. DTI corregistered to T1w automatic Hp & Th segmentations	**Fx:** ↑FA α long delayed free recall in verbal learning (CVLT-II), information processing speed (SDMT), and phonemic and semantic fluency (COWAT). **Cg:** ↑FA, ↓MD (R) α information processing speed (PASAT). **Hp:** ↓MD α information processing speed (PASAT) and visuospatial skills (JLO). **Th:** ↓MD (R) α PASAT.
Koubiyr et al. 2018 *(Front. Neurol.)* [314]	56 CIS, 38 HC (46 CIS & 20 HC re-scanned a year after)	3 T, b=1000 s/mm^2, 21 diffusion directions, 1.6 mm isotropic voxels (irregular MD values)	DTI corregistered to T1w automatic deep GM segmentations	**Hp:** ↑MD at baseline in CIS vs HC (only deep GM structure that showed baseline changes). After a year, ↑MD in the L frontal, temporal, cingulate and bilateral parietal lobes CIS vs HC.

Woitek et al. 2020 *(Acta Radiologica)* [412]	14 MS (7 SP, 7 PP)	3 T, b=800 s/mm², 32 diffusion directions, voxel size 1.75×1.75×2 mm^3	Manual FLAIR segmentations of substantia nigra, red nucleus, and all deep GM except Hp and registered to DTI	No DTI differences in SPMS vs PPMS.
Beaudoin et al. 2021 *(Front. Neurosci.)* [413]	24 RRMS, 11 HC	3 T, 8 b=300 s/mm^2, 32 b=1,000 s/mm^2, 60 b=2,000 s/mm^2 directions, 2 mm isotropic voxels	Probabilistic tractography (10 seed per voxel and 0.1 fODF amplitude threshold)	**Fx:** No differences in MS vs HC. **Cg:** ↓FA, ↑MD in L Cg in MS vs HC. **UF:** ↓FA, ↑MD in MS vs HC.
Bernabeu-Sanz et al. 2021 *(Diagnostics)* [414]	30 MS, 30 HC	3 T, b=800 s/mm², 32 directions, 2 mm isotropic voxels	TBSS & tractography	**Fx:** ↓FA, ↑MD in MS vs HC. **Cg:** ↓FA, ↑MD in MS vs HC. **UF:** ↓FA, ↑MD in MS vs HC.

EDSS: Kurtzke Expanded Disability Status Scale, CVLT: California Verbal Learning Test, BVRT: Benton Visual Retention test, BVMT-R: Brief Visuospatial Memory Test-Revised, SDMT: Symbol Digit Modalities Test, PASAT: Paced Auditory Serial Addition Test, RAVLT: Rey Auditory Verbal Learning Test, PDQ: Perceived Deficits Questionnaire, COWAT: Controlled Oral Word Association Test, JLO: Judgment of Line Orientation, SRT: Selective Reminding Test, HC: Healthy controls, RR: relapsing remitting, SP: secondary progressive, PP: primary progressive, CIS: Clinically isolated syndrome, ROI: Regions of interest, TBSS: Tract-based spatial statistics, VBA: Voxel based analysis, α: correlated/related to, fODF: fiber orientation distribution function

Appendix D: Fornix Tracts for the Healthy and MS cohorts at 3 T for Chapter 3[4]

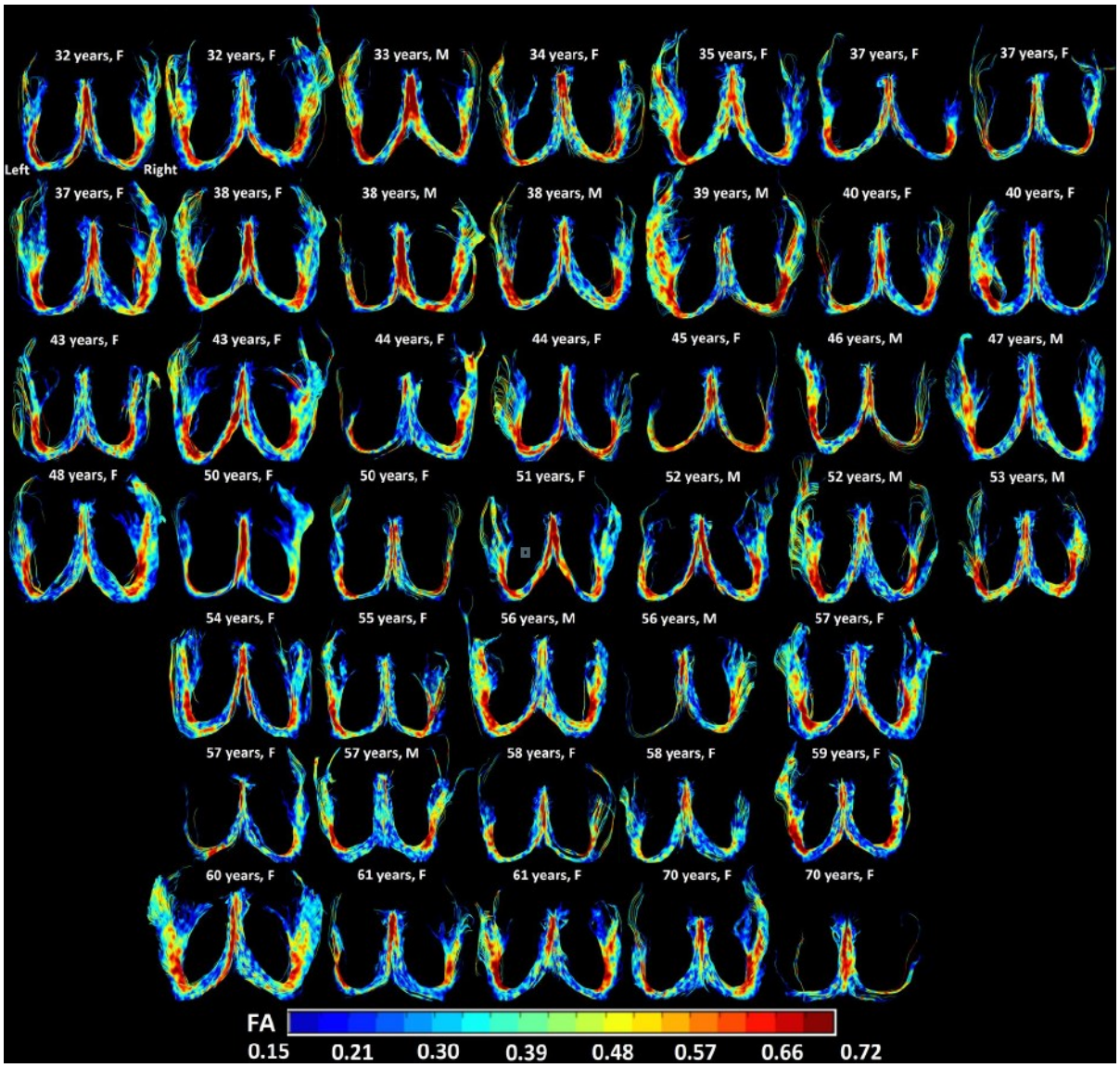

Figure D.1: All fornix tracts (viewed from above in neurological format) for the healthy cohort (n=43) are shown here with an FA color encoding scale. Fornix tracts are equally scaled for size and were sorted by age with each participant's age and sex listed. Fornix FA and tract volume (to a lesser degree) appear to decrease with healthy aging.

---

[4] Published as Supplementary Material in: Valdés Cabrera, D., Smyth, P., Blevins, G., Emery, D., & Beaulieu, C. Diffusion imaging of fornix and interconnected limbic deep grey matter is linked to cognitive impairment in multiple sclerosis. European Journal of Neuroscience 2022, 55(1), 277– 294. https://doi.org/10.1111/ejn.15539.

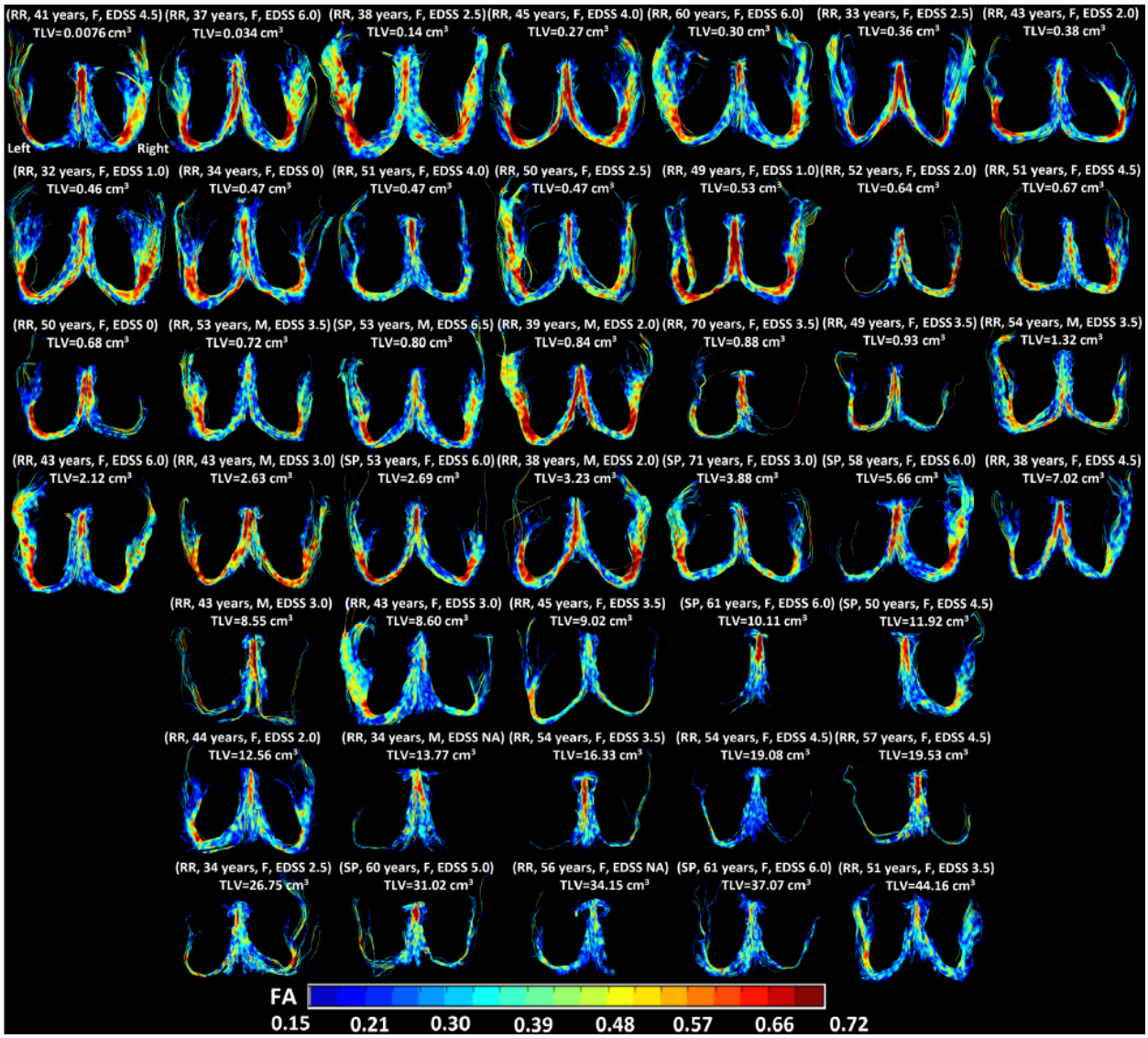

Figure D.2: All the fornix tracts (viewed from above in neurological format) for the entire MS cohort (n=43) are shown here with an FA color encoding scale. Fornix tracts were sorted by total lesion volume (TLV) with each MS participant's MS phenotype, age, sex, EDSS score, and TLV in cm³ listed. Fornix volume and FA both tend to decrease with greater TLV particularly above 10 cm³.